Faculty of Electrical Engineering
Department of Measurement

Precise Magnetic Sensors and Their Applications

Habilitation Thesis

Prague, 2024 **Vojtěch Petrucha**

Content

Preface

This habilitation thesis is a compilation of multiple papers that reflect my work in the field of magnetic sensors, their calibration, and applications. A vast majority of the papers are published in journals listed in the Web of Science, predominantly showcasing research presented at prestigious international conferences focused on magnetism, sensors, and measurements. A few of them are published in conference proceedings. Generally, the topic concentrates on the development of precise, highly linear, and low-noise sensors intended for vectorial measurement of "Earth-like" magnetic fields (with a magnitude typically below 100 μT). The proper development of the sensors and magnetometers is closely related to the calibration of the devices, which allows for the characterization of their properties and continually improves upon those parameters. Therefore, several papers are concentrated on this topic. Very useful feedback comes also from the real applications of the sensors; thus, several examples primarily from the field of geomagnetism or electric current measurement are mentioned. A short section at the beginning of this thesis explores current state-of-the-art in the field of magnetic sensors in relation to the thesis objective. This paper will later also discuss the instruments and results developed within various projects in recent years, which demonstrate some possible applications of magnetic sensors. The aim of this thesis is to compile all these papers and information into a cohesive framework, facilitating faster orientation in this field.

Pronouncement

Almost all the papers mentioned in this thesis have co-authors, typically comprised of members of the Sensors and Magnetics Laboratory (**MAGLAB.cz**) at the Department of Measurement, the Faculty of Electrical Engineering, Czech Technical University in Prague, as well as a few external and international co-authors. Namely Pavel Ripka, Petr Kašpar, Antonín Platil, Michal Janošek, David Novotný, Michal Dressler, Mattia Butta, and others. Formally, the author's contribution to each paper (ranging from 10% to 100%) is mentioned in a short foreword presented prior to each paper and is also summarized in paragraph 6.1.

Acknowledgement

I would like to thank all my colleagues and co-authors of the papers for their kind support and for creating a pleasant atmosphere that makes my research and work on these projects both enjoyable and fascinating. I would also like to express my special gratitude to my former supervisor, P. Kašpar, for his continuous kind support and valuable advice. I extend the same thanks to the head of **MAGLAB** group, P. Ripka, who has helped me in my endeavors ever since I became engaged with magnetic measurements sometime back in 2004 during my master's degree studies. I would also like to thank J. Holub for his patience and support. And of course, I wish to thank my family for their unlimited support and love.

Most of the research presented in this thesis was supported by several grants: Czech Technical University in Prague SGS grants (SGS10/206/OHK3/2T/13, SGS18/081/OHK3/1T/13, SGS19/177/OHK3/3T/13, SGS22/170/OHK3/3T/13), Czech Science Foundation (13-39088P, 16-10591Y, 20-19686S), Technology Agency of the Czech Republic (TA01010298, TE02000202), Ministry of interior (VI20172019089), European Commission (FP7-SPACE, ISP-1, 218849), and European Space Agency (AO10986 - LVICE2).

1 Introduction & Motivation

Magnetism. An invisible yet powerful force that has fascinated humans since the first observations thousands of years ago. Quite well described since the nineteenth century, it still offers many phenomena awaiting discovery and theoretical explanation, for example, in magnetic material science and quantum effects. With countless applications in science, industry, medicine, and everyday life. Continuous research in the field of magnetism brings new knowledge and practical outputs. Some breathtaking applications that were not possible before have been brought to life thanks to new developments in material science and technology. In order to properly study and use magnetism, we must be able to measure its effects. This work is focused on the development of magnetic sensors, related technologies, and some applications of these sensors.

A magnetic compass with fluxgate sensors was the subject of the author's master thesis, in which he encountered magnetic sensors more seriously for the first time. Since then, the fascinating combination of physics, material science, analog and digital electronics, mathematics, programming, and countless applications has helped maintain his interest in the subject. He simulated, developed, used, or applied magnetic sensors in many projects. Some of them are mentioned in the text, some are described in the attached papers.

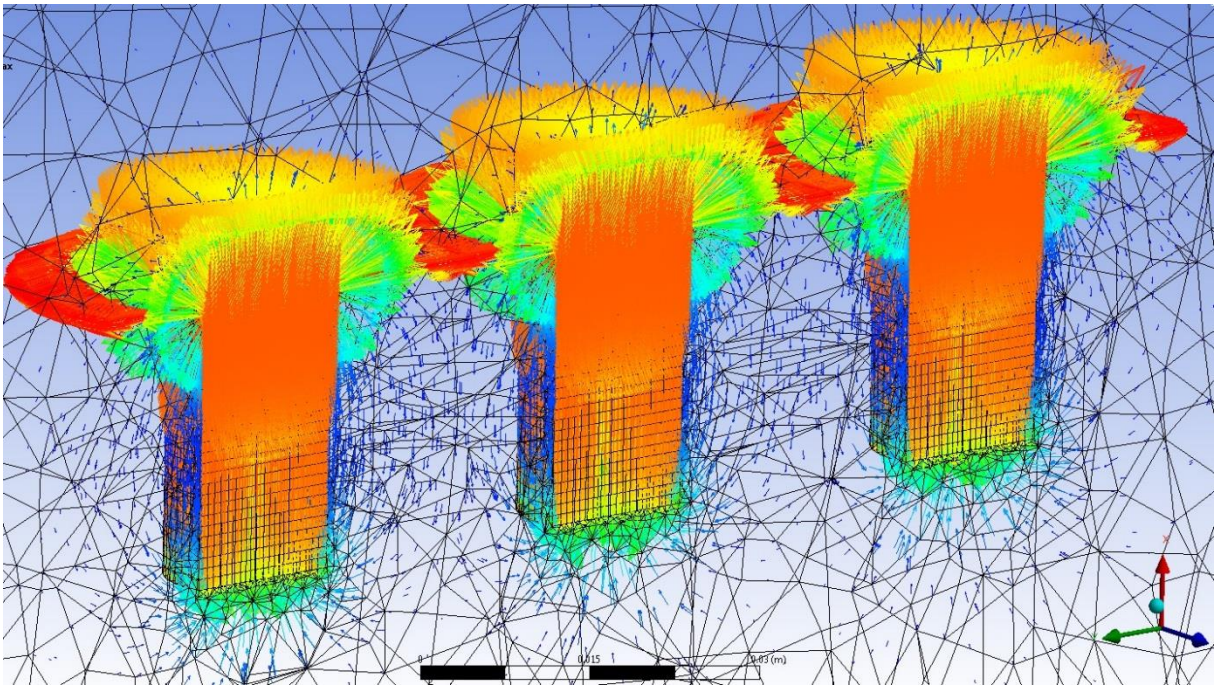

The beauty of FEM magnetic field simulation (ANSYS Magnetostatic, triple SmCo annealing setup)

2 Magnetic Sensors

In the following text, “magnetic sensor” is understood to be a device that measures magnetic induction in Tesla units. Either as a scalar sensor, which can sense only the magnitude of the magnetic field vector, or as a vectorial sensor that can independently measure all three mutually orthogonal components of the magnetic field vector. To be more specific, this thesis, deals more in detail with sensors that are able to measure static and low-frequency (typically below 50 Hz) magnetic fields with magnitudes below 100 µT, which roughly corresponds to the value of a geomagnetic field (typically 20...65 µT).

Some of the principles of magnetic field sensing have been well known for decades (Hall sensor, Fluxgate, Magnetoresistance – AMR, GMR, TMR) and the current development aims to improve performance of these sensors, decreasing noise, dimensions, power consumption, etc. For example, the latest development in orthogonal fluxgate technology allows for the use of sensors for biomedical applications where recently only very expensive and big SQUID-based units were applied [1-4]. But also, entirely new principles are appearing, exploring quantum effects and progress in material science and technology – e.g. magnetic sensors based on nitrogen vacancy centers in diamonds [5-9] or miniature and ultra-low-noise optical scalar and vector magnetometers [10-35]. The following chapters provide a brief overview of magneto-resistive, fluxgate, and scalar sensors and magnetometers, as those are closely related to the author’s work and presented thesis and it is interesting to observe their current state-of-the-art.

2.1 Magneto-resistive sensors

Electrical resistance is the measurement quantity for magneto-resistive sensors of a magnetic field. The first was the AMR effect, which was discovered in as early as 1856 by William Thomson; it is still used for precise sensors, as it offers relatively high linearity, low hysteresis, and low noise. The drawback is a higher power consumption, both due to lower resistance of the sensing elements (typically 100-2000 Ω) and the typical use of flipping to re-align the magnetic domains and reduce offsets, perming, and temperature effects [36]. The principle of the AMR effect is a quantum mechanical property of electrons, anisotropic scattering probability. When the magnetization is parallel to the current traveling through the conductor, which is most often from magnetic material (Fe, Ni, Co), the resistance is the highest. The AMR effect can be relatively easily demonstrated with a strip of magnetic material, current source, and voltmeter. With a piece of 20 µm-thick amorphous METGLAS 2714A and 1 A constant current source, the measured resistance was 175 mΩ and the change 0.01 % (magnetization direction change provided by a rotation of NdFeB permanent magnet). For a 0.25mm-thick strip of Permalloy79, the resistance was 6.3 mΩ with a resistance change of 0.8% (both measured with a 6.5-digit Agilent 34401 DMM). See Figure 1.

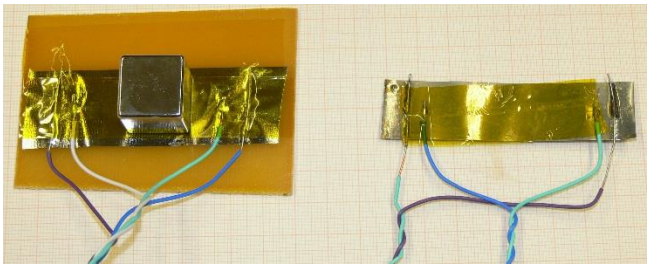

Figure 1. A four-wire, magneto-resistance measurement on the MG2714A (left) and Py79 (right)

The GMR effect was discovered independently by Albert Fert and Peter Grünberg in 1988. It relies on the dependence of electron scattering on spin orientation. In this case, in a sandwich of two magnetic layers separated by a non-magnetic but electrically conductive layer. The thickness of the layers is in nanometers. The GMR effect offers a much higher resistance change when compared to AMR, higher electrical resistance, but the response is typically non-linear with a higher hysteresis, making it useful more for switching or position detection applications rather than for precise bipolar magnetic field sensing [37].

The TMR effect was first observed in 1975 by Michel Jullière and has been investigated ever since. The breakthrough came after the year 2000 when Fe/MgO/Fe junctions proved promising. Tunnel magneto-resistance is again a purely quantum mechanical effect as an electron tunnel through a thin, electrically non-conductive layer sandwiched between two ferromagnetic layers. TMR sensors are currently largely deployed in numerous applications (Hard-drive read heads, angle and position sensing, compassing…) as they offer high resistance and thus lower power consumption when compared to AMR or Hall-effect sensors [38-43].

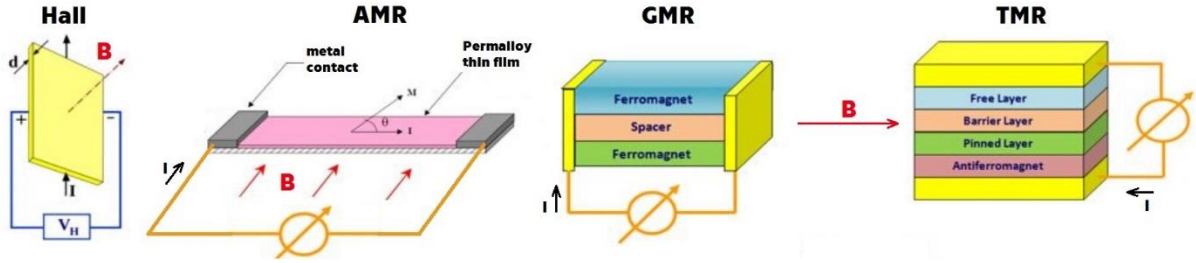

Figure 2. Four technologies of magnetic field sensing, AMR and TMR providing the lowest noise (source: modified from dowaytech.com)

For practical application, the manufacturers supply either the individual sensing elements (preferably arranged into Wheatstone bridge with additional supporting elements, e.g. coils) or complete triaxial sensors with digital outputs. The individual elements are useful for the construction of high-precision sensors with a higher dynamic range than is common for the integrated sensors (limited by 16- to 20-bit internal ADCs). Several constructions available on the market rely on the AMR sensors manufactured by Honeywell, either the HMC1001, the 1002, or the 1021, or similar [44-46].

Table 1 gives a summary of currently commercially available sensor elements. The noise parameters are datasheet values; several sources suggest significantly lower values for some parts [47, 48]. For example, the TMR9082 is currently 46x times more expensive than the HMC1021, but theoretically offers 27x lower power consumption (only on bridge power). Unfortunately, there is not much published data concerning the sensor's testing. Even though the principle of AMR is simple, the technological implementation and manufacturing of a low-noise sensor element is still challenging. Around 2015, the company Sensitec introduced an AMR sensor called the AFF755B, which is basically an alternative to the Honeywell HMC1021. Our testing has indicated that some of the devices suffer from excessive, low-frequency noise caused probably by bad quality or treatment of the magnetic layer and/or an unideal flipping coil configuration **[refP 14]**. Fortunately, Honeywell still maintains production of the HMC1021, but even in this case we observed some less and more noisy batches of the parts.

Table 1. Commercially available, single-axis, magneto-resistive sensors without embedded signal conditioning or ADC

Part	Vb (V)	R (Ω)	Range (μT)	Noise (pT/√Hz @1Hz)	Linearity (±% FS)	Manufacturer	Technology
HMC1001	2-12	850	±200	187, Vb = 5V	0.2 (±100 μT)	Honeywell	AMR
HMC1021	2-12	1 100	±600	960, Vb = 5V	0.2 (±100 μT)	Honeywell	AMR
AFF755B	1.2-9	2 500	±500	168, Vb = 5V, >100 Hz	0.15 (±100 μT)	Sensitec	AMR
AMR2501	1.8-12	700	±200	100	0.2 (±100 μT)	Dowaytech	AMR
AA002-02E	1-24V	5 000	150-1050	not specified	2, 4 % hyster.	NVE	GMR
TMR9082	1-3	30 000	±100	250	0.4	Dowaytech	TMR
ALT021-10E	0-10	20 000	±250	4000	2	NVE	TMR
STJ-210	0.01-12	10 000	±100-1000	5k (>100 Hz)	0.25 (±100 μT)	MicroMagnetics	TMR
CT100	1-5.5	30 000	±50 000	31k (at 10Hz)	0.5 (±20mT)	Murata (Crocus)	TMR

The market for magneto-resistive, triaxial, magnetic field sensors with digital output seems to be currently dominated by TMR technology (see Table 2). In our lab, the Memsic MMC5883 and the newer MMC5983 are extensively used for applications where the required precision allows for that. The newly available AK09940A based on TMR should offer the same noise but requires only < 50 % of power. Unfortunately, the datasheet does not mention the linearity performance of the device at all. The price of the AK09940A is currently 165% of the MMC5983. The Hall-based sensor (AK09919) is mentioned only for comparison; the sensitivity is significantly worse, measurement range and power consumption higher, but the mechanical dimensions are extremely small (0.8 x 0.8 x 0.5 mm), making it suitable for space-constrained applications (e.g. smart watches, mobile phones, or miniature robots). Interestingly, there is a device with exactly the same size also offered by MEMSIC (the MMC5603NJ), made with AMR technology, offering a ±3 mT measurement range and 20-bit resolution.

Table 2. Best-performance, magneto-resistive (+Hall) sensors available with integrated signal conditioning electronics

Part	Vcc (V)	I (μA)	Range (μT)	Noise	Lin (±% FS)	Manufacturer	Note
ADAF1080	4.5-5.5	6500	±8000	80 nT_{RMS}	0.2 (±2mT)	Analog Devices	AMR, single axis, analog
RR112-1D92-532	1.7-5.5	40	±2000	not specified	not specified	RedRock	TMR single axis, analog
BM1422AGMV	1.7-3.6	150	±1200	not specified, 42 nT/LSB	0.5	ROHM semiconduct.	magneto-imped., triaxial, digital
AK09919	1.65-1.95	1500	±4912	not specified, 150 nT/LSB	not specified	AsahiKASEI	Hall, triaxial, digital
MMC5983	2.8-3.6	450	±800	40 nT_{RMS}	0.1, 0.01 hyster.	Memsic	AMR, triaxial, digital
LIS3MDL	1.9-3.6	270	±400…1600	320 nT_{RMS}	0.12	ST Micro	TMR, triaxial, digital
BMM350	1.8 (IO to 3.6)	350	±2000	x,y 190 nT_{RMS}, z 450 nT_{RMS}	0.5, 0.02 hyster.	Bosch	TMR, triaxial, digital
AK09940A	1.8 (IO to 3.6)	200	±1200	40 nT_{RMS}	not specified	AsahiKASEI	TMR, triaxial, digital
MAG3110	1.95-3.6	900	±1000	250 nT_{RMS}	0.3, 0.25 hyster.	NXP	TMR, triaxial, digital

Figure 3. An interesting multi-chip inner structure of a modern TMR sensor, source: Yolo SystemPlus, 2023

Commercial magnetometers based on magneto-resistive sensors (currently mostly AMR sensors) are used for various purposes, ranging from general field monitoring, navigation, position measurement, sensing electric currents, and magnetic material detection to more specific tasks like parking lot occupancy detection (which might be quite tricky due to extremely different magnetic signatures of modern cars) or non-destructive testing. The long-time produced HMR2300 by Honeywell can be a typical representative of this class. The HMR2300 is based on three HMC1001 sensors and three 16-bit $\Delta\sum$ AD converters for simultaneous sampling of the measured magnetic field. Sensors are integrated with the read-out electronics, which limits performance as the offset can easily be changed by magnetization of the nearby components via strong external fields. See Figure 4 for the concept and Table 3 for the basic parameters.

High-performance magnetometers based on AMR sensors are often used for space-research applications, either as a main scientific instrument for smaller satellites, as part of an Attitude Determination and Control System (ADCS), or as part of a scientific magnetometer package to de-noise the main sensor data by measuring the disturbances produced by the satellite itself – typically for missions with a limited main magnetometer sensor boom length (SOSMAG instrument [49]). Figure 5 and Figure 6 present two space magnetometers; both again use three HMC1001 sensors and both have a remote sensor head. The magnetometer for the small cubesat project Trio-CINEMA uses commercial off-the-shelf (COTS) components, while the magnetometer for the GEO-KOMPSAT-2A mission seems to be built using space-qualified components.

Figure 4. The Honeywell HMR2300, an AMR-based triaxial magnetometer with digital output

+

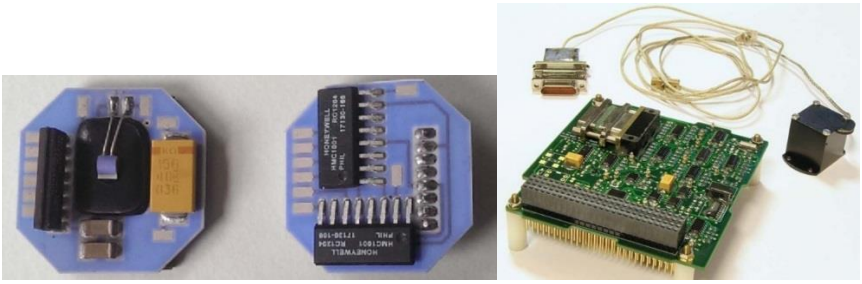

Figure 5. An AMR-based magnetometer for the Trio-CINIEMA mission, left: sensor head built on the HMC1001 AMR sensors, right: electronics in PC104 format, source: Brown 2014 [48]

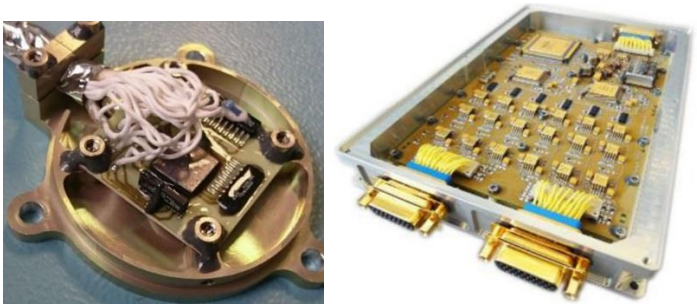

Figure 6. An AMR triaxial sensor head (HMC1001-based) and signal electronics made using space-qualified components, part of a SOSMAG package deployed on the GEO-KOMPSAT-2A satellite, source: W. Magnes, 2020 [49]

Our development, which is described in the applications chapter (4.1), concentrates on the application of integrated AMR sensors with digital output for laboratory tools and a middle-class AMR magnetometer built using HMC1021 sensors and COTS components. The slightly noisier HMC1021 is used because it offers a much more favorable compensation coil constant than the HMC1001 (4.6 mA versus 47.5 mA / 100 µT), which helps to decrease overall power consumption. At first, we tested signal conditioning based on traditional analog signal processing and DAQ **[refP 1]**, later the digital signal processing was used **[refP 2]**. The direct competitor to the miniDAMR (miniature digital AMR magnetometer) is NewSpace's Pegasus-1 (see Table 3), which is a bit worse in terms of noise and power consumption. Until now, it seemed unreasonable mainly due to limited financial resources to cooperate within the university or even with an external entity (several companies have IC design centers in the Czech Republic) on development of a specific ASICs for AMR or fluxgate sensor signal conditioning [50, 51], as this might help to improve the radiation hardness of the instrument. We concentrated on radiation testing of the current concept instead (described in [**refP 3]** and He nuclei testing mentioned in [**refP 17]**).

Table 3. Magneto-resistive sensor-based magnetometers

Part	Vcc (V)	Power (mW)	Range (µT)	Noise /√Hz @1Hz	Lin (±% FS)	Manufacturer	BW(Hz) -3dB	Note
STJ-3D	<24V	?	±2000	10nT	not specif.	MicroMagnetics	DC-7MHz	TMR, triaxial, analog output (960 USD)
HMR2300	6-15	250	±200		± 0.12 for 80 µT	Honeywell	10-154 Sa/s	AMR, triaxial, RS422 / 485
MAGIC	12	<1000	±60	2nT sensitivity	not specif.	Imperial College London	1-10 Sa/s	AMR, triaxial
PEGASUS-1 [NMRM-Bn25o485]	5	<750	±60	<16 nT *	not specif.	NewSpace Systems	25 Hz update rate	AMR, triaxial, RS485
MM200	?	<10mA	±800	1.18 nT	not specif.	aac-clyde space	<500 Sa/s	I2C interface
VMR	5-12	450	±100	300 pT	not specif.	Twinleaf	>200	GMR?, triaxial, serial interface
miniDAMR v1.2	4.5-5.5	<600	±100	<300 pT	± 0.01	CTU in Prague/FEE /MAGLAB	126/3906 Sa/s	AMR, triaxial, UART-422/485 interface
DSTASM**	4.5-5.5	150 / channel	±80	12nT resolution	0.022, 1σ	Honeywell	20 Sa/s	dual redundant triaxial AMR (HMC1022, 1021), RS422 - CAN

* datasheet: <16 nT rms/Hz @ 1 Hz (Hz or √Hz?)

**Dual String Three-Axis Space Magnetometer

An interesting instrument is the VMR by Twinleaf. The labeling on its package as well as a note in the data processing description suggest that it uses GMR sensors, but the author has not found any corresponding commercially available part that could be used (low in noise, linear GMR sensor with bipolar response).

2.2 Fluxgate sensors

The fluxgate sensor relies on a specific application of Faraday's law of electromagnetic induction (1), where a time-variable, magnetic flux appears and is detected even for a static measured magnetic field due to permeability modulation of the sensor's magnetic core material provided by a driving alternating current. The first publication on the ring-core fluxgate was introduced by Aschenbrenner and Goubau in 1936; the principle still offers excellent noise properties at room temperature. Nowadays, strong competition appears in the form of vectorized quantum magnetometers based, for example, on optically read quantum states of rubidium atoms [22], cesium atoms [18], or defects in silicon carbide [34]. In any case, simplicity, robustness, reliability, history of use, or new discoveries will most likely keep fluxgate sensors in service for decades to come.

$$v_i = N.S.\mu_0.H(t).\frac{d\mu_r}{dt} \quad \text{(V, -, m}^2\text{, H/m, A/m)} \tag{1}$$

The author's work concentrated exclusively on the development and application of so-called parallel fluxgate sensors of ring-core or race-track topology (see Figure 7) where the measured and excitation magnetic fields are parallel. Recently the performance of a different type - orthogonal fluxgate sensors - was significantly improved, reaching sub-picotesla noise levels even at sub-Hertz frequencies [1-4]. That makes them competitive with modern quantum optical sensors for various applications including geological prospection or biomedical measurements [2]. The drawback with respect to parallel fluxgates seems to be currently a worse time/temperature offset stability (<50pT/K versus tens of nT/K) making the parallel fluxgates more suitable, for example, for geomagnetic field observatory monitoring or all applications where absolute field value is important and not only the variations, even though there was also a significant improvement achieved for the orthogonal fluxgate by application of bias switching technique [3, 52, 53].

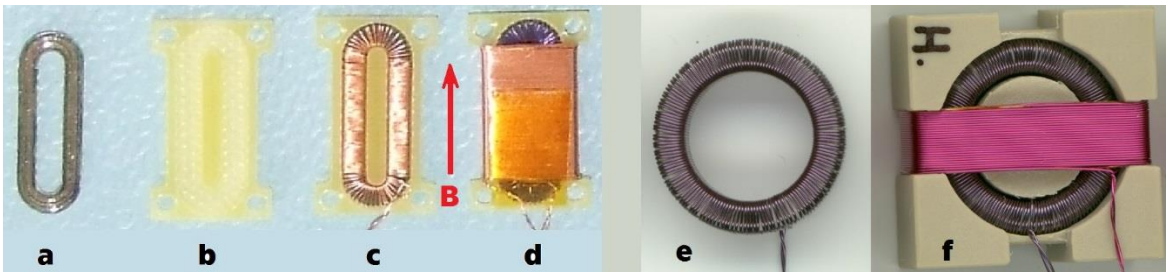

Figure 7. Construction of the fluxgate sensor with a race-track core (a,b,c,d) and ring core (e,f). "a" is a flat amorphous magnetic core in a holder, "b" is a pick-up holder, "d" and "f" are finished sensors with a sensitivity direction indicated by the red arrow, in "e" the core is already covered by excitation winding.

There are numerous possibilities of how to construct the sensors and a sensor head in case of a triaxial magnetometer as well as the signal conditioning. In this thesis, two concepts of a sensor head design can be found (Figure 8). The first one uses three single-axis or two dual-axis sensors and the compensation field is created directly within the sensors [54-57] (fluxgate sensors are usually operated as zero indicators where the measured magnetic field corresponds to the compensation current). This simple topology is used in the UAV magnetometer (section 4.2.2). Vectorial compensation is another concept where the compensation field is common for all the sensors. This topology is typically used for high-performance scientific magnetometers as it offers better time/temperature stability, but at the price of increased mechanical complexity and cost [49, 58-62]. This concept was explored in **[refP 4]** and **[refP 5]**, and applied in **[refP 12]**. Digital signal conditioning of the pick-up and compensation signals is often used for magnetometers deployed in space [63-66], where the digital circuits better resist the radiation. In the scope of this thesis a classical approach of analog signal processing followed

by high-precise analog-to-digital conversion was used with good results. Recently we explored the digital processing principle in [**refP 7]** (fluxgate sensor signal processing in FPGA).

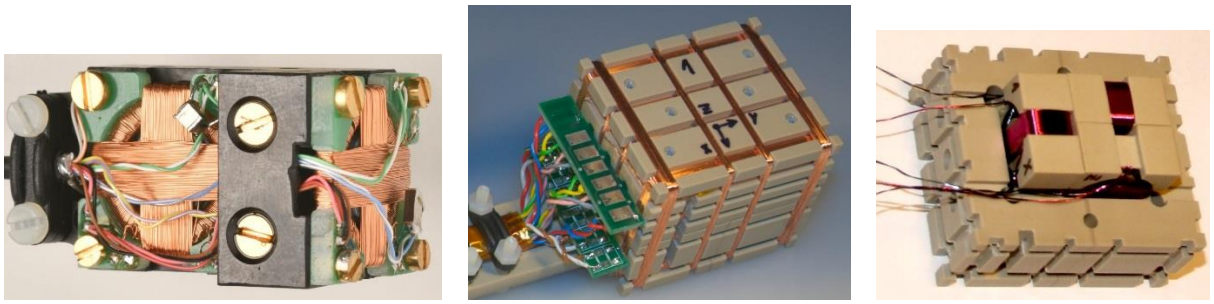

Figure 8. Left: UAV magnetometer individually compensated sensor head with two dual-axis sensors, right: vectorially compensated sensor head with three single-axis ring-core sensors inside

It seems that there are currently no fluxgate sensors available on the commercial market, meaning only the sensors (ring-core, race-track, or Vacquier) without any additional electronics - driving and/or signal conditioning. This is probably due to a relatively small market for these devices and the fact that it requires some precise handling and optimal electrical parameters for each specific type to work as expected. Table 4 summarizes currently available, single-axis sensors mostly from the category of low-precision types intended for more basic applications. There is one specific part among them – the DRV425 - currently the only commercially available, chip-scale-integrated fluxgate sensor produced by Texas Instruments, for example, for current measurement applications - [**refP 15]**. We applied the sensor also in [**refP 16]** (a laboratory magnetic field probe with USB output, useful, for example, for EMC measurements).

Table 4. Single-axis fluxgate sensors

Part	Vcc (V)	Power (mW)	Range (µT)	Noise /√Hz @1Hz	Lin (±% FS)	Manufacturer	BW(Hz) -3dB	Note
FL1-100	±12 to 16	540	±100	<20 pT	not spec.	Stefan Mayer Instr.	0-1 kHz	analog output; 0.1 V/µT, max. ±10 V; <0.1 nT/K offset drift; 10g
FLC 100	5	10	±100	~150 pT	not. spec.	Stefan Mayer Instruments	0-1 kHz	analog output ±1 V/50 µT, max. ±2,5 V; 2 nT/K offset drift
FG-3+	4.5-5.5	60	±50	not. spec.	not. spec.	FGsensors	0-20 kHz	period vs. field output
Mag646	±11-17	230	±100-1000	>10 - ≤25pT	0.01%	Bartington	0-1 kHz	analog output ±10V; 1nT/K; 10 g
DRV425	3-5.5	35	± 2000	1.5 nT (1kHz)	0.1 %	Texas Instruments	0-32 - 47 kHz	analog output; 1.55 nT/K chip-scale sensor

The author of the thesis developed, manufactured, and tested multiple triaxial, vector fluxgate magnetometers for development and laboratory measurement and calibration purposes. There was a continual effort to develop both the sensors themself as well as the corresponding signal and data acquisition electronics. Sensor development is tied to the development of the sensor's magnetic core. It is the core material and its properties which mostly define the sensor's performance. Great effort was spent on the annealing (thermomagnetic treatment and/or stress-annealing) of amorphous magnetic materials (e.g. the Metglas 2714AZ, Vitrovac 6025Z, and Vitrokov 8116) typically in the form of a 2.5mm-wide, 15-25µm-thick ribbon. Those ribbons were used as a wound ring or race-track shaped core for the fluxgate sensor. Even though some of them gave promising results, generally the assembly was difficult and suffered from repeatability problems (with noise, excitation feedthrough, temperature stability). Flat cores together with a specific annealing technique were introduced in [**refP 6]** (typically laser-cut from a wide tape - again the amorphous Vitrovac 6025). Noise performance of

samples of various size is presented in [**refP 8]**. Sensors with this flat-core construction were sucessfully applied in various applications. Very useful during the development is a tool for BH-loop measurement. The author recently supervised a bachelor thesis (Nejezchleb 2023 [67]) in which a simple but precise compact module for BH-loop measurement of closed-loop soft-magnetic material was developed.

The noise of a magnetometer with digital output is limited by the available dynamic range of the data acquisition system. A fluxgate sensor with an analog signal processing unit can reach >150 dB of dynamic range. That is extremely difficult to cover in a single-range regime as the best commercially available ADCs offer not more than 145 dB [68]. Two types of AD converters can be used - $\Delta\sum$ or the oversampled SAR. Both of them are currently offered with 32-bit-wide digital output word. The first to appear was the ADS1281, later followed by the LTC2508. Currently the best available ADC (in terms of dynamic range for DC and low-frequency signals) seems to be the AD7177. Instruments with sub-ranging and partial compensation of the measured magnetic field can overcome this DAQ limitation but might have problems with linearity while sweeping over the whole range (which is a problem for application on moving platforms). However, this principle of partial field compensation with a very low-noise constant current source that is fed into a separate compensation coil was used in an observatory magnetometer presented in chapter 4.2.5.

Figure 9. A triaxial vector fluxgate magnetometer with digital output (ADS1281-based DAQ) and a detachable, vectorially compensated sensor (as shown in Figure 8)

Table 5 presents a selection of commercially available, fluxgate-sensor-based magnetometers. The first idea was to list only magnetometers with digital output, but later the table was expanded in favor to show more manufacturers. Some of the instruments present an ADCS solution for space, some are high-performance laboratory instruments or compact sensors for general use. Two instruments offer 32-bit ADC - the LEMI-029 and the DFM32. The LEMI mentions some form of partial field compensation without further description; the DFM32 probably operates as a single-range instrument.

Table 5. Fluxgate magnetometers (a selection of precise instruments with analog and digital output, ADCS space hardened, scientific magnetometers)

Part	Vcc (V)	Power (mW)	Range (µT)	Noise /√Hz @1Hz	Lin (±% FS)	Manufacturer	BW(Hz) -3dB	Note
SpinMeter-Ultra-3D	5V	?	±1000	5nT	not specif.	MicroMagnetics	1000	analog ±10V output and digital USB (9000 USD)
WFG-D-140	+4.9-9	~350	±60/100	2nT	±1%	Wuntronic GmbH	0-70	16-bit ADC; RS232/TTL ASCII/binary;
MAG658	10-20	1000	±524	<10nTrms (digitizer noise)	0.01%	Bartington	>15 Hz	RS422, 62.5 pT/bit; 3nT/K
Spacemag-Lite	5, 3.3	203	±60	>10 to ≤50pT	not specif.	Bartington	0-1000	analog output
MACM	16-40	860	±120	<200 pT, 228pT/LSB	±0.025	MAGSON	not. specif.	fully space-qualified components
MFG-2S	4.5-9 /9-18/ 18-36	800	±65	<15 pT; 10pT typical	not spec.	MAGSON	1/10/50/ 100 Hz sampling	RS422; <10nT/year long-term stab.
DTFM100S	5	110	±80	3nT dig. resolution	<0.05	Billingsley A&D	66 Sa/s	triaxial fluxgate, RS485/CAN, 30kRAD tolerant
DFM32	20-28	1500	±65	<5 pT, 2.6 pT digital noise floor	±0.007	Billingsley A&D	0-3000	RS485, 9600-921600 bd
TAM-2	28	560	±100	<10nTrms (0-100 Hz)	0.05%	MEDA	0-60	Radiation protection >100 kRads, analog output 100kV/T
LEMI-029	±5V & 3.3 V	425	±78, compensated ±5.4	6 pT	not spec.	Lemi Sensors	0-180	32-bit ADC; RS232/SPI
Model 1540	4.95-12V	~400	±65	±0.5 nTpp, 30pT resolution	±0.05	Applied Physics	0-400	22-bit ΔΣADC, RS232/TTL ASCII or binary 20 vectors/s max.; 1nT/K
FGM3D/100	±12... 15V	624	±100	10-20 pT/ 7-10pT	<20ppm	Sensys	0-4000 6.3kSa/s dig. max	analog output with external 24-bit digitizer; 0.3nT/K
DMM*	14-16	1500	±60	8nT resolution	<1%	Antrix Corporation	0-30	16-bit digital interface, fluxgate ring-core techn.

* Digital Miniature Magnetometer

2.3 Scalar sensors - magnetometers

Scalar magnetometers can only measure the magnitude of the magnetic field vector. That can be used for calibration of the main vectorial instrument or when equipped with some extra coil system, it can work in a vectorized mode, and also measure the three components of the magnetic field vector, but often with less precision. Typically, a scalar instrument is a proton precession magnetometer. Even though the first instruments appeared in the late 1950s, they are still produced commercially for mineral, archeological, or UXO exploration (e.g. the SatisGEO PMG-2, Geometrics G-857, or Gemsys GSM-19T). Greatly improved sensitivity, more tolerance to magnetic gradient, lower power consumption, and faster sampling come with an introduction of Overhauser magnetometers [69]. They exploit the Overhauser effect when polarization of electron spins of specific free radicals provided by low-power RF field (e.g. 60.4 MHz for the Gemsys GSM19) is coupled to the protons. Overhauser magnetometers are produced commercially by several companies, e.g. the GEM Systems GSM-19, GeoDevice SmartMag, or Quantum magnetometry laboratory from Ural Federal University (series of POS-x instruments, any website currently unreachable). Even more sensitivity offer instruments based on optically pumped alkali atoms (Cesium, Potassium, Rubidium...) where Zeeman shift of atomic energy levels is used to sense the external magnetic field. Several companies offer magnetometers based on this technology, e.g. the GeoDevice Cesium magnetometer QuantumMag, Geometrics G-864, Scintrex CS-L, or Gemsys GSMP.

The optically pumped magnetometer technology got a big boost during the recent hunt for a chip-scale atomic clock for military purposes. The technology developed is similar to what is needed for magnetic field measurement and thus miniature magnetometers started to appear. Currently there are few companies offering commercial instruments and more groups with sensors in development. Geometrics offers the MFAM developer kit, a laser pumped cesium magnetometer that measures field magnitude in a range of 20-100 µT, with a noise floor of 2 pT/√Hz, but at relatively high power of 8-10 W. Twinleaf offers two interesting products: the microSERF dual-axis vector sensor with a noise of 30 fT/√Hz and operational range of ±200 nT and the OMG gradiometer with two total field sensors with an operational range of 1-100 µT and <0.2 pT/√Hz sensitivity, both relatively power hungry (5 and 6 W). QuSpin provides the dual and tri-axial QZFM Gen-3 instrument with <15 and <23 fT/√Hz respectively, but with a very limited dynamic range of ±5 nT (5 W power consumption). The QTFM Gen-2 total field magnetometer has a much wider dynamic range of 1-150 µT, but the noise is higher <3 pT/√Hz, while the vectorized option has <0.1 nT/√Hz (power consumption is 2.5 W). The company QuantX offers a rubidium atoms-based, compact, quantum total field magnetometer with <1 pT/√Hz sensitivity and a 1-100 µT measurement range.

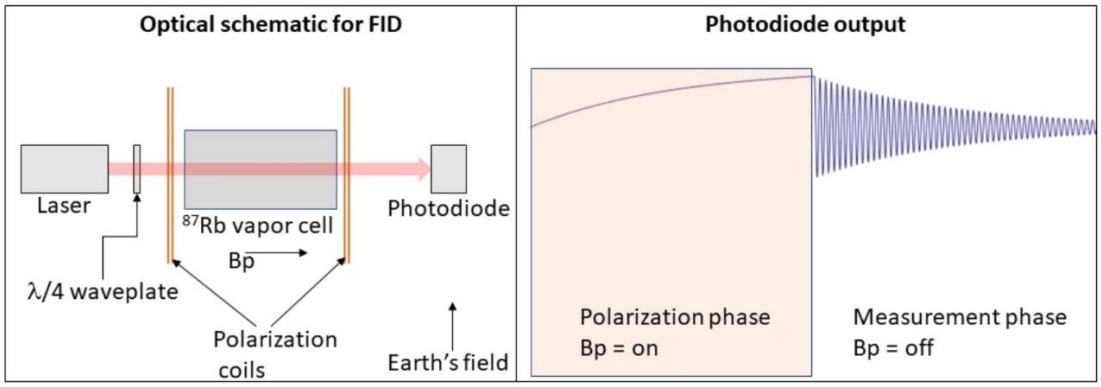

Figure 10 Principle of a pulsed, rubidium, optically pumped magnetometer (left - sensor topology, right - photodiode signal in two phases - polarizing field Bp switched on and off during the measurement phase where free induction decay occurs and the background magnetic field is measured)

Products based on nitrogen vacancy centers in diamonds are in development - Q.ANT promises interesting parameters while SBQuantum is developing diamond quantum magnetometers for vectorial measurements of the Earth's magnetic field within the MagQuest Challenge.

There are also groups developing this kind of scalar instrument (with possible vectorized modes) for applications in space for in-flight calibration of precise, vector, fluxgate magnetometers and as a possible back-up for those instruments. For example, CEA-Leti (with CNES and IPGP support) designed the ASM (Absolute Scalar Magnetometer) for the ESA SWARM mission. This instrument uses optically pumped ^{4}He atoms and Zeeman splitting of the absorption and emission lines to measure the ambient magnetic field with a resolution of <1.4 pT/√Hz (2 nT/√Hz in vector mode). The company continues to research this type of magnetometer, introducing a miniaturized version of the optically pumped magnetometer with 0.7 pT/Hz scalar resolution in the static Earth ambient magnetic field, with possible applications in brain magnetic field imaging - mag4Health. Another interesting instrument is developed in cooperation between the Austrian Academy of Sciences - Space Research Institute and the Technical University of Graz: the Coupled Dark State Magnetometer (CDSM) developed and flown aboard the ESA's JUICE mission to explore the magnetic field of Jupiter. The scalar magnetometer is intended to provide in-flight calibration of vectorial instruments (vector fluxgate magnetometers provided by Imperial College London and TU Braunschweig). The CDSM instrument was flown also on

the Chinese CSES satellite [70]. The CDSM instrument can measure a field of up to 150 µT, with an accuracy of 0.19 nT (σ) while power consumption is 3.4 W and mass 1672 g [16].

The author of the thesis experimented for some time with a proton magnetometer construction and its signal processing. Within a master's thesis (Ondřej Bureš 2021 [71]), several hardware signal processing circuits were tested as well as several principles of proton precession, signal frequency estimation (simple comparator signal processing using a hardware MCU timer, high resolution FFT of a sampled signal, and estimation using an analytical signal derived by Hilbert transform). The best results were provided by FFT processing with a 10 mHz bin width - 0.35 nT (σ). The motivation for this project was partly a curiosity – a demonstration of a quantum mechanical scalar sensor to students and the general public during various events - and it was also a desired supplement for the vector magnetometer - observatory magnetometer (see 4.2.5) for providing online, on-site calibration. Currently, the author is preparing a test of another precession frequency estimation method - based on an iterative use of the Goertzel algorithm that should work easily in the microcontroller of the current magnetometer prototype (STM32F767 with 512 kbytes of SRAM). In this case, the precession frequency is firstly estimated by FFT (with a relatively low order of 10-14) and then iteratively refined by the Goertzel algorithm until the requested precision is reached.

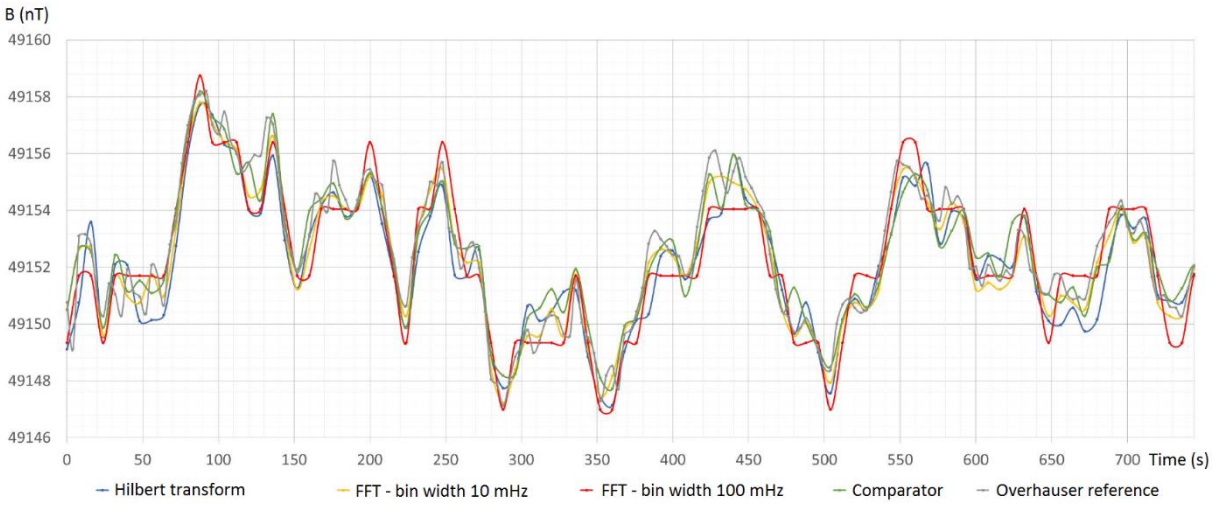

Figure 11. Proton precession magnetometer testing (different precession signal frequency estimation methods) Source: modified from Ondřej Bureš [71]

3 Testing and Calibration of Magnetic Sensors

During the development and deployment of magnetic sensors and magnetometers, it is essential to have the possibility to characterize the main parameters and test the instruments' functionality in conditions as close as possible to the real operating conditions. Preferably the test facility should be available in house to shorten the development cycle. This is problematic for some types of measurements unless extremely expensive infrastructure is available (e.g. a large, magnetically shielded space) because the urban generated magnetic noise can be very intense in the middle of a city environment (Prague city center in our case).

Multilayer magnetic shielding is a basic tool for measurement of the offset and its time/temperature stability. Currently we use several types of three- to six-layer shieldings. The six-layer MuMETAL shield from Magnetic Shield corp. is the newest (two three-layer combined - 9x27" and 12x36"). When

compared to an older six-layer Permalloy shielding (with 50% smaller dimensions), we got significantly smaller noise on lower frequencies (<1Hz), see Figure 12.

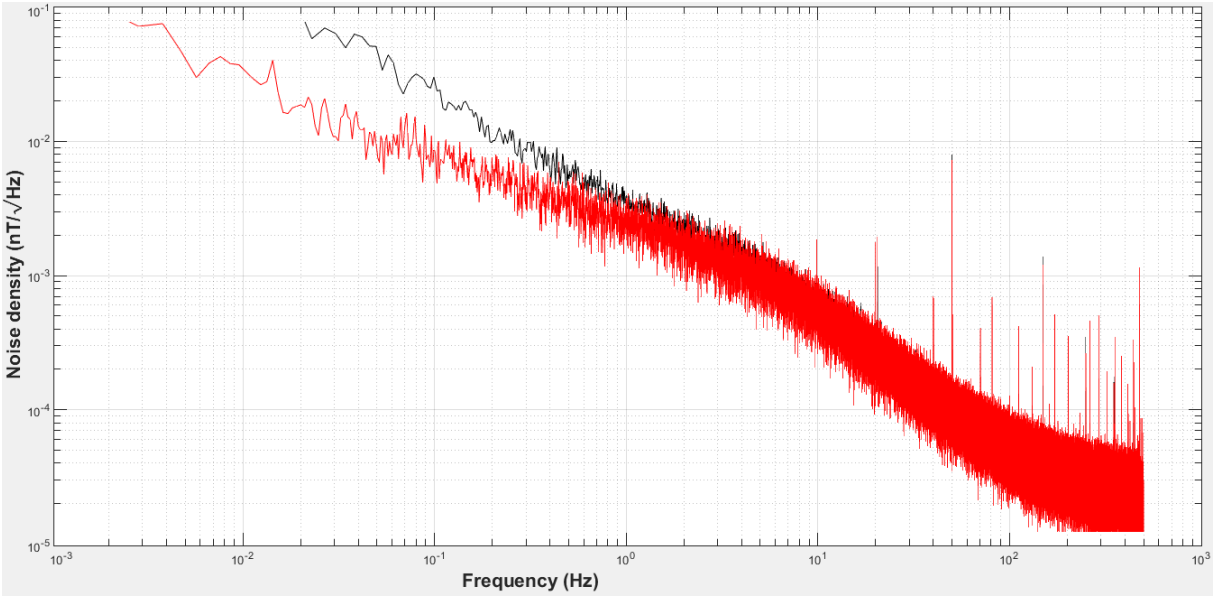

Figure 12. Noise measurement of a single axis race-track fluxgate sensor, red - MuMetal shield, black - smaller and older Permalloy shield (both 6-layer).

For offset temperature dependence, we use a complex setup of a specific, six-layer Permalloy magnetic shield equipped with a Dewar flask for temperature isolation and a custom non-magnetic heat exchanger through which an anti-freeze liquid is pumped. Either from an electrically powered thermostat or from a large tank placed in a dedicated commercial food refrigerator (heating or cooling switched by a three-way valve). The setup operated at IWF Graz and presented by Magnes [49] offers a much wider range but uses only a three-layer magnetic shield, which probably offers much more space for the Dewar flask and the instruments under test.

The author of this thesis continuously contributed to the development of the testing infrastructure here at MAGLAB. He designed, simulated, and built several single and triaxial coil systems with a two-segment-Helmholtz or four-segment-Merritt topology for in-house preliminary testing of the magnetometers (see Figure 13 and Figure 14). The coils are controlled by either a fluxgate-based, closed-loop, arbitrary magnetic field generator system or by a precise, computer-controllable, three-channel current source (both developed in MAGLAB, Michal Dressler 2017 [72], Michal Dressler 2019 [73]). One of the coil systems is equipped with another heat exchanger (in this case, based on a PVDF pipe), where the heating/cooling liquid is provided by the Lauda ECO RE1050S. Commercially available coil systems with controllers are provided e.g. by Billingsley Aerospace and Defense (an Apex CS, closed-loop, fluxgate-based arbitrary field controller, together with two sizes of Helmholtz coil systems). MAGLAB operates one APEX-CS unit in our non-magnetic laboratory in Průhonice. Bartington instruments offers, again, triaxial Helmholtz coil systems of various sizes (350, 500, and 1000 mm) and a specific "Helmholtz Coil Control System" with the possibility of closed-loop operation. The instrument offers a wide field range of ±1 mT from DC to 440Hz. MicroMagnetics offers a range of triaxial Helmholtz coil systems, also together with a specific controller: the SpinCoil-CTRL. DEXINMAG from China offers several sets of single or triaxial coil systems and also complete setups for magnetic field generation or compensation. An interesting fact is that the coils are placed in a multi-layer, magnetic shield and, thus, they can probably generate a relatively low-noise field (the offset field induced in the shield by powered coils as well as the coil constant influenced by the nearby soft magnetic material can be probably calibrated or suppressed by feedback operation). Another calibration possibility was

suggested by Zikmund [74]: it uses a coil system and scalar magnetometer to calibrate the coil system first and then the vector sensor. The ultimate solution for magnetic calibration is a visit to a dedicated magnetic calibration facility e.g. at IABG Ottobrunn - Germany or PTB Braunschweig [75].

Figure 13. Custom 3D coils developed, built, and used at MAGLAB. Left – the triaxial Helmholtz with a closed-loop, arbitrary field controller, middle – the single-axis Merrit and two-axis-modified Helmholtz with a heat exchanger for temperature sensitivity calibration, right – the triaxial Merritt coil for sensitivity and orthogonality calibration.

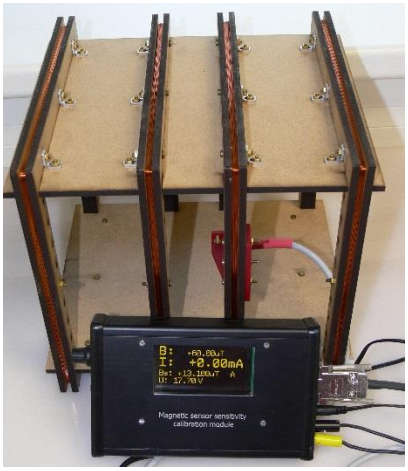

Figure 14 The miniature, single-axis Merritt coil and precise current source for sensitivity calibration of magnetic sensors – used, for example, during noise measurements to quickly estimate sensor sensitivity - developed within the scope of the bachelor thesis Rais 2023 [76]).

Another approach for sensitivity and orthogonality calibration might be the application of the Earth's magnetic field. The author still occasionally uses two non-magnetic platforms developed during his Ph.D. studies and improved over time - see Figure 15. The principle is in exposing the calibrated instrument to a set of approximately equally distributed points on an imaginary sphere with a radius equal to the magnetic field vector magnitude. The reference is a scalar magnetometer placed nearby, whose readings are synchronously recorded. That can compensate for slow variations of the Earth's magnetic field, the method is not very suitable for areas with high urban (gradient) magnetic noise reaching higher frequencies (above 0.1 Hz). The principle together with an algorithm description provided by Olsen [77] and Merayo [78], the hardware, and method explored in [**refP 9]** and [**refP 10]**. Adding a small thermostat onto the rotation platform allows for the additional evaluation of temperature dependences of the scale factors and orthogonalities, see [**refP 11**].

Figure 15. Left – a non-magnetic computer-controllable calibration platform for magnetometers and accelerometers, operated with a temperature chamber for temperature sensitivity dependence calibration, right - simple, absolutely non-magnetic, hand-operated calibration platform laser-cut from 5mm-thick transparent plexiglass.

For the testing of magnetometers with analog outputs, we developed a new specific DAQ (Data Acquisition) module (master's thesis M. Indrych 2024 [79]), which should replace a previously used, very valuable module based on three ADS1281s and one REF5050 voltage reference. The new module is based on current state-of-the-art 32-bit $\Delta\sum$-ADC by Analog Devices AD7177-2 (three of them used for simultaneous sampling). We used four voltage references REF7050 in parallel to decrease the noise of the instrument. Preliminary testing indicates that the noise is similar to what was presented at CERN (HPM7177 by Beev [80]). The module offers two input voltage ranges, 150 nV/√Hz at 0.1 Hz is the spectral noise density for ±10 V input range and <10 nV/√Hz at 0.1 Hz for the ±0.5V input range (both for shorted inputs). The instrument offers <±1 ppm linearity with a potential for further reduction by calibration. The commercial market does not really offer too many DAQ modules with the required parameters - simultanous sampling of at least three channels, ±10V range (for typically used 100kV/T magnetometer output scaling), at least 100 Hz analog bandwidth, variable sample rate, excellent linearity, and low noise on low frequencies and ideally also the possibility of internal data logging (on µSD memory card in our case). See Figure 16 for the first prototype of the module.

Figure 16. The three-channel DAQ module for analog magnetometer output digitization

4 Applications of Magnetic Sensors

Magnetic sensors can be used in many different ways to navigate, read stored data, measure magnetic field strength, electric current or position, to sense magnetic field generated by human body itself or by drugs with attached magnetic markers to help with medical treatment, or to find hidden objects or minerals that are either conductive, ferromagnetic, or both. And probably in many more ways. This chapter mentions several applications that the author has dealt with in recent years. Here AMR and fluxgate applications are mentioned, a Hall probe was used in [**refP 13**] to sense the rotational speed of a cryogenic propellant electric pump – under a FP-7 SPACE project called "In-Space-Propulsion-1".

4.1 Applications of magneto-resistive sensors

Magneto-resistive sensors can be conveniently used for applications where small size, low power consumption, and low price are the main selection criteria, while an increased value of noise and worse linearity or hysteresis is not a limiting factor [43, 81-84].

The author cooperated on a project in which scope a vehicle parking lot occupancy detector was developed. The work started with the construction of a state-of-the-art AMR magnetometer with analog signal processing, which was intended to serve for preliminary car magnetic signature testing and as a reference for testing of more cost- and size-optimized sensors (see Figure 18 and [**refP 14]**). The first tests were done in an underground parking lot with a sensor positioned under the ceiling (Figure 18).

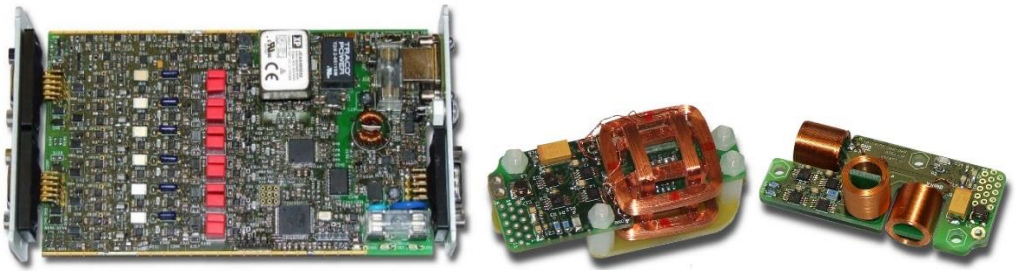

Figure 17. An AMR-based, dual triaxial vector magnetometer with a traditional analog signal processing followed by a high resolution ADC. Right: two sensor heads developed by the author - one with vectorial compensation of the measured field, another with an individual compensation using external coils to provide a more homogeneous compensation field and better coil constant.

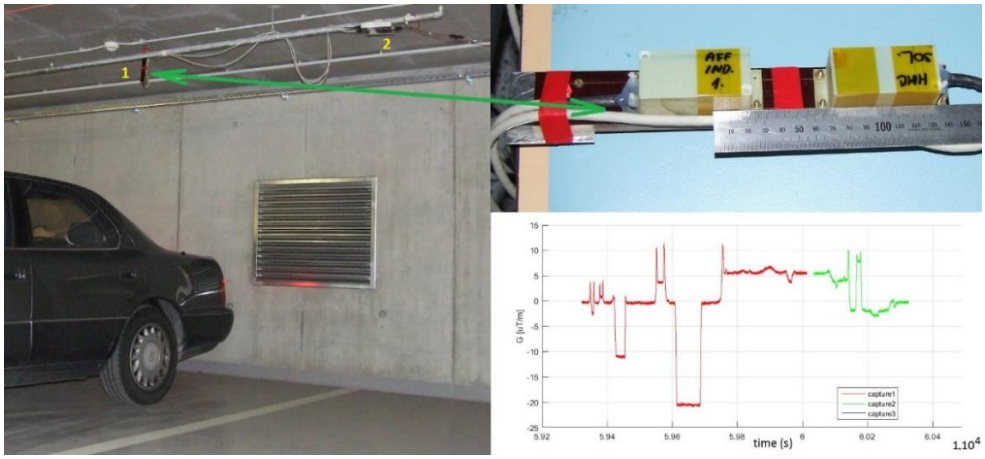

Figure 18. Left: a gradiometric sensor head below the ceiling, sensing the vertical gradient caused by the present car, right: a detail of the sensing head with a 120mm gradiometric base and a sample of the measured data (a car entering and leaving the lot).

The task proved to be quite challenging mainly due to the very variable magnetic signature of the cars as well as the environmental sensitivity (temperature dependence) of lower cost sensors in case the sensor was placed in the outdoor environment. Several types of sensors were tested, e.g. digital triaxial AMRs (MMC5883), single axis integrated fluxgates (DRV425). The last version, which was used for long-term outdoor evaluation on our faculty's parking lot, was equipped with four HMC1021 AMR sensors. One pair measured the field gradient while an extra pair of orthogonally placed sensors allowed for the easy calibration of the device (alignment of the gradiometric pair by a scalar calibration algorithm).

Figure 19. The AMR sensor-based module for car detection experiments, developed under the TACR (Technology Agency of the Czech Republic) project "Advanced Sensors". The module with four single axis AMR sensors was able to measure a magnetic field vector and its gradient in one axis. The author cooperated on its development and testing.

The author cooperated on the radiation testing of an AMR-based, triaxial compact magnetometer with a digital feedback [**refP 3]**. The miniDAMR instrument developed at MAGLAB is intended as an ADCS (Attitude Determination and Control System) component for small satellites or as a main scientific instrument for smaller missions, where application of a fluxgate sensor is not possible due to mass/power/budgetary constraints. It was also proposed for the LVICE2 mission as an auxiliary instrument for the cancelation of the satellite- generated magnetic noise (see Figure 20 and [**refP 17]**).

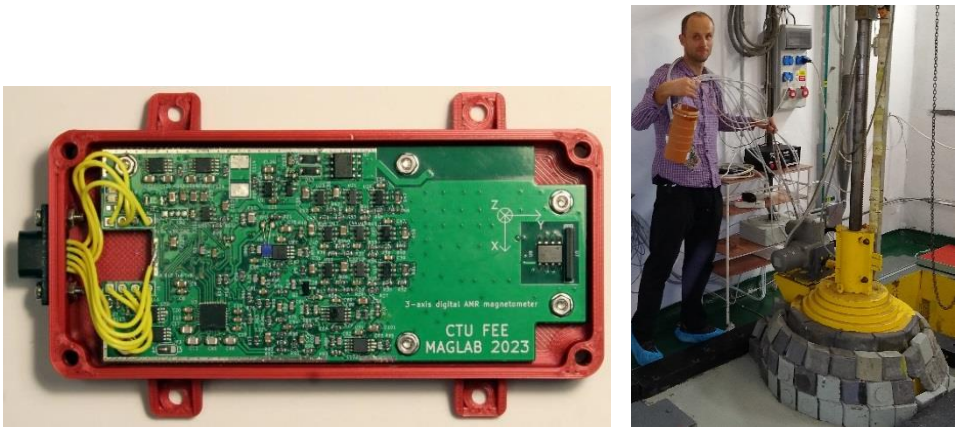

Figure 20. Left: Prototype of the AMR magnetometer for the LVICE2 mission, right: preparation of radiation testing using 60Co γ-source "Prazdroj" at ÚJV Řež

Figure 21 presents a very handy magnetic probe, which was developed within the scope of a student team project. It uses the triaxial AMR MMC5983 with an I2C interface and the STM32 MCU to measure and indicate the magnetic field and its gradient along probes long-side. Even though the noise of the

sensor is quite high (total noise of 40 nT RMS), the device proved to be very useful for fast checking of magnetic field magnitude, orientation, and gradients (range of ± 800 µT). A similarly sized device, but with a single-axis Hall probe was constructed within the scope of a bachelor thesis by Radomír Macíček 2022 [85]; in this case the measurement range was ±2.6 T and noise around 5 µTpp at the lowest range of 20 mT.

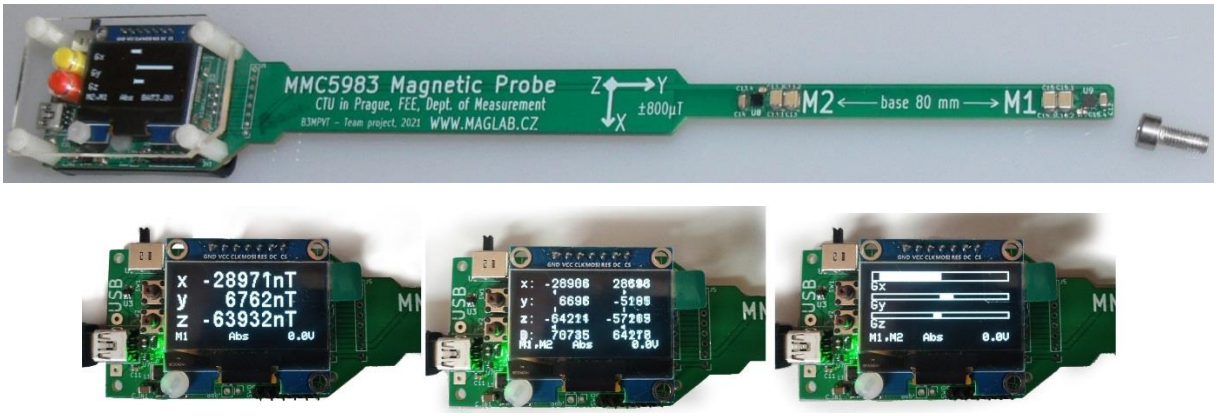

Figure 21. The application of an integrated triaxial AMR sensor (MMC5983) in a compact probe for orientational measurements of a magnetic field and its gradient. Student team project supervised by V. Petrucha, 2021.

4.2 Applications of fluxgate sensors

The development and application of fluxgate sensors is the main author's interest. Several projects are mentioned in this chapter. For some of them, the results were already published, in some projects more detailed testing and measurements need to be completed. Generally, the fluxgate sensors are used for the most demanding applications where the higher cost, dimension, and power consumption is justifiable [86, 87].

4.2.1 LVICE2 - magnetometers for the Lunar Vicinity Complex Environmental Explorer

Since May 2022, the author had been working on the ESA project LVICE2, which was proposed under the "Czech Ambitious Mission" call. The project lasted until September 2023 when Phase A and Phase B1 (project development) were completed. Currently, the project is suspended as a different project was selected for further financing and realization in the final review. The author of this thesis was responsible for the development of the main scientific magnetometer of this mission for DC and low-frequency field measurements (a triaxial, vectorially compensated fluxgate magnetometer), while Ph.D. student David Novotný developed the auxiliary AMR magnetometer to support satellite-produced disturbances cancelation. There was also supposed to be a search-coil magnetometer for higher frequencies provided by the Institute of Atmospheric Physics CAS. We prepared a short summary of the magnetometer's development, and it was accepted for presentation at the IEEE Sensors 2023 conference in Vienna as a poster with the topic "Magnetometry Package for LVICE2 Mission". The corresponding proceedings paper is attached as **[refP 17]**. We have been hoping the project would continue as it might bring a new, fascinating experience, but even if does not, we plan to test the interference cancelation algorithms using a test setup, as the developed instruments might be used in another similar mission.

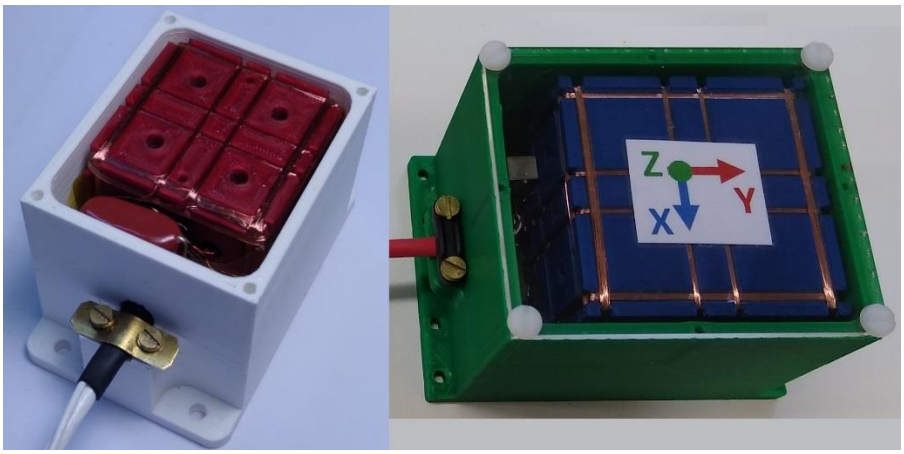

Figure 22. Two fluxgate sensor heads developed for the LVICE2 mission, left - 30mm side cube (embeds six race-track fluxgate sensors with a 17.4mm magnetic core length, two symmetrically placed for each axis), right - 50mm side cube (embeds three race-tracks with a 30mm long magnetic core). See the proceedings paper for parameters summary refP 17.

4.2.2 UAV-MAG (Fluxgate magnetometer for surveys using a small unmanned aerial vehicle)

Since 2013, we have been cooperating with Dr. Gunther Kletetschka (Institute of Hydrogeology, Engineering Geology and Applied Geophysics, Faculty of Science, Charles University, Prague, Czech Republic). We got together to cooperate on the localization of the Chelyabinsk meteorite. We adapted a development prototype of a vectorially compensated triaxial fluxgate magnetometer (construction similar to the described in [**refP 5]**) for underwater measurements and provided additional equipment for GNSS-referenced gradiometric mapping over Lake Chebarkul. That exploration led to the successful localization of a magnetized object in the lake (see [**refP 12]**). Later, we began to cooperate on magnetic surveys using a commercial unmanned aerial vehicle (UAV). We prepared and delivered sets of two identical, miniaturized, triaxial vector fluxgate magnetometers (mobile unit and base station) and provided support during data processing (additional calibration and/or filtering). Since then, the "UAV-MAG" was flown over multiple locations around the world (e.g. Alaska, Czech Republic, Australia, and Russia). For example, during its long-term testing in Australia, the system was used both for scientific purposes (e.g. mapping the magnetic signature around Acraman Lake – an old impact crater location) and test mapping for purposes of geological surveys for mineral prospection. See Figure 23 for an example of setup and Figure 24 for measured data. The fluxgate sensor construction in this case corresponds to [**refP 6]**. Currently, we are preparing an updated version of the instrument, mostly consisting of the improvement and miniaturization of the electronics unit. More information can be found here: https://maglab.fel.cvut.cz/products/uav-mag-v-1-1/ .
The magnetic survey instrument and results were presented at several meetings/conferences, e.g., Takáč 2019 - *The AGU-SEG Airborne Geophysics Workshop* [88], Takáč 2020 - *11th Planetary Crater Consortium [89],* or Takáč 2022 *-85th Annual Meeting of the Meteoritical Society [90].* Another publication concerning the Acraman's crater measurements is currently in the review process. Interestingly, fluxgate magnetometers can also be used to detect UAVs [91] or to map magnetic fields in indoor environments for localization applications [92].

Figure 23. The UAV drone with a 2m-long, flexible boom with the fluxgate magnetometer sensor head. The colored skirt stabilizes the sensor head during flight, improving data quality. The set of the UAV-MAG is shown in the right-hand picture – in the top-left is a ground unit for setting-up the measurements with a control display, in the middle is the magnetometer's electronics box with the attached GNSS module while the smaller, blue box is the triaxial sensor head. (Left photo by Marian Takač)

Figure 24. An example of magnetic mapping done with the UAV-MAG (author: Marian Takač)

4.2.3 Zero-field compensation unit and calibrator

For orientational calibrations and in-lab testing, the author developed a system for feedback compensation of the Earth's magnetic field with the possibility of applying an extra offset and, thus, generating any arbitrary magnetic field vector (with approximately a ±150 µT range, triaxial race-track fluxgate being the feedback sensor, size "A" from [**refP 8]**). **MAGLAB** is renting a small, non-magnetic building for more precise measurements in the area of Průhonice Park, where the Department of Paleomagnetism of Institute of Geology of the Czech Academy of Sciences is also based. They operate a precise magnetic zeroing system for procedures consisting of the thermal demagnetization of rock/soil/mineral samples for paleomagnetic investigations [93]. Their current system (MAVACS) is based on three rotating coil magnetometers [94]; two dual-axis sensors provide feedback for online compensation of the Earth's magnetic field including possible urban made disturbances and the third

is used to calibrate precise zero in the desired sample area. The big advantage of the rotating coil magnetometer is the near-zero offset. But the system is old, prone to mechanical failures, and very acoustically noisy (the air-driven sensor rotation is very audible), so we decided to test the fluxgate-based compensation system. See Figure 25. The preliminary testing indicated good potential of the system and, thus, a dedicated unit was built (Figure 26). Figure 27 presents the results from our in-house lab testing; suppression of the low frequency disturbances by approximately 40 dB is visible. The instrument was operated with 800mm side-length, 4-square segment Merritt coils; the final coils will have a side dimension of 2600 mm.

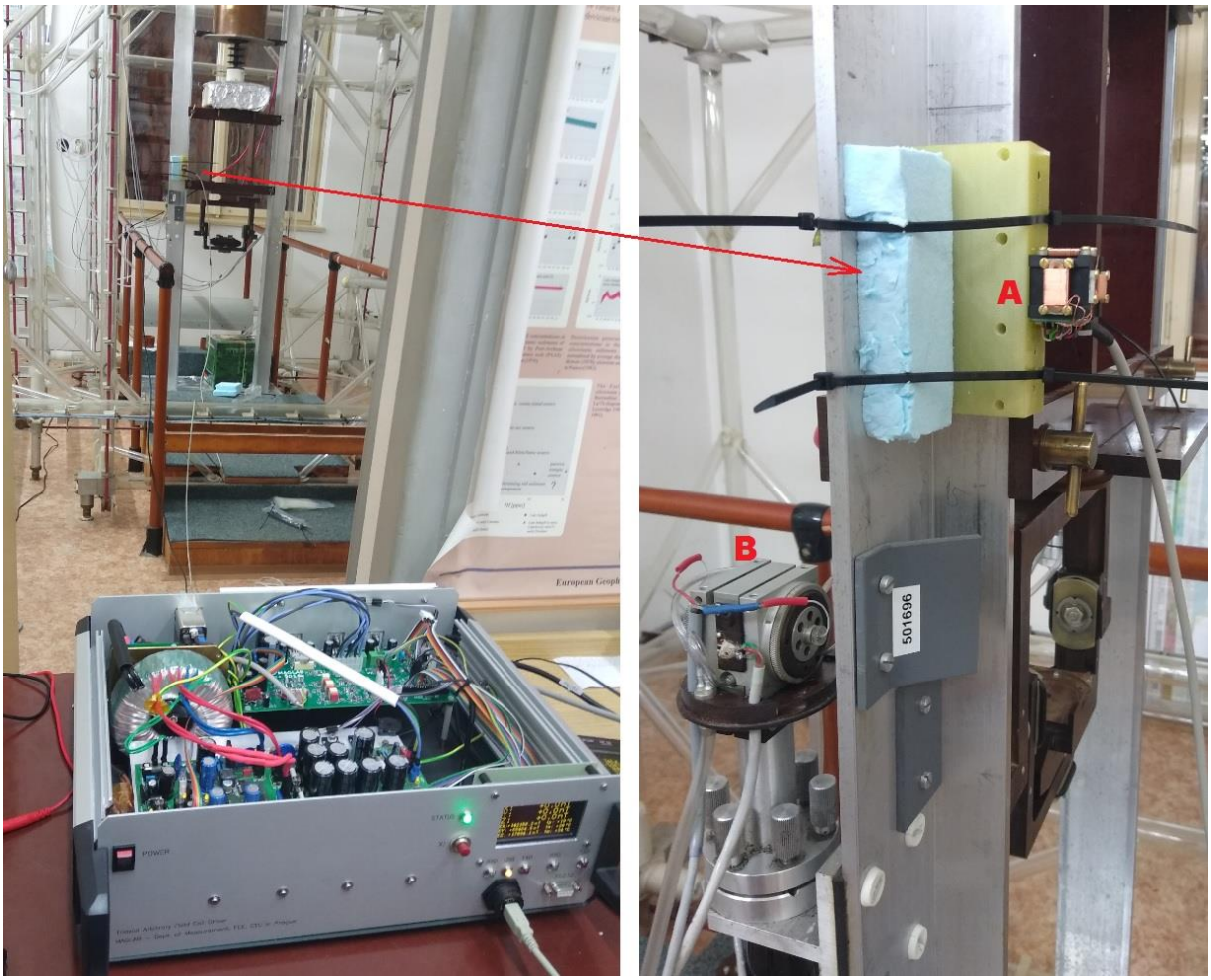

Figure 25. Successful preliminary testing of the first version of the compensation system in the Helmholtz coil system at the Geological institute in Průhonice; the detail of the feedback compensation triaxial fluxgate sensor is shown on the right-hand side (marked "A", with the improvised fixation "B" marking the sensor of the actual compensation system – rotating-coil magnetometer). The Helmholtz coil system support is made up of glass tubes and, thus, is very stable, but the high-field homogeneity region is very limited, so newly built coils will use the Merritt, four-square coils design.

Figure 26. The second version of the compensation system developed directly for the Geological institute of CAS. The custom box is made up of aluminum and the only big magnetic part is the toroidal transformer.

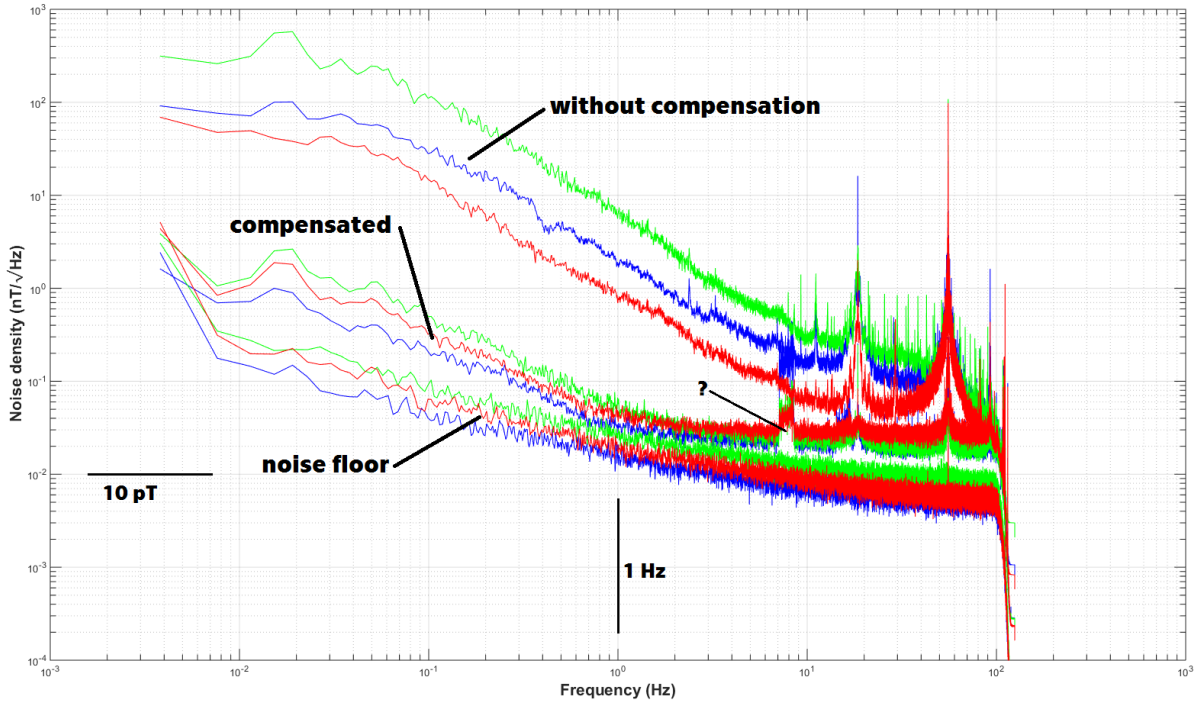

Figure 27. A power spectral density plot of three different situations: a) without compensation, b) feedback compensation switched on, c) noise floor measured in a 6-layer, Permalloy magnetic shield. Measurement setup: Stefan Mayer FL3-100 (triaxial fluxgate magnetometer with 100 µT measurement range, 100kV/T sensitivity, DC-2 kHz frequency range and <20 pT/√Hz @ 1 Hz noise specification) sampled by an in-house made data acquisition USB module based on 3x ADS1281 ADCs (3x 250 Sa/s). The question mark points to some problematic part in the compensated state, around 7-8 Hz, probably some instability that will have to be fixed. red-blue-green = x-y-z magnetic field components (z vertical).

4.2.4 Zero field calibrator

The new compensation system is based on fluxgate sensors, which have an offset that drifts with time and temperature. This spells serious trouble for the paleomagnetic applications where the desired field residua should ideally be below 1 nT [95]. So, we came up with the idea of using a rotating-fluxgate

instead of a rotating-coil magnetometer. In this case, the rotation is only 180 degrees, but that is enough to measure the sensor offset and subtract it from subsequent measurements. So, an almost completely non-magnetic device was designed, built, and tested that allows for the in-spot rotation of two dual-axis, ring-core fluxgate sensors ([**refP 6]** design). See Figure 28, the only magnetic component is a stepper motor with a low magnetic signature, which drives the rotational motion through a 2 m-long shaft.

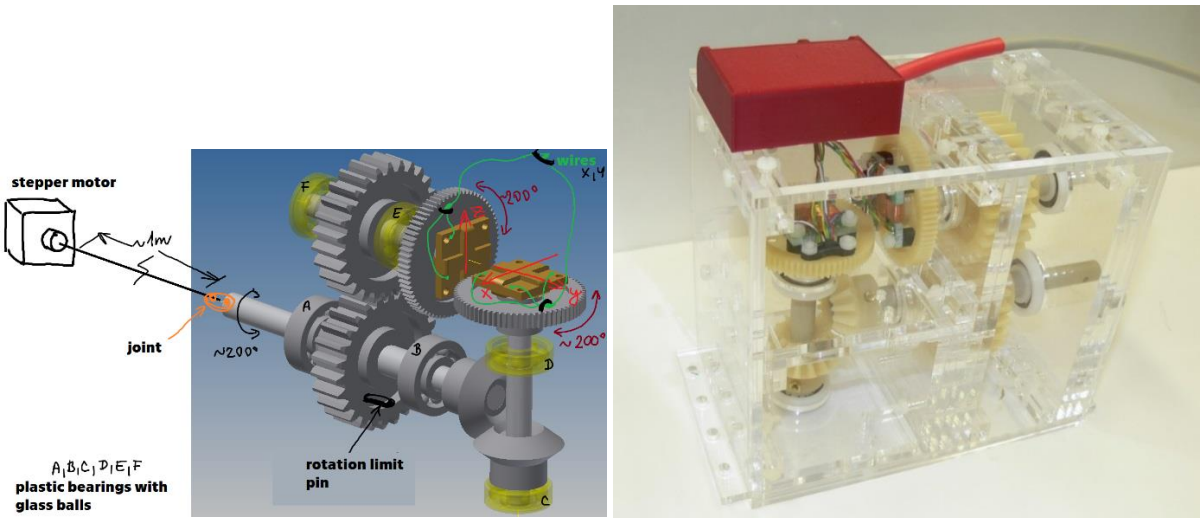

Figure 28. ZeFiCa sensor head - two dual axis, flat-ring-core fluxgate sensors (just under the red-wire terminal box), rotatable in order to measure its offset and thus be able to calibrate zero field in the desired position within the coils. Rotation of the sensor is via a remotely placed stepper motor (specific type with low stray field). Left - design, right - realization with laser-cut PMMA enclosure, polyketone gears and POM plastic bearings.

Figure 29 shows the testing of the calibrator instrument in our laboratory conditions. The calibrator sensor head (R) is placed in 3D Merritt coils, equipped with a feedback fluxgate sensor (F) for the compensation unit (A). The current source was used to null the main part of the Earth's magnetic field, as the same will be done in the real application (to save power and improve reliability - the gross compensation can be powered by a high efficiency switched power supply and the linear driver of the precise feedback compensation system is only slightly loaded).

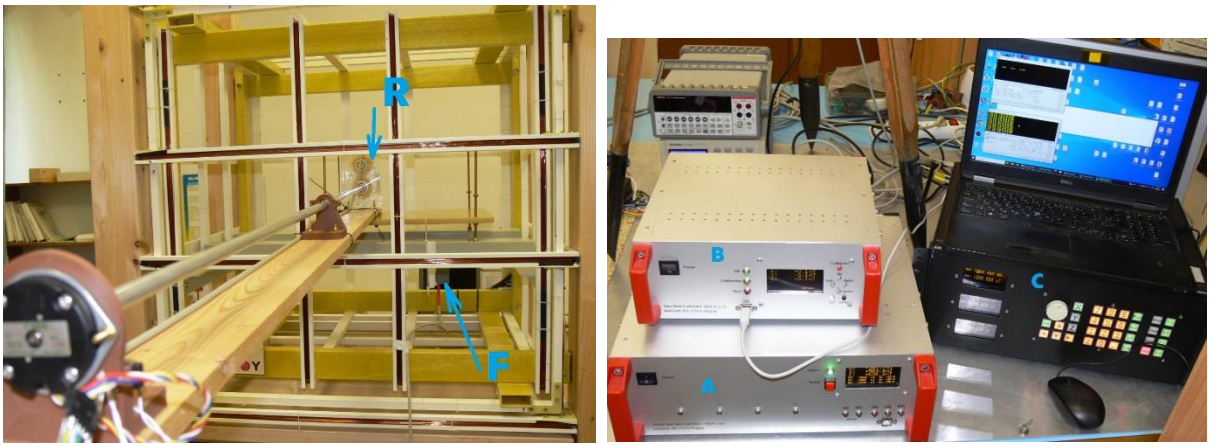

Figure 29. Left: The ZeFiCa sensor head (R) placed in Merritt coils with the feedback sensor (F), right: instrument setup A - compensation unit, B - ZeFiCa calibrator, C - precise three-channel current source for raw field compensation (and laptop to collect the data via USB link).

Figure 30, Figure 31, and Figure 32 demonstrate the behavior of the system during initial laboratory testing. The residual field decreased in each step. The compensation system did not use an

orthogonality calibration of the coils, which could have otherwise led to a faster approach to zero. We expect the residual field to be within the desired <1nT limit when operated in a quieter environment (free of gradient noise).

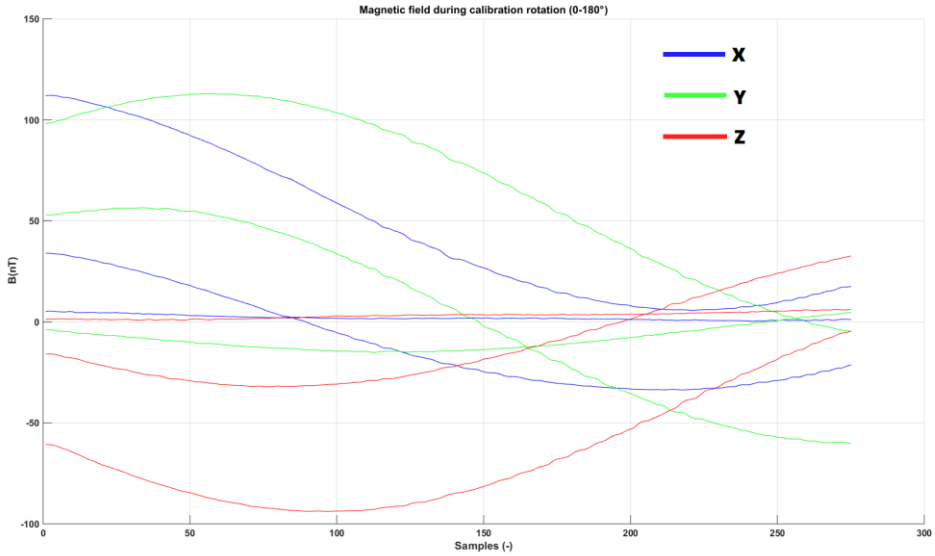

Figure 30. ZeFiCa measurements - three consecutive runs (calibration iterations); the field approaches the desired zero value. Y-axis with a bit worse residual, possibly some problem in the firmware code as the final measurement indicated low value also for Y, see Figure 32

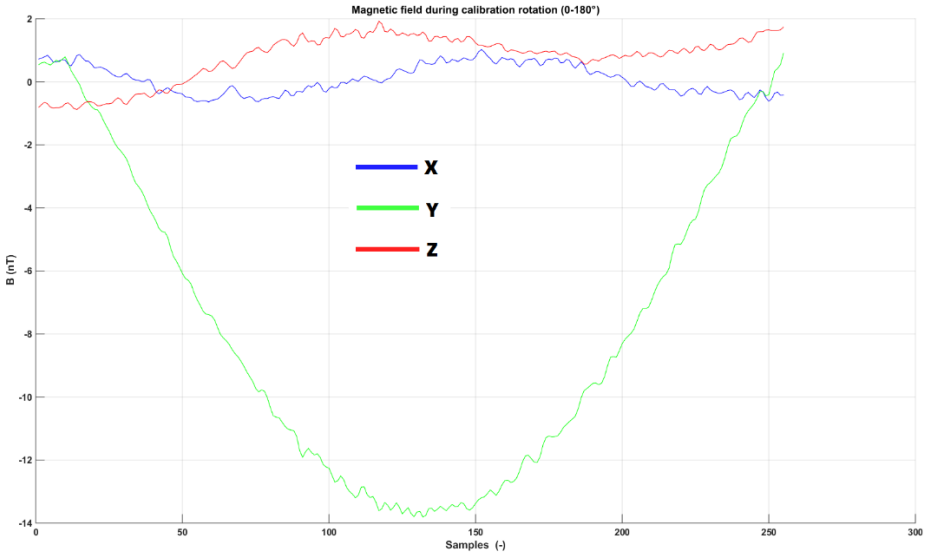

Figure 31. ZeFiCa - zoomed into the third measurement, the noise is given by the insufficient dynamic range of the AD conversion and probably also mechanical vibration during the motion (sensor noise is about 8 $pT_{RMS}/\sqrt{Hz}$ at 1 Hz). Averaging could help as well as some curve fitting algorithm. 250 samples shown acquired with a native speed of the ADC (62.5 Sa/s, LTC2508-32)

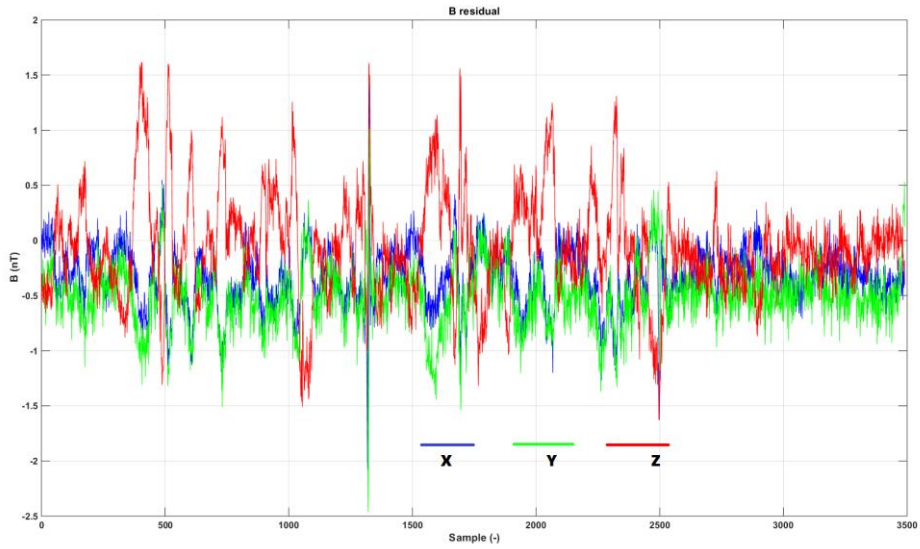

Figure 32. The magnetic field inside the coils measured by the ZeFiCa instrument after the zero-calibration procedure (field brought to zero iteratively by several adjustments of the compensation coil driver based on ZeFiCa measurements during sensor rotations). The noise in the gradient prevents better results, the lab is close to tram tracks. Approximately 10-minute interval shown, Z is the vertical component.

4.2.5 Observatory magnetometer

One possible application of the ultra-low-noise fluxgate sensors is in the observatory magnetometers for monitoring the variations of the Earth's magnetic field (size "C" [**refP 8]**). As there is long-term cooperation between our group and the geomagnetic observatory in Budkov (run by the geophysical institute of the Academy of Sciences of the Czech Republic - ASCR), we decided to build a magnetometer that would fulfill the requirements of the Intermagnet network (noise <10pT at 0.1 Hz) [96]. The instrument has partial compensation of the measured magnetic field (in two axes - vertical and North-South), two switchable measurement ranges (to solve a problem with an insufficient dynamic range of available Analog-to-Digital converters), and a simple digital interface (RS232), see Figure 33. We successfully tested the instrument in the laboratory (see Figure 34) and also during several weeks of operation at the Budkov observatory, where the output data could be compared with the local observatory magnetometer. The results were encouraging, and it seemed that the performance was limited by the location.

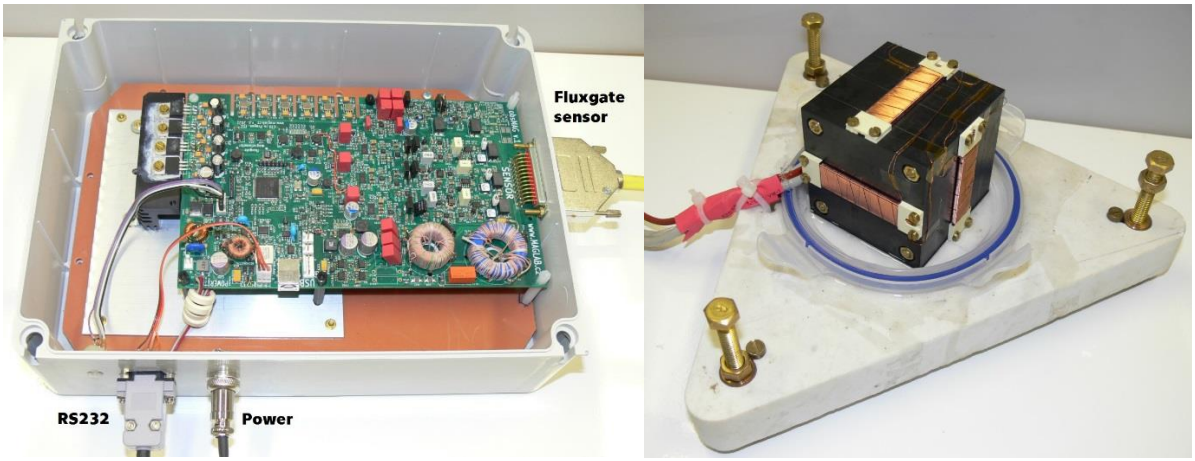

Figure 33. Triaxial fluxgate magnetometer electronics and the sensor head - three 60mm, race-track fluxgate sensors on the ULTEM 2400 holder fixed in a marble plate (with the improvised sensor cover removed).

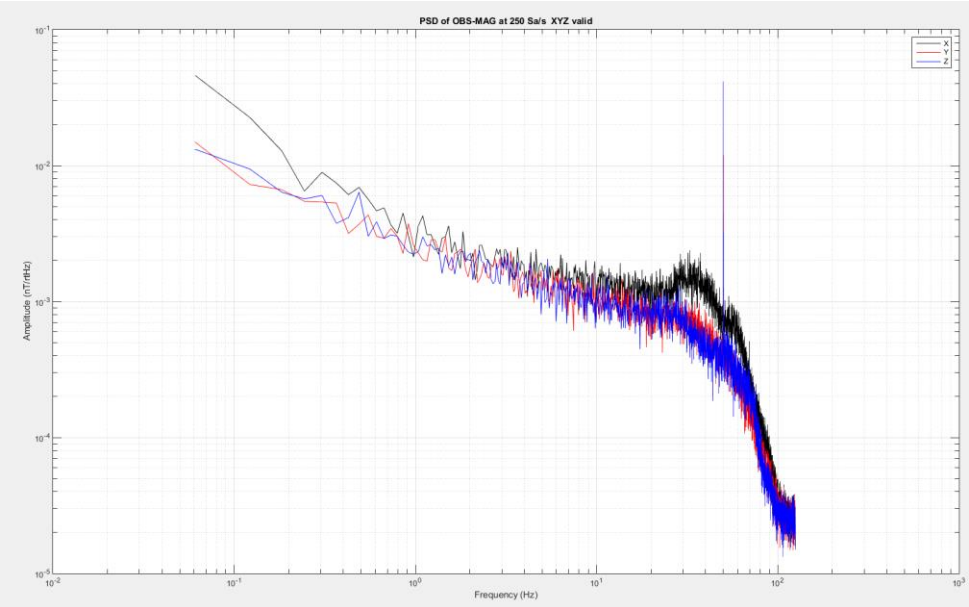

Figure 34. Noise measurement (power spectral density) of the observatory magnetometer, low-field range, measured in a 6-layer Permalloy shield. The latest experience shows that the noise at lower frequencies is probably a bit lower, we got 35 pT at 0.01 Hz and 8 pT at 0.1 Hz for a similar sensor measured in a new MuMetal® 6-layer shield (instead of 100 pT at 0.01 Hz and 25pT at 0.1 Hz measured in the old shield). Unfortunately, the sensor head is now fixed to the marble pedestal and does not fit the shielding.

We decided to do a test measurement in another location – a former gold-bearing tunnel in Kašperské hory, where the seismologic observatory of the ASCR is operated, so there is some infrastructure potentially available. The instrument was placed at the very end of the tunnel, far from all possible sources of magnetic disturbances, powered by a 12V LiFePo battery and with the output data recorded using our proprietary RS232->SDcard data logger (see Figure 35). Figure 37 presents a comparison of the measured data (vertical component of the magnetic vector) for the magnetometer and three nearby magnetic observatories (see Figure 36). The data matches quite nicely, there are some disturbances visible, but the red trace of the presented device seems to be the least noisy. Looking at the very end of the record, it could be seen that the sequence of the field change corresponds to the geographical placement of the observatories from east to west, possibly showing the positional progress of diurnal variation (trying to mutually align the coordinate systems in MATLAB did not bring any change). Currently we are exploring the possibilities to deploy the instrument for long term testing in the Kašperské hory location.

Figure 35. The magnetometer placed at the very end of "Kristýna" stole near Kašperské hory, Czech Republic (the seismologic observatory of the Geophysical institute, Academy of Sciences of the Czech Republic). A 12 V LiFePo battery was used to power up the magnetometer and universal RS232 datalogger to capture the data.

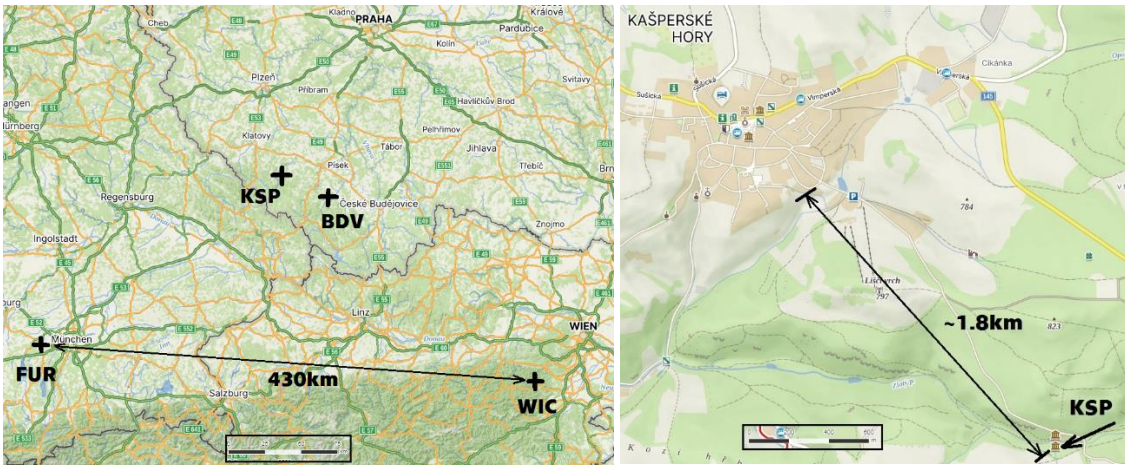

Figure 36. The geographical position of the four mentioned geomagnetic observatories (FUR - Fürstenfeldbruck, KSP - Kasperske hory, BDV - Budkov, WIC - Conrad observatory); the distant location of the KSP from the nearby village means low urban noise.

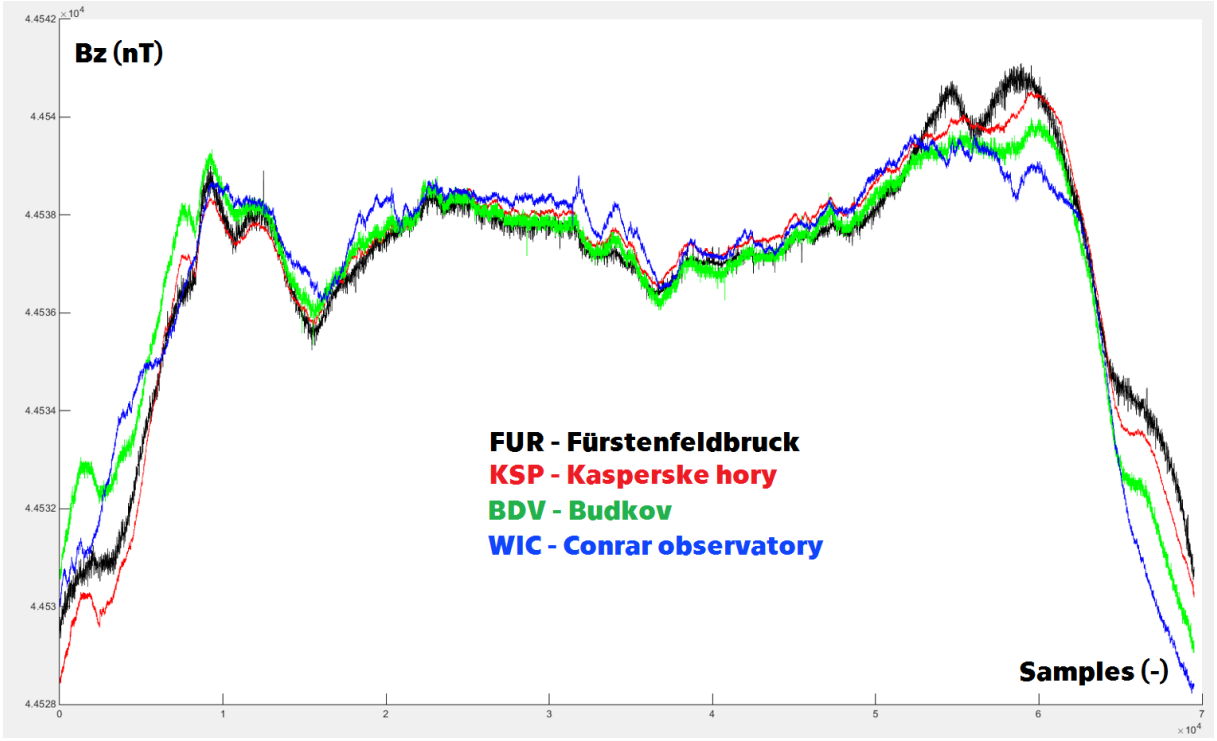

Figure 37. A vertical component of the Earth's magnetic field, a comparison of measured data for four geomagnetic observatories (the night between 22-23.8.2022). KSP data measured with the presented magnetometer, BDV and WIC data downloaded from the Intermagnet repository and FUR data kindly provided directly by Fürstenfeldbruck observatory staff (Andrea Balasso). The static offset between the observatories has been subtracted.

4.2.6 Security applications of fluxgate sensors

Magnetic anomaly detectors were among the main security applications of fluxgate sensors in WWII and beyond. Submarine detection by fluxgate sensors is still used as well as magnetic mapping of the magnetic signature of various military vessels (including submarines) in order to minimize that signature by passive or active measures [97]. The author participated in a project dealing with soft target protection by applying another layer of protection with unobserved detection of carried ferromagnetic objects (possibly weapons or explosive devices with metal shrapnel, etc.). The author

developed and tested a full-tensor detector comprising of a set of four triaxial fluxgate magnetometers (commercial Bartington Mag612 sensors were used for testing) and a custom-developed DAQ unit (simultaneous sampling of up to 24 analog channels with 24-bit resolution ADC - AD7768). The detector worked but the desired online signal processing was challenging, even though we tested several different methods presented in literature [98-106]. The final version used a system of two slightly separated, linear triaxial sensor arrays together with more suitable correlation signal processing (a method proposed by Dr. Janošek). The results were not published but a **national utility model was registered (together with the cooperating company - URC Systems, No. 2019-36609 by Čechák, Křemže, Petrucha, Janošek) [107].**

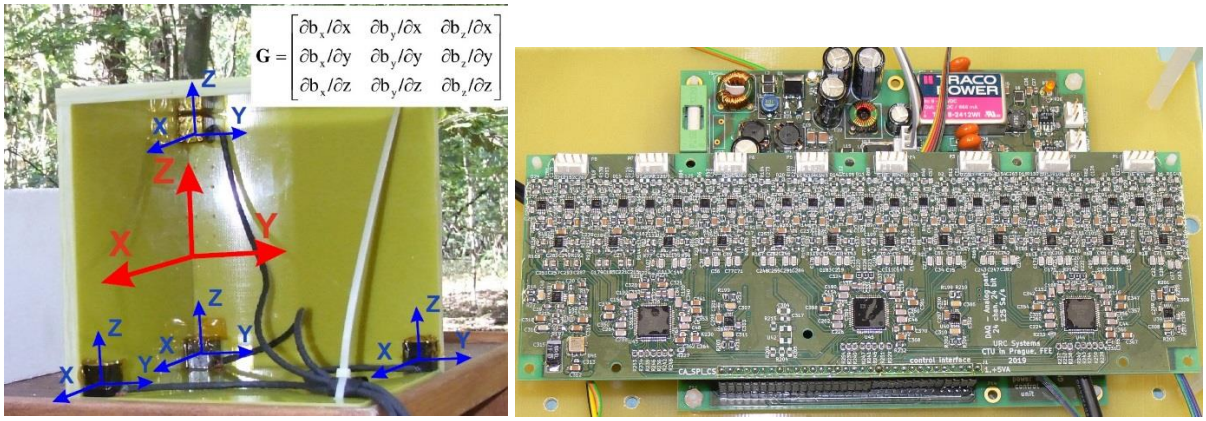

Figure 38. Left: a sensor head of a passive, ferromagnetic objects detector based on full-magnetic tensor data processing, gradiometric base of 160 mm, right: 24-channel, 24-bit DAQ with ±10V input range and simultaneous sampling.

5 Conclusions

This work presents the author's comprehensive efforts in the development and follow-up applications of precise magnetic sensors. The selected publications cover the entire process chain, presenting the development of individual sensors and their characterization, use in magnetometers with associated calibration and testing, and finally various real-world applications for both industrial and scientific purposes. The developed sensors and magnetometers are directly comparable with or surpass the currently available state-of-the-art instruments, especially in the case of noise performance of parallel fluxgates with a race-track core topology. This enables wider deployment in some other application areas, such as security applications. A small fluxgate magnetometer with specific characteristics for use on small unmanned aerial vehicles (UAVs) has made it possible to collect fascinating geological data with high spatial resolution thanks to its accuracy and ability to fly at low altitudes. Future research should focus a little more on the development of proven sensors with race-track core in order to make them easier to produce in higher volumes, as the current high production costs limit the application portfolio. Interesting applications (e.g. UAV-borne magnetometers for various purposes) could entice students to participate in research at all academic levels (from undergraduate to doctoral studies), as the subject of magnetic measurements offers a wide range of expertise to be acquired, from precision analog and digital electronics to complex mathematical data processing and algorithms in calibrations and measurements with a bit of mechanics and solid-state physics.

6 References

6.1 Own publications contained in the present thesis

(with author's contribution percentage)

Section 2.1 AMR based magnetometer development

refP 1 **Petrucha, V.**; Fúra, V.; Platil, A., "Cross-field Effect in a Triaxial AMR Magnetometer with Vector and Individual Compensation of a Measured Magnetic Field," IEEE Transactions on Magnetics. 2017, 53(4), ISSN 0018-9464 /author's contribution 80 %/

refP 2 Novotný, D.; **Petrucha, V.**; Janošek, M., "A Digitally Compensated AMR Magnetometer," IEEE Transactions on Magnetics. 2019, 55(1), ISSN 0018-9464 /author's contribution 25 %/

refP 3 Novotný, D.; **Petrucha, V.**; Dressler, M.; Platil, A., "Characterization of a Digital AMR Magnetometer for Space Applications," IEEE Transactions on Instrumentation and Measurement. 2021, 70(1), ISSN 0018-9456 /author's contribution 20 %/

Section 2.2 Fluxgate based magnetometer development

refP 4 **Petrucha, V.**; Janošek, M.; Azpurua, M. A., "Fluxgate magnetometer vector feedback homogeneity and its influence on sensor parameters," In: Proceedings of Instrumentation and Measurement Technology Conference (I2MTC) 2014. Vail, Colorado: IEEE Instrumentation and Measurement Society, 2014, pp. 460-463. ISSN 1091-5281. ISBN 978-1-4673-6385-3 /author's contribution 33 %/

refP 5 **Petrucha, V.**; Janošek, M.; Azpúrua, M. A., "Vector Feedback Homogeneity and Inner Layout Influence on Fluxgate Sensor Parameters," IEEE Transactions on Instrumentation and Measurement. 2015, 64(5), 1293-1299. ISSN 0018-9456 /author's contribution 40 %/

refP 6 **Petrucha, V.**, "Low-cost dual-axes fluxgate sensor with a flat field-annealed magnetic core," In: 2016 IEEE Sensors Applications Symposium (SAS 2016) Proceedings. Piscataway: IEEE, 2016. pp. 140-143. ISBN 978-1-4799-7249-4 /author's contribution 100 %/

refP 7 Novotný, D.; **Petrucha, V.**, "High Dynamic Range Digital Fluxgate Magnetometer," In: 2020 IEEE SENSORS Proceedings. Orlando, Florida: IEEE Sensors Council, 2020. ISSN 2168-9229. ISBN 978-1-7281-6801-2 /author's contribution 30 %/

refP 8 **Petrucha, V.**; Butta, M., "Race-track fluxgate sensor scaling versus noise," In: IEEE SENSORS 2021 proceeding. Irvine, CA: IEEE Sensors, 2021. ISSN 1930-0395. ISBN 978-1-7281-9501-8 /author's contribution 80 %/

Section 3 Testing and calibration of magnetic sensors

refP 9 **Petrucha, V.**; Ripka, P.; Kašpar, P.; Merayo, J., "Automated System for the Calibration of Magnetometers," Journal of Applied Physics. 2009, 2009(105), 07E704-1-07E704-3. ISSN 0021-8979 /author's contribution 25 %/

refP 10 **Petrucha, V.**; Kašpar, P., "Calibration of a Triaxial Fluxgate Magnetometer and Accelerometer with an Automated Non-magnetic Calibration System," In: IEEE SENSORS 2009 - The Eighth IEEE Conference on Sensors. Christchurch: IEEE Sensors Council, 2009. pp. 1510-1513. ISSN 1930-0395. ISBN 978-1-4244-4548-6 /author's contribution 70 %/

refP 11 Petrucha, V.; Kašpar, P., “Measurement of the Temperature Dependence of the Sensitivity and Orthogonality of a Triaxial Vector Magnetometer,” Journal of Electrical Engineering. 2012, 63(7s), 31-34. ISSN 1335-3632 /author’s contribution 50 %/

Section 4 Applications of magnetic sensors

refP 12 Kletetschka, G.; Vyhnánek, J.; Kawasumiova, D.; Nabelek, L.; **Petrucha, V**., “Localization of the Chelyabinsk Meteorite from Magnetic Field Survey and GPS Data,” IEEE Sensors Journal. 2015, 2015(15), 4875-4881. ISSN 1530-437X /author’s contribution 20 %/

refP 13 Petrucha, V.; Ripka, P., “Rotational Speed Measurement and Angular Position Reference for a Cryogenic Propellant Electric Pump,” Journal of Electrical Engineering. 2015, 66(7), 199-202. ISSN 1335-3632 /author’s contribution 50 %/

refP 14 Fúra, V.; **Petrucha, V**.; Platil, A., “Construction of an AMR magnetometer for car detection experiments,” In: Proceedings of 5th International Conference on Materials and Applications for Sensors and Transducers (IC-MAST2015). Bristol: IOP Institute of Physics, 2016. IOP Conference Series: Materials Science and Engineering. ISSN 1757-899X /author’s contribution 34 %/

refP 15 Ripka, P.; Grim, V.; **Petrucha, V**., “A Busbar Current Sensor With Frequency Compensation,” IEEE Transactions on Magnetics. 2017, 53(4), 1-5. ISSN 0018-9464 /author’s contribution 30 %/

refP 16 Petrucha, V.; Novotný, D., “Testing and application of an integrated fluxgate sensor DRV425,” Journal of Electrical Engineering. 2018, 2018(69), 418-421. ISSN 1335-3632 /author’s contribution 50 %/

refP 17 Petrucha V., Novotný D. and Šobíšek K., "Magnetometry Package for L VICE2 Mission: Triaxial Fluxgate and AMR Magnetometer for Scientific Data Production Near Moon," 2023 IEEE SENSORS, Vienna, Austria, 2023, pp. 1-4, doi: 10.1109/SENSORS56945.2023.10325159 /author’s contribution 60 %/

6.2 6.2 Other publications of the author

Petrucha, V.; Mlejnek, P.; Ripka, P.; Chvojka, M.; Posolda, P., “Tester for a Space Micro-accelerometer,” Sensors and Actuators. 2010, 2010(A162-2), 324-328. ISSN 0924-4247 /author’s contribution 40 %/

In this publication we present an electronic simulator of the sensor element of the micro-accelerometer designed for the ESA’s SWARM mission. It is almost impossible to test the instrument in the lab, as it is saturated by gravity. So, in the cooperation with the VZLU we designed and tested electronic module which could be put together with analog front-end electronics of the micro-accelerometer to simulate its operation in space. Author’s percentage is 40%, he provided main design, assembly and measurement work.

Sarkar, P.; Janošek, M.; **Petrucha, V.**; Včelák, J.; Ripka, P., “Study of Stress-Induced Anisotropy in METGLAS 2714,” IEEE Transactions on Magnetics. 2014, 50(11), ISSN 0018-9464 /author’s contribution 20 %/

Janošek, M.; Vyhnánek, J.; Platil, A.; **Petrucha, V**., “Compact Full-tensor Fluxgate Gradiometer,” Journal of Electrical Engineering. 2015, 66(7/s), 146-148. ISSN 1335-3632 /author’s contribution 10 %/

Janošek, M.; **Petrucha, V.**; Vlk, M., “Low-noise magnetic observatory variometer with race-track sensors,” In: Proceedings of 5th International Conference on Materials and Applications for Sensors and Transducers (IC-MAST2015). Bristol: IOP Institute of Physics, 2016. IOP Conference Series: Materials Science and Engineering. ISSN 1757-899X /author’s contribution 10 %/

Ripka, P.; Přibil, M.; **Petrucha, V**.; Grim, V.; Draxler, K.. “A Fluxgate Current Sensor With an Amphitheater Busbar,” IEEE Transactions on Magnetics. 2016, 52(7), ISSN 0018-9464 /author’s contribution 20 %/

Novotný, D.; **Petrucha, V.,** ”High dynamic range fluxgate magnetometer,” In: Proceedings of IEEE Student Branch Conference Blansko 2018. Brno: Vysoké učení technické v Brně, 2018. p. 33-36. 1. ISBN 978-80-214-5661-7

Presentation of the bachelor thesis of D. Novotný (thesis with excellent technical quality and with exceptional results) on local Czech conference. D. Novotný later became Ph.D. student within the MAGLAB group and concentrates mainly of the development of AMR sensors, again with excellent results. Supervisor specialist is V. Petrucha. Author’s percentage is 50%.

Janošek, M.; Dressler, M.; **Petrucha, V**.; Chirtsov, A., “Magnetic Calibration System with Interference Compensation,” IEEE Transactions on Magnetics. 2019, 55(1), ISSN 0018-9464 /author’s contribution 10 %/

Takáč M., Kavkova R., Kletetschka G., **Petrucha V**., “Detecting Magnetic Anomalies of Crater Fields by a Drone,” The AGU-SEG Airborne Geophysics Workshop, 2019 (abstract)

Takáč M., Kletetschka G., **Petrucha V.**, "UAV magnetometer survey of the Acraman’s crater epicenter," 85th Annual Meeting of the Meteoritical Society, 2023 (abstract)

Takac M., Kletetschka G., Kavkova R., **Petrucha V.,** Dressler M., "Tunguska Event and magnetic signature over the epicenter," 11th Planetary Crater Consortium 2020 (abstract)

6.3 Other - utility models

Čechák, J.; Marek, M.; **Petrucha, V**.; Janošek, M., “Detektor nesených feromagnetických částí,” Czech Republic. Utility Model CZ 33608. 2020-01-21 /author’s contribution 25 %/

Janošek, M.; **Petrucha, V**., “Feromagnetická sonda,” Czech Republic. Utility Model CZ 27638. 2014-12-18 /author’s contribution 50 %/

6.4 Other references

[1] M. Butta, and B. P. Schutte, “Low-Noise Orthogonal Fluxgate Using Flipped Current Joule Annealing,” *IEEE Transactions on Magnetics,* vol. 55, no. 7, Jul, 2019.

[2] M. Janosek, M. Butta, M. Dressler *et al.*, “1-pT Noise Fluxgate Magnetometer for Geomagnetic Measurements and Unshielded Magnetocardiography,” *IEEE Transactions on Instrumentation and Measurement,* vol. 69, no. 5, pp. 2552-2560, May, 2020.

[3] M. Butta, M. Dressler, and M. Janosek, “Offset drift in orthogonal fluxgate and importance of closed-loop operation,” *Sensors and Actuators a-Physical,* vol. 342, AUG 1 2022, 2022.

[4] M. Butta, M. Janosek, J. Parez *et al.*, “An Improved Composition of CoFeSiB Alloy for Orthogonal Fluxgates,” *Sensors,* vol. 22, no. 6, Mar 2022, 2022.

[5] L. Myeongwon Lee and Jungbae Yoon and Donghun, "Atomic Scale Magnetic Sensing and Imaging Based on Diamond NV Centers," *Magnetometers*, C. Sergio, ed., Rijeka: IntechOpen, 2019.

[6] S. Alsid, J. Schloss, M. Steinecker *et al.*, “Solid-State Microwave Magnetometer with Picotesla-Level Sensitivity,” *Physical Review Applied,* vol. 19, no. 5, May 31 2023, 2023.

[7] T. Wolf, P. Neumann, K. Nakamura *et al.*, “Subpicotesla Diamond Magnetometry,” *Physical Review X,* vol. 5, no. 4, Oct, 2015.

[8] J. Webb, J. Clement, L. Troise *et al.*, “Nanotesla sensitivity magnetic field sensing using a compact diamond nitrogen-vacancy magnetometer,” *Applied Physics Letters,* vol. 114, no. 23, Jun 10 2019, 2019.

[9] Z. Y. Jiashen Tang, Connor A. Hart, John W. Blanchard, Jner Tzern Oon, Smriti Bhalerao, Jennifer M. Schloss, Matthew J. Turner, Ronald L. Walsworth, "Quantum diamond microscope for dynamic imaging of magnetic fields," *AVS Quantum Sci. 5, 044403*, 2023

[10] M. Brookes, J. Leggett, M. Rea *et al.*, “Magnetoencephalography with optically pumped magnetometers (OPM-MEG): the next generation of functional neuroimaging,” *Trends in Neurosciences,* vol. 45, no. 8, pp. 621-634, Aug 2022, 2022.

[11] H. Korth, J. Kitching, J. Bonnell *et al.*, “Flight demonstration of a miniature atomic scalar magnetometer based on a microfabricated rubidium vapor cell,” *Review of Scientific Instruments,* vol. 94, no. 3, Mar 1 2023, 2023.

[12] H. Korth, K. Strohbehn, F. Tejada *et al.*, “Chip-Scale Absolute Scalar Magnetometer for Space Applications,” *Johns Hopkins Apl Technical Digest,* vol. 28, no. 3, pp. 248-249, 2010.

[13] Y. Lu, L. Liu, Y. Shi *et al.*, “A High-Sensitivity Cesium Atomic Magnetometer Based on A Cesium Spectral Lamp,” *Applied Sciences-Basel,* vol. 13, no. 14, Jul 2023, 2023.

[14] Z. Pan, J. Shang, L. Lu and Y. Ji, "Chip-scale scalar atomic magnetometer operating in geomagnetic environment," 2017 18th International Conference on Electronic Packaging Technology (ICEPT), Harbin, China, pp. 720-725, 2017.

[15] A. Pollinger, C. Amtmann, A. Betzler *et al.*, “In-orbit results of the Coupled Dark State Magnetometer aboard the China Seismo-Electromagnetic Satellite,” *Geoscientific Instrumentation Methods and Data Systems,* vol. 9, no. 2, pp. 275-291, Jul 16 2020, 2020.

[16] A. Pollinger, R. Lammegger, W. Magnes *et al.*, “Coupled dark state magnetometer for the China Seismo-Electromagnetic Satellite,” *Measurement Science and Technology,* vol. 29, no. 9, Sep 2018, 2018.

[17] A. Pollinger, M. Ellmeier, W. Magnes *et al.*, "Enable the inherent omni-directionality of an absolute coupled dark state magnetometer for e.g. scientific space applications," *2012 IEEE International Instrumentation and Measurement Technology Conference*, pp. 33-36, New York: IEEE, 2012.

[18] W. Sun, Q. Huang, Z. Huang *et al.*, “All-Optical Vector Cesium Magnetometer,” *Chinese Physics Letters,* vol. 34, no. 5, May 2017, 2017.

[19] X. Bai, K. Wen, D. Peng *et al.*, “Atomic magnetometers and their application in industry,” *Frontiers in Physics,* vol. 11, Jun 8 2023, 2023.

[20] Y. Chen, J. Wang, N. Zhang *et al.*, “In Situ Study of the Magnetic Field Gradient Produced by a Miniature Bi-Planar Coil for Chip-Scale Atomic Devices,” *Micromachines,* vol. 14, no. 11, Nov 2023, 2023.

[21] A. Fabricant, I. Novikova, and G. Bison, “How to build a magnetometer with thermal atomic vapor: a tutorial,” *New Journal of Physics,* vol. 25, no. 2, Feb 1 2023, 2023.

[22] I. Novikova, E. E. Mikhailov, A. Toyryla, M. Gonzales, A. Matsko, J. McKelvy, I. Fan, Y. Li, and J. Kitching, "Vector atomic magnetometer based on EIT in Rb vapor," in CLEO 2023, SW4O.4, *Technical Digest Series, Optica Publishing Group,* 2023

[23] Y. Lu, T. Zhao, W. Zhu *et al.*, “Recent Progress of Atomic Magnetometers for Geomagnetic Applications,” *Sensors,* vol. 23, no. 11, Jun 3 2023, 2023.

[24] J.A. McKelvy, I. Novikova, E.E. Mikhailov, M.A. Maldonado, I. Fan,Y. Li, Y. Wang, J. Kitching, A. Matsko, "On the Development of an Optical Rubidium Vector Atomic Magnetometer," *IGARSS 2023 - 2023 IEEE International Geoscience and Remote Sensing Symposium*, pp.730-733, 2023

[25] V. Schultze, T. Scholtes, G. Oelsner *et al.*, “An Optically Pumped Magnetometer with Omnidirectional Magnetic Field Sensitivity,” *Sensors,* vol. 23, no. 15, Aug 2023, 2023.

[26] K. Xu, X. Ren, Y. Xiang *et al.*, “Multi-Parameter Optimization of Rubidium Laser Optically Pumped Magnetometers with Geomagnetic Field Intensity,” *Sensors,* vol. 23, no. 21, Nov 2023, 2023.

[27] J. Z. Zinan Wu, Mengyang He, Bokang Ren, Zilong Wang, Chen Wei, Zhonghua Ou, Huimin Yue, Xiaojun Zhou, and Yong Liu, “A high-sensitivity single-light-source triaxial atomic magnetometer with double-cell and orthogonally pumped structure,” *Opt. Express,* vol. 31, no. 6, pp. 10411--10419, Mar, 2023.

[28] W. Fourcault, R. Romain, G. Le Gal *et al.*, “Helium-4 magnetometers for room-temperature biomedical imaging: toward collective operation and photon-noise limited sensitivity,” *Optics Express,* vol. 29, no. 10, pp. 14467-14475, May 10 2021, 2021.

[29] M. T. Fourcault W., Josselin V., Beato F., Le Gal G., Le Prado M., Labyt E., Palacios-Laloy A., "Helium-4 optically pumped magnetometers for medical imaging," *CEA - LETI Scientific report 2019 / Systems*, 2020.

[30] J. Rutkowski, W. Fourcault, F. Bertrand *et al.*, “Towards a miniature atomic scalar magnetometer using a liquid crystal polarization rotator,” *Sensors and Actuators a-Physical,* vol. 216, pp. 386-393, Sep 1 2014, 2014.

[31] R. Zhang, R. Mhaskar, K. Smith *et al.*, “Vector measurements using all optical scalar atomic magnetometers,” *Journal of Applied Physics,* vol. 129, no. 4, Jan 28 2021, 2021.

[32] Osborne J., Orton J., Alem O., Shah V., “Fully integrated standalone zero field optically pumped magnetometer for biomagnetism,” in *Steep Dispersion Engineering and Opto-Atomic Precision Metrology XI, pp. 105481G, 2018*.

[33] J. Kitching, “Chip-scale atomic devices,” *Applied Physics Reviews,* vol. 5, no. 3, Sep 2018, 2018.

[34] C. Cochrane, J. Blacksberg, M. Anders *et al.*, “Vectorized magnetometer for space applications using electrical readout of atomic scale defects in silicon carbide,” *Scientific Reports,* vol. 6, Nov 28 2016, 2016.

[35] H. Korth, K. Strohbehn, F. Tejada *et al.*, “Miniature atomic scalar magnetometer for space based on the rubidium isotope 87Rb,” *Journal of Geophysical Research-Space Physics,* vol. 121, no. 8, pp. 7870-7880, Aug 2016, 2016.

[36] B. Lim, M. Mahfoud, P. Das *et al.*, “Advances and key technologies in magnetoresistive sensors with high thermal stabilities and low field detectivities,” *Apl Materials,* vol. 10, no. 5, May 1 2022, 2022.

[37] I. Ennen, D. Kappe, T. Rempel *et al.*, “Giant Magnetoresistance: Basic Concepts, Microstructure, Magnetic Interactions and Applications,” *Sensors,* vol. 16, no. 6, Jun 2016, 2016.

[38] P. J. Andrés C., Schnieders C.,Traute J., Ronald L., Leven B., Burkard H., Casper F., Gerhard J., Kläui M., “Sensors Based on Tunnel Magnetoresistance - New Technology, New Opportunities,” pp. 234-239, 10.5162/sensor2015/B3.2, AMA Conferences 2015 – SENSOR 2015 and IRS2 2015.

[39] M. Rasly, T. Nakatani, J. N. Li *et al.*, “Magnetic, magnetoresistive and low-frequency noise properties of tunnel magnetoresistance sensor devices with amorphous CoFeBTa soft magnetic layers,” *Journal of Physics D-Applied Physics,* vol. 54, no. 9, Mar, 2021.

[40] S. Shao, N. Yu, X. Xu *et al.*, “Tunnel Magnetoresistance-Based Short-Circuit and Over-Current Protection for IGBT Module,” *IEEE Transactions on Power Electronics,* vol. 35, no. 10, pp. 10930-10944, Oct. 2020, 2020.

[41] Crocus Technology, "From Hall Effect to TMR," application note AN117, rev.0.1, 2018.

[42] J. G. Deak, Z. M. Zhou, and W. F. Shen, “Tunneling magnetoresistance sensor with pT level 1/f magnetic noise,” *Aip Advances,* vol. 7, no. 5, May, 2017.

[43] C. Zheng, K. Zhu, S. de Freitas *et al.*, “Magnetoresistive Sensor Development Roadmap (Non-Recording Applications),” *IEEE Transactions on Magnetics,* vol. 55, no. 4, Apr 2019, 2019.

[44] D. Novotny, V. Petrucha, and M. Janosek, “A Digitally Compensated AMR Magnetometer,” *IEEE Transactions on Magnetics,* vol. 55, no. 1, Jan, 2019.

[45] F. Qiu, J. Wang, Y. Zhang *et al.*, “Resolution limit of anisotropic magnetoresistance(AMR) based vector magnetometer,” *Sensors and Actuators a-Physical,* vol. 280, pp. 61-67, Sep 1 2018, 2018.

[46] V. Petrucha, V. Fura, and A. Platil, “Cross-Field Effect in a Triaxial AMR Magnetometer With Vector and Individual Compensation of a Measured Magnetic Field,” *IEEE Transactions on Magnetics,* vol. 53, no. 4, Apr, 2017.

[47] J. Vyhnanek, M. Janosek, and P. Ripka, "Low Frequency Noise of Anisotropic Magnetoresistors in DC and AC-excited Metal Detectors," *Sensors & Their Applications Xvii*, Journal of Physics Conference Series, Bristol: Iop Publishing Ltd, 2013.

[48] P. Brown, B. J. Whiteside, T. J. Beek *et al.*, “Space magnetometer based on an anisotropic magnetoresistive hybrid sensor,” *Review of Scientific Instruments,* vol. 85, no. 12, Dec, 2014.

[49] W. Magnes, O. Hillenmaier, H. Auster *et al.*, “Space Weather Magnetometer Aboard GEO-KOMPSAT-2A,” *Space Science Reviews,* vol. 216, no. 8, Oct 21 2020, 2020.

[50] S. Sordo-Ibáñez, B. Piñero-García, M. Muñoz-Díaz *et al.*, “A Front-End ASIC for a 3-D Magnetometer for Space Applications by Using Anisotropic Magnetoresistors,” *IEEE Transactions on Magnetics,* vol. 51, no. 1, Jan 2015, 2015.

[51] S. Leitner, A. Valavanoglou, P. Brown *et al.*, “Design of the Magnetoresistive Magnetometer for ESA's SOSMAG Project,” *IEEE Transactions on Magnetics,* vol. 51, no. 1, Jan, 2015.

[52] M. Butta, I. Sasada, and M. Janosek, “Temperature Dependence of Offset and Sensitivity in Orthogonal Fluxgate Operated in Fundamental Mode,” *IEEE Transactions on Magnetics,* vol. 48, no. 11, pp. 4103-4106, Nov, 2012.

[53] N. Murata, and A. Matsuoka, “Practical Method for Drastic Improvement of Output Offset Stability in Bias-Switched Fundamental Mode Orthogonal Fluxgate,” *IEEE Sensors Journal,* vol. 21, no. 17, pp. 18641-18649, Sept 1 2021, 2021.

[54] D. M. Miles, M. Ciurzynski, D. Barona *et al.*, “Low-noise permalloy ring cores for fluxgate magnetometers,” *Geoscientific Instrumentation Methods and Data Systems,* vol. 8, no. 2, pp. 227-240, Sep, 2019.

[55] T. Horbury, H. O'Brien, I. Blazquez *et al.*, “The Solar Orbiter magnetometer,” *Astronomy & Astrophysics,* vol. 642, Sep 30 2020, 2020.

[56] J. Connerney, J. Espley, P. Lawton *et al.*, “The MAVEN Magnetic Field Investigation,” *Space Science Reviews,* vol. 195, no. 1-4, pp. 257-291, Dec 2015, 2015.

[57] S. Lee, K. Ryu, D. Choi *et al.*, “Design and Testing of an Adaptive In-phase Magnetometer (AIMAG), the Equatorial-Electrojet-Detecting Fluxgate Magnetometer, for the CAS500-3 Satellite,” *Remote Sensing,* vol. 15, no. 19, Oct 2023, 2023.

[58] D. Hercik, H. U. Auster, J. Blum *et al.*, “The MASCOT Magnetometer,” *Space Science Reviews,* vol. 208, no. 1-4, pp. 433-449, Jul, 2017.

[59] K. H. Glassmeier, H. U. Auster, D. Heyner *et al.*, “The fluxgate magnetometer of the BepiColombo Mercury Planetary Orbiter,” *Planetary and Space Science,* vol. 58, no. 1-2, pp. 287-299, Jan, 2010.

[60] H. U. Auster, K. H. Glassmeier, W. Magnes *et al.*, “The THEMIS Fluxgate Magnetometer,” *Space Science Reviews,* vol. 141, no. 1-4, pp. 235-264, Dec, 2008.

[61] B. Weiss, J. Merayo, J. Ream *et al.*, “The Psyche Magnetometry Investigation,” *Space Science Reviews,* vol. 219, no. 3, Apr 2023, 2023.

[62] K. Greene, C. Hansen, B. Narod *et al.*, “Tesseract - a high-stability, low-noise fluxgate sensor designed for constellation applications,” *Geoscientific Instrumentation Methods and Data Systems,* vol. 11, no. 2, pp. 307-321, Aug 23 2022, 2022.

[63] H. O'Brien, P. Brown, T. Beek *et al.*, “A radiation tolerant digital fluxgate magnetometer,” *Measurement Science and Technology,* vol. 18, no. 11, pp. 3645-3650, Nov, 2007.

[64] M. H. Zhi, L. Tang, X. Cao *et al.*, “Digital Fluxgate Magnetometer for Detection of Microvibration,” *Journal of Sensors*, 2017.

[65] M. Scherzer, M. Auer, A. Valavanoglou *et al.*, *Circuit Design and Verification Method of Integrated Sensor-Front-End Elements for Spaceborne Fluxgate Magnetometers*, 2019.

[66] S. Belyayev, and N. Ivchenko, “Digital fluxgate magnetometer: design notes,” *Measurement Science and Technology,* vol. 26, no. 12, pp. 11, Dec, 2015.

[67] L. Nejezchleb, “Module for hysteresis loop measurement of soft ferromagnetic materials,” bachelor thesis, Czech Technical University in Prague, Faculty of Electrical Engineering, 2023.

[68] N. Beev, "Analog-to-digital conversion beyond 20 bits," 2018 IEEE International Instrumentation and Measurement Technology Conference (I2MTC), pp. 1-6, Houston, TX, USA, 2018

[69] I. Hrvoic, "Overhauser Magnetometers For Measurement of the Earth’s Magnetic Field," GEM Systems Inc., Magnetic field Workshop on Magnetic Observatory Instrumentation Espoo, Finland. 1989.

[70] B. J. Cheng, B. Zhou, W. Magnes *et al.*, “High precision magnetometer for geomagnetic exploration onboard of the China Seismo-Electromagnetic Satellite,” *Science China-Technological Sciences,* vol. 61, no. 5, pp. 659-668, May, 2018.

[71] O. Bureš “Proton magnetometer and precession signal processing,” bachelor thesis, *Czech Technical University in Prague, Faculty of Electrical Engineering*, 2021.

[72] M. Dressler, “Current Source for a Test Coil System,” bachelor thesis, *Czech Technical University in Prague, Faculty of Electrical Engineering*, 2017.

[73] M. Dressler, “Stabilized Triaxial Coil System for Magnetometer Calibrations,” Master thesis, *Czech Technical University in Prague, Faculty of Electrical Engineering*, 2019.

[74] A. Zikmund and M. Janosek, "Calibration procedure for triaxial magnetometers without a compensating system or moving parts," *2014 IEEE International Instrumentation and Measurement Technology Conference (I2MTC) Proceedings,* Montevideo, Uruguay, pp. 473-476, 2014

[75] A. Zikmund, P. Ripka, R. Ketzler *et al.*, “Precise Scalar Calibration of a Tri-Axial Braunbek Coil System,” *IEEE Transactions on Magnetics,* vol. 51, no. 1, Jan 2015, 2015.

[76] Š. Rais, “Module for sensitivity calibration of magnetic sensors,” bachelor thesis, *Czech Technical University in Prague, Faculty of Electrical Engineering*, 2023.

[77] N. Olsen, T. Risbo, P. Brauer *et al.*, “In-flight calibration methods used for the Ørsted mission,” *ESA - SP on Calibration of Magnetometers*, pp. 13, 2000.

[78] J. M. G. Merayo, P. Brauer, F. Primdahl *et al.*, “Scalar calibration of vector magnetometers,” *Measurement Science and Technology,* vol. 11, no. 2, pp. 120-132, Feb, 2000.

[79] M. Indrych, “High resolution data acquisition module,” Master thesis, *Czech Technical University in Prague, Faculty of Electrical Engineering,* 2024.

[80] N. Beev, M. C. Bastos, M. Martino and D. Valuch, "A Metrology-grade Digitizer for Power Converters in the High Luminosity Large Hadron Collider," *2022 IEEE International Instrumentation and Measurement Technology Conference (I2MTC),* pp. 1-6, Ottawa, ON, Canada, 2022

[81] L. K. Quynh, B. D. Tu, C. V. Anh *et al.*, “Design Optimization of an Anisotropic Magnetoresistance Sensor for Detection of Magnetic Nanoparticles,” *Journal of Electronic Materials,* vol. 48, no. 2, pp. 997-1004, Feb, 2019.

[82] P. V. Sreevidya, J. Khan, H. C. Barshilia *et al.*, “Development of two axes magnetometer for navigation applications,” *Journal of Magnetism and Magnetic Materials,* vol. 448, pp. 298-302, Feb, 2018.

[83] Q. F. Wei, and B. Yang, “Adaptable Vehicle Detection and Speed Estimation for Changeable Urban Traffic With Anisotropic Magnetoresistive Sensors,” *IEEE Sensors Journal,* vol. 17, no. 7, pp. 2021-2028, Apr, 2017.

[84] S. Taghvaeeyan, and R. Rajamani, “The Development of Vehicle Position Estimation Algorithms Based on the Use of AMR Sensors,” *Ieee Transactions on Intelligent Transportation Systems,* vol. 13, no. 4, pp. 1845-1854, Dec, 2012.

[85] R. Macíček, “Compact Hall probe magnetometer,” bachelor thesis, *Czech Technical University in Prague, Faculty of Electrical Engineering*, 2022.

[86] C. P. Gooneratne, B. D. Li, and T. E. Moellendick, “Downhole Applications of Magnetic Sensors,” *Sensors,* vol. 17, no. 10, pp. 32, Oct, 2017.
[87] P. Ripka, *Magnetic sensors and magnetometers, 2nd ed.*, Boston, London: Artech House, 2021.
[88] *M. Takáč*, *R.* K*avkova*, *G.* K*letetschka et al.*, "*Detecting Magnetic Anomalies Of Crater Fields By a Drone*," *The AGU-SEG Airborne Geophysics Workshop*, 2019.
[89] *M. Takáč*, *G.* K*letetschka*, *R.* K*avkova et al.*, "Tunguska Event and Magnetic Signature Over the Epicenter," *11th Planetary Crater Consortium,* 2020.
[90] *M. Takáč*, *G.* K*letetschka*, and *V.* P*etrucha*, "*UAV magnetometer survey of the Acraman’s crater epicenter*," *85th Annual Meeting of the Meteoritical Society*, 2022.
[91] B. Pavol Lipovský and Jozef Novotňák and Josef, “Possible Utilization of Low Frequency Magnetic Fields in Short Range Multirotor UAV Detection System,” *Transportation Research Procedia,* vol. 65, pp. 106-115, 2022.
[92] P. Lipovsky, K. Draganová, J. Novotnák *et al.*, “Indoor Mapping of Magnetic Fields Using UAV Equipped with Fluxgate Magnetometer,” *Sensors,* vol. 21, no. 12, Jun 2021, 2021.
[93] Elbra, T., Schnabl, P., Čížková, K. et al. Palaeo- and rock-magnetic investigations across Jurassic-Cretaceous boundary at St Bertrand’s Spring, Drôme, France: applications to magnetostratigraphy. Stud Geophys Geod 62, pp. 323–338, 2018.
[94] P. K., “MAVACS - a new system for creating a non-magnetic environment for paleomagnetic studies,” *Geologia Iberica,* vol. no. 12, pp. pp. 233, 1988.
[95] D. W. Collinson, “Methods in Rock Magnetism and Palaeomagnetism: Techniques and Instrumentation,” *Springer Dordrecht,* 1983
[96] C. Turbitt, "INTERMAGNET Definitive One-second Data Standard," INTERMAGNET Technical note *TN6*, 22 Oct 2014, 2014.
[97] C. I. Mahdi, H. Nain, H. Nik *et al.*, "An Overview of Ship Magnetic Signature and Silencing Technologies," Defence S&T Technical Bulletin, Vol.22, Num.2, Science & Technology Research Institute for Defence (STRIDE), 2019.
[98] Y. Gang, Y. Zhang, Z. Li *et al.*, “Detection of ferromagnetic target based on mobile magnetic gradient tensor system,” *Journal of Magnetism and Magnetic Materials,* vol. 402, pp. 1-7, Mar 15 2016, 2016.
[99] B. Oruç, “Location and depth estimation of point-dipole and line of dipoles using analytic signals of the magnetic gradient tensor and magnitude of vector components,” *Journal of Applied Geophysics,* vol. 70, no. 1, pp. 27-37, Jan 2010, 2010.
[100] Y. Y. Sui, H. S. Miao, Z. J. Zhou *et al.*, “Correction and compensation of an airborne fluxgate magnetic tensor gradiometer,” *Exploration Geophysics,* vol. 49, no. 5, pp. 726-734, Oct, 2018.
[101] Y. Sui, K. Leslie, and D. Clark, “Multiple-Order Magnetic Gradient Tensors for Localization of a Magnetic Dipole,” *IEEE Magnetics Letters,* vol. 8, 2017.
[102] B. Zuo, L. Wang, and W. Chen, “Full Tensor Eigenvector Analysis on Air-Borne Magnetic Gradiometer Data for the Detection of Dipole-Like Magnetic Sources,” *Sensors,* vol. 17, no. 9, Sep 2017, 2017.
[103] Smith, D.V., Phillips, J.D., and Hutton, S.R., "Active tensor magnetic gradiometer system final report for Project MM–1514," U.S. Geological Survey Open-File Report 2013–1228, 39 p, 2014.
[104] J. A. Young and D. A. Clark, "Magnetic tensor gradiometry in the marine environment," *2010 International Conference on Electromagnetics in Advanced Applications*, Sydney, NSW, Australia, pp. 701-704, 2010.
[105] R.E. Bracken and P.J. Brown, “Reducing tensor magnetic gradiometer data for unexploded ordnance detection,“ USGS Numbered Series - Scientific Investigations Report 2005-5046, 2005.
[106] D. Clark, “New methods for interpretation of magnetic vector and gradient tensor data I: eigenvector analysis and the normalised source strength,” *Exploration Geophysics,* vol. 43, no. 4, pp. 267-282, Dec 2012, 2012.
[107] J. Čechák, M. Marek, V. Petrucha *et al.*, "Supported ferromagnetic parts detector," 2019.

7 Reprints of Articles Included in the Thesis

An introduction to each paper adding to the overall content complete with a detailed author contribution note (contribution percentages shown as is listed in the V3S information system https://v3s.cvut.cz).

7.1 Sensor and magnetometer development

7.1.1 refP 1

Petrucha, V.; Fúra, V.; Platil, A., "Cross-field Effect in a Triaxial AMR Magnetometer with Vector and Individual Compensation of a Measured Magnetic Field," IEEE Transactions on Magnetics. 2017, 53(4), ISSN 0018-9464

This research was motivated by an effort to build a "reference" design of an AMR magnetometer that could be used for studies and measurements within an industrial project. Two versions of the triaxial sensor heads were built, one with individual field compensation and the second with vectorial compensation. The individually compensated sensor head exhibited a large cross-field error when the disturbing field was present in parallel with the chip plane. Interestingly, later, during development of the digitally compensated AMR magnetometer, we did not observe this kind of cross-field error. The only explanation to this seems to be the difference in topological placement of the sensors between the two constructions, although that should not theoretically affect the phenomena. The author's contribution is 80%, having served as the design and measurements leader and supervisor of the second author's master's thesis.

Cross-Field Effect in a Triaxial AMR Magnetometer With Vector and Individual Compensation of a Measured Magnetic Field

Vojtěch Petrucha, Viktor Fúra, and Antonín Platil

Faculty of Electrical Engineering, Czech Technical University, 166 27 Prague, Czech Republic

Magnetic field sensors based on anisotropic magnetoresistance (AMR) are widely used in many scientific and industrial applications. The AMR sensor sensitivity is superior to Hall probes and size and power consumption is superior to fluxgates. However, the noise properties and the temperature stability of AMR sensors are typically worse than for fluxgates. These properties define the typical applications—less precise vectorial or gradient measurements of the magnetic field within less than ±1 mT range. AMR sensors are typically calibrated for sensitivity, offset, and orthogonality errors. However, there is another important source of error—sensitivity to the magnetic field applied in the perpendicular direction to the measurement axis. This so-called cross-field error is inherent to AMR sensors and can influence the measurements significantly. Flipping (set/reset pulses) and closed-loop operation of the sensor can reduce the cross-field error. In this paper, we present a novel approach using full vectorial compensation of the measured magnetic field resulting in a complete elimination of the cross-field effect. The vectorial compensation provided superior results over alternative approaches that were also evaluated.

Index Terms—**Anisotropic magnetoresistance (AMR), cross-field error, magnetic field, vector compensation.**

I. Introduction

MAGNETIC field sensors based on anisotropic magnetoresistance (AMR) are widely used in many scientific and industrial applications. Their sensitivity is superior to Hall probes and size and power consumption is superior to fluxgates. However, the noise properties and the temperature stability of AMR sensors are typically worse than for fluxgates [1]. These properties define the typical applications—less precise vectorial or gradient measurements of the magnetic field within lesser than ±1 mT range. Compassing and other navigation tasks are typical, as well as current measurements and metal objects detection (e.g., car detection) [2].

AMR sensor function is based on resistance change in the thin layer of a magnetic material caused by shifting of the magnetization vector by the measured external field [3]. The sensor is intrinsically sensitive to the field perpendicular to the sensitivity axis. In the literature, this effect is often described as cross-field error [4]. The effect is non-linear and can cause significant errors in the measured data. The cross-field effect can also be present in other types of sensors, such as fluxgates [5], [6], where the manifestation is different. Several techniques for overcoming this issue have been presented. Significant reduction of the cross-field error is expected for magnetometers that use flipping and closed-loop feedback operations [4], [7]. Flipping is a method that periodically changes the magnetization direction by applying a strong current pulse to a coil that is tightly coupled with the magnetic material (flipping coil). This procedure further reduces the low-frequency noise of the sensor. Closed-loop feedback is used to improve the dynamic range of the sensor and its linearity. The output of an AMR sensor can be described with

$$V_{\mathrm{OUT}} = a \cdot \frac{H_{\mathrm{SENSITIVE}}}{H_{\mathrm{ANISOTROPY}} + H_{\mathrm{CROSS\text{-}AXIS}}}. \quad (1)$$

The sensor output is dependent on the measured field along the sensitive axis $H_{\mathrm{SENSITIVE}}$, anisotropy field $H_{\mathrm{ANISOTROPY}}$, and the perpendicular cross-axis field $H_{\mathrm{CROSS\text{-}AXIS}}$. By keeping the sensor output close to zero, in the closed-loop operation mode, the effect of $H_{\mathrm{CROSS\text{-}AXIS}}$ should be minimized. Methods for (numerical) cross-axis sensitivity correction have also been presented for designs where flipping and closed-loop operation are not possible. The technique is based on the measurement of the anisotropy field [8]. Another possibility is the advanced digital processing of the sensor output signal instead of the simple averaging typically used in the flipping mode [9]. Recently, Ouyang *et al.* [10] presented a cross-axis compensation method for AMR sensors but showed results only for the total field, not for the components. Mohamadabadi *et al.* [11] presented a method for the cross-axis effect compensation based on modeling and flipping.

This paper presents the results of cross-field error measurements with respect to the compensation system used. This hardware-based approach has not been presented earlier. Data for three different compensation topologies in terms of linearity performance and calibration results are compared. The motivation for this paper was the development of a precise AMR-based laboratory magnetometer and a comparison between the proven Honeywell HMC1021S and the newly available Sensitec AFF755 AMR sensor. They were compared mainly from the noise point of view, and the results can be found in [12]. In all measurements presented here, HMC1021S sensors were used.

II. Experiment Setup

The magnetometer used for the measurements has a modular conception. The first part is a sensor head that contains an orthogonal triplet of the AMR sensors, precise current

Manuscript received August 10, 2016; revised October 4, 2016; accepted October 5, 2016. Date of publication October 12, 2016; date of current version March 16, 2017. Corresponding author: V. Petrucha (e-mail: petruvoj@fel.cvut.cz).

Color versions of one or more of the figures in this paper are available online at http://ieeexplore.ieee.org.

Digital Object Identifier 10.1109/TMAG.2016.2617121

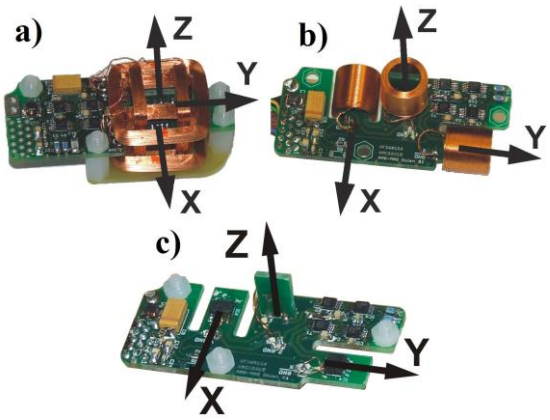

Fig. 1. Three different versions of the AMR-based sensor heads. (a) Vector compensation. (b) Solenoid coil compensation. (c) On-chip embedded compensation. The electrical circuit is the same in all cases.

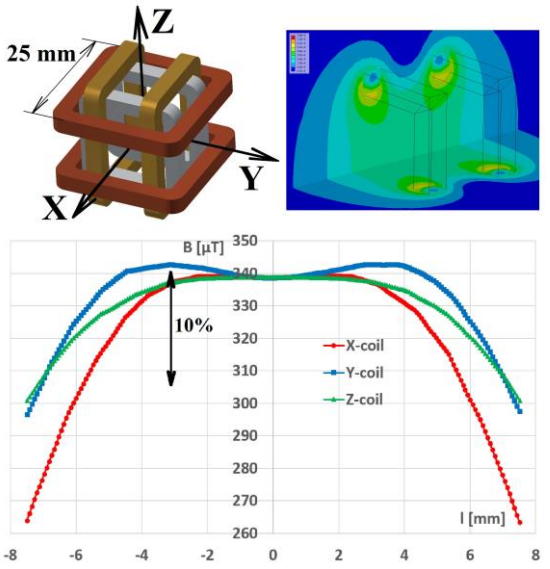

Fig. 2. Top left: construction model of the vector compensation system. Top right: all the coils were optimized using FEM modeling; the FEM model of the Z-axis is shown. Bottom: compensation system provides approximately 10% field homogeneity for the $12 \times 12 \times 12$ mm^3 volume, where the AMR sensors HMC1021S are located.

source for sensor bridge excitation, low-noise instrumentation amplifiers to amplify the sensor output voltage, and a full MOSFET H-bridge for applying the flipping pulses. Three different versions of the sensor heads were designed, manufactured, and tested. All were operated in a closed-loop operation mode and were electrically identical. They differed in how the compensation field was applied (see Fig. 1). The heads were constructed to minimize the ferromagnetic material content as much as possible (use of non-magnetic versions of passive components and selection of non-magnetic materials).

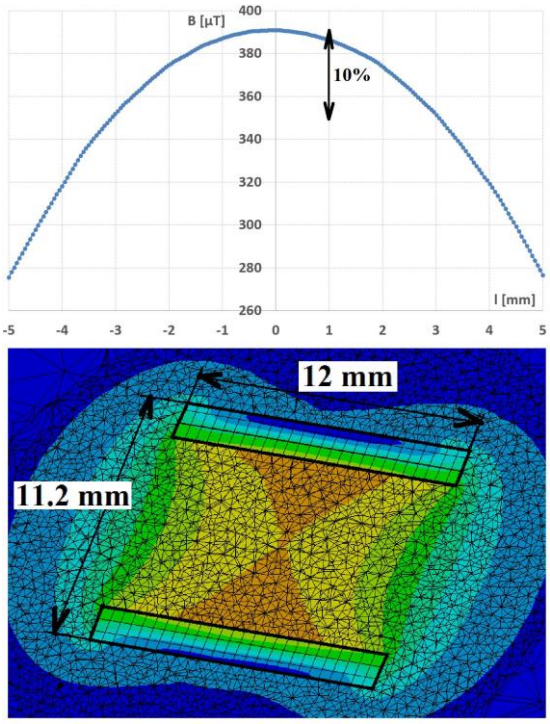

Fig. 3. FEM simulation of the magnetic field homogeneity for the solenoid compensation. The 10% homogeneity region is approximately 6-mm wide.

The first version [Fig. 1(c)] used coils embedded in the sensor itself. No extra cost, no additional assembly work, and small size are the advantages. However, the low coil constant given by the manufacturer limits the full-scale range of the closed-loop system (e.g., ± 217 μT for ± 10 mA of compensation current). The second sensor head [Fig. 1(b)] uses an external solenoid coil to create the compensation magnetic field. The advantage is a higher field constant (± 390 μT for ± 10 mA) and possibly slightly better field homogeneity when compared with the embedded compensation. The third sensor head [Fig. 1(a)] uses three pairs of rectangular coils to create a vector field compensation. The advantage is complete zeroing of the measured magnetic field simultaneously in all three sensitive directions and reasonable coil constant (± 340 μT for ± 10 mA). Bigger size and increased price due to complicated self-supporting coil manufacture and assembly are the drawbacks. The external coils were designed with the use of finite-element method simulations to provide as homogenous magnetic field as possible while keeping the other requested parameters (coil constant and dimensions) reasonable. See Figs. 2 and 3 for the external coil design and performance.

Sensor heads are connected to signal conditioning and analog-to-digital conversion unit. The signal conditioning consists of an input buffer, a synchronous detector, an integrator, and compensation current sensing. The current was measured simultaneously for all three channels and digitized with

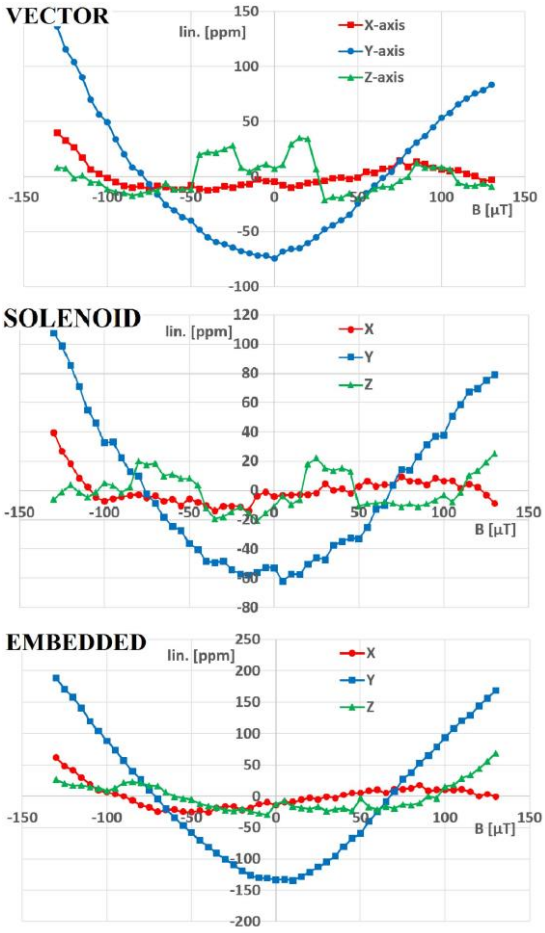

Fig. 4. Results of linearity error measurements for the three different compensation systems. The linearity was typically better than ±50 ppm for the X- and Z-axes; the results were slightly worse for the Y-axis (less than ±150 ppm).

a 24-b $\Delta\sum$ A/D converter (ADS1274). The digital data were further processed (averaged) and sent to the computer via a universal serial bus or RS232 interface. Typical noise values measured with the HMC1021S sensor heads (independently of the type of compensation used) were 120–300 $pT_{RMS}/\sqrt{Hz}$ at 1 Hz. Thus, the dynamic range of the instrument is around 120 dB.

The linearity and the calibration presented in Section III were measured at a special magnetic laboratory in a calm environment at the outskirts of Prague, which is equipped with two 3-D coil systems. The first coil system with approximately 2.5-m coil dimensions was used to roughly cancel Earth's magnetic field (coils driven by constant current sources). There was a second 3-D coil system (HELM-3 by Billingsley, ~1-m size) in the middle of the first one. The APEX-CS digital current driver controlled this coil triplet. The controller runs in a closed loop. There is a fluxgate sensor in the coil system. The

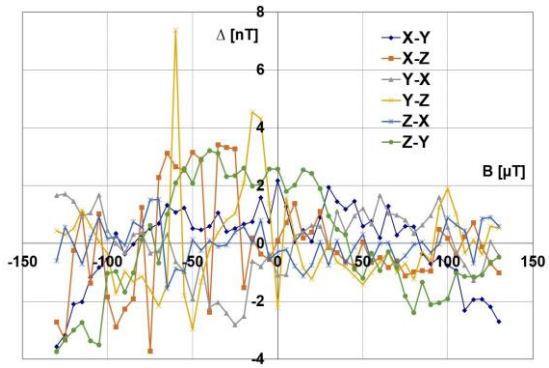

Fig. 5. Cross-field response for the vectorially compensated sensor head. The error was typically below ±4 nT for all cases (less than ±31 ppm). X–Y means "the response in the Y-axis when excited in the X-axis."

complete setup allows any arbitrary field vector to be created with a maximum magnitude of approximately 130 μT (with approximately 20-b precision), while the urban and natural field disturbances are effectively suppressed (including 50 Hz).

III. Measurements and Results

A. Linearity and Cross-Field Measurements

Linearity and cross-field error were measured at the same time. The sensor axes were approximately aligned with coil axes. For each of the three sensor heads, a "staircase"-like waveform was created individually for each axis (X, Y, and Z) by the coil system (53 steps with ±130 μT span). All outputs were monitored and logged in the times when the generated field was stable, and the magnetometer output was settled. By observing the sensor output in the axis where the excitation was applied, we got the transfer functions. See Fig. 4 for the non-linearity errors. The characteristics were almost perfectly linear; we got less than ±50 ppm residua for the X- and Z-axes. The results were slightly worse (less than ±150 ppm) for the Y-axis. However, as it was very systematic for all three sensor heads, we assume that it was either a problem with the coil system or one specific channel of the signal processing electronics. Unfortunately, we did not have time to repeat the measurement with the sensor head rotated 90°, which would have helped identify the cause.

By observing the output of the two axes (e.g., Y and Z) while the excitation sweep was applied on the third axis (e.g., X), we collected information about the cross-field response. As the first step, the linear part of the response was subtracted as it might be considered (and possibly also calibrated out) sensor offset and sensitivity axis misalignment. After this step, we got residua that represented the unwanted non-linear cross-field effect. The sensors were operated in a closed loop and continuously flipped to both magnetization vector polarities for all measurements.

In the vectorially compensated sensor head, virtually no cross-field effect was observed (see Fig. 5). The residua were below ±4 nT, which corresponds to less than ±31 ppm of the

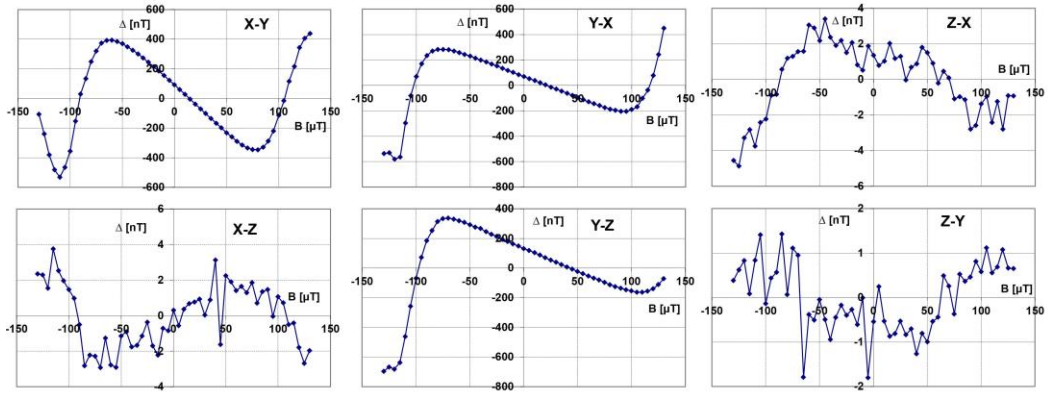

Fig. 6. Cross-field error for the individual compensation with solenoid coils. The linear component was subtracted (can be interpreted as offset and misalignment). The marking (e.g., *X–Y*) is the same as in Fig. 5.

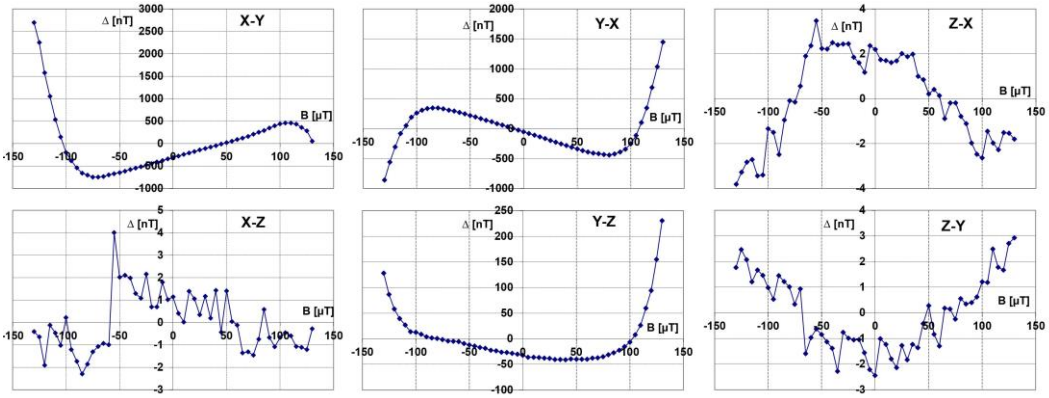

Fig. 7. Cross-field error for individual compensation with on-chip embedded coils. The error is up to +2500 to −700 nT (+19230 to −5380 ppm).

maximum applied field. Any possible systematic behavior was already hidden in noise.

The situation was completely different for both types of individually compensated sensor heads. Fig. 6 shows the cross-field response of the sensor head with solenoid compensation coils, while Fig. 7 shows the sensor head with on-chip embedded compensation coils.

One can observe two different situations. When the exciting field is perpendicular to the plane of the AMR sensor chip, again virtually no cross-field error is visible (less than ±31 ppm). However, when the excitation field is applied in the perpendicular direction to the sensitive axis and in the plane of the chip, a huge cross-field response is present in an order of several hundreds up to several thousands of nanotesla (approximately 10 000 ppm). See Fig. 1(c) for the orientation of the sensors.

B. Calibration

All the probes were calibrated using the algorithm presented in [13]. It consists of applying a set of field vectors with constant magnitude to the calibrated sensor head and calculating the nine calibration parameters (sensitivities, offsets, and non-orthogonalities). The vectors were applied in two ways. In the first method, the device was rotated in Earth's uniform magnetic field, and the vector magnitude was monitored and logged with an Overhauser scalar magnetometer. The second method used the 3-D coil system to generate the vectors. The results from both methods were practically the same. The results using the coil generated test vectors are presented in Table I. The best results were achieved with the vectorially compensated sensor head, and almost reached the performance

TABLE I
SCALAR CALIBRATION RESULTS

Type	Residua (nT_{P-P})	Residua (nT_{RMS})	Residua (ppm of F.S.)
EMBEDDED	±20 nT	5.6	±200 ppm
SOLENOID	±50 nT	12.8	±500 ppm
VECTOR	±5 nT	1.5	±50 ppm*

*approximately one order of magnitude worse than our best fluxgate sensor

of some common commercial fluxgate sensors. Significantly worse but still very usable results were reached with the individually compensated heads; the one with embedded compensation gave unexpected better results.

The cross-field error responses seemed to have a well-defined shape, so we approximated the curves with the fifth-order polynomial functions (which provided an excellent fit) and tried to correct the effect for the calibration data. Unfortunately, we did not experience any improvement. Further testing showed that the curve is dependent not only on the perpendicular field but also on the in-axis field. Thus, the compensation would have to use at least 2-D inputs to cover all possible data. Unfortunately, the time and temperature stability of such calibration would probably be very questionable.

IV. Conclusion

A triaxial AMR-based modular magnetometer with three different sensor head designs is presented. The vector compensation of the measured magnetic field used in one of the sensor heads provided excellent results regarding the linearity and calibration residua. To the best of our knowledge, this level of precision has not been presented before for AMR magnetometers. The vector compensation practically eliminated the cross-field error that would otherwise significantly limit the sensor performance. Unlike modeling or "software"-based corrections, the vector compensation is due to its principal very robust with excellent time-temperature stability. Of course, the disadvantage lies in the increased complexity of the sensor assembly, and thus, it is appropriate only for the state-of-the-art applications. Further research is planned to explore the stability of possible cross-field compensation based on 2-D mapping of the effect as mentioned in Section III-B.

Acknowledgment

This work was supported by the Technology Agency of the Czech Republic under Project TE02000202—Advanced Sensors Competence Center.

References

[1] P. Ripka, *Magnetic Sensors and Magnetometers*. Norwood, MA, USA: Artech House, 2001.

[2] M. J. Caruso and L. S. Withanawasam, *Vehicle Detection and Compass Applications Using AMR Magnetic Sensors*. New Jersey, NJ, USA: Honeywell, 1999.

[3] S. Tumanski, *Thin Film Magnetoresistive Sensors*. Boca Raton, FL, USA: CRC Press, 2001.

[4] J. Včelák, P. Ripka, A. Platil, J. Kubik, and P. Kašpar, "Errors of AMR compass and methods of their compensation," *Sens. Actuators A, Phys.*, vol. 129, nos. 1–2, pp. 53–57, May 2006.

[5] P. Brauer, J. M. G. Merayo, O. V. Nielsen, F. Primdahl, and J. R. Petersen, "Transverse field effect in fluxgate sensors," *Sens. Actuators A, Phys*, vol. 59, nos. 1–3, pp. 70–74, Apr. 1997.

[6] M. Janosek, M. Butta, and P. Ripka, "Two sources of cross-field error in racetrack fluxgate," *J. Appl. Phys.*, vol. 107, p. 09E713, May 2010.

[7] J. Kubik, J. Vcelak, and P. Ripka, "On cross-axis effect of the anisotropic magnetoresistive sensors," *Sens. Actuators A, Phys.*, vol. 129, nos. 1–2, pp. 15–19, May 2006.

[8] P. Ripka, M. Janosek, and M. Butta, "Crossfield sensitivity in AMR sensors," *IEEE Trans. Magn.*, vol. 45, no. 10, pp. 4514–4517, Oct. 2009.

[9] J. Kubik, J. Vcelak, and P. Ripka, "On cross-axis effect of the anisotropic magnetoresistive sensors," *Sens. Actuators A, Phys.*, vol. 129, nos. 1–2, pp. 15–19, May 2006.

[10] J. Ouyang *et al.*, "Compensation method of cross-axis effect for AMR sensor," in *Proc. Int. Conf. Elect. Control Eng.*, Jun. 2010, pp. 604–606.

[11] K. Mohamadabadi, C. Coillot, and M. Hillion, "New compensation method for cross-axis effect for three-axis AMR sensors," *IEEE Sensors J.*, vol. 13, no. 4, pp. 1355–1362, Apr. 2013.

[12] V. Fúra, V. Petrucha, and A. Platil, "Construction of an AMR magnetometer for car detection experiments," in *Proc. IOP Conf. Series, Mater. Sci. Eng.*, vol. 108. 2016, p. 012028.

[13] N. Olsen, T. Risbo, P. Brauer, J. Merayo, F. Primdahl, and T. Sabaka. *In-Flight Calibration Methods Used for the Ørsted Mission*, accessed on Mar. 15, 2016. [Online]. Available: http://citeseerx.ist.psu.edu/viewdoc/summary?doi=10.1.1.41.3567

7.1.2 refP 2

Novotný, D.; Petrucha, V.; Janošek, M., "A Digitally Compensated AMR Magnetometer," IEEE Transactions on Magnetics. 2019, 55(1), ISSN 0018-9464

This article presents a new effort to make the AMR magnetometer more compact and power-efficient, employing a modern microcontroller for signal processing as the previous construction used the standard analog signal processing approach and was very power hungry. This construction paved the way to even more compact and later successful designs. The author's contribution is 25%, having concentrated primarily on the sensor's design, calibration, and characterization.

A Digitally Compensated AMR Magnetometer

David Novotný, Vojtěch Petrucha, and Michal Janošek

Department of Measurement, Faculty of Electrical Engineering, Czech Technical University in Prague, 16627 Prague, Czech Republic

This paper considers the possibilities of using digital feedback for precise anisotropic magneto-resistance (AMR) magnetometers using commercial off-the-shelf (COTS) components. Requiring only a few analog parts, most of the signal processing is done digitally within an STM32 microcontroller. Because most of the precision is made by the feedback circuit, the analog-to-digital converter (ADC) can be a low-cost type. The compensation source is made with a pulsewidth modulation-driven H-bridge sourced from a voltage reference, so the cost reduction when compared to a "full-analog" design is large. The demodulation of a flipped-AMR signal is done with software after the AD conversion because it improves the offset stability and brings the reduction of the preamp's and ADC's LF noise. This paper presents the full characterization of a real instrument, including its noise, linearity, stability, and power consumption.

***Index Terms*—Anisotropic magneto-resistance (AMR), commercial off-the-shelf (COTS), digital feedback, magnetic sensor, STM32.**

I. Introduction

ANISOTROPIC magneto-resistance (AMR)-based magnetometers are typically used for measuring weak magnetic fields (2 nT/1 mT). They generate a higher noise than traditional fluxgate sensors (approximately one order of magnitude or more) but can have a smaller sized sensor head (by mass and volume), lower power consumption, and their sensors are generally available on the commercial market [1], [2]. Typical applications include compassing, general navigation, current measurements, and recently even space research [3], [4]. AMRs can be used as the main sensor [5] or as an auxiliary sensor to clean out the measurements of a precise fluxgate sensor—to remove disturbances caused by the satellite itself [6].

Most magnetometers [1], [7], [8] use a "analog feedback" solution because a digital feedback design has been related to costly application-specified integrated circuit (ASIC) ICs [9], [10]. In this paper, we show a novel method of how a readily available commercial off-the-shelf (COTS) STM32 microcontroller (MCU) can replace an ASIC while preserving the precision of an analog or ASIC digital solution. Using digital feedback is also very advantageous for possible applications in space where it is generally easier to provide radiation tolerance for the digital parts [(with a single field-programmable gate array (FPGA)] rather than for a large amount of precise analog parts.

Feedback compensation of a sensor is an indirect measurement method that uses the sensor only as a "zero indicator." The measurement output is proportional to the compensation value, which is the current through the compensation coil. This improves the main measurement parameters, because a sensor operates only in a small range, with close to a zero value. Nonlinearity, hysteresis, and gain drift are minimized and are caused mostly by the compensation system itself. Offset drift and noise are still given by sensor parameters and can potentially be a bit worsened by feedback compensation.

The main part of a compensation concept is the controlled current source for the feedback coil. One possibility is to use a precise, COTS DAC, but the relatively high cost must be considered. On the other hand, almost all modern MCUs have many pulse-width modulation (PWM) channels; when an MCU is combined with an external H-bridge and a precise voltage reference, a precise, low-cost DAC is created. However, the disadvantage to this method is the low resolution of the PWM, since its output frequency is given by the main MCU peripheral frequency divided by the resolution. If the output frequency is high, a high main frequency is also needed. High resolution can be obtained, for example, by using an FPGA, for which multiple delay-locked loops, delay lines, or ring oscillators are available, or by using a special type of microcontroller. STM32F334 is designed particularly for use with dc/dc and motor drivers. It can generate a PWM signal with the equivalent of 4.6 GHz main frequency by calibrated delay taps, which interpolate 32 fractions of a single PWM cycle, running at ~144 MHz.

The DAC's voltage to current conversion is accomplished according to Ohm's law and uses a stable serial resistor with a much larger value than the feedback coil's resistance. This simple, efficient method has some constraints. The added resistance value must be much larger than the coil's resistance; however, the maximum current is limited by the DAC's full-scale (FS) output divided by this resistance, which constrains the magnetometer's FS range.

A vector compensation of the measured magnetic field was used so that it should cause a better cross-field effect attenuation [11]. However, the comparison with an individual compensation which was also realized did not show any significant difference.

II. Magnetometer Design

A. Principle of Operation

Because the feedback-compensated sensor works only in a small range around zero, the preamplifier and analog-to-digital

Manuscript received July 15, 2018; revised September 6, 2018; accepted September 17, 2018. Date of publication October 24, 2018; date of current version December 18, 2018. Corresponding author: D. Novotný (e-mail: novotd12@fel.cvut.cz).

Color versions of one or more of the figures in this paper are available online at http://ieeexplore.ieee.org.

Digital Object Identifier 10.1109/TMAG.2018.2873235

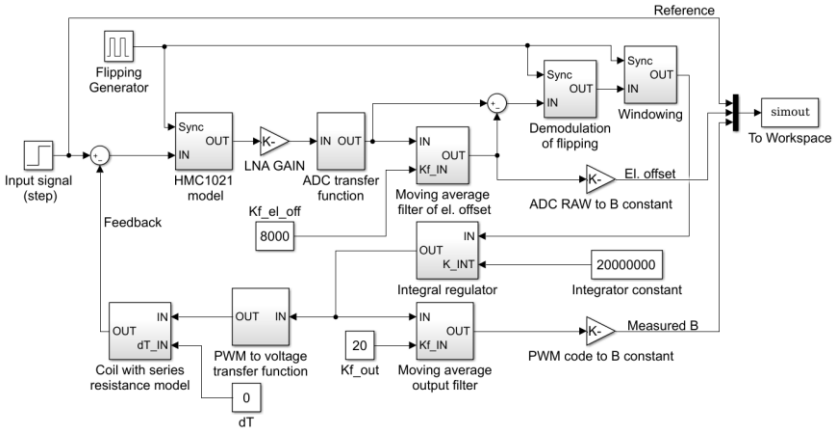

Fig. 1. Simulink model of magnetometer.

converter (ADC) gain can be set at a high value to achieve the noise floor below the sensor's noise. Only a large signal response can be affected by a large gain, since the feedback loop propagation delay causes the ADC to go over-range and thus causes a short-term nonlinear behavior in a feedback loop. This effect can, however, be reduced if the compensation is faster than the desired magnetometer output bandwidth by using output smoothing/filtering.

The measured magnetic field is completely compensated. Our approach uses a single range bipolar-PWM DAC (using an SMT32 high-resolution timer), which has a better linearity and a simpler design compared to a two-DAC solution [9]. The PWM duty cycle is also held in 5%–95% range to keep the nonlinearity low in the FS range (50% ≡ zero compensation field). The disturbing signal at the PWM frequency is suppressed through multiple means. First, a capacitor is connected parallel to the compensation coil, effectively short-circuiting the ac component of the PWM signal.

Care must be taken to avoid the resonance mode of the *RLC* circuit. In this manner, an attenuation of about 60 dB is achieved. Suppression is performed by the ADC input filter (about 20 dB). Last, the sigma-delta ADC's (MCP3912) over-sampling ensures a further attenuation of about 60 dB. A total attenuation of >140 dB is sufficient to prevent the PWM waveform from affecting the measurement.

To keep offsets and offset drifts low, the AMR sensors are periodically "flipped" with a frequency of ∼420 Hz, which also suppresses the LF noise of the preamplifier and ADC through modulation and demodulation [12].

A simulation circuit of the magnetometer can be seen in Fig. 1. This MATLAB-Simulink model has been used for the magnetometer's behavior verification.

B. Feedback Compensation

A current source for the compensation coils is created by a PWM-controlled voltage source with a large resistance in series with the coils as can be seen in Fig. 2.

For a coil with a resistance of R_C [Ω], a magnetic constant K [T/A], a voltage source with a maximum

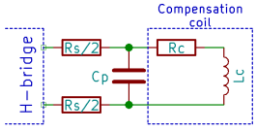

Fig. 2. Compensation coil connection.

voltage U_{ref} [V], a PWM codeword C [−], and a serial resistance R_S [Ω], we get (1) for the compensation field if an N [bit]-resolution PWM is used. The maximum compensated field can be then calculated by (2)

$$B = K \cdot \frac{2 \cdot U_{\text{ref}}}{(R_c + R_s)} \cdot \left(\frac{C}{2^N} - 0.5\right)[T] \tag{1}$$

$$B_{\text{MAX}} = \pm K \cdot \frac{U_{\text{ref}}}{(R_c + R_s)}. \tag{2}$$

Temperature drifts caused by this method can be derived by substituting both resistances in (3), and the resulting absolute drift rate is shown in (4)

$$R_x(\Delta T) = R_{0_x}(1 + \alpha_x \Delta T) \tag{3}$$

$$\frac{\partial B}{\partial \Delta T} = -K \cdot \frac{2 \cdot U_{\text{ref}} \cdot (R_c\alpha_c + R_s\alpha_s)}{(R_c + R_s + (R_c\alpha_c + R_s\alpha_s) \cdot \Delta T)^2} \cdot \left(\frac{C}{2^N} - 0.5\right)\left[\frac{T}{K}\right]. \tag{4}$$

The relative drift rate is then equal to (5) and neglecting the temperature-dependent term leads to (6) since it has a very small influence

$$\frac{\frac{\partial B}{\partial \Delta T}}{B} = -\frac{R_c\alpha_c + R_s\alpha_s}{R_c + R_s + (R_c\alpha_c + R_s\alpha_s) \cdot \Delta T}[\text{K}^{-1}] \tag{5}$$

$$\frac{\frac{\partial B}{\partial \Delta T}}{B} \cong -\frac{R_c\alpha_c + R_s\alpha_s}{R_c + R_s}[\text{K}^{-1}]. \tag{6}$$

It can be seen that for the lowest drift, R_s, should be kept as high and as stable as possible. Also, the coil's resistance and drift should be minimized if the design allows, also the geometric stability affects the coil's constant. In the developed prototype, the following values were used: $R_c = 100\ \Omega$,

$\alpha_c = 3900$ ppm/K, $R_s = 2000\ \Omega$, and $\alpha_s = 20$ ppm/K. These inputs lead to the overall sensitivity drift of the magnetometer being equal to 205 ppm/K. For the best performance of the FS range-to-drift rate ratio, U_{ref} and the coil's constant K should be kept as high as possible.

In our case, the reference voltage was 10 V and the coil constant $K = 34\ \mu$T/mA. The magnetometer range calculated by (2) is $B_{\text{MAX}} = \pm 162\ \mu$T.

The parallel capacitor C_P used to attenuate the PWM's ac component had a value of 3.3 μF.

C. Theoretical Noise Limits of the AMR Sensor (HMC1021)

If the magnetic noise is neglected (since it cannot be removed by any signal processing method), the noise limits can be calculated only through the thermal noise of the equivalent bridge resistance. Using the AMR's sensitivity S [V/T] and its equivalent bridge resistance R [Ω], the theoretical limit of the noise density B_n can be calculated as follows:

$$B_n = \frac{\sqrt{4k_B T R}}{S} \cong \frac{1.3 \cdot 10^{-10} \cdot \sqrt{R}}{S} \left[\frac{T}{\sqrt{\text{Hz}}}\right] \tag{7}$$

where k_B is Boltzmann's constant $[J/K]$, T is the absolute temperature $[K]$.

For the Honeywell HMC1021 sensors used, which are powered by a voltage 10 V ($R = 1100\ \Omega$, $S = 100$ V/T), a value of $B_n \cong 43\ pT/\sqrt{\text{Hz}} \equiv U_n \cong 4,3$ nV/$\sqrt{\text{Hz}}$ is obtained. A preamplifier with a white noise density of 1–3 nV/$\sqrt{\text{Hz}}$ does not add much noise to the measurement. With a bridge resistance of 1100 Ω, the current noise of the op-amp is non-negligible—an amplifier with a maximum current density of 1–2 pA/$\sqrt{\text{Hz}}$ should be used.

The total noise of the magnetometer is mostly given by the root of the sum of the squares of the sensor noise and preamplifier voltage and current noise (8)

$$B_{\text{TOT.}} = \sqrt{B_{n\_\text{SENSOR}^2} + \left(\frac{U_{n\text{PREAMP}}}{S}\right)^2 + \left(R_B \cdot \frac{\text{I}_{\text{nPREAMP}}}{S}\right)^2}. \tag{8}$$

The bridge amplifier developed for this purpose uses low-cost, low-noise ADA4004 op-amps with a total voltage and current noise of $U_{n\text{PREAMP}} = 2.5$ nV/$\sqrt{\text{Hz}}$ and $I_{n\text{PREAMP}} = 1.7$ pA/$\sqrt{\text{Hz}}$, and leads to 53 pT/$\sqrt{\text{Hz}}$ theoretical noise density of the magnetometer. Additional, amplification ($G = 32$) provides a gain stage built into the ADC converter.

D. Power Considerations

The setup requires minimal power, most of which is needed for the AMR bridges excitation with their low-noise preamps and feedback compensation. Because the AMR's noise level indirectly depends on the voltage/current supply value, it is best to keep the supply as high as possible, unless lowering power consumption is of higher priority. Attention must be given when increasing the AMR bridge supply current/voltage because power dissipation within the sensor is quadratically dependent on the current/voltage.

In a feedback circuit, the main cause of power dissipation is considered to be the current through the compensation coils times the H-bridge voltage, with the dropout voltage in a regulator (because the power of a bipolar PWM-waveform is constant over the full range).

A low-noise amplifier is another non-negligible source of power loss that should be considered. The amplifier with two ADA4004s per channel has a power consumption of 0.2 W for all three measurement axes together.

The contribution of these different parts to the total power consumption of the developed magnetometer is shown in Table I.

Other factors that increase power consumption include the microcontroller, ADC, H-bridge drivers, and flipping. Because one input voltage is desired, the power supply efficiency plays an important role.

TABLE I
CONTRIBUTIONS TO TOTAL POWER CONSUMPTION

Attribute	Value
Bridge power	3x 0.15 W (0.45 W)
Compensation	3x 0.08 W (0.24 W)
Preamplifier	3x 0.07 W (0.21 W)
Total	3x 0.3 W (0.9W)

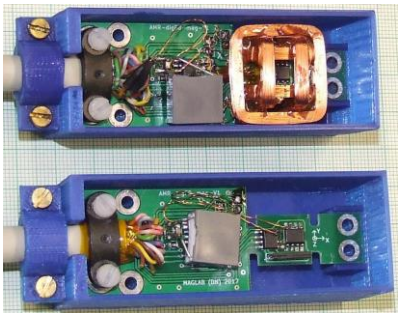

Fig. 3. Photograph of both individual and vector-compensated sensor heads.

III. PROTOTYPE OF THE MAGNETOMETER–PARAMETERS

In Fig. 3, a photograph of both the individual and the vector-compensated sensor heads can be seen.

As an important parameter of any measurement device, the linearity of the digitally compensated magnetometer has been tested. The sensor head has been placed in the Lee-Whiting coils [13] driven by a PC-controlled current source. The magnetic field has been swept and the output of the magnetometer is recorded. The FS linearity error of the vector-compensated sensor head can be seen in Fig. 4 (four independent measurements; the spikes at zero field are most likely caused by the current source used). It is clear that the linearity error is within about ± 60 ppm of FS for a ± 150-μT range; for a smaller range, e.g., $\pm 100\ \mu$T, a linearity error of ± 20 ppm can be achieved.

The noise floor—as it limits the dynamic range—has also been measured. Fig. 5 shows a comparison of the calculated and measured values of noise density versus the frequency using Welch's method. For further comparison, the noise density at 10 Hz can be used as it is above the $1/f$ corner

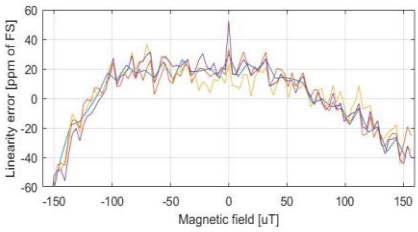

Fig. 4. Linearity error in magnetic field range ±150 μT.

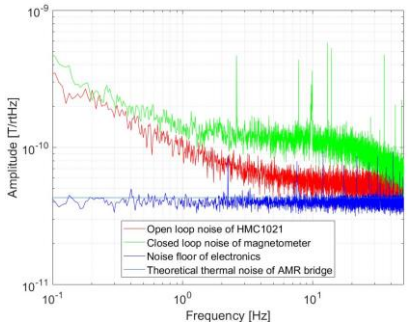

Fig. 5. Comparison of noise density spectra.

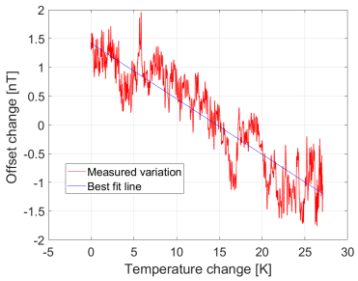

Fig. 6. Measured offset drift as temperature changes.

of the magnetic LF noise. The noise floor of the electronics, when measured with an equivalent bridge resistance, was found to be 38 pT/$\sqrt{\text{Hz}}$ and the overall magnetometer noise in an open loop was 55 pT/$\sqrt{\text{Hz}}$ with a limited ±15-μT range. It increased in a closed loop to 110 pT/$\sqrt{\text{Hz}}$. It can be seen that for very low frequencies (<1 Hz), the magnetic noise dominates as the noise in the open and closed loop slowly converges toward similar values greater than the electronics noise. All measurements have been made with flipping and were obtained inside a six-layer, permalloy magnetic shield.

In Fig. 6, the offset measurement can be seen. The sensor head has been placed inside a thermostatic, six-layered magnetic shield. The temperature slope has been created and the magnetometer output is recorded. The best-fit line has a slope of ~0.1 nT/K. Such a good value for an AMR magnetometer has been achieved through the software demodulation of flipping because the resulting drift is caused only by the magnetic drift of the sensor. The gain drift was found as approximately 200 ppm/K, which has been measured simultaneously with the offset drift by applying an ac magnetic field with a constant amplitude of about 10 μTpp created in the Lee-Whiting coils, in which the sensor was placed.

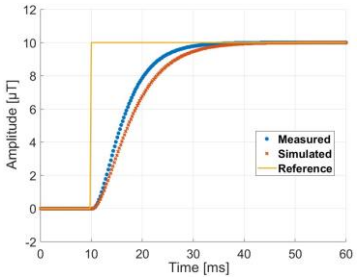

Fig. 7. Simulated and measured step response comparison.

TABLE II
PARAMETERS OF THE DEVELOPED TRI-AXIAL MAGNETOMETER

Attribute	Value
Full-scale range	± 150 µT
Nonlinearity	± 60 ppm
Noise density at 1 Hz	150 $pT/\sqrt{Hz}$
Integral noise (0.1-10 Hz)	440 pT_{RMS}
Offset drift	0.1 nT/K
Gain drift	200 ppm/K
Digital resolution	20 bit
Datarate (max/normal)	4000/250 Sa/s
Power consumption	2.2 W
Input voltage range	10-30 V

Fig. 7 shows the measured dynamic behavior (10-μT step response) which agrees with the waveform predicted by the Simulink model. The sensor head in this measurement has been placed into the Lee-Whiting coil, which has been connected to the square wave generator with a high output amplitude (20 V_{PP}) and a high series resistance because it lowers the L/R time constant while achieving the desired magnetic field step.

IV. Conclusion

This paper has presented a complete design and operating model for a digitally compensated magnetometer using COTS components, together with the measured parameters of a real prototype (Table II). The measured noise, linearity, and stability proved the usability of the concept because the parameters were comparable to a state-of-the-art magnetometer [9].

A second prototype is currently in development, with the aim of decreasing the power consumption by improving the power supplies as well as lowering the gain drift using feedback coils with a higher field constant and a lower resistance.

Acknowledgment

This work was supported by the Czech Technical University, Student Grant Competition Award No SGS18/081/OHK3/1T/13.

References

[1] P. Ripka, *Magnetic Sensors and Magnetometers*. Norwood, MA, USA: Artech House, 2001.
[2] M. J. Caruso, T. Bratland, C. H. Smith, and R. Schneider, "A new perspective on magnetic field sensing," *Sensors Mag.*, vol. 15, no. 12, pp. 34–46, Dec. 1998.

[3] M. Díaz-Michelena, "Small magnetic sensors for space applications," *Sensors*, vol. 9, no. 4, pp. 2271–2288, 2009.
[4] W. Magnes and M. Díaz-Michelena, "Future directions for magnetic sensors for space applications," *IEEE Trans. Magn.*, vol. 45, no. 10, pp. 4493–4498, Oct. 2009.
[5] P. Bown *et al.*, "Corrigendum: Magnetoresistive magnetometer for space science applications," *Meas. Sci. Technol.*, vol. 23, no. 5, p. 025902, 2012.
[6] U. Auster *et al.*, "Space weather magnetometer set with automated AC spacecraft field correction for GEO-KOMPSAT-2A," in *Proc. ESA Workshop Aerosp. (EMC)*, 2016, pp. 1–6, doi: 10.1109/AeroEMC.2016.7504585.
[7] J. M. G. Merayo, P. Brauer, F. Primdahl, J. R. Petersen, and O. V. Nielsen, "Scalar calibration of vector magnetometers," *Meas. Sci. Technol.*, vol. 11, no. 2, pp. 120–132, 2000.
[8] V. Fúra *et al.*, "Construction of an AMR magnetometer for car detection experiments," *IOP Conf. Mater. Sci. Eng.*, vol. 108, no. 1, p. 012028, 2016.
[9] S. Leitner *et al.*, "Design of the magnetoresistive magnetometer for ESA's SOSMAG project," *IEEE Trans. Magn.*, vol. 51, no. 1, Jan. 2015, Art. no. 4001404.
[10] W. Magnes *et al.*, "Highly integrated front-end electronics for space-borne fluxgate sensors," *Meas. Sci. Technol.*, vol. 19, no. 11, p. 115801, 2008.
[11] V. Petrucha, V. Fúra, and A. Platil, "Cross-field effect in a triaxial AMR magnetometer with vector and individual compensation of a measured magnetic field," *IEEE Trans. Magn.*, vol. 53, no. 4, Apr. 2017, Art. no. 4000305.
[12] J. Včelák, P. Ripka, A. Platil, J. KubÍk, and P. Kašpar, "Errors of AMR compass and methods of their compensation," *Sens. Actuators A, Phys.*, vol. 129, nos. 1–2, pp. 53–57, 2006.
[13] J. L. Kirschvink, "Uniform magnetic fields and double-wrapped coil systems: Improved techniques for the design of bioelectromagnetic experiments," *Bioelectromagnetics*, vol. 13, no. 5, pp. 401–411, 1992.

7.1.3 refP 3

Novotný, D.; Petrucha, V.; Dressler, M.; Platil, A., "Characterization of a Digital AMR Magnetometer for Space Applications," IEEE Transactions on Instrumentation and Measurement. 2021, 70(1), ISSN 0018-9456

In this paper, we presented another step in the development of a digitally compensated AMR magnetometer - a unique construction with excellent parameters and results of preliminary radiation testing using a gamma ray source (^{60}Co). With the use of a complex measurement setup (a PXIe frame-based system), we were able to explore the radiation tolerance of most of the critical components used in the design (both analog and digital circuits). A slightly modified version of this construction was proposed as an auxiliary magnetometer for a currently proposed space mission (a micro-satellite to the moon region, LVICE2). The author's contribution is 20%, having participated mainly in the process of radiation testing and calibrations of the magnetometer.

Characterization of a Digital AMR Magnetometer for Space Applications

David Novotny, *Graduate Student Member, IEEE*, Vojtech Petrucha, *Member, IEEE*, Michal Dressler, *Graduate Student Member, IEEE*, and Antonin Platil

***Abstract*— In this article, we present research, development, calibration, and characterization of a novel concept of a digitally compensated, low-noise magnetometer based on anisotropic magnetoresistance sensors that is suitable for space applications. The main idea of the design was to reduce the number of precise analog components while using the digital signal processing power available in a modern microcontroller. Our most recent effort targeted lowering power consumption, enhancement of radiation hardness, and overall improvement of the parameters. The principle of operation is presented in detail, along with a detailed description of the instrumentation used to characterize the real instrument, including its noise, linearity, and temperature stability in the range of −20 °C to +70 °C. The results of total ionizing dose (TID) testing at a gamma-ray irradiation facility are discussed at the complete magnetometer and part levels. This is an extended version of an article presented at I2MTC 2020 that contains the results of a second radiation test done with a slightly modified design. The instrument worked well throughout the entire irradiation session (TID of 1.05 kGy over 72 h), and the stability of main parameters was very good (50 pT/Gy offset and 1 ppm/Gy sensitivity stability).**

***Index Terms*— Anisotropic magnetoresistance (AMR), commercial off-the-shelf (COTS), digital compensation, microcontroller, radiation tolerance, SmallSat, space magnetometer.**

I. Introduction

MAGNETOMETERS are used in many different applications in space. Navigation and orientation stabilization of a satellite using different actuators (e.g., magnetotorquers and reaction wheels) is a typical example, as is space weather monitoring to protect sensitive instruments, e.g., ESA's SOSMAG project [1], but they also have purely scientific applications like studying the magnetosphere of Earth, other planets, and celestial bodies [2]. Precise magnetic sensors used here are usually based on the fluxgate principle [3], [4] or anisotropic magnetoresistance (AMR) [5], [6]. While fluxgates achieve lower noise and better stability, AMRs are cheaper, lighter, and more widely available commercially; they can also potentially achieve stability similar to fluxgates, as presented in [7]. These factors make AMRs attractive for low-cost, low-power applications.

Manuscript received July 31, 2020; revised October 31, 2020; accepted November 24, 2020. Date of publication December 10, 2020; date of current version January 8, 2021. This work was supported by the Grant Agency of the Czech Technical University in Prague, grant No. SGS19/177/OHK3/3T/13. The Associate Editor coordinating the review process was Dr. Chao Wang. *(Corresponding author: David Novotny.)*

The authors are with the Department of Measurement, Czech Technical University in Prague, 16627 Prague, Czech Republic (e-mail: novotd12@fel.cvut.cz; petruvoj@fel.cvut.cz; dressmic@fel.cvut.cz; platil@fel.cvut.cz).

Digital Object Identifier 10.1109/TIM.2020.3043867

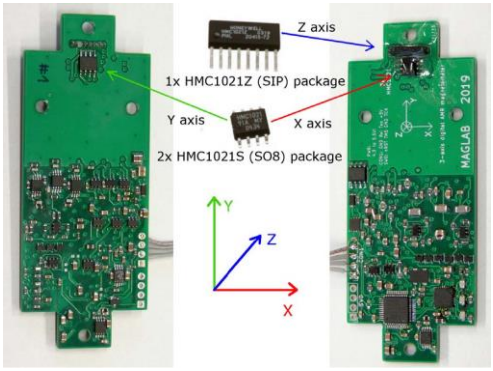

Fig. 1. Photograph of the AMR magnetometer (top and bottom side of the PCB; the AMR sensor triplet is visible on top of the picture)

Space-grade magnetometers use special parts—application-specific integrated circuits (ASICs) [6], [8] or radiation hardened field programmable gate arrays (FPGAs)—to achieve better radiation immunity and lower power consumption. But the use of ASICs or other special radiation-tolerant devices makes them costly and thus not easily obtainable for smaller projects with limited budgets.

In the magnetometer described in this article (see Fig. 1), we used only COTS parts, without any specification of those components' radiation tolerance. While lists of COTS-tested parts exist [9], they do not include many modern active components: microcontrollers, operational amplifiers, voltage stabilizers, references, analog-to-digital converters (ADCs), and so on. Some parts, including AMR magnetic sensors, have been tested in different published projects [10]–[13], but these devices have been submitted to only one test—a total ionizing dose (TID) using ^{60}Co gamma rays, neutrons, and heavy ions—and do not provide complete information concerning their behavior in space conditions.

In this article, we present significant improvements and a detailed characterization and testing of the second version of the magnetometer. The changes are based on the results of the first version's radiation testing and parameter evaluation presented in [14]. Our goal was to construct a device that can survive 1 kGy of gamma radiation without a significant

change in the main parameters (satellites in low Earth orbit can experience 0.04–0.4 kGy/year of mission [13]) while keeping the price and power consumption low enough to be suitable for the small satellite segment.

Section II describes the entire concept and details its operating principle, with an emphasis on digital feedback and the improvements referred to above.

In Section III, we present the set-up and method used to characterize the overall instrument's performance (e.g., noise and linearity measurements) and the estimation of the temperature dependencies of the main calibration parameters (sensitivities, nonorthogonality angles, and offsets).

In Section IV, we present the results of a TID test done at a ^{60}Co gamma irradiation facility. We used identical setup as during the first measurement because it proved to be accurate and reliable. The access to the facility is extremely limited for us, so we designed the test setup to collect the maximum amount of information. A custom measurement system based on a PXIe frame, two data acquisition cards, and the LabView control software was employed to acquire a variety of analog and digital signals during a 72-h irradiation session that involved a TID of 1.05 kGy (105 krad) (same values as in the previous one [14]). Two identical magnetometers were tested simultaneously in order to assess the credibility of the results. We acquired 15 channels per one magnetometer to determine the degradation of different components, such as the effects of drifting voltage reference, any op-amp offset shift, or problems in the AMR sensor itself (which were not anticipated—with respect to our experience from the first testing as well as the available publications [15]).

Finally, all the main parameters of the magnetometer are summarized and compared with a commercial device.

II. Description of Magnetometer Prototype

The concept presented uses only commercial off-the-shelf (COTS) components. As an MCU (microcontroller unit), the STM32F334 [16] was chosen for its high-resolution pulsewidth modulation (PWM) capability for digital feedback compensation. All signal processing after analog-to-digital conversion is software-based. The magnetic field in each axis is sensed by HMC1021 [17], and the AMR sensor is operated as a closed-loop compensation system using the built-in offset coil. This sensor was chosen because its sensitivity is among the highest available on the market. Although the HMC1001 provides higher sensitivity, the HMC1021 has the advantage of an internal offset coil with a sufficiently high current to magnetic field ratio. Moreover, it is available at a much lower price. Both are also available in SO8 (S) and SIP (Z) packages for simpler implementation of vector field measurement.

With feedback compensation, the sensor is used only as a zero indicator, and measurement output is the level of compensation current that is fed to the offset coils. Because this indirect method of measurement has traditionally enabled higher performance in terms of linearity, stability, and hysteresis [18], it was chosen. It can be compared to open-loop parameters of a sensor from its datasheet (nonlinearity in CL: 40 ppm, in OL: 1000 ppm, gain stability; 5 ppm/K in CL, 600 ppm/K in OL with constant current supply; 3000 ppm/K in OL with constant voltage).

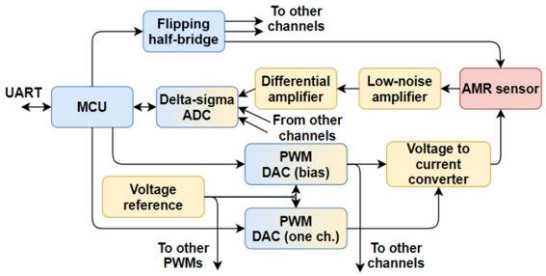

Fig. 2. Block diagram of the magnetometer (only one axis is shown).

As this is an enhanced version of our previous design, we were able to replace parts identified as problematic during the first radiation test campaign (the low-drop voltage regulator and voltage reference). The feedback current source was also modified to improve transfer function (TF) linearity.

This approach extended the durability of the magnetometer under irradiation from 500 to at least 1000 Gy. Component optimization in the PWM-digital-to-analog converter (DAC) design also improved linearity and offset temperature stability. Higher loading impedance (lower current) for the multiplexer ($U1$ and $U2$ in Fig. 3) that creates a precise-amplitude PWM signal led to better linearity of the concept. Bias compensation resistors used in front of inverting inputs of operating amps decreased offset drift with temperature by balancing the input current bias that caused excess drift.

Fig. 2 presents a simplified block diagram of the magnetometer's electronics; for the sake of clarity, only one axis is shown.

AMR sensors often implement flipping (set/reset) coils that can be used to change (or "flip") the polarity of sensor sensitivity. This process is usually carried out periodically with frequencies in the Hz to kHz range and offers advantages such as electrical offset elimination, which is why we chose it. During a flipping pulse (0.65 A for 10 μs in our case), the measurement reported by the AMR sensor is very noisy. Flips represent only a fraction (2%) of the total measurement time, but they can still cause excess noise. To solve this problem, the measurement during flipping and the measurement immediately after are not used flipping (because of settlings in the analog path); demodulation is stopped for these two samples per flip pulse. This means that for 3906 Sa/s and a 216-Hz flipping frequency (18 samples per flipping period), four samples (two during set and two during reset flip) are not used and thus 22% of measurements per flip period are discarded.

The static TF of the magnetometer in the SET/RESET state of the flipping mode is described in (1) and (2). Equation (3) represents the result of a synchronous demodulation applied to the measurement data modulated by the flipping process

$$V_{\text{set}} = K_A \cdot (O_{\text{AE}} + K_{\text{LNA}} \cdot (O_{\text{LE}} + O_{\text{SE}} + K_{\text{AMR}} \cdot (B_m + O_B))) \quad (1)$$

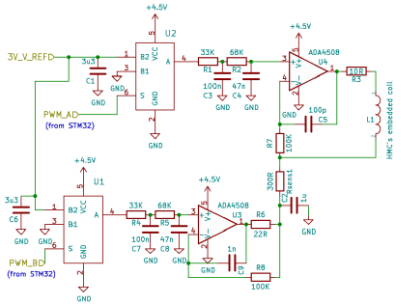

Fig. 3. Circuit diagram of a PWM-based differential compensation circuit.

$$V_{\text{res}} = K_A \cdot (O_{\text{AE}} + K_{\text{LNA}} \cdot (O_{\text{LE}} + O_{\text{SE}} - K_{\text{AMR}} \cdot (B_m + O_B))) \tag{2}$$

$$V_{\text{out}} = V_{\text{set}} - V_{\text{res}} = 2 \cdot K_A \cdot K_{\text{LNA}} \cdot K_{\text{AMR}} \cdot (B_m + O_B) \tag{3}$$

where $V_{\text{set}}, V_{\text{res}}$ is the voltage output of the bridge in the SET/RESET state (V), V_{out} is the output voltage after demodulation (V), K_A is the internal gain of ADC $(-)$, O_{AE} is the offset of ADC (V), K_{LNA} is the gain of low noise amplifier (LNA) $(-)$, O_{LE} is the offset of LNA (V), O_{SE} is the electrical offset of AMR bridge (V), K_{AMR} is the sensitivity of the AMR bridge (V/T), B_m is the measured magnetic field (T), and O_B is the magnetic offset of the sensor (T).

Equation (3) shows that, after demodulation carried out in the firmware, the offset of the magnetic measurement is given only by the magnetic offset of the sensor itself. There is no contribution of the signal conditioning chain, making it unnecessary to use dc-precise operational amplifiers or ADC converters. Another important advantage is implied; there are no low-frequency (LF) noise requirements on the signal chain. The flipping frequency is set to approximately 216 Hz as a compromise between the useful bandwidth of the magnetometer and the digital signal processing speed (3.91-kSa/s sample rate of ADC). This frequency was also selected to ensure minimal interference with the local 50-Hz line frequency disturbing signal and its harmonics. For sensor preamplifier design, only noise at this frequency and the bandwidth of the magnetometer are relevant. Most op-amps have $1/f$ corner on lower frequencies, so at 216 Hz only their white noise is significant (should be at least two times smaller than Johnson–Nyquist noise of AMR bridge, for HMC1021—1100 Ω and 25 °C it is 4.3 $\text{nV}/\sqrt{\text{Hz}}$, so white noise density of amplifier below 2 $\text{nV}/\sqrt{\text{Hz}}$ is suitable).

In the feedback topology, the gain stability is given only by the compensation circuit (Fig. 3). The dynamic performance is affected only by the gain change of the sensor itself and its conditioning circuit. This can be obtained from the frequency response at a zero frequency.

Equation (4) describes output voltage of AMR bridge, (5) relates to computed DAC value based on AMR bridge voltage in Laplace image domain, and (6) is obtained by combining (4) and (5) together. It describes transfer function of DAC in relation to measured magnetic field and we can use it to show that for a zero frequency (dc gain, $s = 0$), TF is given only by (7)

$$V_{\text{out}} = K_{\text{AMR}} \cdot \left(B_m - \text{DAC}_{\text{COMP}} \cdot K_{\text{coil}} \cdot \frac{V_{\text{DAC\_ref}}}{\text{R}_{\text{sens}}} \right) (\text{V}) \tag{4}$$

$$\text{DAC}_{\text{comp}} = \frac{K_i}{s} \cdot K_{\text{LNA}} \cdot \frac{\text{ADC}_{\text{range}}}{\text{V}_{\text{ADC\_ref}}} \cdot V_{\text{out}} (-) \tag{5}$$

$$H(s) = \frac{\text{DAC}_{\text{comp}}}{\text{B}_m} = \left(\frac{\text{V}_{\text{ADC}_{\text{ref}}}}{K_i \cdot K_{\text{LNA}} \cdot \text{ADC}_{\text{range}} \cdot K_{\text{AMR}} \cdot} \cdot s + K_{\text{coil}} \cdot \frac{V_{\text{DAC\_ref}}}{\text{R}_{\text{sens}}} \right)^{-1} (T^{-1}) \tag{6}$$

$$H(0) = \frac{R_{\text{sens}}}{K_{\text{coil}} \cdot V_{\text{DAC}_{\text{ref}}}} (T^{-1}) \tag{7}$$

where DAC_{comp} is the value set on compensation-DAC $(-)$, $V_{\text{ADC\_ref}}$ is the reference voltage of ADC (V), $\text{ADC}_{\text{range}}$ is the top value of ADC $(-)$, K_i is the integrator constant $(-)$, K_{coil} is the embedded coil constant (T/A), R_{sens} is the sense resistor of the voltage to current converter (Ω), and $V_{\text{DAC\_ref}}$ is the reference voltage of DAC (V).

This means that the only contribution to gain drift is given by the constant of the compensation coil, sensing resistor in the voltage to current converter, and the reference voltage source. The stability of the compensation system should be inherent (single pole TF), but this description is only approximate and does not consider delays of preamplifier or ADC's sampling that can cause oscillations. Stability must be ensured by the proper setting of the integrator constant K_i.

In a practical implementation, this means that there are only a very few requirements on the design of the electronics

1) stability and noise of the main voltage reference;
2) stability of the feedback current sensing resistor;
3) white noise (at 180–250 Hz) of the bridge amplifier;
4) stability and LF noise of op-amps in the voltage-to-current converter and in the voltage reference buffer.

A band-gap voltage reference was selected because it should be less susceptible to irradiation than Zener diode-based reference [19]. Our previous design used REF3430, while LTC6655 is used in the present design. As a low-noise preamp, OPA2210 was chosen for its low voltage and current noise at a flipping frequency and its low-voltage, rail-to-rail operation. For all other op-amps, where low LF noise was necessary, a low-voltage, rail-to-rail ADA4805 was used.

During radiation testing the current consumption of the magnetometer was precisely monitored. A sawtooth-like signal with an amplitude of several milliamps appeared superimposed on the steady current value of 122 mA (Fig. 4). This is caused by the function of an internal voltage regulator in the STM32 MCU. In another project that used the same microcontroller (STM32F334) and a high-resolution timer (HRTIM), we also observed that the duty cycle of the PWM signal from the HRTIM drifted with the sawtooth shape at a magnitude of several ppm. Fortunately, this problem was solved by using a differential DAC design. The distortion is the same for all channels; it behaves like a varying offset, and when the voltages generated by two channels are subtracted, the effect is suppressed.

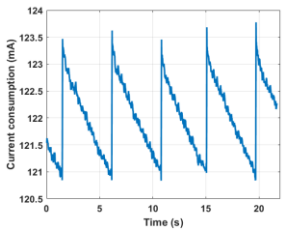

Fig. 4. Current consumption of the magnetometer; sawtooth distortion caused by STM32 internal voltage regulator.

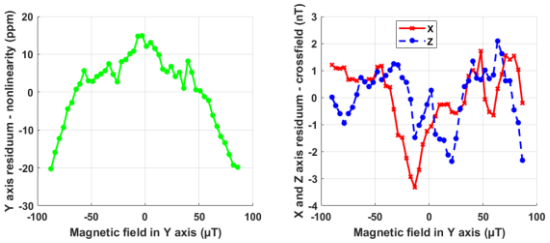

Fig. 5. Linearity (left) and cross-field (right) errors.

III. Conventional Measurements

A. Linearity and Cross-Field Measurement

The linearity of the magnetometer was measured using precise PC-controlled current source driving a Lee–Whiting coil system (single axis). The magnetometer itself was placed in the precise center of this coil. While LabView-based software controlled current to the coil system in a staircase-like linear sweep, it also recorded data from the magnetometer. This process contained 50 points of measurement in the ±90-μT range and was repeated 10 times; the results were averaged to decrease noise. Those results are shown in Fig. 5. The linearity error (INL) is approx. ±20 ppm of FS, while the cross-field error is within ±3 nT and mostly due to environmental noise.

B. Noise Measurement

The magnetic noise of the prototype was measured in a six-layer permalloy shielding. The attenuation factor of the shielding is approximately 10^5 in the horizontal direction and 10^3 in the vertical, allowing sub-pT/$\sqrt{\text{Hz}}$ noise density to be measured (Fig. 6). The sensor was placed at the bottom of the shielding while it sent data over a serial link to the PC that recorded the data. From the data record, power spectral density was calculated using Welch's method (10 min length, 126 Sa/s, NFFT = 32768).

The results indicate that the sensor itself can perform even better because noise is dominated by acquisition and compensation electronics noise, which is due to a power consumption tradeoff: a prototype developed in our previous research [7] performed with approximately half the noise but consumed three times more power. This is an unfortunate consequence of the linear dependence of the sensor's sensitivity to the sensor supply voltage while its power consumption is quadratically dependent.

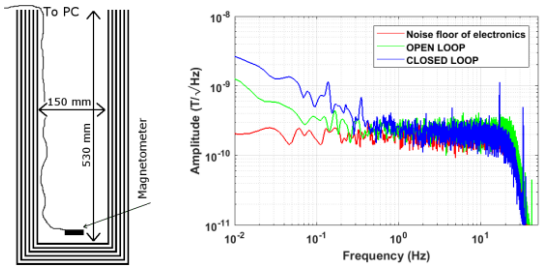

Fig. 6. Drawing of the measurement setup (left). Noise spectrum density comparison for one axis (magnetometer implements digital low-pass filter with 30-Hz cutoff frequency, so higher frequencies are not shown) (right).

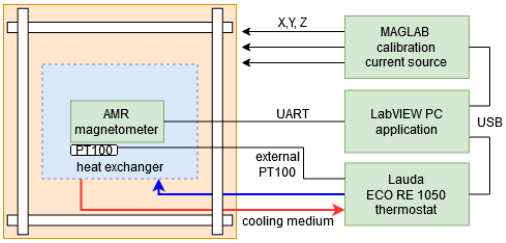

Fig. 7. Block diagram of calibration system. The PC LabView application communicates with the current source and thermostat via a USB virtual COM port. The AMR magnetometer temperature is measured by a PT100 platinum sensor connected to the Lauda thermostat's external input.

C. Temperature Drifts Measurement

Magnetometer calibration parameters and their temperature dependence were measured using a tri-axial coil system equipped with a custom temperature-controlled chamber (Fig. 7). The calibration system consists of a 60-cm Merritt (E–W) coil pair and two modified-Helmholtz (N–S, vertical) coil pairs driven by a custom-built three-channel current source and a LabView application. The temperature chamber is made of a hollow plastic cylinder (10 cm inner diameter, 25 cm length) wrapped with PTFE tubing as a heat exchanger used with a Lauda ECO-RE1050S heating and cooling thermostat that can control the temperature of a circulating media (Kryo-51, polydimethylphenylsiloxane, basically a silicon oil) in the range of −50 °C to 120 °C. However, due to insufficient chamber isolation and low heat conductivity between the heat exchanger and the AMR magnetometer, the lowest temperature in the calibration temperature sweep achievable in a tolerable time span is −20 °C.

The procedure for obtaining magnetometer calibration linear coefficients is based on a thin shell method [20], [21], which typically uses a coil system to create a set of known field vectors with constant magnitude that are distributed uniformly on the surface of a virtual sphere. The method was modified to enable easier realization in our laboratory with nonnegligible magnetic noise disturbances, where the magnetic noise values are about 100 nT_{pp} in horizontal components and up to 1 μT_{pp} in vertical (0–10-Hz band). To overcome magnetic field variations and human-made disturbances (appearing as a $1/f$ noise), each vector from the 55-point thin shell vector

set was measured relatively in two steps. In the first step (8), the coil system field $\mathbf{b}_c$ was set to a manually adjusted value to create approximately zero field inside, and the magnetometer output $\mathbf{e}_m$ measuring field $\mathbf{b}_m$ (which also contains the immediate value of external disturbance $\mathbf{d}$) was recorded. This first step $\mathbf{b}_c$ value stays constant during the entire calibration because it compensates for Earth's field constant component. In the second step (9), the thin shell vector field is added to the coil system and the magnetometer output is recorded

$$\mathbf{b}_m(1) = \mathbf{b}_c(1) + \mathbf{d}(1) \tag{8}$$

$$\mathbf{b}_m(2) = \mathbf{b}_c(2) + \mathbf{d}(2) \tag{9}$$

$$\Delta\mathbf{b}_m = \Delta\mathbf{b}_c + \Delta\boldsymbol{d}. \tag{10}$$

By taking the difference of (8) and (9), the relative values can be established in (10). Assuming a fast magnetometer with short settling time, the steps can be applied rapidly enough for $\Delta\mathbf{d}$ to approach zero and the external field disturbance contribution to be suppressed.

The calibration parameters are obtained by solving a set of linear equations given by the following (11) magnetometer output model [20]:

$$\Delta\mathbf{b}_c = \begin{bmatrix} r_{11} & r_{12} & r_{13} \\ r_{21} & r_{22} & r_{23} \\ r_{31} & r_{32} & r_{33} \end{bmatrix} \begin{bmatrix} \mathrm{S}_1 & \mathrm{V}_{12} & \mathrm{V}_{13} \\ 0 & \mathrm{S}_2 & \mathrm{V}_{23} \\ 0 & 0 & \mathrm{S}_3 \end{bmatrix} \left(\Delta\mathbf{e}_m - \begin{bmatrix} O_1 \\ O_2 \\ O_3 \end{bmatrix} \right) \tag{11}$$

where r parameters are components of the rotation matrix between the magnetometer sensor triplet frame and the coil frame, S and O are sensitivities and offsets, and V parameters are related to sensor frame nonorthogonality; $\Delta\mathbf{e_m}$ is the magnetometer raw reading difference corresponding to $\Delta\mathbf{b_m}$ (10).

Since the procedure uses only relative magnetic field values, the information about the magnetometer sensor's offset absolute value is lost; only sensitivities, nonorthogonality angles, and the rotation matrix between sensor frame and coil frame can be retrieved.

This method is further described in [22], which also offers a description of active field variation compensation from a closely placed (2 m from coil center) magnetometer; however, that was not used for active compensation during sensitivity and nonorthogonality measurement in this case, only for offset drift estimation.

The calibration thin shell sequence radius magnitude was set to 70 μT, which is in the sensor's linear region (see Fig. 5). The chopping frequency was roughly 1 Hz; therefore, one full calibration took less than 2 min. The rms residues [21] of calibration fit are, on average, 5 nT for axes in the horizontal direction of Earth's magnetic field and 40 nT for the vertical (or 71 and 570 ppm relative error from the shell radius). The achievable calibration uncertainty of a fixed magnetometer (estimated from the standard deviation of multiple full calibration results) is about 100 ppm for sensitivity parameters and 10^{-3} degrees for angular parameters. The anticipated magnetometer parameters' drift values are lower, so the calibration sequence is repeated multiple times at each temperature. The total length of the calibration test was 10 h; the temperature profile is shown in Fig. 8.

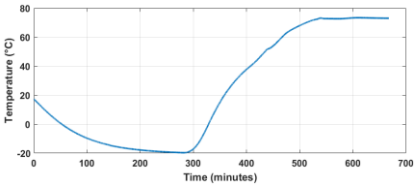

Fig. 8. Estimate of magnetometer temperature measured by an attached PT100. The temperature was controlled by setting the thermostat bath temperature to first minimum then maximum values (without closed-loop control from external sensor). Most of the thin shell calibrations (full 55 points) were done when the temperature was settled at the minimum or maximum values.

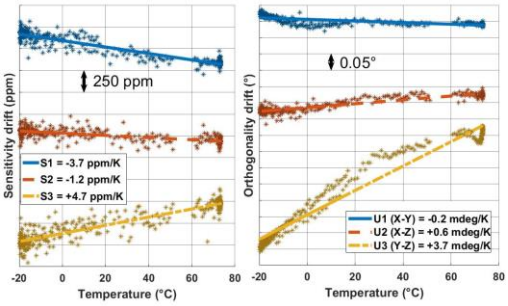

Fig. 9. Magnetometer sensitivity and nonorthogonality temperature dependence. The cross-axis angle notation is taken from [20]. The drift of parameter U3 (angle *YZ*, caused by the tilt of vertically mounted AMR IC) with the most significant drift is also clearly not linear, as it is probably caused by temperature expansion of the epoxy glue fixing the package.

1) Sensitivity and Nonorthogonality Calibration: The three sensitivity parameters and three angles describing the magnetometer's nonorthogonal frame were obtained from solution of a data set made from (11) by QR decomposition. The drift dependence of both parameter triplets is shown in Fig. 9. Its slope is clearly visible even during the heating process, where calibration counts were sparse and parameters thus more scattered. The most widely drifting channel is from the AMR sensor, which was in a vertically mounted SIP package on PCB, while the others were in a standard SO8 package.

2) Offset Drift Estimation: The offset drift can be only estimated from magnetometer data when no calibration vector is applied to the coil system. To distinguish drift from Earth's field variation, the magnetic field was simultaneously recorded by an external fluxgate magnetometer located approximately 0.5 m above the coil system. The external magnetometer coordinate frame did not have to be precisely aligned to the calibrated magnetometer frame because the method described in [22] was used to provide automatic alignment. The rotation transformation matrix was obtained from several minutes of recording magnetic field variations (assuming their zero-gradient, i.e., long-distance sources). Then, the offset drift can be plotted simply as the difference between the AMR magnetometer and the rotated-frame external magnetometer reading. The results (−0.9, 0.25, and −0.42 nT/K for *X*-, *Y*-, and *Z*-axis, respectively) are a bit worse than what we published in our previous research [7] and can be seen in Fig. 10. This is caused by

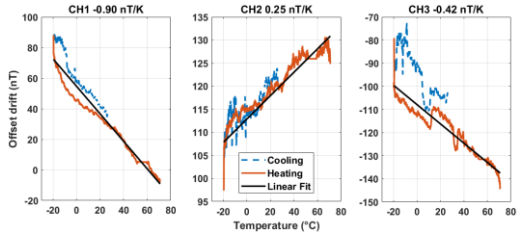

Fig. 10. Magnetometer offset temperature drift estimation for each magnetometer axis. The data are selected from simultaneously recording the AMR magnetometer and the external fluxgate during the calibration sequence. Only the data when no field is applied to the coil system are shown

integrating electronics and sensors much closer to each other (our magnetometer from [7] had separate sensor head and processing electronics). Electronics parts (especially ceramic capacitors) display remanent magnetization drifting with temperature.

IV. Radiation Testing

Because electronics operating in space must survive all types of radiation present in free space—gamma rays, neutron radiation, heavy ions, proton, and electron beam radiation—it would be optimal to test for all types. However, different radiation sources are not easily accessible even for academic and research purposes, so we have used ^{60}Co based gamma-ray irradiation that we could access through the ÚJV Řež facility near Prague. We consider this a first step in the instrument's qualification process. The test was planned in accordance with MIL-STD-883. The TID, based on the alanine-EPR dosimetry method, was 1.05 ± 0.03 kGy (105 ± 3 krad). This dose is related to the energy absorbed by water; for silicon (the main element in the tested electronics), it can be recalculated by (12) from [23]

$$D_{\mathrm{Si}} = D_{\mathrm{H_2O}} \cdot \frac{\mu_{\mathrm{Si}}/\rho_{\mathrm{Si}}}{\mu_{\mathrm{H_2O}}/\rho_{\mathrm{H_2O}}} = 0.898 \cdot D_{\mathrm{H_2O}}. \quad (12)$$

The corrected value for the TID absorbed by silicon is thus 943 ± 30 $\mathrm{Gy_{(Si)}}$(94.3 ± 3 $\mathrm{krad_{(Si)}}$). Irradiation by this dose was performed in 72 h. The results place the test in the low irradiation-rate category (0.36 rad/s). Second testing (actual prototype) was done in the same setup and TID as described for our first radiation testing.

A. Testing Setup (PXIe)

Monitoring of internal signals of the magnetometer and logging serial data and the generation of the testing signal to the external coil were implemented with a PXIe frame with an embedded controller, an NI-4302 data acquisition card, and an auxiliary NI-6251 card as a software watchdog for the magnetometer (performing reset in case the magnetometer would stop sending serial data) and the generation of the sinusoidal signal to the testing coil (Figs. 11 and 12). Measurement setup was controlled through LabView-based software with a remote access possibility.

Selected signals measured in the magnetometer are marked by letters A–M in Fig. 13. Voltage channels A–I were sampled

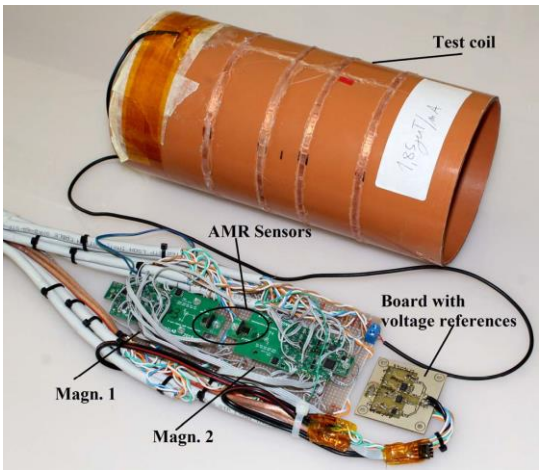

Fig. 11. Photograph of D.U.T. pulled out of testing coil.

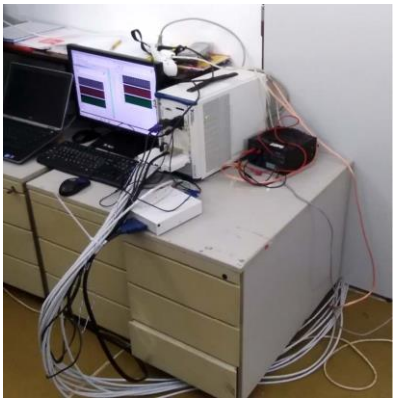

Fig. 12. Photograph of PXIe frame with PC in control room during irradiation.

at 60 Sa/s while J, K, L, and M signals were acquired at 5 kSa/s, fast enough to measure the square (flipped) signal at 216 Hz. Channel A was the current measurement through a 0.25-Ω shunt resistor. Signal G was measured on a 300-Ω sense resistor of a voltage-to-current converter. For one of the magnetometers, axes X and Z were operated in open loop mode, while the Y-axis was in a closed loop. The X-axis had completely disconnected feedback (see the strikethrough of the signal in the diagram), while the Z-axis had a constant value set on digital compensation to measure the drift of compensation current. Second magnetometer operated in closed-loop for all axes, without intervention to its normal operation by measurement.

B. Results of Irradiation

All data acquired using the PXIe measurement system were postprocessed (filtered, decimated, subtracted, or demodulated, depending on the signal) and are presented in Figs. 14–19. Some also contain data from the first radiation testing to show

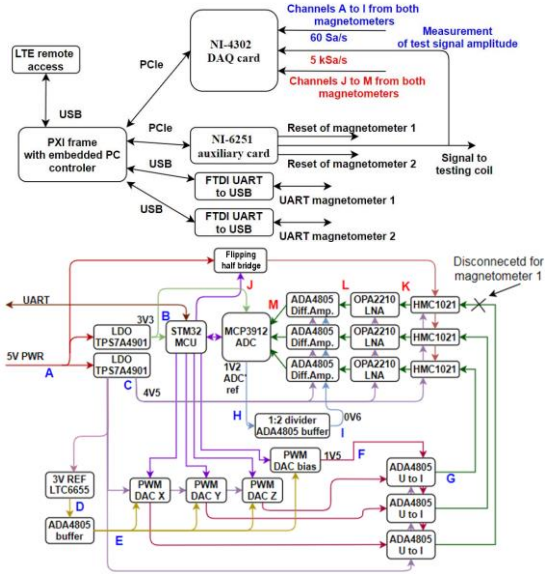

Fig. 13. Circuit diagram of PXIe acquisition system with highlighted test points on the magnetometer's circuit.

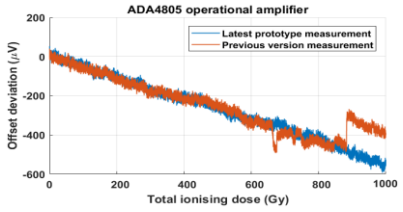

Fig. 14. Drift of ADA4805 op. amp. offset with increasing TID.

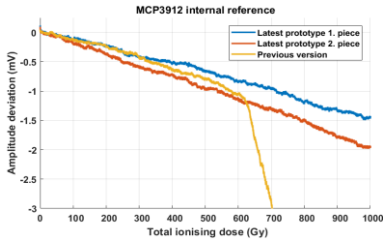

Fig. 15. Drift from initial value of AD converter's internal reference.

that the behaviors were similar (in case of parts that worked nominally). All graphs use TID (Gy) on the horizontal axis. Fig. 14 shows the offset drift for the ADA4805 operational amplifier (approximately -0.5 μV/Gy). The curve is very similar for both measurements; the jumps in the previous version trace were caused by a power supply failure that occurred at 550 Gy. The internal voltage reference of the AD converter showed -1.7 μV/Gy drift (Fig. 15); again, the low-dropout (LDO) regulator malfunction influenced the previous

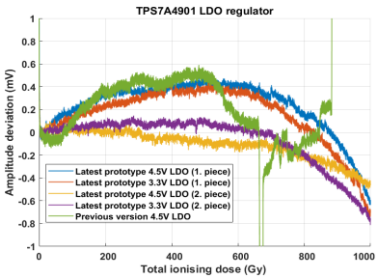

Fig. 16. Comparison of drifts from nominal voltage of five pieces of LDO voltage regulators.

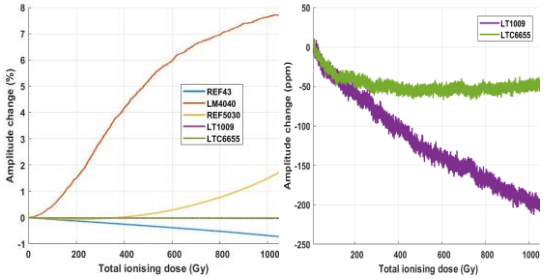

Fig. 17. Comparison of different voltage references to test their nominal voltage drift with irradiation (LTC6655 and LT1009 are very small in comparison with the others; they are overlaid in the graph on the left, so a detail of these two references is provided on the right).

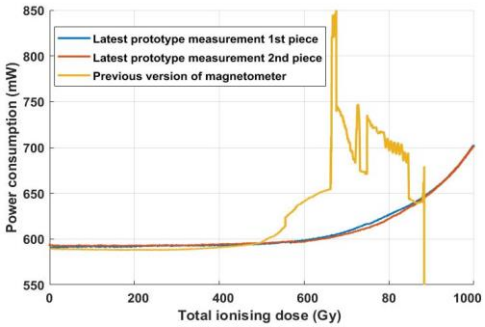

Fig. 18. Comparison of power consumption of two recent prototypes with increasing TID.

version. The TPS7A4901 voltage regulator worked very well in all cases, exhibiting almost negligible drift with respect to irradiation (Fig. 16). Main voltage reference is used to define the scale factors, so we took special care to select the part with the lowest drift. Fig. 17 shows the drift of five different parts; we observed that the LTC6655 was superior to all the others; it was thus chosen for the final design. Power consumption (Fig. 18) remained practically constant through approximately 500 Gy, at which point an exponential rise was observed; again, this was very consistent for both units tested during the second campaign.

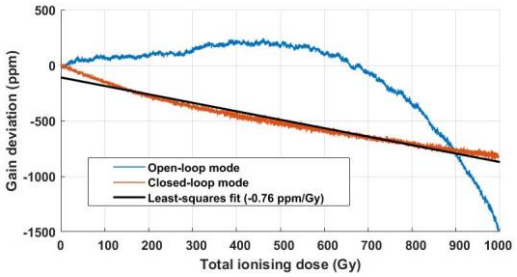

Fig. 19. Gain drift of magnetometer derived from analysis of recorded serial data from irradiated magnetometers.

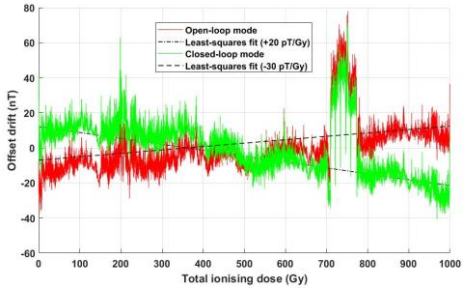

Fig. 20. Offset drift of magnetometer during irradiation.

TABLE I
COMPARISON OF PRESENTED WITH COMMERCIAL MAGNETOMETER

Parameter	Magn. described in this paper	Commercial magnetometer
Range	± 100 μT	± 60 μT
Nonlinearity	± 20 ppm	NA
Offset TC	< 1 nT/K	NA
Sensitivity TC	< 5 ppm/K	NA
Orthogonality TC	< 0.01 °/K	NA
Crossfield sensitivity	± 50 ppm	NA
Noise density @ 1 Hz	250 $pT_{RMS}/\sqrt{Hz}$	<8000 $pT_{RMS}/\sqrt{Hz}$
Integral noise 0.1-10Hz	780 pT_{RMS}	NA
Bandwidth (-3 dB)	30 Hz	< 9 Hz
Sample rate	126 Sa/s	< 18 Sa/s
Maximum TID	1000 Gy	100 Gy
Irradiation gain drift	<1 ppm/Gy	NA
Irradiation offset drift	<50 pT/Gy	NA
Power consumption	600 mW @ 5V	550 mW @ 5V
Interface	TTL UART	RS485
Dimensions	35 x 90 x 7 mm	45 x 69 x 20 mm

Data streamed from both magnetometers over a serial link (UART/USB converter) allowed us to obtain gain (sensitivity) and offset (bias) drifts with increasing TID. As one axis of both prototypes was excited by an external coil (3-Hz sinewave, 12 μT_{p-p} amplitude), we were able to obtain sensitivity drift by bandpass filtering data to extract 3-Hz excitation signal and calculate its envelope. The envelope magnitude drift from the initial value equals gain drift of −76 ppm/Gy (Fig. 19). Offset drift (Fig. 20) was calculated by low-pass filtering of the serial data to remove the excitation sine wave and environmental noise (but a very low frequency noise still cannot be fully suppressed by filtering—see the peak between 700 and 800 Gy caused by opening and closing neighbor irradiation chamber).

V. CONCLUSION

As expected, replacing parts identified as problematic during the first irradiation campaign significantly improved the magnetometer's resistance to gamma radiation. The level of >1000 Gy is more than sufficient for most short-duration missions in low Earth orbit. Two pieces were tested, and both provided practically identical results, which creates even more confidence in the results. Some of the STM32 microcontrollers were reported to be prone to single-event upsets (SEUs) or latch-ups (SELs) when bombarded with neutrons or heavy ions [11]. As SELs are reversible, power cycling by the power management unit would solve the problem. Still, much testing remains to be done (thermal vacuum, EMC, vibration testing, etc.).

Despite the limitations noted in the preceding paragraph, the updated prototype presented here behaves very well under gamma irradiation and temperature change. The parameters are either comparable to commercial solutions such as NewSpace Systems NMRM-001-485 [24] or perform significantly better, as in the case of noise density (Table I). So, this novel COTS concept of digital feedback AMR magnetometer is very promising and, it is hoped, can be deployed in space soon.

ACKNOWLEDGMENT

The authors wish to express our thanks to Dr. Plaček and Dr. Cabalka from ÚJV Řež, a. s. for giving us a chance to perform radiation testing and for their helpfulness.

REFERENCES

[1] S. Leitner *et al.*, "Design of the magnetoresistive magnetometer for ESA's SOSMAG project," *IEEE Trans. Magn.*, vol. 51, no. 1, pp. 1–4, Jan. 2015, doi: 10.1109/TMAG.2014.2358270.
[2] J. L. Burch, T. E. Moore, R. B. Torbert, and B. L. Giles, "Magnetospheric multiscale overview and science objectives," *Space Sci. Rev.*, vol. 199, nos. 1–4, pp. 5–21, Mar. 2016.
[3] M. Díaz-Michelena, "Small magnetic sensors for space applications," *Sensors*, vol. 9, no. 4, pp. 2271–2288, Mar. 2009, doi: 10.3390/s90402271.
[4] D. M. Miles *et al.*, "A miniature, low-power scientific fluxgate magnetometer: A stepping-stone to cube-satellite constellation missions," *J. Geophys. Res., Space Phys.*, vol. 121, no. 12, pp. 11839–11860, Dec. 2016, doi: 10.1002/2016JA023147.
[5] P. Brown *et al.*, "Space magnetometer based on an anisotropic magnetoresistive hybrid sensor," *Rev. Sci. Instrum.*, vol. 85, no. 12, Dec. 2014, Art. no. 125117, doi: 10.1063/1.4904702.
[6] P. Brown *et al.*, "Magnetoresistive magnetometer for space science applications," *Meas. Sci. Technol.*, vol. 23, no. 2, Feb. 2012, Art. no. 025902, doi: 10.1088/0957-0233/23/2/025902.
[7] D. Novotný, V. Petrucha, and M. Janošek, "A digitally compensated AMR magnetometer," *IEEE Trans. Magn.*, vol. 55, no. 1, pp. 1–5, Jan. 2019, doi: 10.1109/TMAG.2018.2873235.
[8] S. Sordo-Ibáñez *et al.*, "A front-end ASIC for a 3-D magnetometer for space applications by using anisotropic magnetoresistors," *IEEE Trans. Magn.*, vol. 51, no. 1, pp. 1–4, Jan. 2015, doi: 10.1109/TMAG.2014.2356976.
[9] *ESCIES—European Space Components Information Exchange System*. Accessed: Nov. 10, 2020. [Online]. Available: https://escies.org
[10] R. Kingsbury *et al.*, "TID tolerance of popular CubeSat components," in *Proc. IEEE Radiat. Effects Data Workshop (REDW)*, Jul. 2013, pp. 1–4, doi: 10.1109/REDW.2013.6658220.
[11] H. Quinn, T. Fairbanks, J. L. Tripp, G. Duran, and B. Lopez, "Single-event effects in low-cost, low-power microprocessors," in *Proc. IEEE Radiat. Effects Data Workshop (REDW)*, Jul. 2014, pp. 1–9, doi: 10.1109/REDW.2014.7004596.

[12] R. Netzer, K. Avery, W. Kemp, A. Vera, B. Zufelt, and D. Alexander, "Total ionizing dose effects on commercial electronics for cube sats in low Earth orbits," in *Proc. IEEE Radiat. Effects Data Workshop (REDW)*, Jul. 2014, pp. 1–7, doi: 10.1109/REDW.2014.7004607.
[13] K. Avery *et al.*, "Total dose test results for CubeSat electronics," in *Proc. IEEE Radiat. Effects Data Workshop*, Jul. 2011, pp. 1–8, doi: 10.1109/REDW.2010.6062504.
[14] D. Novotný, V. Petrucha, M. Dressler, and A. Platil, "AMR magnetometer with digital feedback for space applications," in *Proc. IEEE Int. Instrum. Meas. Technol. Conf. (I2MTC)*, Dubrovnik, Croatia, May 2020, pp. 1–6, doi: 10.1109/I2MTC43012.2020.9129039.
[15] R. Sanz, A. B. Fernández, J. A. Dominguez, B. Martín, and M. D. Michelena, "Gamma irradiation of magnetoresistive sensors for planetary exploration," *Sensors*, vol. 12, no. 4, pp. 4447–4465, Apr. 2012.
[16] ST Microelectronics. (Sep. 2018). *STM32F334 Datasheet*. [Online]. Available: https://www.st.com/resource/en/datasheet/stm32f334k4.pdf
[17] Honeywell Aerospace. (Apr. 2019). *1- and 2-Axis Magnetic Sensors HMC1001/ 1002/ 1021/ 1022*. [Online]. Available: https://www.aerospace.honeywell.com
[18] K. Mohamadabadi, C. Coillot, and M. Hillion, "New compensation method for cross-axis effect for three-axis AMR sensors," *IEEE Sensors J.*, vol. 13, no. 4, pp. 1355–1362, Apr. 2013, doi: 10.1109/JSEN.2012.2236511.
[19] F. J. Franco, Y. Zong, J. A. Agapito, and A. H. Cachero, "Radiation effects on XFET voltage references," in *Proc. IEEE Radiat. Effects Data Workshop*, Jul. 2005, pp. 138–143, doi: 10.1109/REDW.2005.1532680.
[20] P. Brauer, J. M. G. Merayo, T. Risbo, and F. Primdahl, "Magnetic calibration of vector magnetometers: Linearity, thermal effects and stability," in *Proc. ESA Conf. SP-490*, 2001, pp. 1–7. [Online]. Available: http://citeseerx.ist.psu.edu/viewdoc/summary?doi=10.1.1.36.1718
[21] N. Olsen *et al.*, "Calibration of the Ørsted vector magnetometer," *Earth, Planets Space*, vol. 55, no. 1, pp. 11–18, Jan. 2003, doi: 10.1186/BF03352458.
[22] M. Janošek, M. Dressler, V. Petrucha, and A. Chirtsov, "Magnetic calibration system with interference compensation," *IEEE Trans. Magn.*, vol. 55, no. 1, pp. 1–4, Jan. 2019, doi: 10.1109/TMAG.2018.2874169.
[23] *ESCIES—European Space Components Information Exchange System, Radiation: Theory, Definitions—Gamma Radiation*. Accessed: Nov. 10, 2020. [Online]. Available: https://escies.org
[24] NewSpace Systems. *NMRM-001-485 Magnetometer*. Accessed: Nov. 10, 2020. [Online]. Available: https://www.newspacesystems.com

David Novotny (Graduate Student Member, IEEE) received the M.Sc. degree from Czech Technical University in Prague, Prague, Czech Republic, in 2018, with a focus on magnetic gradiometer for car detection and speed measurements, where he is currently pursuing the Ph.D. degree with the Department of Measurement, Faculty of Electrical Engineering.

His current research interests include radiation tolerant low-noise magnetic sensors, mainly anisotropic magnetoresistors (AMR) and digital signal processing methods and low-noise electronics.

Vojtech Petrucha (Member, IEEE) was born in Prerov, Czech Republic, in 1982. He received the M.Sc. degree in measurement and instrumentation and the Ph.D. degree in the same branch for work on the calibration of magnetometers from the Faculty of Electrical Engineering, Czech Technical University in Prague, Prague, Czech Republic, in 2007 and 2012, respectively.

He is currently a Research Assistant with the Department of Measurement, Faculty of Electrical Engineering, Czech Technical University in Prague. His research interests include the development, construction, calibration, testing and applications of sensor systems, especially the magnetic field sensors (AMR and fluxgate).

Michal Dressler (Graduate Student Member, IEEE) received the M.Sc. degree from Czech Technical University in Prague, Prague, Czech Republic, in 2019, with a focus on coil system for magnetometer calibrations with interference compensation, where he is currently pursuing the Ph.D. degree in gradiometer based on magnetic microwires with the Department of Measurement, Faculty of Electrical Engineering.

His current research interests include precise magnetometer calibrations and development of magnetometer electronics.

Antonin Platil received the M.Sc. degree from Faculty of Electrical Engineering, Czech Technical University in Prague, Prague, Czech Republic, in 1997, and the Ph.D. degree from the Department of Measurement, Faculty of Electrical Engineering, Czech Technical University in Prague.

Since 2010, he has been an Associate Professor with the Department of Measurement and mainly deals with various aspects of magnetic measurements, sensors, and systems.

7.1.4 refP 4

Petrucha, V.; Janošek, M.; Azpurua, M. A., "Fluxgate magnetometer vector feedback homogeneity and its influence on sensor parameters," In: Proceedings of Instrumentation and Measurement Technology Conference (I2MTC) 2014. Vail, Colorado: IEEE Instrumentation and Measurement Society, 2014, pp. 460-463. ISSN 1091-5281. ISBN 978-1-4673-6385-3

The author of this thesis had been developing fluxgate-based magnetometers since working on his master's thesis where individually compensated, race-track sensors made completely in PCB technology were used as a triaxial magnetometer for underground drilling navigation / compassing. Later, he specialized in sensor constructions that used vectorial compensation of the measured field. In the presented conference proceedings paper, we explore the influence of the compensation system on the parameters. Thanks to our collaboration with an external scientist, we were able to improve the compensation system parameters and retrieve some data for further improvement of the construction. The author's contribution is 33%, shared equally between the authors; the author worked primarily on the design, construction, and characterization of the magnetometer.

Fluxgate magnetometer vector feedback homogeneity and its influence on sensor parameters

V. Petrucha, M. Janošek
Department of Measurement, FEE
Czech Technical University in Prague
Prague, Czech Republic
petruvoj@fel.cvut.cz

M. A. Azpúrua
Applied Electromagnetics Laboratory
Instituto de Ingeniería
Caracas, Venezuela

Precise fluxgate sensors are built with a vector feedback, which eliminates the cross-field effect and improves linearity. The sensor axes orthogonality should be then defined primarily by the orientation of the feedback coils while the sensitivities are defined by feedback coil constants. The influence of the homogeneity of the feedback field on calibration parameters of a vectorially compensated tri-axial fluxgate magnetometer is presented.

Keywords—fluxgate sensor, scalar calibration, field homogeneity

I. INTRODUCTION

There is a long-term effort to develop high precise fluxgate magnetometers at the Department of Measurement, FEE, CTU in Prague. Their application is in vertical and horizontal underground drilling navigation, archeological and geological prospection or Earth's magnetic field observation for scientific purposes. One of the latest development steps at our department is an application of vector compensation. The vector compensation of measured magnetic field brings several benefits. It almost completely eliminates the cross-field effect (sensitivity to perpendicular magnetic field) and also the sensitivity and orthogonality should be defined primarily by the robust and mechanically stable compensation coils system [1]. It also brings complexity and increased price but the benefits are more important when the high precision is a goal. The feedback coils should ideally provide homogenous compensation field in the inner volume of the sensor where the magnetic cores of the fluxgate sensors are present. In order to further improve the properties of a compact vectorially compensated fluxgate sensor [2] we enhanced the homogeneity of the feedback coils. Former coil design is based on Merritt [3] four square-coil arrangement for each axis. With the help of semi-analytical technique [4] we were able to further improve the field homogeneity in all three axes, which was verified by FEM modeling (ANSYS Magnetostatic). The X and Z axes were redesigned to three-coils while only the coil spacing and turns count were modified for Y-axis. Experimental tests were made to check the real influence of the feedback field homogeneity on sensor properties. In order to decrease the field homogeneity, extra turns were added to each one outer section of the X, Y and Z feedback coils, together with switches, which allowed to disconnect the turns or to connect them in series or anti-series with the basic turns. We evaluated the influence by conducting a number of scalar calibrations [5] for various extra-turns configurations (extra turns active for X, Y, Z, XY, XZ and YZ axes, tested in both polarities).

There was also an assumption that the field homogeneity could influence the behavior of offset temperature dependences. There are microscopic movements or rotations of the fluxgates sensors in the compensation body when the temperature is changed. This could theoretically mean that the offset will be less affected in a compensation system with better homogeneity. Experiments to study this behavior were also conducted.

II. SENSOR DESCRIPTION

The vectorially compensated triaxial vector fluxgate sensor consists of several parts. In the middle there are three single-axis fluxgate sensors. Each of them has a magnetic core shaped in a toroidal support (made of MACOR or BNP-2 machinable ceramics), excitation and pick-up windings. The effective core diameter is approximately 13 mm; total dimensions of a one single axis sensor are 20 mm × 20 mm × 10 mm. The magnetic material (amorphous tape, 2.5 mm width) in the current version of the sensor is Vitrokov 8116, which is replaced by a specifically magnetic field annealed Metglas 2714 tape in a new version of the sensor. The Metglas 2714 provides lower noise at lower excitation energy which helps to prevent self-heating of the sensor head. The feedback coils support was made of PEEK GF30 engineering plastic and is now machined from MACOR ceramics which is more mechanically stable with respect to temperature changes but is also unfortunately much more brittle. The support is made of two halves; each of them has milled grooves for the coils and a cavity for the set of three single axis fluxgates. There is also an excitation resonant capacitor visible in Fig.1 as well as the connecting terminals.

III. ENHACEMENT OF FIELD HOMOGENEITY

Scalar calibration technique is used during the sensor development to evaluate sensor properties. The method provides very accurate and well repeatable calibration information: three sensitivities, three orthogonality angles and three offsets. The orthogonality was worse (-0.44°) than we have expected it to be (<0.1°), taking into account the precision of machining and assembly.

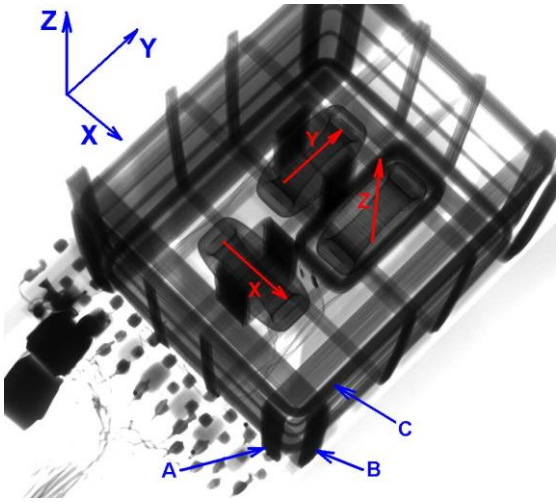

Fig. 1. X-ray image of the former sensor design. Each set of feedback coils has four section. A, B and C mark the sections where the extra turns were added (A is a part of X-axis compensation, B is a part of Y-axis compensation and C is a part of Z-axis compensation).

There was an assumption that the higher orthogonality error comes from poor homogeneity of the compensation field or the non-ideal non-symmetrical placement of the three single-axis fluxgate sensors in the inner volume of the compensation coils. We prefer to keep the current topology of placement of the three single-axis sensors because it brings some benefits with respect to more complicated but more symmetric layouts [6]. Even the state of the art sensors use similar approach [7]. Each single-axis sensor can be individually tuned for minimum feed-through signal and noise before the assembly. So the enhancement of the homogeneity of the compensation field is an option.

The temperature dependence of the orthogonality has been measured using a non-magnetic thermostat and multiple scalar calibrations at different temperatures [8]. Relatively strong dependence of the orthogonality has been found (up to 0.38 arcsec/°C) and thus it is very welcomed to decrease the non-orthogonality and thus possibly decrease its temperature variations.

The former feedback coils design is based on Merritt 4-coil setup slightly modified with the use of FEM modeling to make the support machinable. Nevertheless, it was difficult to evaluate the magnetic field homogeneity in the volume of the sensors. The FEM modeling software usually allows evaluating the magnetic induction along a path or a plane but not the homogeneity in a specific volume. To overcome this problem the semi-analytical method has been used [4]. This method uses analytical calculation of the magnetic field from Biot-Savart law and iterative algorithm which uses objective function (average magnitude of the magnetic flux density in the volume of interest) to find best values for coil section spacing and number of turns. The method provided significant improvement over the initial design as is summarized in Table I. The homogeneity H is evaluated with respect to (1), B_{MAX} and B_{MIN} being the maximal and minimal values and B_{MEAN} the mean value of magnetic flux density in the volume of interest. The results were later confirmed by FEM simulation in ANSYS Magnetostatic and Flux3D. The X and Z axes were redesigned to have only three sections which is also favorable for machining and coil winding. The new design of Y-axis has still four sections but the spacing and number of turns were slightly modified. Fig.2 shows the plot of magnetic flux density in X-axis for original 4-coil "modified Merritt" design and new 3-coil "semi-analytical" design. In the middle of the picture is marked a region of interest where the fluxgate sensor cores are positioned.

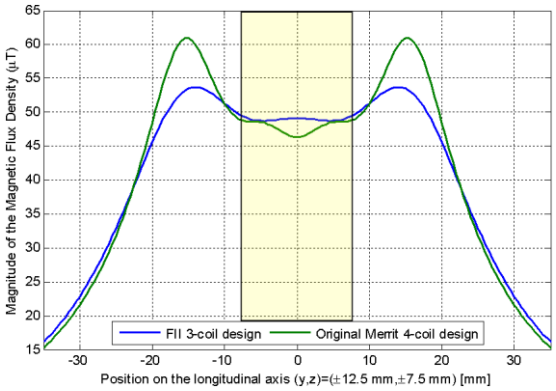

Fig. 2. Magnetic flux density distribution for X-axis; comparison of former and new design, region of interest is marked in the middle of the picture

$$H = \left(1 - \frac{B_{MAX} - B_{MIN}}{B_{MEAN}}\right).100\% \qquad (1)$$

TABLE I. FIELD HOMOGENEITY IMPROVEMENT

Field homogeneity H	***Axis***		
	X	Y	Z
Former "Merritt"	92.98%	97.4%	91.57%
New "Semi-analytical"	97.62%	99.1%	96.46%

IV. EXPERIMENTS

Experiments were prepared to check the real influence of the feedback magnetic field non-homogeneity on orthogonality angles. The feedback field non-homogeneity has been created by changing the symmetry in turns count in the modified Merritt four-coil design by adding or subtracting turns from one outer coil. The FEM simulation confirms that a gradient of approximately ±66μT/m is created (see Fig. 3).

The X. Y and Z outer sections have nominally 186, 196 and 189 turns, respectively, and in total 492, 558 and 462 turns. Twelve extra feedback turns were added to one outer section of the X, Y and Z feedback coils (see Fig.1). Non-magnetic switches allowed to connect the extra turns in series or anti-series with the basic turns (or to disconnect them).

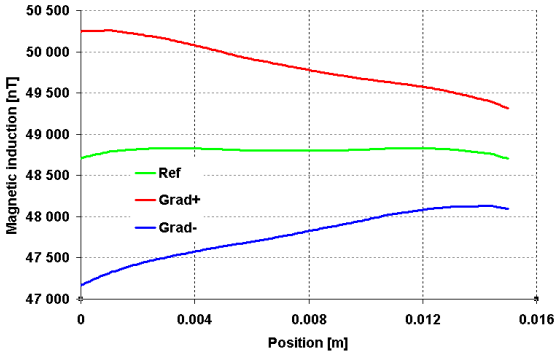

Fig. 3. Simulation of feedback field non-homogeneity created by connecting the extra turns in series (Grad+), anti series (Grad-) and the normal field (Ref). The non homogeneity is ~±66 μT/m. Sensor center is in 0.075 m position.

At first we evaluated the influence of extra turns active only in one axis, later we tried also some other possible combinations of extra-turns active in two axes simultaneously. Together we evaluated 15 combinations: "000", "+00", "-00", "0+0", "0-0", "00+", "00-", "++0" "+-0","-+0", "--0", "+0+", "-0-", "0++", "0--" ("0" means "extra turns not connected", "+" extra turns connected in series, "-" extra turns connected in anti-series, applies for compensation coils X, Y and Z). For each combination at least two scalar calibrations were done to be sure that the results are repeatable.

Theoretically, feedback field gradient along the respective sensor should also affect the offset temperature dependence because of the sensor changing its position due to thermal expansion. Another experiment was performed in order to test this influence. The sensor was placed in a 6-layered permalloy magnetic shielding equipped with a thermostatic box which allowed to control the sensor temperature. Computer based data-logging system has been assembled, logging the sensor temperature and the three magnetometers outputs. The switching of feedback extra-turns was also manual in this case.

V. Results

During two measurement campaigns over 38 scalar calibrations were made with various data length (56 positions or 161 positions), each extra-turn combination was measured two or three times. The sensitivities were affected as was expected from the simulation - the extra turns changed the coil constant and thus the sensitivity in appropriate axis, which was compensated in the later calculations.

On the other hand the behavior of orthogonality angles is more complex. The scalar calibration uses three angles which define the orthogonality of the sensor's intrinsic coordinate system (α, β, γ correspond to ν_{12} ν_{23} ν_{13} in [5]). The α-angle is basically the error of orthogonality between X and Y axes, β and γ defines the error of Z axis orthogonality with respect to plane defined by X and Y axes.

The α-angle is influenced by any combination of the extra turns in X and Y axes while the Z-axis extra turns have almost no visible effect. Please see Fig.4. The change is up to ±0.121°

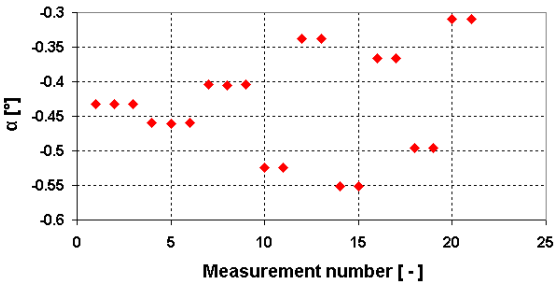

Fig. 4. α angle vs. part of the measurements (no extra turns applied for three most left measurements, no change in α also for calibrations with only Z-axis extra turns).

from its nominal value of -0.432° for combination of extra turns in X and Y axes. The α-angle exhibits "linear dependence" on the non-homogeneity created by extra turns in X-axis (unfortunately the dependency was measured only in three points: negative gradient, no extra gradient, and positive gradient, see Fig. 3). Similar dependency was observed also for the non-homogeneity in Y-axis. The β-angle was practically insensitive to variation in Y and Z-axes, but there was again a strong linear dependence for X-axis non-homogeneity. There is almost no change for γ-angle for non-homogeneity introduced in X and Y-axes, it stays within ±0.002° from its nominal value of -0.0405°. But it is linearly sensitive to non-homogeneity in Z-axis. A summary of the influences is shown in Table II.

TABLE II. Extra-turns influence on orthogonality angles (does not include their combinations)

	α-angle	***β-angle***	***γ-angle***
X-axis	**<±0.0931°**	**<±0.0131°**	<±0.001°
Y-axis	**<±0.0278°**	<±0.001°	<±0.002°
Z-axis	<±0.002°	<±0.002°	**<±0.116°**

The offsets resulting from the scalar calibration were also affected by the introduced non-homogeneity. For all three axes temperature dependence has been observed. The temperature of the sensor has risen by ~15°C during the continuous scalar calibration campaign by the energy dissipated in the excitation circuit and due to the rise of the ambient temperature. The temperature offset coefficient is approximately -0.3nT/°C.

After compensation on this effect, the offsets changed according to Table III. However the offsets are the least stable calibration parameter and the changes of <2nT can be considered as "noise".

TABLE III. Sensor offsets versus introduced non-homogeneity

	X-axis	***Y-axis***	***Z-axis***
Absolute offset value	-14.5nT	125nT	58nT
Relative change for ±Grad	±1.5nT	±10nT	±3nT

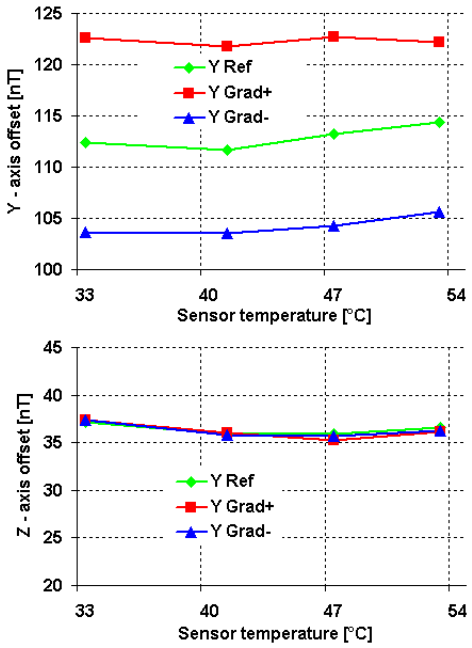

Fig. 5. Offset temperature dependence versus non homogeneity in Y-axis ("Grad+" Y-axis extra turns in series, "Grad-" turns in anti-series, "Ref" no extra turns)

Another evaluation of offset temperature dependence was done in the magnetic shield. The results indicate that an absolute offset value is affected in the axis where the non-homogeneity is applied (Fig. 5). There was basically no visible change for the other two axes. The Y-axis offset was thus influenced when there was a non-homogeneity introduced in the Y-axis feedback, there was no change on X or Z-axes. We did not find any significant change in temperature dependence of the offset when introducing non-homogeneity – it might be well below our measurement error. This was caused mainly by the measurement procedure: in order to switch between various extra-turns configuration the sensor was repeatedly removed from the magnetic shielding and then placed back. This resulted in uncertainty of the offset caused by remanence in the magnetic shield (below 5 nT) and also by temperature shocks applied to the sensor due to the procedure.

VI. Discussion and Conclusions

An interesting feature observed is that the non-orthogonality angles are closer to their ideal zero values for non-ideal field homogeneity. With "in-series" turns applied (creating feedback field non-homogeneity in X-axis) the α-angle value is closer to zero than for "ideal" no-extra turns condition. An explanation to this effect might be the sensor asymmetry in the coil system (see Fig. 1) combined with the introduced non-homogeneity.

TABLE IV. Non-orthogonalities of the sensors with improved compensation field homogeneity

	α-angle	*β-angle*	*γ-angle*
Sensor 03a	0.29727°	-0.01233°	0.10869°
Sensor 03b	0.42601°	-0.04690°	-0.07329°

Two new sensors with the improved compensation coil system field homogeneity have been manufactured. Sensor *03a* uses three ring-core based fluxgates, very similar in design to the previous generation of sensors, which were used for the described measurements. Second sensor *03b* uses race-track core topology which is supposed to provide lower noise. However from scalar calibrations results we did not find any significant improvement on the sensor parameters, mainly orthogonality error, since the results are not statistically relevant (two samples), see Table IV.

From the results, we assume that the physical topology of the sensors is more important than the compensation field homogeneity at this scale, since we did not find any dependence on offset temperature coefficient with artificial non-homogeneity. As long as the sensor and compensating coil material is stable enough, it is possible to use the results from scalar calibration and compensate for offset and even orthogonality temperature dependence.

The results indicate that further improvement can be obtained by bringing all three single-axis sensors closer together.

VII. Acknowledgment

The presented work has been supported by the Czech Science Foundation, grant No. 13-39088P.

References

[1] F. Primdahl, P. Anker Jensen, "Compact spherical coil for fluxgate magnetometer vector feedback," J. Phys. E: Sci. Instrum. 15 221α

[2] V. Petrucha, P. Kaspar, "Compact fluxgate sensor with a vector compensation of a measured magnetic field," Sensors, 2010 IEEE, 1795 – 1798.

[3] J. Kirschvink, "Uniform magnetic fields and double-warpped coil systems: Improved techniques for the design of bioelectromagnetic experiments," Bioelectromagnetics, Vol. 13, 401-411, 1992.

[4] M. A. Azpurua, "A semi-analytical method for the design of coil-systems for homogeneous magnetostatic field generation," Progress In Electromagnetics Research B, Vol. 37, 171-189, 2012.

[5] J. M. G.Merayo, P. Brauer, F. Primdahl, J. R. Petersen and O. V. Nielsen, "Scalar calibration of vector magnetometers," Meas. Sci. Technol. 11, 120–132, 2000.

[6] H.U. Auster et al, "The THEMIS Fluxgate Magnetometer," in Space Science Reviews, DOI10.1007/s11214-008-9365-9.

[7] J.M.G. Merayo,"The Vector Field Magnetometer (VFM) on Swarm," ESA's Second Swarm International Science Meeting, Postdam, 2009.

[8] V. Petrucha, P. Kaspar, "Measurement of the Temperature Dependence of the Sensitivity and Orthogonality of a Triaxial Vector Magnetometer," Journal of Electrical Engineering, Vol 63. No 7s, 31-34, 2012

7.1.5 refP 5

Petrucha, V.; Janošek, M.; Azpúrua, M. A., "Vector Feedback Homogeneity and Inner Layout Influence on Fluxgate Sensor Parameters," IEEE Transactions on Instrumentation and Measurement. 2015, 64(5), 1293-1299. ISSN 0018-9456

In this paper, we present another step in the development of the inner structure of the triaxial fluxgate sensor with vector compensation of the measured field. A design that is more symmetrical than the previously used one, composed of three identical ring-core fluxgate sensors. The novel design used only two ring cores placed perpendicularly to each other, with a common center and complex pick-up coils setup enabled by newly available 3D-printing technology. Similar testing was used to characterize the performance - mainly the sensor orthogonality and offset temperature dependence. The author's contribution is higher - 40%, due to more complex work on the development of the sensor.

Vector Feedback Homogeneity and Inner Layout Influence on Fluxgate Sensor Parameters

Vojtěch Petrucha, Michal Janošek, and Marco A. Azpúrua

***Abstract*— Vector feedback is a concept which can significantly improve linearity and stability of a magnetic field sensor. The feedback coils effectively cancel the measured magnetic field in the inner volume of the triaxial sensor. Thus, in case of fluxgates, it suppresses one possible source of nonlinearity—cross-field sensitivity error. The triaxial sensor axes orthogonality should be primarily defined by the orientation of the feedback coils, while the sensitivities are defined by feedback coil constants. The influence of the homogeneity of the feedback field and the influence of the sensor inner layout on calibration parameters of a vectorially compensated triaxial fluxgate magnetometer are presented.**

***Index Terms*— Field homogeneity, fluxgate sensor, scalar calibration.**

I. Introduction

THERE is a long-term effort to develop high-precise fluxgate magnetometers at the Department of Measurement, Faculty of Electrical Engineering, Czech Technical University in Prague. A typical application is in vertical and horizontal underground drilling navigation, archeological and geological prospection, or Earth's magnetic field observation for scientific purposes. Fluxgates sensors offer the lowest noise densities of all vector magnetic sensors working at room temperatures (<3 pT/$\sqrt{}$Hz at 1 Hz) while having very high dynamic range (>120 dB) and excellent time—temperature stability [1]. One of the latest development steps at our department is an application of vector compensation. The vector compensation of measured magnetic field brings several benefits. First, it almost completely eliminates the cross-field effect (sensitivity to perpendicular magnetic field). Second, the sensitivity and orthogonality should be defined primarily by the robust and mechanically stable compensation coils system [2]. The vector compensation design brings complexity and increases price, but the benefits are more important when the high precision is a goal.

The feedback coils should ideally provide homogenous compensation field in the inner volume of the triaxial sensor body where the magnetic cores of the individual fluxgate sensors are present. To further improve the properties of a compact vectorially compensated fluxgate sensor [3], we enhanced the homogeneity of the feedback coils and studied its effect on calibration parameters of the triaxial sensor. Calibration parameters (three sensitivities, three orthogonality angles, and three offsets) are evaluated by scalar calibration technique [4]. The technique provides accurate and well repeatable results and requires only basic equipment. The impulse to conduct this research were nonideal values of orthogonalities we got while calibrating the former sensor [3].

In addition to [5], we evaluated also the influence of the inner layout of the individual sensing elements. Former design uses three separate single-axis fluxgate sensors that are embedded into the vector compensation system structure. This design is convenient because it allows to completely test and tune each single axis fluxgate sensor for main parameters (noise and offset) before the whole triaxial sensor is fully assembled. However, this layout places the individual sensor magnetic cores asymmetrically with respect to the center of symmetry of the feedback coil system. Based on the results of the feedback field homogeneity influence, we proposed another inner layout, partially similar to the design presented in [6], which uses only two magnetic cores. Two ring-shaped fluxgate cores are placed symmetrically in the geometrical center of the feedback system. New triaxial sensor that implements this modified dual-core inner design was built and evaluated.

The main goal of the research was to improve the orthogonality of the vectorially compensated triaxial fluxgate sensor. However, there was an assumption that the compensation field homogeneity and inner structure topology could influence also the behavior of offset temperature dependences, as there are microscopic movements or rotations of the individual fluxgates sensors in the vector compensation body when the temperature is changed. This could theoretically mean that the offset will be less affected in a compensation system with better homogeneity or in a more symmetric topology of the inner sensing elements. Experiments to study this behavior were conducted.

II. Sensor Description

The vectorially compensated triaxial vector fluxgate sensor consists of several parts. In the middle, there are usually three single-axis fluxgate sensors. Each of them has a magnetic core, and excitation and pickup windings. The fluxgate principle is well known, the soft magnetic core is periodically deeply saturated by the current flowing through the excitation winding.

Manuscript received June 21, 2014; revised September 5, 2014; accepted September 24, 2014. Date of publication October 29, 2014; date of current version April 3, 2015. This work was supported by the Czech Science Foundation under Grant 13-39088P. The Associate Editor coordinating the review process was Dr. Theodore Laopoulos.

V. Petrucha and M. Janošek are with the Department of Measurement, Faculty of Electrical Engineering, Czech Technical University in Prague, Prague 166 36, Czech Republic (e-mail: petruvoj@fel.cvut.cz).

M. A. Azpúrua is with the Department of Electronic Engineering, Universitat Politècnica de Caralunya, Barcelona 08034, Spain (e-mail: marco.azpurua.a@ieee.org).

Color versions of one or more of the figures in this paper are available online at http://ieeexplore.ieee.org.

Digital Object Identifier 10.1109/TIM.2014.2362831

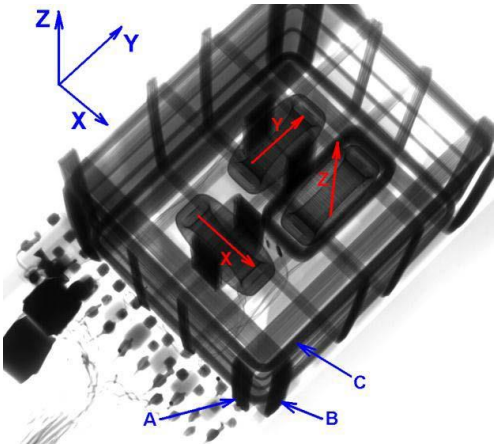

Fig. 1. X-ray image of the former sensor design (02). Each set of feedback coils has four sections. A–C mark the sections where the extra turns were added (A is a part of x-axis compensation, B is a part of y-axis compensation, and C is a part of z-axis compensation).

Polarity and amplitude of the measured magnetic field is related to the phase and amplitude of the second-harmonic voltage sensed across the pickup winding. The single-axis sensor works as a zero detector and its linearity is significantly improved when compensation principle is used. Feedback current is then fed directly to the pickup winding or separate feedback coil is used. In case of the vectorially compensated sensor, all the three components of measured magnetic field vector are compensated simultaneously in the inner volume of the triaxial sensor [2].

Four different sensor designs were used to evaluate the homogeneity and inner structure effects. The sensors are later referenced in the text as (02, 03a, 03b, 04). Sensor marked as (02) is the oldest design. It consists of three single-axis ring-core fluxgate sensors embedded in a compensation structure with external dimensions of 47 mm × 40 mm × 40 mm. The effective core diameter is approximately 13 mm and total dimensions of a one single-axis sensor are 20 mm × 20 mm × 10 mm. The magnetic core material (amorphous ribbon, 2.5 mm width) is Vitrokov 8116 wound on a toroidal support made of BNP-2 machinable ceramics. The feedback coils are of slightly modified Merritt [7] four square-coil arrangement for each axis. Fig. 1 presents the X-ray image of this former design.

With the help of semianalytical technique [8], we were able to further improve the feedback field homogeneity in all three axes, which was verified by Finite Element Method (FEM) modeling (ANSYS Magnetostatic). The x- and z-axes were redesigned to three coils, while only the coil spacing and turns count were modified for y-axis. The details concerning the homogeneity improvement are mentioned in Section III. This new feedback system design was used for sensors (03a) and (03b). There are also some other modifications with respect to sensor (02). The magnetic cores of the individual single-axis sensors were made of a specifically magnetic field annealed Metglas 2714 amorphous ribbon. The Metglas 2714 provides

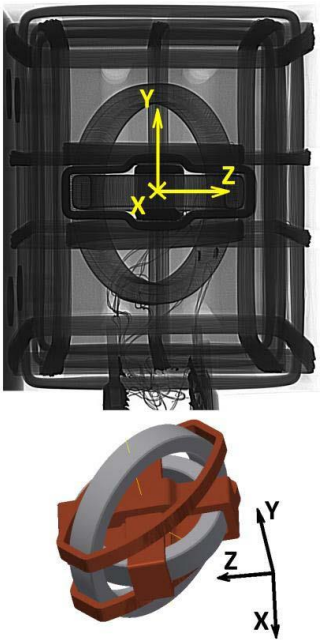

Fig. 2. Side X-ray view of the sensor (04) with the new dual-ring-core inner structure (top). Model of the dual-ring-core design shows the placement of all pickup coils (bottom). The y-axis uses ring core with a slightly higher diameter, which is placed in a diagonal plane with respect to $x-$ and $z-$axes. The pickup coil is splitted into two parts in case of y-axis.

lower noise at lower excitation energy, which helps to prevent self-heating of the sensor head. Sensor (03a) uses the same design of the three ring-core single-axis sensors as sensor (02). To evaluate properties of another design, the triaxial sensor (03b) was built using miniature race-track cores. The race-track cores were designed to fit exactly into the same space as the former ring-core fluxgates, but due to its shape, the length of the race-track is higher than the diameter of the ring. We expected to gain lower noise, but actually the design provided only a small improvement but the construction was very demanding and expensive.

Sensor (04) has a completely different inner structure. It consists of two ring cores with a slightly different diameter, which are embedded one in another in the center of symmetry of the whole sensor. All pickup coils were made as self-supporting coils enabling faster and easy assembly of the whole structure (Fig. 2). The two ring cores were designed to have significantly higher effective diameter of the magnetic cores (22 and 28.7 mm), which considerably helps to decrease sensor noise. The smaller ring core has two mutually perpendicular pickup coils, one for x-axis and second for z-axis. The bigger ring core is placed perpendicularly with respect to the smaller ring and carries the y-axis pickup coil which is split symmetrically into two parts. The bigger ring is tilted with respect to z-axis by 45° to better fit into the space available in the compensation support.

The feedback coils support was made of PEEK GF30 engineering plastic in case of sensor (02), which was changed

TABLE I
SUMMARY OF THE SENSORS USED FOR THE MEASUREMENTS

Sensor	Inner topology	Feedback design	Material
(**02**)	3x ring-core	Modified Merritt	PEEK GF30
(**03a**)	3x ring-core	Semi-analytical	MACOR
(**03b**)	3x race-track	Semi-analytical	MACOR
(**04**)	2x ring-core	Semi-analytical	PA3200GF

for sensors (03a) and (03b) to MACOR. The machinable ceramics is mechanically more stable with respect to temperature changes but is also unfortunately much more brittle. The support is made of two halves; each of them has milled grooves for the coils and a cavity for the set of three single-axis fluxgates or the new dual-core structure. There is also an excitation resonant capacitor visible in Fig. 1 as well as the connecting terminals. The compensation support was made by 3-D printing in case of sensor (04) to speed up the manufacturing process and to easily produce relatively complicated part that supports the pickup coils. The 3-D printer used glass-filled polyamide PA3200GF. See Table I for summary of the used sensors.

III. ENHACEMENT OF FIELD HOMOGENEITY

Scalar calibration technique [4] is used during the sensor development to evaluate sensor properties. The method provides very accurate and well repeatable calibration information: three sensitivities, three orthogonality angles, and three offsets. By orthogonality, we understand the alignment between an ideal orthogonal reference frame of the triaxial sensor and the frame made of real magnetic sensitivity axes that come out from the scalar calibration algorithm. The magnetic axes should be aligned with the compensation coils mechanical axes in the case of a vectorially compensated sensor. The algorithm is based on mathematical processing of data-samples that are collected with the calibrated instrument in a homogenous magnetic field. The samples must cover the whole measurement range of the triaxial sensor for all the three sensitivity axes to get reliable results.

Nevertheless, the orthogonality was worse $-0.44°$ for sensor (02) than we have expected considering the precision of machining and assembly ($<0.1°$). There was an assumption that the higher orthogonality error comes from poor homogeneity of the compensation field or the nonideal nonsymmetrical placement of the three single-axis fluxgate sensors in the inner volume of the compensation coils. We preferred to keep the former topology of placement of the three single-axis sensors because it brings some benefits with respect to more complicated but more symmetric layouts [6]. Even the state-of-the-art sensors use similar approach [9]. Each single-axis sensor can be individually tuned for minimum feedthrough signal and noise before the assembly. Therefore, at first, we considered the enhancement of the homogeneity of the compensation field as an option.

The temperature dependence of the orthogonality has been measured using a nonmagnetic thermostat and multiple scalar calibrations at different temperatures [10].

TABLE II
FIELD HOMOGENEITY IMPROVEMENT

Field homogeneity H	*Axis*		
	X	Y	Z
Former "Merritt"	92.98%	97.4%	91.57%
New "Semi-analytical"	97.62%	99.1%	96.46%

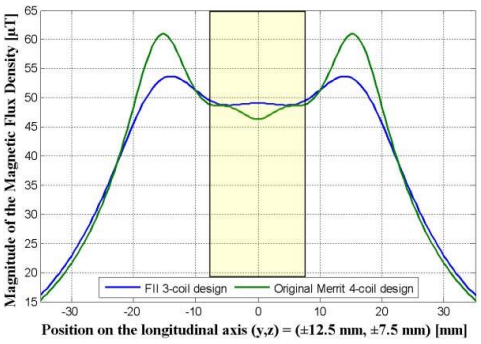

Fig. 3. Magnetic flux density distribution for x-axis; comparison of former and new design, region of interest is marked in the middle of the picture (simulation output, using calculation from Biot–Savart law [8]).

Relatively strong dependence of the orthogonality has been found (up to 0.38 arcsec/°C) and thus it is very welcomed to decrease the nonorthogonality and thus possibly decrease its temperature variations.

The former feedback coils design is based on Merritt four-coil setup slightly modified with the use of FEM modeling to make the support machinable. Nevertheless, it was difficult to evaluate the magnetic field homogeneity in the volume of the sensors. The FEM modeling software usually allows evaluating the magnetic flux density along a path or a plane but not the homogeneity in a specific volume. To overcome this problem, the semianalytical method has been used [8]. This method uses analytical calculation of the magnetic field from Biot–Savart law and iterative search algorithm that uses objective function (average magnitude of the magnetic flux density in the volume of interest) to find best values for coil section spacing and number of turns. The algorithm uses some simplifications that make the processing faster—coils are considered ideally thin and it does not support any ferromagnetic cores. The method provided significant improvement over the initial design, as is summarized in Table II. The homogeneity H is evaluated with respect to (1), B_{MAX}, and B_{MIN} being the maximal and minimal values, and B_{MEAN} the mean value of magnetic flux density in the volume of interest. The results were later confirmed by FEM simulation in ANSYS Magnetostatic and Flux3-D. The $x-$ and $z-$axes were redesigned to have only three sections, which is also favorable for machining and coil winding. The new design of y-axis has still four sections, but the spacing and number of turns were slightly modified. Fig. 3 shows the plot of magnetic flux density in x-axis for original four-coil modified Merritt

design and new three-coil semianalytical design. In the middle of the picture is marked a region of interest, where the fluxgate sensor cores are positioned. The change in coils spacing led to minor increase of the compensation system dimensions (50 mm × 40 mm × 40 mm)

$$H = \left(1 - \frac{B_{\mathrm{MAX}} - B_{\mathrm{MIN}}}{B_{\mathrm{MEAN}}}\right) 100\%. \quad (1)$$

IV. Two-Ring-Core Inner Structure

To evaluate the possible influence of inner parts symmetry on triaxial sensor parameters, we proposed new design of the fluxgate sensing elements. Our experience indicates that fluxgate ring-core sensors with higher effective diameter of the magnetic core provide lower noise [11]. Therefore, we extended the inner volume of the feedback support to maximize the possible ring-core diameter. The external dimensions of the compensation support remained the same (50 mm × 40 mm × 40 mm). The dimensions of a cavity that accommodates the sensing elements are 36 mm × 28 mm × 28 mm. There are only two magnetic cores. The smaller ring (external diameter of 24 mm) is shared by x- and z-axis pickup coils. The bigger ring (external diameter of 30.7 mm) is placed in a diagonal plane with respect to x- and z-axis to fit into the cuboidal cavity in the feedback coils support. This design (04) is perfectly symmetrical, but because of its increased size, the magnetic cores experience even higher field nonhomogeneity than in the previous designs (02) and (03). For simplicity, we used the same improved homogeneity feedback coil design as was developed for sensor (03). This actually means that the results will provide stronger comparison between the field homogeneity versus placement symmetry effect.

V. Experiments

A. Field Homogeneity Influence on Orthogonality

The real influence of the feedback magnetic field nonhomogeneity on orthogonality angles was investigated. The feedback field nonhomogeneity has been created by changing the symmetry in turns count in the modified Merritt four-coil design by adding or subtracting turns from one outer coil. The FEM simulation confirms that a gradient of approximately ±66 μT/m is created (Fig. 4).

To decrease the field homogeneity, twelve extra turns were added to each one outer section of the x, y, and z feedback coils (Fig. 1), together with switches, which allowed to disconnect the turns or to connect them in series or antiseries with the basic turns. We evaluated the influence by conducting a number of scalar calibrations [4] for various extra-turns configurations (extra turns active for x, y, z, xy, xz, and yz axes, tested in both polarities). The x, y, and z outer sections have nominally 186, 196, and 189 turns, respectively, and in total 492, 558, and 462 turns.

At first, we evaluated the influence of extra turns active only in one axis, and later we also tried some other possible combinations of extra-turns active in two axes simultaneously. Together we evaluated 15 combinations: 000, +00, −00, 0+0, 0–0, 00+, 00−, ++0 +−0, −+0, −0, +0+, −0−, 0++, and 0− (0 means extra turns not connected, + extra turns connected in series, and − extra turns connected in antiseries, applies for compensation coils x, y, and z). For each combination, at least two scalar calibrations were done to be sure that the results are repeatable.

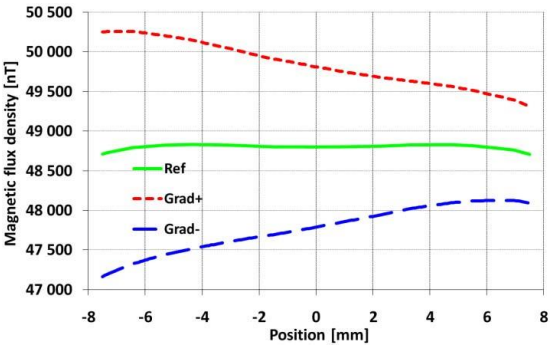

Fig. 4. Simulation of feedback field nonhomogeneity created in x-axis by connecting the extra turns in series (Grad+), anti series (Grad−), and the normal field (Ref). The nonhomogeneity is ∼ ±66 μT/m. Sensor center is in 0 mm position.

B. Influence of the Inner Layout of the Individual Sensing Elements

The sensor (04) with modified inner topology has been built and calibrated using the scalar calibration technique [4]. We can estimate the inner layout influence by comparing the calibration results for different inner topologies (03a) and (03b) versus (04). We repeated the same approach with introduced feedback field nonhomogeneity by adding the extra turns also to triaxial sensor (04). We supposed that a comparison of the results of scalar calibrations for different introduced feedback field nonhomogeneities can provide useful information about the influence of the inner layout topology.

C. Compensation Field Homogeneity Influence on Offset Temperature Dependence

Theoretically, feedback field gradient along the respective sensor should also affect the offset temperature dependence because of the sensor changing its position due to thermal expansion. Another experiment was performed to test this influence. The sensor was placed in a six-layer permalloy magnetic shielding and was equipped with a thermostated box that allowed control over the sensor temperature. Computer-based data-logging system has been assembled, logging the sensor temperature and the three magnetometers' outputs. The switching of feedback extra turns was also manual in this case. The measurement setup is presented in Fig. 5. The magnetic shield is insulated from the thermostated chamber by a Dewar flask. The bifilarly wound heat exchanger placed in the Dewar is cooled/heated by a liquid circulated with a gear pump in a closed loop from an external thermostat. The usage of a Dewar flask ensures that the temperature of the inner layers of the permalloy shielding stays constant and thus there are

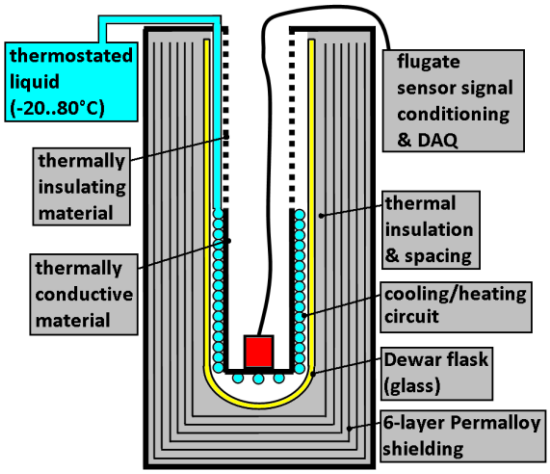

Fig. 5. System for evaluation of offset temperature dependence of the fluxgate sensor.

no thermally induced variations in the residual magnetic field of the shielding.

VI. Results

A. Evaluation of the Field Homogeneity Influence on Orthogonality

During two measurement campaigns, over 38 scalar calibrations were made with various data length (56 positions or 161 positions), each extra-turn combination was measured two or three times. The sensitivities were affected as was expected from the simulation—the extra turns changed the coil constant and thus the sensitivity in appropriate axis, which was compensated in the later calculations.

On the other hand, the behavior of orthogonality angles is more complex. The scalar calibration [4] uses three angles that define the orthogonality of the sensor's intrinsic magnetic coordinate system (α, β, γ correspond to $\nu_{12}\nu_{23}\nu_{13}$ in [4]). The α-angle is basically the error of orthogonality between $x-$ and $y-$axes, and β and γ define the error of z-axis orthogonality with respect to plane defined by $x-$ and y-axes. Although the angle values α, β, and γ come from the mathematical processing of the scalar calibration algorithm, they are usually very stable in time and it has a sense to mention them with up to four decimal places precision. The α-angle is influenced by any combination of the extra turns in $x-$ and y-axes, while the z-axis extra turns have almost no visible effect (Fig. 6). The change is up to $\pm 0.121°$ from its nominal value of $-0.432°$ for combination of extra turns in x- and y- axes, which applies for sensor (02). The α-angle exhibits linear dependence on the nonhomogeneity created by extra turns in x-axis, and unfortunately, the dependency was measured only in three points: negative gradient, no extra gradient, and positive gradient (Fig. 4). Similar dependency was observed also for the nonhomogeneity in y-axis. The β-angle was practically insensitive to variation in y- and z-axes, but there was again a strong linear dependence for x-axis nonhomogeneity. There is almost no change for γ-angle for nonhomogeneity introduced in x- and y-axes, and it stays within $\pm 0.002°$ from its nominal value of $-0.0405°$. But it is linearly sensitive to nonhomogeneity in z-axis. A summary of the influences is shown in Table III.

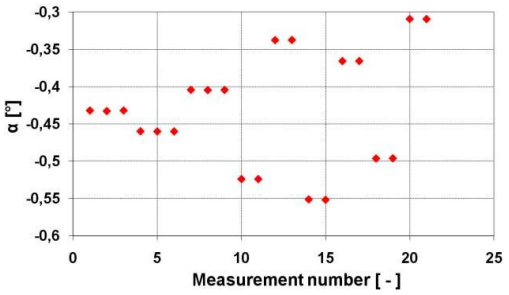

Fig. 6. α-angle versus part of the measurements (no extra turns applied for numbers 1–3; numbers 4–6–turns added in y-axis; numbers 7–9–turns subtracted in y-axis; numbers 10 and 11–turns added in x-axis; numbers 12 and 13–turns subtracted in x-axis; numbers 14–21–various combinations of x- and y-axis turns; and no change in α also for calibrations with only z-axis extra turns). Applies for the triaxial sensor (02).

TABLE III
Extra-Turns Influence on Orthogonality Angles (Does Not Include Their Combinations) for Triaxial Sensor (02)

	α-angle	*β-angle*	*γ-angle*
X-axis	**<±0.0931°**	**<±0.0131°**	<±0.001°
Y-axis	**<±0.0278°**	<±0.001°	<±0.002°
Z-axis	<±0.002°	<±0.002°	**<±0.116°**

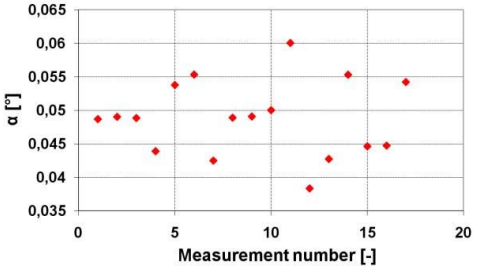

Fig. 7. α-angle versus measurements (no extra turns applied for measurements numbers 1–3; point numbers 4 and 5 are for nonhomogeneity applied in x-axis, numbers 6 and 7 in y-axis, and numbers 8 and 9 in z-axis; and numbers 10–17 are for combinations of nonhomogeneity applied in two axes simultainously). Applies for triaxial sensor (04) with dual-ring-core inner topology.

B. Evaluation of the Field Homogeneity Influence Versus Different Inner Topologies

The results shown in Fig. 7 and Table IV confirms our expectation that more symmetrical inner layout of triaxial sensor (04) should be less affected by the introduced nonhomogeneity. The measured change in orthogonality angles

TABLE IV
EXTRA-TURNS INFLUENCE ON ORTHOGONALITY ANGLES (DOES NOT INCLUDE THEIR COMBINATIONS) FOR TRIAXIAL SENSOR WITH DUAL-RING-CORE CONSTRUCTION (04)

	α-angle	*β-angle*	*γ-angle*
X-axis	<±0.0049°	**<±0.0134°**	<±0.0001°
Y-axis	<±0.0064°	<±0.0003°	<±0.0008°
Z-axis	<±0.0001°	**<±0.02°**	<±0.0003°

TABLE V
NONORTHOGONALITIES OF THE TRIAXIAL SENSORS. SENSOR (02)—FORMER DESIGN, SENSORS (03a) AND (03b)—WITH IMPROVED COMPENSATION FIELD HOMOGENEITY, AND SENSOR (04)—DUAL-RING-CORE INNER DESIGN

Sensor	*α-angle*	*β-angle*	*γ-angle*
(02)	-0.4387°	-0.1830°	-0.0476°
(03a)	0.2973°	-0.0123°	0.1087°
(03b)	0.4260°	-0.0469°	-0.0733°
(04)	0.0468°	-0.2247°	-0.0270°

is practically ten times lower than in the case of sensor (02) listed in Table III.

Three new sensors with the improved compensation coil system field homogeneity have been manufactured. Sensor (03a) uses three ring-core-based fluxgates, very similar in design to the previous generation of sensors that were used for the described measurements of field nonhomogeneity influence. Second sensor (03b) uses race-track core topology, which is supposed to provide lower noise. However, from scalar calibrations results, we did not find any significant improvement on the sensor parameters, mainly orthogonality error, although the results are not statistically relevant (two samples) (Table V). Failure to significantly decrease the orthogonality error by improving the field homogeneity led to the idea of using more symmetric inner topology, and one such is used in triaxial sensor (04).

The value of α-angle for triaxial sensor (03a) is closer to its ideal value (0°), which could indicate the effect of improved feedback field homogeneity. On the other hand, the value is worse for triaxial sensor (03b) that uses race-track fluxgate sensors, which have magnetic cores with higher length than is the diameter of ring cores in (03a). Thus, the race-track sensor cores experience less homogenous compensation field.

The calibration results for triaxial sensor (04) indicate an Improvement, but it is again a statistically unreliable result (currently only one piece manufactured). The high value of β-angle might be caused in this case by error in the mechanical assembly as the 3-D-printed feedback field supports were not ideally precise.

C. Evaluation of the Compensation Field Homogeneity Influence on Offset-Temperature Dependence

The offsets resulting from the scalar calibration were also affected by the introduced nonhomogeneity. For all three axes, temperature dependence has been observed. The temperature of the sensor has risen by ~15 °C during the continuous scalar calibration campaign by the energy dissipated in the excitation circuit and due to the rise of the ambient temperature. The temperature offset coefficient is approximately −0.3 nT/°C.

TABLE VI
SENSOR OFFSETS VERSUS INTRODUCED NONHOMOGENEITY

Sensor / Parameter	*X-axis*	*Y-axis*	*Z-axis*
02- Absolute offset value	-14.5nT	125nT	58nT
02 – Rel. change for ±Grad	±1.5nT	±10nT	±3nT
04- Absolute offset value	116nT	-263nT	-364nT
04 – Rel. change for ±Grad	±2.3nT	±2.2nT	±7nT

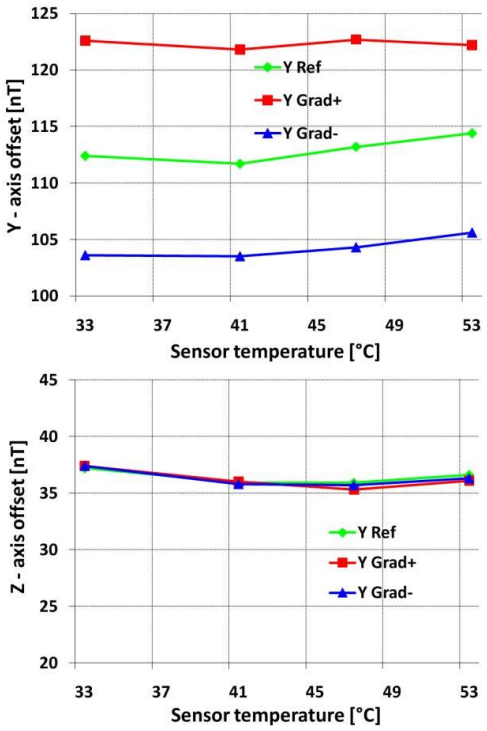

Fig. 8. Offset temperature dependence versus nonhomogeneity in y-axis (Grad+ y-axis extra turns in series, Grad− turns in antiseries, and Ref no extra turns).

After compensation on this effect, the offsets changed according to Table VI. However, the offsets are the least stable calibration parameter and the changes of <2 nT can be considered as noise. The same experiment was repeated also for the triaxial sensor (04) with a symmetrical inner design.

Another evaluation of offset temperature dependence was done in the magnetic shield. The results indicate that an absolute offset value is affected in the axis, where the nonhomogeneity is applied (Fig. 8). There was basically no visible change for the other two axes. The y-axis offset was thus influenced when there was a nonhomogeneity introduced in the y-axis feedback, there was no change on x- or z-axis. We did not find any significant change in temperature dependence of the offset when introducing nonhomogeneity—it might be

well below our measurement error. This was caused mainly by the measurement procedure: to switch between various extra-turns configuration the sensor was repeatedly removed from the magnetic shielding and then placed back. This resulted in uncertainty of the offset caused by remanence in the magnetic shield (below 5 nT) and also by temperature shocks applied to the sensor due to the procedure.

VII. Conclusion

Several experiments and measurements were done to evaluate the influence of the feedback field homogeneity and the inner layout topology on a vectorially compensated triaxial sensor calibration parameters. An interesting feature observed is that the nonorthogonality angles were closer to their ideal zero values for nonideal field homogeneity (in case of the nonsymmetrical three single-axis fluxgate design). With in-series turns applied (creating feedback field nonhomogeneity in x-axis), the α-angle value is closer to zero than for ideal no-extra turns condition. An explanation to this effect might be the sensor asymmetry in the coil system (Fig. 1) combined with the introduced nonhomogeneity. Nevertheless, from the results of calibration of the newly manufactured sensors (03a), (03b), and (04), we assume that the physical topology (inner layout) of the sensors is more important than the compensation field homogeneity at this scale, since we did not find any dependence on offset temperature coefficient with an artificial nonhomogeneity. As long as each individual fluxgate sensor and appropriate feedback coil support material is stable enough, it is possible to use the results from scalar calibration and compensate for offset and even orthogonality temperature dependence.

References

[1] G. Musmann, *Fluxgate Magnetometers for Space Research*. Norderstedt, Germany: Books on Demand, 2010

[2] F. Primdahl and P. A. Jensen, "Compact spherical coil for fluxgate magnetometer vector feedback," *J. Phys. E, Sci. Instrum.*, vol. 15, no. 2, pp. 221–226, 1982.

[3] V. Petrucha and P. Kaspar, "Compact fluxgate sensor with a vector compensation of a measured magnetic field," in *Proc. IEEE Sensors*, Nov. 2010, pp. 1795–1798.

[4] J. M. G. Merayo, P. Brauer, F. Primdahl, J. R. Petersen, and O. V. Nielsen "Scalar calibration of vector magnetometers," *Meas. Sci. Technol.*, vol. 11, no. 2, pp. 120–132, 2000.

[5] V. Petrucha, M. Janošek, and M. A. Azpúrua, "Fluxgate magnetometer vector feedback homogeneity and its influence on sensor parameters," in *Proc. IEEE Int. Instrum. Meas. Technol. Conf. (I2MTC)*, May 2014, pp. 460–463.

[6] H. U. Auster *et al.*, "The THEMIS fluxgate magnetometer," *Space Sci. Rev.*, vol. 141, nos. 1–4, pp. 235–264, 2008.

[7] J. L. Kirschvink, "Uniform magnetic fields and double-wrapped coil systems: Improved techniques for the design of bioelectromagnetic experiments," *Bioelectromagnetics*, vol. 13, no. 5, pp. 401–411, 1992.

[8] M. A. Azpurua, "A semi-analytical method for the design of coil-systems for homogeneous magnetostatic field generation," *Prog. Electromagn. Res. B*, vol. 37, pp. 171–189, 2012.

[9] J. M. G. Merayo, "The vector field magnetometer (VFM) on swarm," in *Proc. ESA's 2nd Swarm Int. Sci. Meeting*, Potsdam, Germany, 2009.

[10] V. Petrucha and P. Kašpar, "Measurement of the temperature dependence of the sensitivity and orthogonality of a triaxial vector magnetometer," *J. Elect. Eng.*, vol. 63. no. 7s, pp. 31–34, 2012.

[11] M. Janošek, J. Vyhnánek, A. Zikmund, P. Butvin, and B. Butvinová, "Effects of core dimensions and manufacturing procedure on fluxgate noise," *Acta Phys. Polonica A*, vol. 126, no. 1, pp. 104–105, 2014.

Vojtěch Petrucha was born in Přerov, Czech Republic, in 1982. He received the M.Sc. degree in measurements and instrumentation and the Ph.D. degree in calibration of magnetometers from the Faculty of Electrical Engineering, Czech Technical University in Prague, Prague, Czech Republic, in 2007 and 2012, respectively.

He is currently a Research Assistant with the Department of Measurement, Faculty of Electrical Engineering, Czech Technical University in Prague. His current research interests include the development and calibration of magnetic field sensors.

Michal Janošek was born in Varnsdorf, Czech Republic, in 1980. He received the M.Sc. degree in measurement and instrumentation from the Faculty of Electrical Engineering, Czech Technical University in Prague, Prague, Czech Republic, in 2007, where he is currently pursuing the Ph.D. degree.

He has co-authored over 20 journal papers. His current research interests include application of magnetic sensors in gradiometers and magnetometers.

Marco A. Azpúrua received the B.Sc. degree in telecommunications engineering from the Universidad Nacional Experimental Politécnica de la Fuerza Armada Nacional, Caracas, Venezuela, in 2008, and the M.Sc. degree in electrical engineering from the Universidad Central de Venezuela, Caracas, in 2013. He is currently pursuing the Ph.D. degree with the Universitat Politècnica de Catalunya, Barcelona, Spain.

He was a Researcher with the Applied Electromagnetics Laboratory, Department of Measurement Technology and Metrology, Electrical and Systems Engineering Center, Instituto de Ingeniería, Caracas. His current research interests include electromagnetic compatibility, antenna and microwave measurement technologies, and estimation of measurement uncertainty in complex systems and validation methods.

7.1.6 refP 6

Petrucha, V., "Low-cost dual-axes fluxgate sensor with a flat field-annealed magnetic core," In: 2016 IEEE Sensors Applications Symposium (SAS 2016) Proceedings. Piscataway: IEEE, 2016. pp. 140-143. ISBN 978-1-4799-7249-4

This paper (even though it is only based on conference proceedings) introduces a concept that proved to be very useful, and it was used consequently in all other fluxgate sensor designs. It presents a construction and method of thermomagnetic treatment of the flat ferromagnetic core, which can significantly improve the properties of the sensor. This design of dual-axes and flat ring-core sensors was later used in multiple instruments developed and sold commercially by MAGLAB group. The author's contribution is 100%.

This full text paper was peer-reviewed at the direction of IEEE Instrumentation and Measurement Society prior to the acceptance and publication.

Low-cost dual-axes fluxgate sensor with a flat field-annealed magnetic core

Vojtěch Petrucha
Faculty of Electrical Engineering
Czech Technical University in Prague
Prague, Czech Republic
petruvoj@fel.cvut.cz

***Abstract*—A low-cost dual-axes fluxgate sensor with a flat ring-shaped core is presented. The amorphous magnetic core material was laser cut from a 20-mm wide ribbon and field annealed prior to sensor assembly. A specific furnace was designed and built to apply the field annealing. A radial magnetic field was created by samarium–cobalt permanent magnets placed directly in the hot volume of the furnace. Perpendicular field anisotropy created by the annealing procedure around the circular core improved the sensor noise properties in the two perpendicular sensitive directions of the dual-axes fluxgate sensor. Results were evaluated in terms of BH-loop measurement, domain observation, and fluxgate sensor noise measurement. The noise of the first prototypes was reduced by annealing from 46 pT/√Hz (400 pT/√Hz for the perpendicular axis) to 24 pT/√Hz at 1 Hz for both axes (axis aligned with original ribbon and perpendicular axis).**

Keywords—fluxgate sensor, magnetic material, field annealing

I. Introduction

Fluxgate sensors of a magnetic field are widely used in many scientific and industrial applications. The most significant applications are Earth's magnetic field exploration, compassing, underground drilling navigation, geological prospection, and metal detection. Their sensitivity and time-temperature stability is superior to other sensors, like AMR or Hall effect sensors [1]. Only SQUID sensors produce less noise, but these require cryogenic conditions for operation. The typical drawback of fluxgate sensors and fluxgate magnetometers is the high cost when compared to other types of devices, especially for low-noise versions (<20 pT/√Hz at 1 Hz) having good time and temperature offset stability (<1 nT/°C). Complicated mechanical structure, winding or assembling of multiple coils, magnetic core treatments, precise materials used, and specific tuning all contribute to the increase in cost. Different methods can reduce the cost, for example, using printed circuit board (PCB) technology to manufacture the sensors [2]. In this case the whole sensor can be supplied by a PCB manufacturer, but there are limitations. The PCB manufacturing restrictions limit the amount of turns applied both for excitation and pick-up/compensation windings. An inappropriate core saturation can lead to higher noise. A small number of turns of the pick-up coil limits the sensitivity and makes the second harmonic tuning of the output signal more difficult. Fluxgate sensors are often operated as null detectors in a closed loop, and a low compensation coil constant means that a high compensation current is needed. A compromise might be to use construction material supplied by the PCB manufacturer (e.g., FR4 is cheap and has a relatively low coefficient of linear thermal expansion ~15 ppm in a plane) and to have a professional coil manufacturer do the winding. In order to need only two sensors for tri-axial magnetometer construction, it is convenient to make the sensor as "dual-axes." The magnetic core might be produced by laser cutting (laser with ultra-short pulses) or wet etched. Both procedures are often available through PCB manufacturers. The problem is with magnetic anisotropy of the material. Regardless of whether we produce the flat ring core from as-cast or annealed ribbon, there will be favorable anisotropy (natural, developed during casting or induced during annealing) only for one axis. This will limit the noise properties of the sensor for the second axis because typically perpendicular field anisotropy reduces the noise [3]. A custom-made annealing furnace was developed and successfully tested to overcome this issue. The flat ring core was selected in front of the tape-wound spiral ring core presented in [3] as it can be easily manufactured by the mentioned techniques and its annealing and assembly is much easier and more repeatable. Other types of fluxgate sensors could also be used, including a Vacquier type with a dual rod core, sensors with a racetrack-shaped magnetic core [4], [5], or orthogonal fluxgates. However, the classic ring-core fluxgate is best suited for the low-cost version as its symmetry simplifies manufacturing and core annealing. The benefit of having two perpendicular sensitive axes in one sensor is also significant.

II. Flat Fluxgate Ring-core Annealing

To create the desired magnetic anisotropy, a radial field had to be applied while keeping the magnetic material slightly below its Curie temperature (approximately 260°C for Vitrokov 8116, supplied by Dr. Butvin from the Institute of Physics, Slovak Academy of Sciences). Two ways to create the radial field were considered. A cylindrical permanent magnet with suitable dimensions and temperature resistance was the first option. Samarium-cobalt (SmCo) permanent magnets offered high temperature resistance (Curie temperature of 700–800°C, operating temperature up to 350°C). The finite element method (FEM, Ansys Magnetostatic) was used to validate the intended setup (see Fig. 1). The simulation proved that the magnetic material is

978-1-4799-7250-0/16/$31.00 ©2016 IEEE

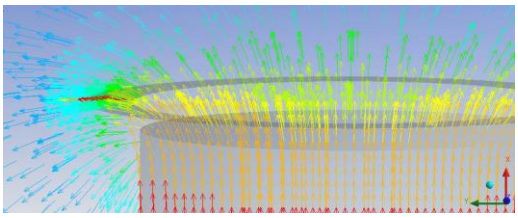

Fig.1 FEM model of the magnetic core annealing setup. A cylindrical SmCo permanent magnet is shown in the lower part of the image and a thin amorphous alloy flat ring core is 1 mm above it. The FEM model indicated that the magnetic material is well saturated in the radial direction by the permanent magnet (B > 0.57 T).

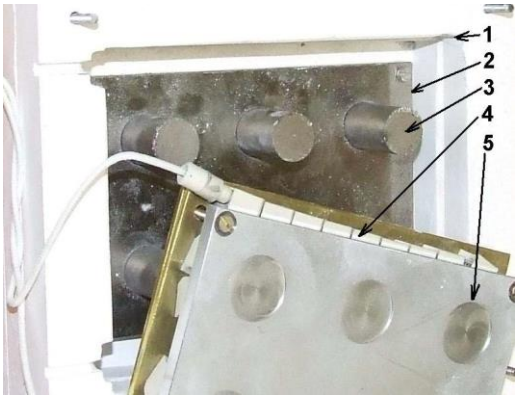

Fig. 2 Photograph of the annealing furnace. "1" is the thermal insulation made of Duratec 750 (bottom, side walls, and top). "2" is the steel plate that fixes the permanent magnets and acts as a yoke in the bottom part of the furnace. "3": Six SmCo permanent magnets generate the magnetic field. "4": Heating is provided by ceramic elements with resistive wire. "5": A hard-chromed CuCr alloy plate equalizes the temperature and fixes the annealed ring cores in the desired center position.

fully saturated when positioned near the edge of the magnet (B > 0.57 T). There was a significant field component perpendicular to the plane of the ring, but this should not have had a significant effect due to the high demagnetization in that direction.

A thin flat coil of several turns (three to six) carrying a high current was the second option. Such a circular coil (diameter identical to the core) placed directly onto the ring core would create the same radial field as the permanent magnet (in fact a better field as there is no out-of-plane component). However, practical realization was considered problematic. First, a wire capable of operating at a high temperature for a long time was not available. Second, the core would be attracted to the coil and thus not in a good contact with the heat exchanger, making it difficult to control the material temperature during the annealing process.

Construction of the annealing furnace is shown in Fig. 2. Permanent magnets (15 mm diameter, 25 mm length) were fixed with a bottom steel plate, which also served as a magnetic yoke. Ceramic elements with resistive wire provided the heating. The topology of the heating elements was specifically designed to cancel out the magnetic field generated by the heating current. The vertical distance between the magnets and the annealed cores was 1 mm as best value estimated by the FEM simulation. The furnace temperature was controlled with a standard industrial PID controller, using a K-type thermocouple for feedback. No protection atmosphere was used as the annealing temperature was low and the Vitrokov material is resistant against oxidation due to its chromium content.

III. Results

A) BH-loop measurement

Twelve cores were annealed, six of them with an annealing time of 30 minutes and six for 60 minutes; the total annealing time was 90 and 120 minutes, respectively (20 minutes heating-up, 40 minutes cooling). Due to the attraction of the permanent magnet's magnetic force, the cores were fixed securely at the desired places during the annealing. Three methods were used to evaluate the results: BH loop measurement, magnetic domain observation, and fluxgate sensor noise measurement. The BH loops of the as-cast Vitrokov 8116 and the two field-annealed samples are presented in Fig. 3. During the measurement, the cores were embedded in supports (made of FR4 PCB manufacturing material), which provided mechanical rigidity, making it possible to wind the primary and secondary coils. The same supports were later used to wind the excitation windings of the fluxgate sensor. The BH-loops were measured with a simple but effective proprietary system. A data acquisition card (National Instruments PCI-6154) with DAC and an external amplifier was used to generate the excitation signal (40 Hz), and two simultaneously sampled ADCs measured the primary current and voltage induced in the secondary winding. The acquired signals were processed using a custom LabView program. The BH-loop of the "as-cast" material was measured with a small secondary coil (7 mm length) in two parts of the core circumference (90° apart). "Long. direction" was aligned with the original ribbon (section was situated close to the ribbon edge). "Perpen. direction" was shifted by 90° and was in the center of the 20-mm-wide tape. The tape exhibited relatively small coercivity (3 A/m) and moderate permeability (~20000). The BH-loop was slightly different for the longitudinal and perpendicular direction, suggesting that some anisotropy is created directly during the tape manufacturing process. The BH-loop from the longitudinal part indicated higher anisotropy, which corresponded to the noise measurements (see Table 1). The effect of induced anisotropy (decreased permeability) was visible on the annealed samples. The difference in BH-loops for the 30- and 60-minute annealing times was not great, but the difference in fluxgate sensor noise was significant. The coercivity decreased to about 2.5 A/m for both samples. Perpendicular field annealing is used to induce a magnetization hard axis along the direction of the ring-core circumference. Magnetization by the fluxgate sensor excitation current is then provided by domain rotation rather than movements; the former makes less noise [6]. Longer annealing times are considered during the following experiments. There should be some optimal anisotropy at

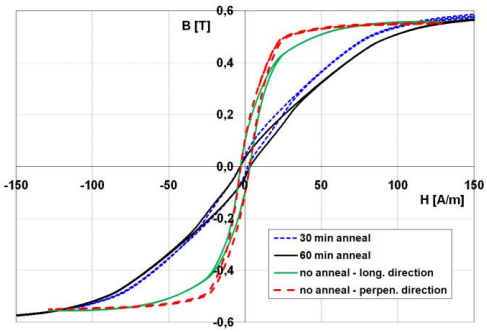

Fig. 3 BH-loops of the magnetic core materials. The effect of perpendicular anisotropy created during the annealing process is clearly visible (annealing temperature 260°C, rate of heating/cooling is approximately 12/5°C/min).

which point the noise will be minimized but the excitation current needed to securely oversaturate the core material will not be excessively large. The optimal material for application in the fluxgate sensors would have a linear BH-loop, with low saturation induction, very low coercivity, and approaching saturation at a low magnetizing field, e.g., see material (a) in Fig.10 in [7]. A high-temperature pre-annealing phase is also considered. The pre-annealing could help to release mechanical stress coming from ribbon straightening (the ribbon is typically distributed wound on some limited diameter). This option was not tested because of the permanent-magnet maximum operation temperature limitation (350°C). However, the pre-annealing/annealing process can be split and the pre-annealing done in a furnace, which does not have this limitation.

B) Magnetic domain observations

Magnetic domain observations were made to check the results of the annealing process. Kerr-effect microscopy was not available so we used standard scanning electron microscope (SEM) equipped with a custom detector and tiltable sample holder. This setup allowed visualizing the magnetic domains by tilting the sample with respect to the electron beam and using the Lorentz force effect [8].

Unfortunately, the contrast provided by this method was weak; the tape surface was not perfectly flat, and thus the magnetic domain effect was a degraded by also observing the surface topology. Nevertheless, the observation was useful. Observation without the magnetic contrast also revealed that the laser cutting process could be improved as there was a slight burn on several edges (possibly unwanted material crystallization), see Fig. 4. Magnetic domains in the radial direction were visible, and thus we confirmed that the magnetic field of the permanent magnet had the desired effect (see Fig. 5). The domains observed were not perfectly regular, which indicated improvement potential by adjusting the annealing conditions (mainly the annealing time, temperature, and cooling rate).

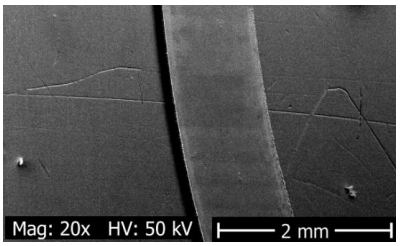

Fig. 4 SEM image of the core. The width of the ribbon is 1.75 mm (not to scale because the sample is tilted to get the magnetic contrast). The core was laser cut from a wide ribbon; there is a slight burn visible on the inner edge.

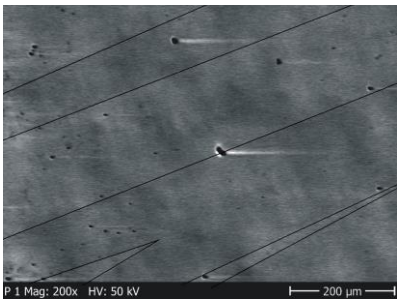

Fig. 5 Magnified center area from Fig.4. The domain observation method used (magnetic contrast by tilting the sample with respect to the electron beam in SEM) provided a weak contrast, so the domain edges are highlighted (sample annealed for 60 minutes is shown).

C) Fluxgate noise measurement

Three fluxgate sensors were constructed. The first had an as-cast core, the second core was annealed for 30 minutes, and the third core was annealed for 60 minutes. The cores were fixed to supports made by the PCB manufacturer from FR4 laminate by high performance acrylic conformal coating. The excitation winding had 212 turns by 0.2 mm CuL wire. The setup was then embedded to another improvised support, and the two pick-up windings were wound, each with 200 turns by 0.2 mm CuL wire (see Fig. 6).

Noise was measured with the following setup: excitation was provided by a custom electric circuit with a mosfet H-bridge driven by a microcontroller. There was a capacitor and a resistor in a series with the excitation coil to create pulsed excitation of 0.7 A_{P-P} (at 10 kHz). This corresponded to 2740 A/m (peak-peak) of a magnetizing field (1). The second harmonic signal tuned by a parallel capacitor to resonance was measured by a lock-in amplifier (SR-830) referenced by the microcontroller, and the data were processed by custom NI LabView software (see Fig. 7). The sensor was placed in six-layered Permalloy magnetic shielding during the measurements. The noise measurement results are summarized in Table 1. The fluxgate sensor sensitive axis aligned with the original tape longitudinal direction was marked “A-direction,” and perpendicular axis was marked “B-direction.” There was a large difference in noise for the as-cast sample, which again suggested that some anisotropy was created during the ribbon manufacturing process.

Fig. 6 Construction of the dual-axis sensor is simple: magnetic core (left) is fixed in a fiberglass laminate support, and the excitation winding is made (center). The core assembly is then placed into another FR4 laminate support, and the two pick-up (compensation) coils are wound.

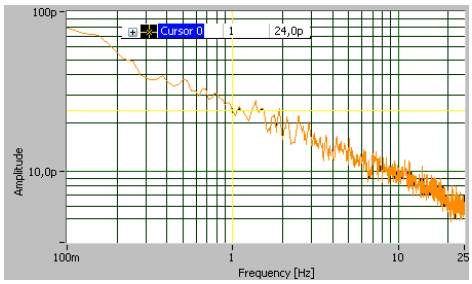

Fig. 7 Noise measurement of the sample annealed for 60 minutes, A-direction, excitation 2740 A/m (peak–peak).

The sample annealed for 30 minutes provided strange results. The "B-direction" noise was reduced significantly, but the "A-direction" noise slightly increased. Measurements of more samples would be needed to improve statistical credibility. The sample annealed for 60 minutes provided the lowest noise that was the same for both directions (sensitive axes).

TABLE I. NOISE PERFORMANCE OF THE SENSORS

Sample	Noise, A-direction	Noise, B-direction
As-cast	46 pT/√Hz	400 pT/√Hz
Ann. 30 min	54 pT/√Hz	35 pT/√Hz
Ann. 60 min	24 pT/√Hz	24 pT/√Hz

$$H = \frac{N.I}{l} \qquad (1)$$

The manufacturing costs of the sensor are given by the material costs and processing costs. All the manufacturing operations, with the exception of annealing, can be done on a large scale by the PCB and coil manufacturers. The annealing procedure would have to be modified or just the furnace significantly scaled up to allow large-scale core annealing (possible with the current design). With respect to previous experience, the costs for 100 pieces might be 10–20 USD/piece (sole sensor without electronics). The comparison with other devices is difficult as they differ by dimensions, noise, power requirements, measurement range, and the fact that fluxgates are typically supplied only with dedicated analog or digital electronics. HMC1021, an AMR-based sensor with 5–10 times higher noise and a ±600 μT measurement range, but much smaller dimensions, is available for 5 USD. Fluxgate sensors (with dedicated electronics) supplied by Stefan Mayer instruments have roughly the same dimensions; the noise is <20 pT/√Hz (FL1-100), 150 pT/√Hz (FLC-100), measurement range ±100 μT, and price 233 and 40 USD (at 100 pieces). The chip-scale fluxgate recently introduced by Texas Instruments (DRV425) has noise of 3.5 nT/√Hz at 1 Hz, range of ±2 mT, and a price of 5.3 USD.

IV. CONCLUSION

The fluxgate sensor presented in this paper is relatively easy and cheap to manufacture, while its noise properties are a compromise between the sensor's dimensions, excitation power and core design, material, and treatment. The presented magnetic core annealing would definitely increase the price and complexity of the manufacturing process, but as indicated by the results, it would be very useful in terms of sensor noise. The noise value of 24 $pT_{RMS}/\sqrt{Hz}$ at 1 Hz can be sufficient for a wide variety of applications (e.g., compassing and navigation). Commercially available devices have noise in a range of 6–200 pT_{RMS} [9]. Nevertheless, there are several possible ways to improve the noise. Modify the core annealing procedure or use a completely different material (e.g., Metglas 2714 or Vitrovac 6025), use multiple slightly separated cores, or use a different core fixation. Several parameters still need to be measured, mainly the time and temperature (offset) stability. The linearity of the sensor, mainly the part caused by the cross-field effect [10], will also be studied.

Acknowledgments

The presented work has been supported by the Czech Science Foundation, grant No. 13-39088P. The magnetic core samples were prepared in the scope of the TACR project TE02000202. The author expresses his thanks to Karel Závěta and Karel Jurek from the Institute of Physics of the Czech Academy of Sciences for the visualization of magnetic domains of the fluxgate core samples.

References

[1] P. Ripka and M. Janosek, "Advances in magnetic field sensors, *IEEE Sensors Journal*," vol. 10, no. 6, pp. 1108–1116, June 2010.

[2] M. Janosek and P. Ripka, "PCB sensors in fluxgate magnetometer with controlled excitation," *Sensors and Actuators* A 151, pp. 141–144, 2009

[3] P. Butvin *et al.*, "Field annealed closed-path fluxgate sensors made of metallic-glass ribbons," *Sensors and Actuators* A: Physical, vol. 184, pp. 72–77, Sep. 2012.

[4] R. Piel, F. Ludwig, and M. Schilling, "Noise optimization of racetrack fluxgate sensors," *Sensor Letters*, vol. 7, pp. 1–5, 2009.

[5] D. Ruhmer, P. Shanmuganathan, F. Ludwig, and M. Schilling, "Spatial and field resolution of wire-wound fluxgates in magnetic dipole fields," *Sensors and Actuators* A 173, pp. 30–35, 2012.

[6] O. V. Nielsen *et al.*, "Analysis of a fluxgate magnetometer based on metallic glass sensors," *Meas. Sci. Technol.* vol. 2 , pp. 435-440, 1991.

[7] G. Herzer, "Modern soft magnets: Amorphous and nanocrystalline materials," *Acta Materialia*, vol. 61, pp. 718–734, 2013.

[8] K. Zaveta, O.V. Nielsen, and K. Jurek, "A domain study of magnetization processes in a stress-annealed metallic glass ribbons for fluxgate sensors," *Journal of Magnetism and Magnetic Materials,* vol. 117, pp. 61–68, 1992.

[9] V. Korepanov and A. Marusenkov, "Flux-gate magnetometers design peculiarities," *Surv Geophys.,* vol. 33, pp.1059–1079, 2012.

[10] M. Janosek, M. Butta, and P. Ripka, "Two sources of cross-field error in racetrack fluxgate," *Journal of Applied Physics,* vol. 107, 09E713, pp. 1–3, 2010.

7.1.7 refP 7

Novotný, D.; Petrucha, V., "High Dynamic Range Digital Fluxgate Magnetometer," In: 2020 IEEE SENSORS Proceedings. Orlando, Florida: IEEE Sensors Council, 2020. ISSN 2168-9229. ISBN 978-1-7281-6801-2

This paper explores the construction of a fluxgate magnetometer with digital-signal processing built on a small commercial FPGA. The concept of digital feedback is very similar to the concept used extensively on AMR magnetometers with a microcontroller, but this time the FPGA had to be used as the fluxgate excitation frequency is at more than an-order-of-magnitude higher frequency and, thus, the microcontroller is not able to make all the necessary calculations in real-time. Preliminary results were interesting as presented in the proceedings paper, but D. Novotný later chose to concentrate on the development of the AMR magnetometers. The author's contribution is 30% - he prepared the fluxgate sensors and helped with the electronics design and measurements.

High Dynamic Range Digital Fluxgate Magnetometer

David Novotný, Vojtěch Petrucha
Dept. of Measurement, Faculty of Electrical Engineering, Czech Technical University in Prague, Czech Republic
novotd12@fel.cvut.cz

***Abstract*— In this paper, we present an advanced fully digital solution of a fluxgate magnetometer with both demodulation and compensation carried out by a low-cost field programmable gate array (FPGA). For feedback operation, we avoid using a costly precise digital-to-analog converter, instead employing an FPGA to generate a hybrid pulse width modulation sigma-delta signal. Even with only a few additional components to process such signals, we were able to achieve excellent linearity, noise, and stability, as supported by measurements. On the front-end side only one pick-up signal preamplifier is necessary, greatly reducing the number of analog circuits needed. This can be an advantage in radiation-hazard sites like space missions, as there are fewer radiation-susceptible parts that can degrade. We provide a short description of the entire setup—electronics, fluxgate sensor construction, and final power budget—and a parameter summary in the conclusion.**

Keywords—fluxgate magnetometer, digital processing, FPGA, PWM DAC, feedback, radiation, tolerant, space, CubeSat

I. INTRODUCTION

Fluxgate sensors and magnetometers are applied in many areas where precise measurement of weak magnetic fields is desired, such as geological surveys [1], navigation [2], and scientific experiments [3]. Traditionally, in parallel fluxgates the second harmonic output signal from pickup winding is processed using amplifiers, band-pass filters, synchronous demodulation, and integration and often fed back to the sensor to compensate the measured magnetic field. This feedback operation then significantly improves parameters like linearity and stability [4]. The analog signal processing chain requires precise analog components that are expensive and sensitive to environmental conditions. Once digital electronic circuits became suitable for this task, efforts have been made to carry out ideally all or at least some of the signal processing using exclusively digital circuits. This should lead to magnetometers that are less susceptible to temperature changes and radiation, simpler, and, thus, less expensive. Analog signal processing with subsequent high-resolution digitalization is typically still used for applications demanding a very high dynamic range (>140 dB) but, as digital circuits become more powerful, the digital approach is quickly catching up.

In 1993 Primdahl et al. [5] digitized the broadband fluxgate output signal using an analog-to-digital converter (ADC) with just an 8-bit resolution to obtain a noise level of 1 nT for a 100 Sa/s data rate. Since then, many other researchers have implemented various topologies and techniques to obtain better parameters.

Auster [6] presented synchronous sampling at twice the signal frequency using ADC, field programmable gate array (FPGA) and digital-to-analog (DAC) topology for space research and geomagnetic applications, the principle was later used in the ROMAP instrument [7] and THEMIS fluxgate magnetometer [8]. A different approach is found in [9], which uses relaxation time measurement via digital counters. Feintuch et al. [10] patented a digital fluxgate magnetometer with multiplication of digitized reference and pick-up signals and further processing (infinite impulse response [IIR] filter and decimation). Korepanov and Berkman [11] analyzed the structure of analog and digital magnetometers and summarized the theoretical limits of their operation. Pedersen [12] presented a concept of a digital fluxgate magnetometer for the Astrid-2 space mission based on DSP and 18-bit DAC for feedback, which limited performance. Later, an application-specific integrated circuit (ASIC) was designed, implementing a similar principle with an analog front-end and digital parts [13,14]. O'Brien [15] designed a radiation-tolerant digital fluxgate magnetometer with second order $\Delta\sum$ modulator implemented in FPGA with good noise properties (10 pT/√Hz) but with an extremely limited measurement range of ±327 nT. Another approach by Zhi et al. [16] involves using two 16-bit DACs to supply the V/I feedback driver. Although the presented noise is low (7 pT/√Hz) with ±65 μT range, there is no detailed information concerning the linearity that might be affected by the dual DAC summing circuit.

In this paper, we present the development of a fluxgate magnetometer with digital signal processing with high dynamic range and excellent linearity and noise. As noted above, the properties are influenced by the DAC used for the compensation feedback. Based on previous good experience with pulse width modulation (PWM)-based DAC [17], we decided to use this technique together with precise 16-bit ADC at the input and state-of-the-art, low-power FPGA, because the data processing would not work at the desired rate (200–400 kHz) within a microcontroller, as was possible for the anisotropic magneto-resistance version flipped at 216 Hz.

II. DESCRIPTION OF OPERATION

The fluxgate magnetic core is excited by MOSFET bridge with resonant capacitor in series connection to an excitation coil for better power efficiency. The induced voltage from the pickup coil (second harmonic of excitation signal) is amplified by an AC-coupled differential amplifier that also acts as a low-pass filter and ADC driver. The signal is then converted to digital domain using a fast successive-approximation ADC (AD4005). Conversions are triggered by FPGA synchronously with an excitation unit (200 kSa/s). The digitized signal is then demodulated by a synchronous demodulator (±1 multiplication). After demodulation, the unwanted part of the frequency spectrum is removed by a

978-1-7281-6801-2/20/$31.00 ©2020 IEEE

synchronous moving average (MA) filter. In the case of open-loop operation, this signal is decimated to a lower sample rate and streamed via a universal asynchronous receiver-transmitter (UART) link. For closed-loop operation, the demodulated and filtered signal is fed to a digital integrator. The output of the integrator is multiplied by a constant to obtain proper response and fed to the PWM module as a duty-cycle value. The PWM value is filtered by another moving average filter and sent through a serial link in closed-loop mode as an output variable (because it is proportional to the compensation magnetic field, which is the measured quantity). A simplified diagram is presented in Fig. 1, and photograph of the electronics is presented in Fig. 2.

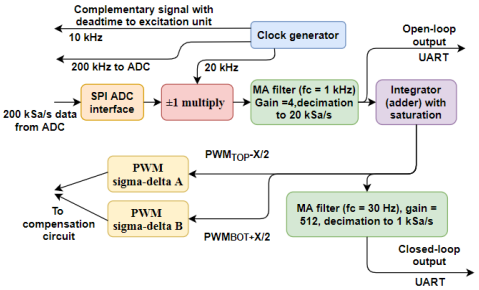

Fig. 1. Block diagram of digital signal processing on FPGA.

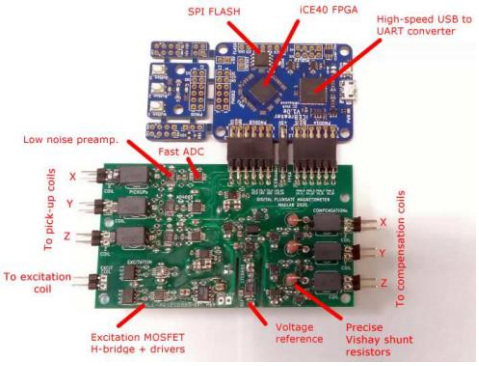

Fig. 2. Photo of three-axis fluxgate magnetometer's electronics (blue board is the iCEBreaker kit; green board is the electronics of the developed magnetometer on which this paper reports).

A. Hybrid PWM delta-sigma DAC

To achieve higher resolution at the same carrier frequency, PWM is improved by the delta-sigma principle. The least significant bit of PWM is modulated to fine trim its duty-cycle mean value. The base frequency of FPGA is 96 MHz; for a 15-bit PWM, this means a maximum frequency of ~3 kHz, while for a 20-bit PWM it is only ~93 Hz. With this hybrid scheme, it is possible to obtain 20-bit resolution at 3 kHz carrier frequency. The attenuation factor at 93 Hz (the worst-case delta-sigma cycle frequency) can then be 2^{15} = 32768 times lower than using 20-bit PWM without delta-sigma.

The DAC hardware is described in the schematic in Fig. 3. Two PWM signals from the FPGA drive analog multiplexers that create precise-amplitude PWM out of voltage reference (LTC6655-4.096V). The signals are then filtered with second order RC low pass filters and fed to voltage to a current converter.

The main challenge was that the analog multiplexer could not be heavily loaded because of its nonlinear R_{ON} resistance versus input voltage behavior that otherwise causes nonlinearity of the entire DAC. On the other hand, high resistance would lead to high Johnson-Nyquist noise. From measurement (Fig. 4), a compromise was found to be 100 kΩ of minimum load resistance.

Rail-to-rail operational amplifiers are another practical design problem, as low-noise versions often have nonlinear behavior of offset voltage/bias current with common-mode voltage that worsens the resulting linearity. To ensure the best performance, it was necessary to keep common mode voltage as close to half the supply voltage as possible, which was obtained by a differential DAC design (using two channels [A, B] of the PWM with an opposite duty cycle to create the resulting signal). This design also suppresses phase-jitter in the main clock by affecting both channels' duty cycles simultaneously. This is subtracted by this design; the residual nonlinear behavior of the loaded multiplexer DAC is also decreased (Fig. 5).

The noise of the current source was measured with an Agilent 35670A dynamic signal analyzer and found to be approx. 400 $pA_{RMS}/\sqrt{Hz}$ at 1 Hz, within ±7.5 mA full-scale range. In relative terms, this is noise of 0.03 $ppm_{RMS}/\sqrt{Hz}$ at 1 Hz. In a magnetometer with a range of ±75 μT, this relative noise will cause additional noise of 4 $pT_{RMS}/\sqrt{Hz}$ at 1 Hz.

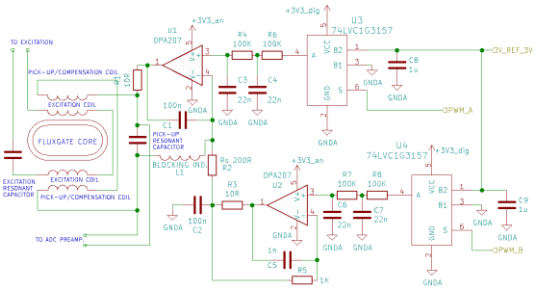

Fig. 3. Scheme of current source based on differential PWM design.

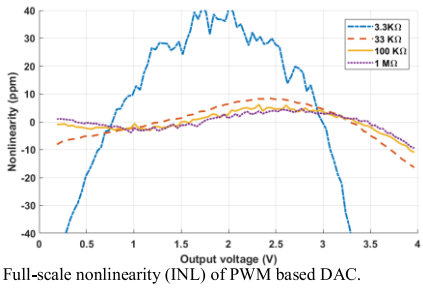

Fig. 4. Full-scale nonlinearity (INL) of PWM based DAC.

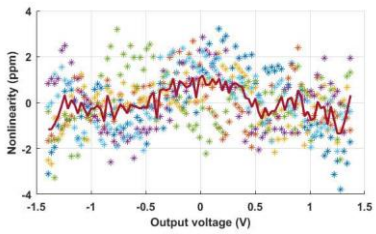

Fig. 5. Full-scale nonlinearity of differential PWM based DAC.

B. Digital demodulation

For simplicity in initial testing, demodulation was performed by ±1 multiplication of acquired signal at twice the excitation frequency. This synchronization signal can be phase-shifted against excitation signal. For best performance, the phase should be adjusted for the highest mean value of demodulated signal when fluxgate is measuring a non-zero magnetic field.

C. Power consumption

Power consumption of each electronic section was measured separately (measurements include losses on low dropout regulators, common 5V input voltage for the entire magnetometer). The compensation circuit has 32 mW consumption (single channel, no compensation current, 68 mW when compensating for full 75 μT). Power consumption of sensor excitation is 320 mW. Input circuit (ADC + amplifier/driver) requires 200 mW/channel. FPGA + UART interface takes 250 mW. Total power drawing is 800 mW for one axis; it should thus be 1.2 W for the tri-axial version.

D. Sensor head

Fluxgate sensor (Figs. 6,7) has a race-track core (17.4 mm long) laser-cut from highly permeable soft magnetic material Vitrovac 6025. The magnetic core was field annealed to decrease sensor noise [18]. Support for compensation winding and the core is CNC milled out of FR4 material (glass-reinforced epoxy laminate). For the tri-axial magnetometer, sensors are mounted on a low thermal expansion composite plastic cube, which is CNC milled with very high precision so that the combination of four mounting holes for each sensor leads to a precise level of orthogonality. The excitation current was measured to be 800 mA_{p-p}. We also tested higher excitation current but obtained no additional improvements in noise.

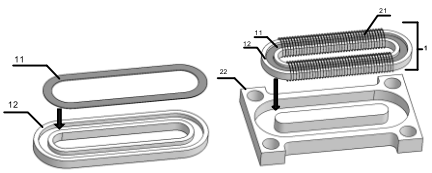

Fig. 6. Drawings of fluxgate sensor construction (11-magnetic core, 12-protection case for core, 22-support for compensation coil, 21-excitation winding; pick-up winding not shown).

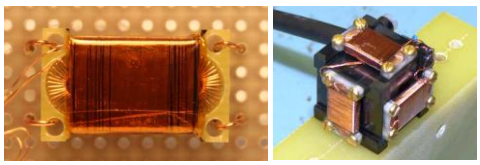

Fig. 7. Photos of fluxgate sensor heads (left-single axis; right-triaxial).

III. MEASURED PARAMETERS

A. Linearity measurement

Measurement of transfer function linearity was performed by sweeping the PWM value throughout its range while sending the actual value by serial link to a PC. The current output of DAC was connected to a precise and stable 120 Ω shunt resistor while an HP34401A multi-meter measured the voltage drop. The HP34401A was also connected to the PC via serial link; LabView-based software saved incoming values (actual PWM and measured voltage) to file for post-processing in MATLAB, where linear fit was subtracted from transfer function and a nonlinearity curve was obtained (Fig. 8). The same technique has also been used in previous linearity measurements (Figs. 4,5) but directly measured voltage without a shunt resistor.

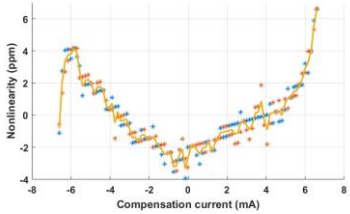

Fig. 8. Full-scale nonlinearity of current source based on differential PWM.

B. Noise measurement

In the first step of noise measurement, a lock-in amplifier SR830 was used instead of ADC and demodulation on FPGA. The sensor was excited by an excitation unit controlled by FPGA which also generated a synchronization signal. With the same excitation waveform and pickup resonant capacitor, the signal was then demodulated by FPGA (in open-loop operation with ±5 μT range). A comparison of the noise spectrum densities appears in Fig. 9. The slightly higher noise of the FPGA demodulated signal is caused by the noise floor of input differential amplifier (based on LTC6362).

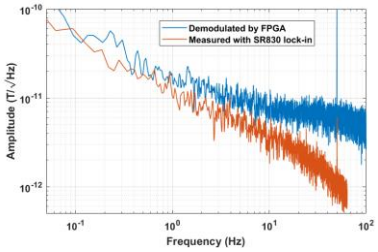

Fig. 9. Spectrum noise density of demodulated fluxgate comparison.

IV. CONCLUSION

The results presented in this paper suggest that even a simple PWM DAC approach can lead to a very precise current source. The presented prototype achieved key parameters of 20-bit resolution, ±5 ppm linearity, and 0.03 ppm/√Hz @ 1 Hz noise; it also has good preconditions for high time and temperature stability (as no voltage dividers or summing nodes can drift with temperature, only with the voltage reference and current sense resistor).

When combined with digital demodulation of the pickup signal, we obtain a fully digital solution of a fluxgate magnetometer at a very low cost in electronics for such a precise instrument. As a next step, the tri-axial version will be tested and optimized for low power consumption. We are also planning to perform measurement of temperature drifts and testing radiation effects by Co^{60} gamma-source.

ACKNOWLEDGMENT

This work was supported by a Student Grant Competition (SGS) at CTU in Prague (No. SGS19/177/OHK3/3T13).

REFERENCES

[1] B. Gavazzi, P. Le Maire, J. Mercier de Lépinay, P. Calou, and M. Munschy, "Fluxgate three-component magnetometers for cost-effective ground, UAV and airborne magnetic surveys for industrial and academic geoscience applications and comparison with current industrial standards through case studies," Geomech. Energy. Envir., vol. 20, Article 100117, December 2019, https://doi.org/10.1016/j.gete.2019.03.002.

[2] J. Věelák, P. Ripka, and A. Zikmund, "Precise magnetic sensors for navigation and prospection," J. Supercon. Nov. Magn., vol. 28, no. 3, pp. 1077–1080, 2015.

[3] C. T. Russell, B. J. Anderson, W. Baumjohann, K. R. Bromund, D. Dearborn, D. Fischer et al., "The magnetospheric multiscale magnetometers," Space Sci. Rev., vol. 199, nos. 1–4, pp. 189–256, March 2016.

[4] P. Ripka, Magnetic Sensors and Magnetometers, Boston: Artech House Remote Sensing Library, 2001.

[5] F. Primdahl, B. Hernando, J. R. Petersen, and O. V. Nielsen, "Digital detection of the flux-gate sensor output signal," Meas. Sci. Technol., vol. 5, no. 4, pp. 359–362, April 1994.

[6] H. U. Auster, A. Lichopoj, J. Rustenbach, H. Bitterlich, K. H. Fornacon, O. Hillenmaier et al., "Concept and first results of a digital fluxgate magnetometer," Meas. Sci. Technol., vol. 6, no. 5, pp. 477–481, May 1995.

[7] H.U. Auster, I. Apathy, G. Berghofer, A. Remizov, R. Roll, K. H. Fornacon et al., "ROMAP: Rosetta Magnetometer and Plasma Monitor," Space Sci. Rev., vol. 128, pp. 221–240, 2007.

[8] H.U. Auster et al, "The THEMIS Fluxgate Magnetometer," Space Sci. Rev., vol. 141, pp. 235–264, 2008.

[9] J. Blazek, J. Hudak, and D. Praslicka, "A relax type magnetic fluxgate sensor," Sens. Actuators A Phys., vol. 59, pp. 287–291, 1997.

[10] Feintuch et al., US Patent 5652512, July 29, 1997.

[11] V. Korepanov and R. Berkman, "Digital flux-gate magnetometer structural analysis," Meas. Sci. Technol., vol. 10, no. 8, 734–737, August 1999.

[12] E. B. Pedersen, F. Primdahl, J. R. Petersen, J. M. G. Merayo, P. Brauer, and O. V. Nielsen, "Digital fluxgate magnetometer for the Astrid-2 satellite," Meas. Sci. Technol., vol. 10, no. 11, pp. N124–N129, November 1999.

[13] W. Magnes, D. Pierce, A. Valavanoglou, J. Means, W. Baumjohann, C. T. Russell, K. Schwingenschuh, and G. Graber, "A sigma–delta fluxgate magnetometer for space applications," Meas. Sci. Technol. vol. 14, no. 11, pp. 1003–1012, July 2003.

[14] W. Magnes, M. Oberst, A. Valavanoglou, H. Hauer, C. Hagen, I. Jernej et al., "Highly integrated front-end electronics for spaceborne fluxgate sensors," Meas. Sci. Technol., vol. 19, no. 11, Article 115801, November 2008, https://doi.org/10.1088/0957-0233/19/11/115801.

[15] H O'Brien, P. Brown, T. Beek, C. Carr, E. Cupido, and T. Oddy, "A radiation tolerant digital fluxgate magnetometer," Meas. Sci. Technol., vol. 18, no. 11, pp. 3645–3650, November 2007.

[16] M. Zhi, L. Tang, X. Cao, and D. Quao, "Digital fluxgate magnetometer for detection of microvibration," J. Sens., vol. 2017, Article 6453243, 2017, https://doi.org/10.1155/2017/6453243.

[17] D. Novotný, V. Petrucha, and M. Janosek, "A digitally compensated AMR magnetometer," IEEE T. Mag., vol. 55, no. 1, pp. 1–5, January 2018.

[18] Petrucha, V. "Low-cost dual-axes fluxgate sensor with a flat field-annealed magnetic core." In 2016 IEEE Sensors Applications Symposium (SAS), pp. 1-4, IEEE, 2016, https://doi.org/10.1109/TMAG.2018.2873235.

7.1.8 refP 8

Petrucha, V.; Butta, M., "Race-track fluxgate sensor scaling versus noise," In: IEEE SENSORS 2021 proceeding. Irvine, CA: IEEE Sensors, 2021. ISSN 1930-0395. ISBN 978-1-7281-9501-8

In this paper, we presented the results of the development of ultra-low-noise race-track fluxgate sensors, namely we concentrated on the scaling of the sensor noise, with respect to sensor dimensions (which affects the core demagnetization). Since then, the 60mm-long race-track sensors were used several times - typically in geophysical applications - and proved to have excellent properties. Recently, we discovered that some of the noise measurements presented in this paper were most probably limited by the 6-layer magnetic shielding that was used. The newly acquired, bigger, 6-layer MuMETAL® shield provides a significantly higher attenuation factor than the old one (made of Permalloy). The author's contribution is 80%; the co-author, M. Butta, helped mainly with the visualization of magnetic domains via Kerr-effect microscopy.

Race-track fluxgate sensor scaling versus noise

Vojtěch Petrucha, Mattia Butta
Faculty of Electrical Engineering, Czech Technical University in Prague, Prague, Czech Republic
petruvoj@fel.cvut.cz

2021 IEEE Sensors | 978-1-7281-9501-8/21/$31.00 ©2021 IEEE | DOI: 10.1109/SENSORS47087.2021.9639560

***Abstract*—Fluxgate sensors with a flat race-track core can provide significant advantages in terms of noise and manufacturing complexity. We present a comparison of parameters of several such sensors of a similar construction but with different dimensions that might be useful for a wide spectrum of applications, including state-of-the-art geomagnetic measurements. The effect of core demagnetization is discussed, and optical Kerr effect microscopy is used to present the results of the thermomagnetic treatment of these cores, which significantly improves overall sensor noise. Noise values between 9 and 2.5 $pT_{RMS}/\sqrt{Hz}$ at 1 Hz can be reached for core lengths of 17.5 to 78 mm.**

Keywords—fluxgate sensor, magnetometer, Kerr effect microscopy

I. Introduction

The measurement of the magnetic field or its gradients has been used in many scientific and industrial applications [1, 2, 3]. Despite rapid development in the field of magnetic sensors (mainly new scalar types) [4, 5], fluxgate sensors are still an excellent choice when a highly sensitive vectorial sensor is needed and when there is no possibility of using a high-temperature superconductor SQUID sensor that can provide much lower magnetic noise [6]. Fluxgate sensors exist in several configurations that differ in their magnetic core shape and functional principles. Parallel-type fluxgates with dual-rod, ring-core, or race-track cores are commonly used. They make use of a second harmonic signal, which appears in the sensing coil and is directly proportional to the measured magnetic field [2]. The excited and sensed magnetic fields are parallel. On the other hand, orthogonal fluxgate sensors, which are quite popular recently, often use a magnetic micro-wire as the magnetic core and utilize a similar "flux-gating" principle; however, in this case, the sensed and excited fields are mutually orthogonal. Recently, very low noise has been achieved with orthogonal fluxgates [7], although some problems persist with offset/temperature stability. In this paper, we present a series of race-track fluxgate sensors with different dimensions but a similar construction, and we compare the sensor's noise for different variants and discuss possible improvements. The excellent performance of the large sensor makes it suitable for state-of-the-art geomagnetic measurements.

II. Race-track fluxgate sensors

One possible configuration of a race-track fluxgate sensor is shown in Fig. 1. The essential element is a magnetic core with a "race-track" shape. In this case, the core is made out of a wide, thin tape of amorphous magnetic material (e.g., Vitrovac), and it is wet-etched or laser-cut into its shape. The other possibility would be a core wound up from several turns of a narrow (1-2.5 mm wide) ribbon. The flat core is easier to handle and mount, as there is no beginning or ending of the tape that has to be fixed.

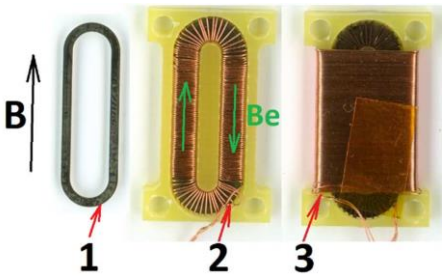

Fig. 1. Race-track fluxgate sensor construction: 1) magnetic core, 2) excitation coil, and 3) pick-up coil (all parts in FR4 supports). Be indicates the excitation field, and B is the measured magnetic field (sensitivity direction).

Core homogeneity is desirable, although some kind of non-homogeneity in the core can sometimes be conveniently used to minimize feedthrough of the excitation signal by shifting core position with respect to the pick-up coil. The excitation coil is wound around the core, which sits in some form of support that provides mechanical stiffness. As there is an excitation current (I_e) running through it (typically a pulsed wave with a frequency [f_e] in the range of 5-30 kHz), excitation magnetic field (Be) is created in the core.

Interacting with the external measured magnetic field on the non-linear hysteresis-loop characteristics of the core magnetic material, a second harmonic ($2 \cdot f_e$) signal appears in the pick-up coil. Synchronous detection of this signal provides information about the amplitude and polarity of the measured magnetic field (B).

Most of the sensor parameters (sensitivity, noise, and temperature stability) are related to the properties of the sensor core magnetic material. In the following text, some of the properties are discussed.

A. Effect of core demagnetization

Kubik and Ripka [8] presented a study in which they derived the influence of the core demagnetization effect on sensor sensitivity and noise. The shape of the magnetic core influences the magnetic field that is created inside the core when the core is exposed to an external magnetic field (H). The inner field, and thereby the useful signal (V_i), is always smaller, as seen in eq. (1).

$$V_i = -N_2 \mu_0 HS \frac{1-D}{[1+D(\mu_r(t)-1)]^2} \frac{d\mu_r(t)}{dt} \quad (1)$$

The field attenuation depends on the demagnetization field, which acts against the external field. To describe the effect, the so-called demagnetization factor (D), a dimensionless number between 0-1, is used. It can be derived

analytically but only for very specific shapes. Ideally, D should be close to zero, which corresponds to long, thin shapes of the magnetic core. Kubik presented an approximation (eq. 2) for the race-track-shaped cores, which was verified through both modeling and measurements.

$$D_{global} \approx 6.58\frac{2Tt}{(l+1.8d)^2} + 23.10^{-6} \quad (2)$$

The parameters used in eq. (2) are the dimensions defined in Fig. 2 and stated for our samples in Table I, together with the calculated demagnetization factor. For simplicity, the calculation does not take the relative permeability of the core into account, as it will differ with the material and annealing procedure used.

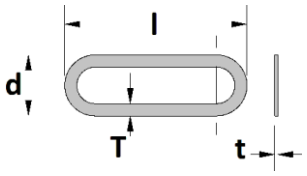

Fig. 2. Race-track fluxgate core dimensions

TABLE I. RACE-TRACK MAGNETIC CORE DIMENSIONS

Size	d (mm)	l (mm)	T (mm)	t (µm)	$10^3.D_{global}$*
A	5.4	17.4	0.9	20	0.345
B	10	30	2	20	0.251
C	10	60	2	20	0.110
D	18	78	2.5	20	0.077

*calculated using equation 2

We can see that the demagnetization factor significantly decreases for a higher length *l* of the core. This implies a possibly higher sensitivity of the sensor and thus lower noise for a given magnetic material. The longer active length of the sensor also means that part of the magnetic noise can ideally average out while being sensed by the pick-up coil covering the entire active length of the sensor. On the other hand, it requires larger dimensions for the final sensor and possibly higher power consumption to properly oversaturate the larger magnetic core.

B. Thermomagnetic treatment of the core

The magnetic properties of the core (material phase/structure, relative permeability, domain orientation, and magnetostriction) can be influenced by processing the material at a temperature close to or exceeding the Curie temperature of the material, with or without the application of an external magnetic field and/or mechanical stress. In the following paragraph, we will discuss the results of the thermomagnetic treatment of the race-track cores, which was done to decrease the magnetic noise by promoting the predictable magnetization process (domain rotation) over unpredictable noise-causing domain jumps and movements [9]. The process aims to orient magnetic domains in a perpendicular direction with respect to the excitation field. Vitrovac 6025 tape used for the experiments comes longitudinally magnetized, as shown in Fig. 3. The arrow shows the direction of the tape casting during its production as well as the sensitivity axis of the future sensor. We can see that the domains are parallel to the excitation field along the straight parts of the sensor where the pick-up winding is placed (and domains are perpendicular as we want them to be in the semi-circular part).

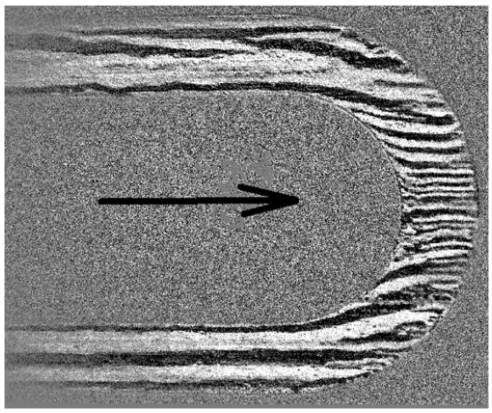

Fig. 3. As-cast domain orientation in the race-track core (size "C")

An annealing setup similar to the one presented in [10] for ring-cores was prepared for the race-track cores. A properly shaped permanent magnet (with a slightly smaller base than the inner part of the race-track and 4-6 mm height) placed approximately 1 mm under the core is used to create the desired radial field along the whole path of the race-track. The samarium-cobalt (SmCo) permanent magnets are preferred for their higher operating temperature range (up to 350°C). The FEM simulation (Ansys magnetostatic) suggests that the thin ribbon should be properly magnetized in all sections (see Fig. 4). The core is fixed in a milled groove in a thick piece of copper, which also provides mechanical fixation for the magnets and equalizes the temperature distribution along the tool. There is no magnetic circuit (yoke) in the current version. Simple resistive heating from an external heat source is used to provide the desired temperature profile for annealing (approximately 10°C below Tc for 0.5 to 4 hours).

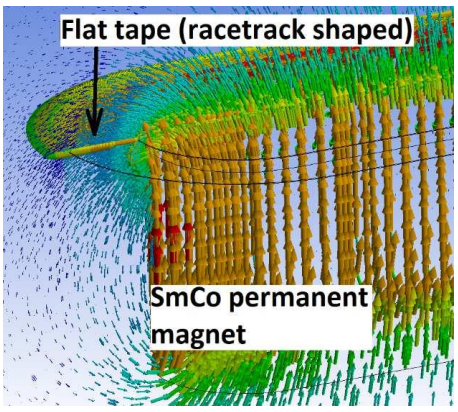

Fig. 4. FEM simulation of the setup for race-track core thermomagnetic treatment

Fig. 5 shows the resulting domain structure viewed using the Kerr-effect microscope. The domains are nicely realigned (almost perpendicular) in the straight parts of the core. Unfortunately, it seems that the annealing made it worse in the round sections of the core, where the original domain structure

looked much better. We are not yet sure what the cause of the change is; the magnetic field layout was probably not ideal as it is quite difficult to create a SmCo magnet with desired outer dimensions and shape.

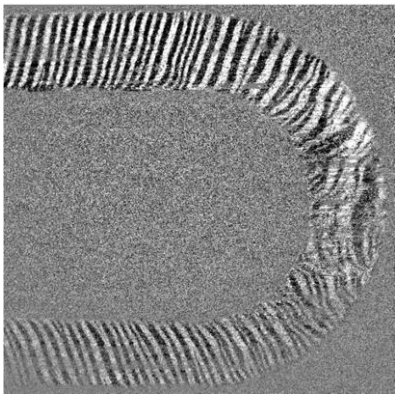

Fig. 5. Magnetic domains after the annealing process (4h) in an external magnetic field (made by a permanent magnet), with magnetic core size "C"

The annealing setup for the biggest core (size "D") is currently being tested, and we hope that in this case, the results will be better, as the higher radius of the inner part should be more tolerant to manufacturing imperfections, and the higher radius would also mean lower demagnetization and thus better saturation of the core during annealing.

The effect of annealing can also be observed by measuring the BH-loop of the magnetic core (see Fig. 6). The red curve showing the highest permeability corresponds to the original parallel domain alignment in the straight core part (measured by a small pick-up coil wound only in that part). The green short-dashed line comes from the round parts where the domains were perpendicular to the excitation field. After annealing, we observed a more inclined BH-loop with lower permeability for both parts. Also, a BH-loop from the round part showed unexpected behavior (lowest permeability and different shape).

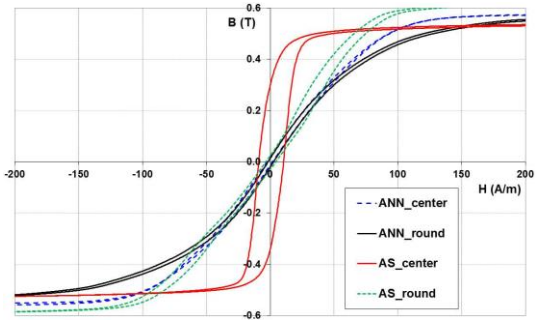

Fig. 6. Hysteresis loop of the race-track magnetic core measured at two locations. "Center": Center section of the straight part of the race-track, "Round": The rounded part, "AS": as received, "ANN": annealed.

Another interesting aspect is the magnetostriction of the core material. Zero magnetostriction materials are believed to be best for application in fluxgate sensors [11]. However, the value may change during the annealing process, so we prepared a setup to characterize this effect using the procedure described in [12] to be presented in the extended paper.

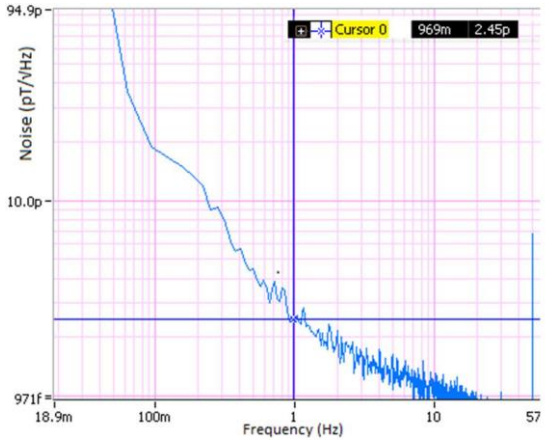

Fig. 7. Sensor noise measured in a 6-layered Permalloy magnetic shielding can (core size "C") - 2.5 $pT_{RMS}/\sqrt{Hz}$ at 1 Hz for 1 A_{P-P} excitation current.

III. Results

Table II presents the noise measurements of the four sensor sizes. Fig. 7 shows one particular noise measurement of the "C"-size race-track (open-loop measurement with a lock-in amplifier). The noise decreases with the increasing dimensions and decreasing demagnetization field (Table I). The noise is also dependent on the excitation current amplitude and shape. The presented numbers are for 1 A_{P-P}, which is a reasonable compromise between power consumption and performance. Without the annealing procedure presented, the noise is roughly 50% higher for this particular amorphous material.

TABLE II. Sensor noise summary

Size	Core dimensions (mm)	Sensor dim. (mm)	Noise ($pT_{RMS}/\sqrt{Hz}$ at 1 Hz)
A	17.4 * 5.4 * 0.02	20 * 12 * 3	8
B	30 * 10 * 0.02	40 * 17 * 3	4
C	60 * 10 * 0.02	70 * 17 * 3	2.5
D	78 * 18 * 0.02	100 * 24 * 3.5	2.5*

*preliminary result (only one sample measured)

IV. Conclusions

There is a continuous demand for low-noise vectorial magnetic sensors. For some specific applications in which the dimensions of the sensor are not critical, one can consider the presented race-track-core-based fluxgate sensors. From the trend of noise measured for A-, B-, and C-sized cores, we infer that the noise for the "D" size sensor would be around 2 pT, although the higher diameter could bring some extra advantage. However, the first manufactured sensor with "D"- sized core provided the same results as sensors with "C"- sized core. There is still some potential to improve the annealing procedure (optimal domain structure, zero magnetostriction), but this is a very complicated task due to the large number of variables at play and the very time-consuming evaluation of the results.

Acknowledgment

The authors would like to thank the Czech Science Foundation for supporting the presented research under project No. 20-19686S – "To the origin of the fluxgate noise."

REFERENCES

[1] P. Ripka, *Magnetic Sensors and Magnetometers*, Artech House Publishers, 2000.

[2] G. Musmann and Y. Afanassiev, *Fluxgate Magnetometers for Space Research*, Books on Demand GmbH, Norderstedt, 2010.

[3] A. Grosz, M. J. Haji-Sheikh, and S. C. Mukhopadhyay, *High Sensitivity Magnetometers*, Springer International Publishing, 2017.

[4] R. Zhang et al., "Subpicotesla scalar atomic magnetometer with a microfabricated cell," *J. Appl. Phys.*, 126, 124503, 2019.

[5] J. L. Webb et al., "Optimization of a Diamond Nitrogen Vacancy Centre Magnetometer for Sensing of Biological Signals," *Front. Phys.*, 19 October 2020, doi.org/10.3389/fphy.2020.522536.

[6] A. Tsukamoto et al., "HTS-SQUID vector magnetometer with low crosstalk configuration," *J. Phys. Commun.*, 3 055001, 2019.

[7] M. Dressler et al., "Reduction of magnetic noise limits of orthogonal fluxgate sensor," *AIP Advances*, 11, 015347, 2021.

[8] J. Kubik and P. Ripka, "Racetrack fluxgate sensor core demagnetization," *Sensors and Actuators A: Physical,* vol. 143, no. 2, pp 237-244, 2008.

[9] P. Butvin et al., "Field annealed closed-path fluxgate sensors made of metallic-glass ribbons," *Sensors and Actuators A: Physical*, vol. 184, pp. 72–77, 2012.

[10] V. Petrucha, "Low-cost dual-axes fluxgate sensor with a flat field-annealed magnetic core", *Proceedings of the IEEE Sensors Applications Symposium 2016*, pp. 140-143, 2016.

[11] P. Ripka, M. Butta, and M. Pribil, "Magnetostriction Offset of Fluxgate Sensors," *IEEE Transactions on Magnetics*, vol. 51, no. 1, 2015.

[12] K. Narita, J. Yamasaki, and H. Fukunaga, "Measurement of saturation magnetostriction of a thin amorphous ribbon by means of small-angle magnetization rotation," *IEEE Transactions on Magnetics*, vol. 16, no. 2, 1980.

7.2 Calibration and testing

7.2.1 refP 9

Petrucha, V.; Ripka, P.; Kašpar, P.; Merayo, J., "Automated System for the Calibration of Magnetometers," Journal of Applied Physics. 2009, 2009(105), 07E704-1-07E704-3. ISSN 0021-8979

During the development of magnetic sensors and magnetometers, the process of calibration is extremely important as it is often the most practical way to evaluate some of the parameters and iteratively improve them. The non-magnetic calibration platform was developed during the author's Ph.D. studies, but it is still in use from time to time as it provides an effective method of calibration of vectorial, triaxial magnetometers. The concept is limited by urban magnetic disturbances that bring noise to the acquired data and also the mechanical construction somehow limits the sensor-head size and interconnection possibilities. The author in the meantime developed several coil-based systems for calibration of magnetometers (based on Helmholtz and Merritt coils), but the non-magnetic platform is still useful as the coil system performance is limited by field homogeneity within the coils. The author's contribution is 25%; the main contribution was the mechanical, electronical, and software design of the system.

JOURNAL OF APPLIED PHYSICS **105**, 07E704 (2009)

Automated system for the calibration of magnetometers

Vojtech Petrucha,[1,a)] Petr Kaspar,[1,b)] Pavel Ripka,[1,c)] and Jose M. G. Merayo[2,d)]
[1]*Department of Measurement, Faculty of Electrical Engineering, Czech Technical University in Prague, Technicka 2, 166 27 Praha 6, Czech Republic*
[2]*National Space Institute-DTU Space, Technical University of Denmark, Elektrovej 327, 2800 Kgs. Lyngby, Denmark*

(Presented 12 November 2008; received 10 October 2008; accepted 29 October 2008; published online 6 February 2009)

A completely nonmagnetic calibration platform has been developed and constructed at DTU Space (Technical University of Denmark). It is intended for on-site scalar calibration of high-precise fluxgate magnetometers. An enhanced version of the same platform is being built at the Czech Technical University. There are three axes of rotation in this design (compared to two axes in the previous version). The addition of the third axis allows us to calibrate more complex devices. An electronic compass based on a vector fluxgate magnetometer and micro electro mechanical systems (MEMS) accelerometer is one example. The new platform can also be used to evaluate the parameters of the compass in all possible variations in azimuth, pitch, and roll. The system is based on piezoelectric motors, which are placed on a platform made of aluminum, brass, plastic, and glass. Position sensing is accomplished through custom-made optical incremental sensors. The system is controlled by a microcontroller, which executes commands from a computer. The properties of the system as well as calibration and measurement results will be presented. © *2009 American Institute of Physics*. [DOI: 10.1063/1.3062961]

I. INTRODUCTION

The idea of a calibration platform comes from a similar project, which was carried out at the National Space Institute of the Technical University of Denmark. The purpose of that project was to build a system for a scalar calibration and testing of high precise (space grade) fluxgate sensors and magnetometers. Scalar calibration of three-axial vector magnetometer is based on positioning of the magnetometer in homogeneous magnetic field. The collected data set should contain enough readings, which are equally distributed in all directions. From these data the nine parameters can be calculated: sensitivities and offsets of individual sensors and the angular deviations between them. The calculation is made by iterative procedure, which minimizes the variation in the scalar value B (with a linear least-squares estimator used).[1] The ideally measured B is constant for every direction. This is achieved by using correction matrices, which can contain the mentioned nine correction parameters. In every iteration step the new values of these corrections are calculated until required precision is reached. The limitations of the mentioned calibration methods include nonhomogeneity of the calibration field, magnetic contamination, Earth's field variation, stability of the position during measurement, and nonlinearity of the sensors.

There are two possibilities how to achieve the mentioned positioning: either the magnetometer is fixed in a precise three-axial calibration system and the artificial field is rotated by proper adjusting of the currents into the calibration coils. Another possibility is to move the magnetometer in the Earth's field using a nonmagnetic positioning platform. The first approach is limited to few special laboratories, which have to be thermostated and periodically calibrated by another complicated procedure. This approach is thus usually limited for testing and calibration of the finalized instruments or complete satellites. The second approach is more convenient for the testing and calibrations during development of new devices. A platform with two axes of freedom (pitch and roll) is sufficient for this application. The only requirement is to place the axis of pitch rotation perpendicularly to the vector of Earth's magnetic field. Then by setting the pitch and roll we can reach arbitrary direction with respect to the Earth's field and thus get all the samples needed to uniformly cover an imaginary unit sphere.

The calibration and testing of navigation systems (e.g., compass modules) at the Czech Technical University was the motivation for continuing to work on that project. Strapdown compass module[2] developed at the CTU comprises of a vector fluxgate magnetometer and vector MEMS accelerometer. The calibration of such a compass module is a more complicated task. Scalar calibration of the magnetometer and accelerometer is the first step. In this step we get the mentioned nine coefficients for each vector instrument. Two axes of rotation are still enough for this step. Afterwards a mutual position of the magnetometer and accelerometer with respect to the reference frame has to be calibrated. For this we have to rotate the device in the following sequence: rotation in azimuth (while roll and pitch are fixed), then in pitch (while azimuth and roll are fixed), and finally in roll (with azimuth and pitch fixed). Three independent axes of rotation are

[a)]Author to whom correspondence should be addressed. Electronic mail: petruv1@fel.cvut.cz. Tel.: +420 224 353 964. FAX:+420233339929.
[b)]Electronic mail: kaspar@fel.cvut.cz. Tel.: +420 224 352 188.
[c)]Electronic mail: ripka@fel.cvut.cz. Tel.: +420 224 353 945. URL: www.maglab.cz.
[d)]Electronic mail: jmgm@space.dtu.dk. Tel.: +45 45253452. FAX: +454588 7133. URL: www.space.dtu.dk

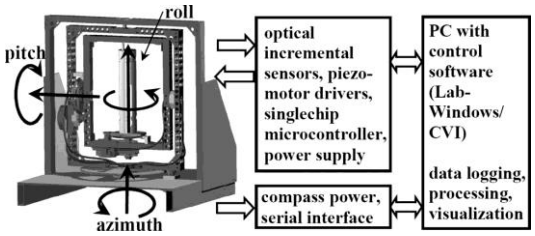

FIG. 1. Block diagram of the nonmagnetic calibration platform.

needed for this step. Very important is the rigidity of the platform, mutual perpendicularity of the axes, and the uniformity of the data acquisition, while the absolute positioning precision is not critical. Such procedures can be performed even during the Earth's field perturbations,[3] however, the field monitoring by Overhauser magnetometer is desirable.

The same platform can be used to check the accuracy of azimuth measurement of the calibrated compass. The azimuth should stay constant for each value of azimuth, while the roll and pitch are changed (roll in the range of ±180°, pitch in the range of approximately ±75°—the azimuth loses its meaning for pitch values close to 90°). In order to check the absolute azimuth accuracy (or linearity), a device with higher resolution of position setting is needed (the target accuracy of our strapdown compass is 0.2°, which requires 0.1° precision of the inclination).

Until now we have used a nonmagnetic theodolite. The drawback of this device is a limited range of available position setting (pitch approximately ±60°); it is not absolutely nonmagnetic and the hand operation is inaccurate, inconvenient, and time consuming. Other method of positioning (for scalar calibration only) is a "free hand" method where the device under test is manipulated by hand, and data are collected during a slow smooth motion. This method is fast and no special equipment is needed but it brings dynamic errors into the process (irregularity of the motion, vibrations). The calibration platform, which is introduced in this paper has three axes of freedom (independent setting of yaw, pitch, and roll), it is fully nonmagnetic and motorized (allows computer controlled operation).

II. SYSTEM CONCEPTION

The system can be divided into three main parts (see Fig. 1). The mechanical part is basically a gimbaled platform—one fixed frame that holds two rotating frames and a rotating center support. Each of them is driven by a piezoelectric motor. Three incremental optical sensors are used to sense the position of the frames and to control the motors in a closed loop. An electronic control unit consists of a single-chip microcontroller, which receives the commands from a computer (via USB interface), evaluates the signals from the incremental sensors, and controls dedicated piezoelectric motor drivers. The whole system is controlled by a personal computer via an application with a simple graphical user interface.

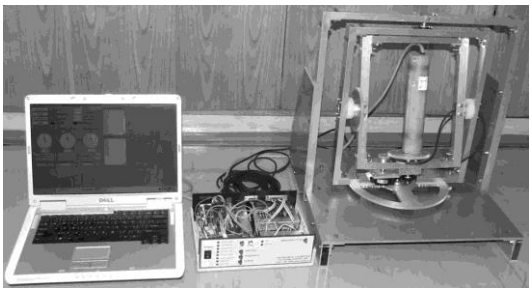

FIG. 2. Calibration platform with control unit and compass module.

III. PLATFORM DESIGN

The ShinSei's USR60 piezoelectric motors are the most powerful nonmagnetic motors available on the market. However their 1 Nm maximum torque is insufficient and gearing was necessary. Aluminum tooth wheels with gearing ratios of 1:4 and 1:10 (for the outer vertical frame) were used. The frames are made of aluminum profiles, which are lightened by drilling as many holes as possible (while the frame has to stay rigid). In order to bring down the friction, plastic bearings with glass balls were used instead of a plastic friction bearing. The wiring of the motor and sensor cables goes through the axes of rotation in order not to significantly limit the range of motion. There are no brakes needed; the piezoelectric motors have sufficient static momentum.

The angular position is measured by incremental optical sensors. Only 1° resolution is required, but the magnetic cleanliness should be very high, as these sensors are very close to the devices under test. We found no really nonmagnetic optical incremental sensor on the market. Thus the sensors were custom built using a code wheel made of a printed circuit board. The problem is a contamination of most electronic components with ferromagnetic materials. Even small surface mount device (SMD) parts represent serious problem. Therefore there are only SMD infrared light emitting diodes and phototransistors (GL100MN and PT100MF) in the vicinity of the device under test. All other circuits are placed several meters away from the platform.

The electronic control unit is based on the ATMEL AVR microcontroller (ATMEGA128). The personal computer (PC) user interface is written in National Instruments LabWindows/CVI programming environment (Fig. 2).

IV. RESULTS

The three-axial platform development is in the testing phase. We present results of scalar calibration of the vector MEMS accelerometer. Raw data and corrected data are shown in Fig. 3. The rms variance of the gravity scalar value is 14.65 mg before correction and 1.73 mg after the calibration constants are applied. Compared with similar data taken during a smooth slow motion (hand driven)—raw data are 18.37 mg and corrected data 10.56 mg. It is evident that the errors caused by motion irregularity are suppressed. Other benefits are the increased speed of the calibration, repeatabil-

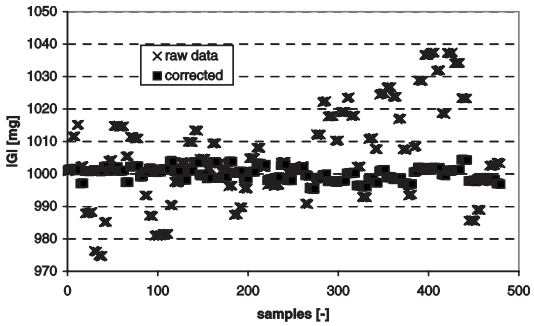

FIG. 3. MEMS accelerometer calibration results.

ity, and the possibility to create a map of residuals, which can detect some systematic errors such as nonlinearity or cross-field errors.

V. CONCLUSION

The parameters of the system are summarized in Table I. One of the most important parameters is a magnetic cleanliness. The fluxgate vector magnetometer used in the compass module has a resolution far better than 1 nT and therefore the level of influence of ferromagnetic components has to be safely below this level. The piezoelectric motors are specified as nonmagnetic but our measurements show that there is a small amount of ferromagnetic material present (magnetic field change about 0.5 nT at 50 mm distance). This limits the present achievable accuracy. We will try to evaluate and suppress this influence.

TABLE I. Summary of calibration platform parameters.

Projected sensor dimensions	$100\times100\times300$ mm^3
Maximum sensor weight	0.75 kg
Degrees of freedom	3
Positioning precision	1°
Positioning stability	~0°/1 min
Rotation speed (pitch, roll)	30°/1 s
Rotation speed (azimuth)	15°/1 s
Range of motion	±360°
Projected magnetic cleanliness	<.05 nT in the sensor area
Power requirements	25 W
Total weight	~12 kg

[1]J. M. G. Merayo, P. Brauer, F. Primdahl, J. R. Petersen, and O. V. Nielsen, Meas. Sci. Technol. **11**, 120 (2000).
[2]J. Vcelak, V. Petrucha, and P. Kaspar, Sens. Lett. **5**, 279 (2007).
[3]J.-H. Wang and G. Yang, Meas. Sci. Technol. **17**, 153 (2006).

7.2.2 refP 10

Petrucha, V.; Kašpar, P., "Calibration of a Triaxial Fluxgate Magnetometer and Accelerometer with an Automated Non-magnetic Calibration System," In: IEEE SENSORS 2009 - The Eighth IEEE Conference on Sensors. Christchurch: IEEE Sensors Council, 2009. pp. 1510-1513. ISSN 1930-0395. ISBN 978-1-4244-4548-6

This paper presents the results of calibration of multiple magnetometers and an accelerometer made with the above-mentioned, non-magnetic calibration platform. This calibration campaign proved that the system provides reliable results as multiple commercial sensors were measured and the results could be compared. The author's contribution was 70%, having provided most of the measurements and data processing. P. Kašpar helped with interpretation of the data.

Calibration of a Triaxial Fluxgate Magnetometer and Accelerometer with an Automated Non-magnetic Calibration System

Vojtech Petrucha, Petr Kaspar
Department of Measurement
Czech Technical University in Prague
Prague, Czech Republic
petruvoj@fel.cvut.cz, kaspar@fel.cvut.cz

***Abstract*— A method, instrumentation used and results of calibration and testing of tri-axial magnetometers, accelerometers and also possibly gyroscopes are presented. The method is based on a scalar calibration technique with the use of an innovative computer controllable non-magnetic platform [1]. The speed, precision, comfort and repeatability of the measurement are superior to techniques which use hand-driven tools.**

I. INTRODUCTION

Three axes magnetometers are widely used for navigation purposes (an electronic compass) as well as three axes accelerometers for a compass tilt compensation. Magnetometers form one part of Attitude Heading Reference Systems (AHRS) for initial azimuth alignment and azimuth gyro drift correction. Heading, pitch and roll are the basic output data but in some cases it can be useful to operate with the raw sensor outputs and perform the data processing outside the navigation units. Than we need to calibrate the basic sensors (magnetometers, accelerometers and in case of AHRS also gyroscopes) and test the accuracy of a resulting system. An innovative and efficient approach of calibration is presented, as well as results of basic scalar calibration of several devices.

II. MOTIVATION

The presented way of calibration uses second generation of an automated non-magnetic positioning platform. The idea of a non-magnetic platform comes from Danish National Space Institute, where a similar dual-axis instrument has been developed in order to bring a fast in-sight method for evaluation of space-grade magnetometer sensors (as an alternative to very expensive vector coil calibration center). The work with navigation units at the Czech Technical University was the main motivation to enhance the design. The addition of a third rotational axis introduces the possibility of a full evaluation of a tilt-compensated electronic compass. Basic calibration and testing of AHRS units is also possible. See Fig.1.

III. CALIBRATION

Navigation units use AMR or Fluxgate magnetometers to measure the Earth's magnetic field. Three axes coil system can be used for calibration. Unfortunately this equipment is very expensive and it requires a proper maintenance (temperature stable environment, periodical calibration). Second possible approach has been presented in several papers [2]. Scalar calibration uses predefined positioning of a calibrated instrument in a stable and homogenous field with a known magnitude value. The Earth's magnetic field can fulfill these requirements, especially during a (magnetically) quiet period of a day. The magnitude of the field can be easily monitored with an absolute scalar magnetometer during the calibration. Nine parameters of magnetometer sensors can be estimated with this technique: three offsets, three sensitivities and three non-orthogonality angles.

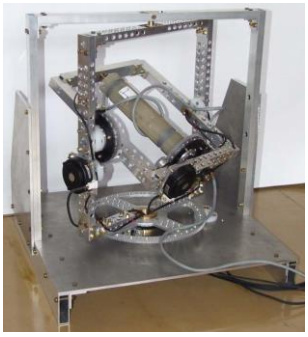

Figure 1. A triple-axes non-magnetic calibration platform.

Identify applicable sponsor/s here. *(sponsors)*

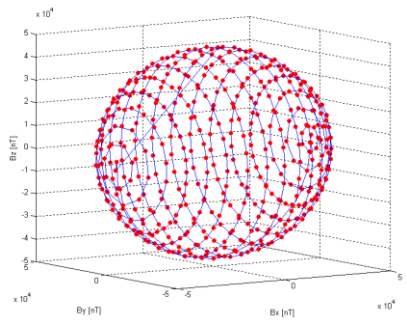

Figure 2. Uniform data samples distribution on a unit sphere. (magnetic field samples collected with Device Under Test (DUT) 5. – see Tab.1)

Three other angles define the alignment with an external reference frame (defined for example by an instrument case). All these twelve parameters entirely describe the magnetometer. During the scalar calibration procedure, the magnetometer is positioned with respect to Earth's magnetic field vector in such a way, that the sensors are exposed to a full range of the field (the measured data samples uniformly cover a virtual unit sphere see Fig.2). The non-magnetic platform allows an automation of the process of data collection. The calibration of alignment of magnetometers (and accelerometers) with respect to an external reference frame is done by rotation in three perpendicular axes. The speed, precision and repeatability of the measurement are superior to techniques which use hand-driven tools. Magnetic cleanliness of the platform is an extremely important but it is very difficult to achieve, see following discussion.

Accelerometers with a measurement range of several g (those are typically used in navigation units) can be calibrated using the same technique. Earth's gravity vector is used which means that the sensor is effectively calibrated only in a range of ±1g. In this case very important requirement is a stability of the measurement platform. Any vibration of the sensor during the calibration is strictly undesirable (in contrast to magnetometers which can be calibrated during a smooth slow motion).

The presented platform allows to measure the basic properties of gyroscopes. The sensor offset is estimated during a motion-less state. Sensitivity is determined during a constant-speed rotational motion of the platform (speed range 0.07 to 1.25rad.s^{-1}). Wired connection of the sensor does not allow to make more than two or three rotations in one direction. This problem could be overcome with an application of a wireless link between the gyroscope and data acquisition unit (in case of magnetometer, the presence of any electrical parts is unwanted because of their magnetic contamination). While rotating in one axis which is well aligned with a sensitivity axis of one gyroscope, the other two gyroscopes will provide output proportional to the non-orthogonality of their alignment. The gyroscopes should be always placed into the center of rotation, which is usually hard to achieve for a fully-enclosed commercial units, where the position of sensors is not clearly marked.

The non-magnetic feature and the possibility to move the tested device into any azimuth-pitch-roll direction is excellent for testing of the AHRS units. Short simultaneous azimuth-pitch-roll maneuvers can be programmed and used to evaluate the quality and response of data processing algorithm (e.g. Kalman filtering).

IV. Measurements

Two magnetometers (Honeywell HMR2300, Stefan-Mayer FL3-100) were calibrated. Other devices are: two electronic compasses with an electronic tilt error compensation (Honeywell HMR3000 and proprietary compass module with PCB fluxgate sensors and Colibrys MEMS accelerometers [3]), two AHRS units (InnaLabs M3, MicroStrain 3DM-GX2). At least two measurements were performed for each sensor. There were 118 data points in each scalar calibration dataset (500 for the proprietary compass module). It takes approximately 5-15min to collect this amount of samples. It is mostly dependent on the duration of data acquisition delay between the positioning (the data are collected when the platform is still and all the motors and sensors are not powered). The Earth's field magnitude has been monitored with a GEM System GSM-19 scalar Overhauser magnetometer. Unfortunately relatively high field variations were observed (18nT p-p value), see Fig.3.

The HMR2300 module provides three digital values (RS232 interface) which are proportional to applied magnetic field (factory defined sensitivity 30000EU - 200μT). The output data noise was partially suppressed by averaging the output values (10 samples averaged at 100Sa/s conversion rate). The HMR3000 module provides raw digital data output (RS232) in "RCD sentence" mode. The RCD sentence consists of ten values, three of them are proportional to the applied magnetic field and three represents an actual offset of each sensor. The four tilt sensor output values were not processed (the sensor is only dual axes and thus is incompatible with the scalar calibration algorithm). The output data were scaled with an artificial constant (1EU - 5nT), so the absolute value of calculated sensitivities is not important.

The Stefan-Mayer FL3-100 magnetometer has analog voltage outputs. The voltages were measured with a GPIB based system comprising three simultaneously sampled Agilent 34401 multimeters.

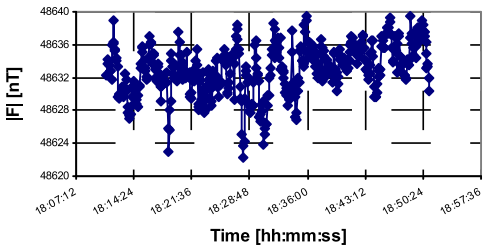

Figure 3. Earth's magnetic field magnitude during measurements.

Prior to calibration, the measured voltages were scaled with a factory defined coefficient (10V - 100μT).

The compass module with PCB fluxgate sensors [3] is custom made module designed for underground drilling applications. The module with a RS232 interface provides raw data outputs of three fluxgate magnetometers and three MEMS Colibrys MS7202 accelerometers. The data are only roughly scaled in the compass module; the compensation of sensitivities, offsets and non-orthogonalities is done in a master unit.

The InnaLabs M3 AHRS module has several possible output data modes. At first the internally conditioned accelerometer data were used for the scalar calibration algorithm ("Orientation Angles + Sensors Output" mode). Sequentially the scalar calibration procedure was repeated with an accelerometer raw sensor output ("Full Output Data" mode). The inbuilt magnetometer was evaluated only in raw data mode. Due to difficulties with module cabling the gyroscopes were not calibrated yet.

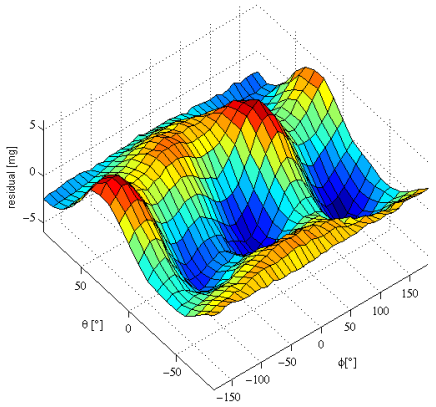

Figure 4. Map of residuals after scalar calibration algorithm is applied (Compass module – Gravity Field)

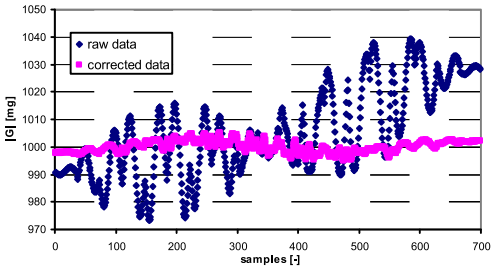

Figure 5. Gravity vector magnitude before and after calibration constants were applied (proprietary compass module – Colybris MS7202 accelerometers)

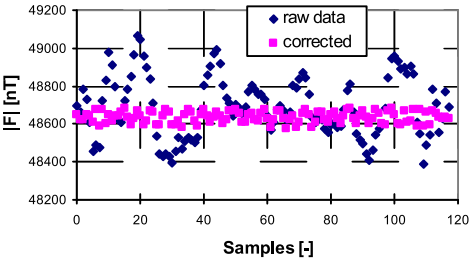

Figure 6. Magnetic field magnitude before and after calibration constants were applied (Stefan Mayer – FL3-100)

We have used the same approach for the MicroStrain 3DM-GX2 AHRS module. Scalar calibration algorithm had two input data sets, one with an internally conditioned acceleration vector and second with a raw sensor outputs ("0xC1" command). The manufacturers do not provide any scale factors for the raw data outputs, so the data were scaled to mg with estimative values.

V. Results

A slightly modified version of an algorithm presented in [4] was used to process the scalar calibration (the definition of non-orthogonality angles was modified). The scalar calibration results are summarized in Tab.1. The last column shows the RMS misfit (1) - this value is minimized during the scalar calibration algorithm. It can't be generally compared to the same value from other sources because the calculation algorithms usually use some kind of data weighing (σ) which eliminates the outlaying data samples. $B_{Magnitude}$ is a field magnitude calculated from the field components; B_{Scalar} is measured with an absolute scalar magnetometer during the data collection. The plot of residuals can be drawn (Fig.4) because an angular position of each sample is known (sphere surface, θ <-90, 90> degree, φ <-180, 180> degree). Systematic behavior of the residuals can indicate possible problems (in order to present the chart better, 700 data points were measured, but only selected amount was used for calibration – because of dataset uniformity). Two plots showing the effect of scalar calibration on the field magnitude are presented (Fig.5, Fig.6).

$$\text{RMSmisfit}^2 = \sum_{n=1}^{N}\left(\frac{B_{Magnitude} - B_{Scalar}}{\sigma}\right)^2 = Min! \quad (1)$$

The result of calibration of the HMR2300 magnetometer indicates that the piece we measured has very high misalignment of Z sensor axis (>9deg.). This value is already directly visible (after disassembly of the magnetometer - Fig.7) and it comes from the mounting technology used (insufficient mechanical fixing of this sensor).

TABLE I. RESULTS OF SCALAR CALIBRATION

Device Under Test	Sens. X [-]	Sens. Y [-]	Sens. Z [-]	Offset X	Offset Y	Offset Z	Non-orthogonality angles			RMS misfit
							α [deg]	β [deg]	γ [deg]	
1. HMR2300	1.0322	1.0236	1.0338	705.2 nT	-336.4nT	828.2nT	1.499	-9.076	-0.021	105.1nT
2. HMR3000	1.0864	1.0088	0.9646	-1774 nT	1296 nT	-527.3 nT	0.068	-0.519	-0.158	69.70 nT
3. FL3-100	0.9983	0.9991	0.9992	36.48 nT	1.91 nT	-17.72 nT	-0.092	-0.642	-0.267	28.75 nT
4. InnaLabs M3 Mag. Raw-Data	1.0080	1.0115	1.0424	-2963 nT	-508.9 nT	-716.1 nT	-3.737	-1.368	-2.860	63.92 nT
5. Compass Mag.	0.8903	0.9106	0.8864	76.85 nT	84.30 nT	-23.10 nT	2.360	3.068	1.524	96.15 nT
6. Compass Acc.	0.9899	1.0018	0.9987	-16.6 mg	0.36 mg	-1.63 mg	2.167	0.996	-0.086	1.84 mg
7. InnaLabs M3 Acc. Corr.-Data	1.0000	1.0001	1.0002	0.22 mg	0.01 mg	-0.01 mg	0.011	-0.011	-0.011	0.32 mg
8. InnaLabs M3 Acc. Raw-Data	0.9986	0.9894	0.9847	1.47 mg	-5.51 mg	14.58 mg	-0.8656	-3.031	-0.178	1.03 mg
9. 3DM-GX2 Acc Corr.-Data	0.9994	0.9997	0.9996	0.24 mg	-0.56 mg	0.78 mg	-0.011	-0.025	0.052	0.06 mg
10. 3DM-GX2 Acc. Raw-Data	0.9768	0.9813	0.9758	10.30 mg	9.16 mg	-15.6 mg	-0.061	3.273	-0.239	0.60 mg

Acc. – Accelerometers, Mag. – Magnetometers, Raw Data – sensor output data without inner calibration, Corr. Data- internally conditioned data, Compass – Proprietary compass module [3]

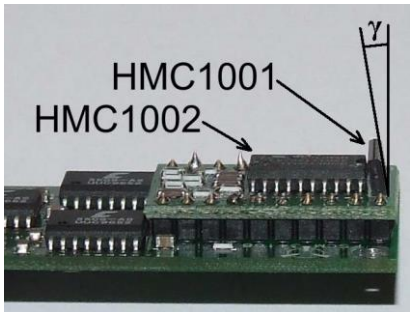

Figure 7. HMR2300 electronics – visible misalignment of Z axis. HMC1002 is a dual axes and HMC1001 single axis AMR sensor.

The HMR3000 electronic compass provides better results but still it is clear that an AMR based device cannot reach the accuracy of fluxgate magnetometers. The FL3-100 fluxgate magnetometer has very well defined sensitivity, low offset and acceptable sensor triplet non-orthogonalities. With a suitable DAQ (analog output) it can provide excellent navigation accuracy. The limitation of accuracy of the proprietary compass module lies in the poor orthogonality of the sensor triplets and also the non-compensated temperature dependence constitutes a problem.

The AHRS units exhibit excellent results when the conditioned data outputs are used. It means that the significant misalignments are well compensated. Worse results of scalar calibration (RMS misfit compared) of their raw-data outputs are probably caused by the lack of temperature compensation outside the unit (the calibration was not done in a temperature controlled area).

Preliminary tests of calibration of the sensor triplet alignment with respect to an external reference frame were made. A key success factor is the ability to provide precise and reliable absolute positioning, as well as the sensor fixing has to be improved (current design does not provide sufficient axial symmetry).

VI. CONCLUSIONS

The results presented show that current measurement setup is well suited for scalar calibration of magnetometers and accelerometers. But we have to mention that some little magnetic contamination of the platform was discovered just before the measurements (two components - machined brass axes - have to be replaced). This could directly negatively influence the scalar calibration results as well as the instability of the Earth's magnetic field.

In order to provide the full calibration possibility (triplet alignment calibration) the platform has to be slightly modified and proper sensor (DUT) holder developed. The development of more accurate non-magnetic sensor for controlling platform operation is also necessary (current accuracy – 1deg is well sufficient only for scalar calibration). Wire-less data transfer could solve the problem with cabling when calibrating gyroscopes.

Our goal is to develop a system which will provide precise, reliable and fast calibration of magnetometers, accelerometers and gyroscopes.

REFERENCES

[1] V. Petrucha, P. Kaspar, P. Ripka, J.M.G. Merayo, Automated system for the calibration of magnetometers, Journal of Applied Physics, 105, 07E704, 2009

[2] J.M.G. Merayo, P.Brauer, F. Primdahl, J.R. Petersen and O.V. Nielsen, "Scalar Calibration of Vector Magnetometers," Measurement Science and Technology, 11 (2000), pp 120-132.

[3] J. Vcelak, V. Petrucha, P. Kaspar, Electronic compass with miniature fluxgate sensors, Sensors Letters Vol.5,3/2007, pp.279-282.

[4] N. Olsen, T. Risbo, P. Brauer, J. Merayo, F. Primdahl, T. Sabaka: In-Flight Calibration Methods Used For The Orsted Mission, Technical University of Denmark, unpublished.

7.2.3 refP 11

Petrucha, V.; Kašpar, P., "Measurement of the Temperature Dependence of the Sensitivity and Orthogonality of a Triaxial Vector Magnetometer," Journal of Electrical Engineering. 2012, 63(7s), 31-34. ISSN 1335-3632

This paper again makes use of the non-magnetic positioning platform; in this case it is used with additional hardware (a specifically constructed and controlled, non-magnetic thermostat) to evaluate temperature dependence of sensitivities and orthogonalities of vectorial magnetometers. Later these measurements were repeated several times in order to find the best material for the vector compensation coil support structure. The author's contribution was 50%; P. Kašpar again helped with the data's interpretation.

Journal of ELECTRICAL ENGINEERING, VOL 63. NO 7s, 2012, 31-34

MEASUREMENT OF THE TEMPERATURE DEPENDENCE OF THE SENSITIVITY AND ORTHOGONALITY OF A TRIAXIAL VECTOR MAGNETOMETER

Vojtěch Petrucha* — Petr Kašpar*

The temperature dependence of the sensitivity and orthogonality of a tri-axial vector magnetometer is measured with the use of a dedicated thermostatic system and a non-magnetic positioning platform. The dependency is obtained from the results of repeated scalar calibrations for different temperatures.

Keywords: magnetometer calibration, scalar calibration, sensitivity and orthogonality temperature dependence

1 INTRODUCTION

Sensitivity and orthogonality temperature dependences are basic parameters which characterize a vector magnetometer. Strict values of these parameters are required for applications that experience a wide range of temperatures (*eg* space exploration, underground drilling). The temperature dependence of the sensitivity depends on the properties of the sensor and on the stability of the signal processing electronics. Sensor sensitivity is usually defined by the constant of the compensation coil. The stability of the compensation coil constant depends on the support material and technology of the winding. The temperature dependence of the sensitivity can be measured with the use of a single or multiple-axis coil system equipped with a thermostatic box. There are strong requirements on the electrical and mechanical stability of the whole system if small sensitivity variation values are expected.

The orthogonality and the temperature stability of the orthogonality depend mainly on the mechanical design of the sensor and on the materials that are used. A vector coil system is used to measure the orthogonality. Alternatively, it is possible to employ a different approach which uses precise mechanical construction allowing rotations by exact angles. High preciseness of the system is again required if small angles are to be measured. This paper suggests the use of a scalar calibration technique with additional accessories to make precise measurements of the parameters mentioned above. The method is fast, reliable and, with some limitations, can use fairly inexpensive equipment.

2 SCALAR CALIBRATION

Scalar calibration is a well-known method that obtains nine intrinsic parameters which characterize a vector sensor of a magnetic field (*ie* three sensitivities, three orthogonalities and three offsets). The method uses data collection and mathematical processing of samples measured by the DUT (Device Under Test) to evaluate the parameters. A good introduction is given in Merayo [1]. A typical dataset consists of a couple of tens or hundreds of measured vectors. A greater number of samples can provide higher precision but some short-term drifts can negatively influence the processing if the data acquisition takes too long. The DUT should ideally measure a stable and homogenous field, *eg* the Earth's magnetic field. It should be noted that the method works the same for accelerometers, where the Earth's gravity field is sampled.

Specific additional equipment has been proposed in [2] in order to make the scalar calibration procedure easier and more convenient to conduct. An almost completely non-magnetic computer-controllable platform is used to rotate the DUT in such a way that a required set of samples is automatically measured. The advantage with respect to random "hand-driven" motion lies in the perfect uniformity of the acquired samples. The speed and repeatability of the measurement is also very good.

3 EXPERIMENTAL SETUP

A simplified block diagram of the whole system is shown in Fig. 1.

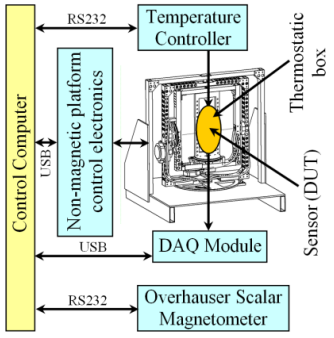

Fig. 1 Block diagram of the system for calibrating the temperature dependencies of sensitivity and orthogonality

The design has been customized to accommodate a vectorially-compensated vector fluxgate magnetometer. For

*Czech Technical University in Prague, Faculty of Electrical Engineering, Department of Measurement, Technická 2, 166 27 Praha 6, Czech Republic, petruvoj@fel.cvut.cz

ISSN 1335-3632

details, see [3]. The sensor is a cuboid with dimensions of 48 x 40 x 40 mm. The expected working temperature range of the sensor is from -50°C to +100°C. During the measurement, the sensor is fixed in the center of the non-magnetic calibration platform. The fixation is provided by two heater plates, see Fig.2. The heater plates were developed in order to provide excellent magnetic cleanliness and sufficient power to maintain the desired temperature range. The base of the heater (a) is a plate milled from a standard 2mm thick FR4 PCB material. The second plate (b) is a thin copper plate (0.5 mm), which helps to eliminate temperature gradients. The heating element itself (c) is a double layered Kapton-based PCB with a bifilar meander track. On the sensor side, there is another 2mm thick copper plate (d) that helps to minimize the temperature gradients along the surface of the heater.

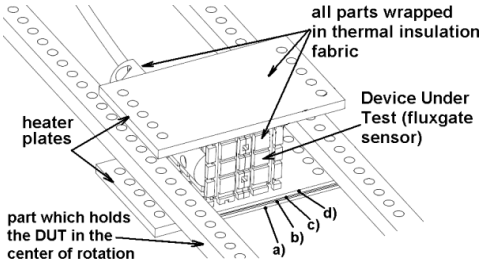

Fig. 2 The measured sensor is fixed by the heating plates and protected by thermal insulation

All the parts are fixed together by screws, and by a thermally conductive paste which was applied between the copper plates and the Kapton heating element. Experience now suggests the use of a double-layered heating element, but with the heating trace etched only on one side. The second side should be left untouched to improve the thermal conditions and simplify the construction. The sensor and heater plate assembly is protected by multi-layered thermal insulation made of PTFE-coated fabrics. The heater plates were supplied with current, and the temperature was controlled by a standard commercial temperature regulator (CoolTronic TC3215). The temperature sensing element was a PT1000 sensor, which is embedded close to the center of the fluxgate sensor. The absolute reference for the magnetic measurements was provided by a scalar Overhauser magnetometer (Gemsys GSM-19). The scalar magnetometer was placed approximately 20 meters away from the calibration platform. It provides the absolute reference for the calibration algorithm and compensates for the variations in the magnitude of the Earth's magnetic field during data acquisition. All the parts were controlled by a laptop computer with custom software equipment through multiple RS232 ports.

4 MEASUREMENTS

Two identical fluxgate sensors were used for the measurements. Two scalar calibrations were performed for each temperature. Sensor 1 was measured for two different temperatures, sensor 2 for three different temperatures.

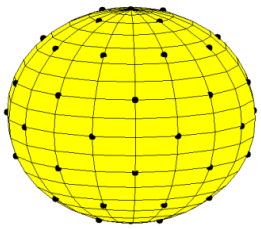

Fig. 3 The 55 measured vectors (black dots) uniformly cover the virtual sphere with a radius equal to the Earth's field magnitude

This gives ten scalar calibrations in total. The number of calibrations was limited by the available time. Although the number is not ideal, it provides a sufficient amount of information about the desired parameters. Each dataset was composed of 55 identical vectors (see Fig. 3), and it took approximately 5 minutes to collect each dataset. Much more time was needed between the measurements (20-40 minutes) in order to stabilize the temperature in the whole volume of the sensor. Due to some software problems with the heater control, the heating was switched completely off during the 5-minute calibration cycle. This means that there was a slight variation in the sensor temperature and probably also some thermal gradient in the volume of the sensor. It was originally expected that the heater would be switched off only during the period needed to take each sample (two seconds for output stabilization and one second for data acquisition) and that it would maintain a constant sensor temperature while the platform was being positioned.

5 RESULTS & DISCUSSION

The results are presented as graphs showing the temperature dependence of each parameter. All the measured values are plotted, together with a linear approximation of the dependency. The graphs can also be used to compare absolute values of the parameters for Sensor 1 and Sensor 2, see Figs. 4 and 5. The temperature dependencies are summarized in Table 1.

The main construction material of the fluxgate sensor is PEEK GF30 (PolyEtherEtherKetone with 30% of glass filling). The manufacturer specifies the coefficient of linear thermal expansion as follows: an average value between 23 and 150°C is 30 ppm, an average value over 150°C is 65 ppm. The compensation coil windings are made of copper, which has a coefficient of linear thermal expansion of 17 ppm. So the final sensitivity of the compensation coil constant to temperature changes is given by a combination of the two values. The winding technique (*ie* the initial tension) can influence the result. An average value for the measured temperature dependencies is 37

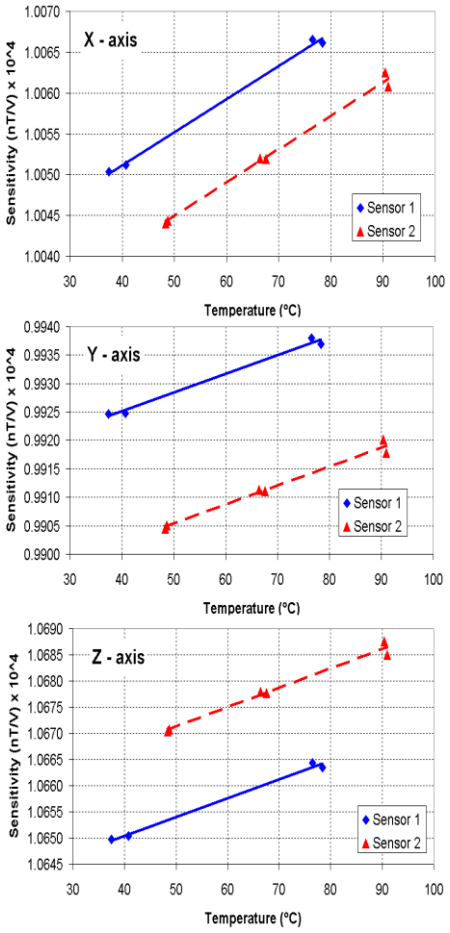

Fig. 4 Temperature dependence of sensitivity for Sensors 1 and 2

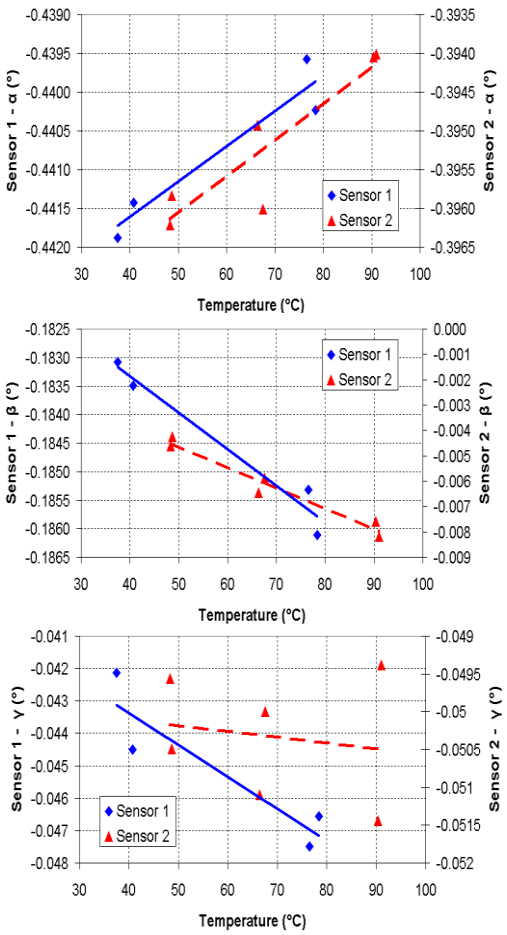

Fig. 5 Temperature dependence of orthogonality 2 for Sensors 1 and

ppm, which is in good agreement with the expected result. The different values for each axis could depend on the mechanical design of the compensation coil system (*eg* non-symmetry).

The orthogonalities were expected to have small and rather random dependency, but actually the measured values indicate relatively strong and quite precisely defined temperature sensitivity. This sensitivity is probably due to the mechanically asymmetrical design of the sensor, which is caused by manufacturing issues.

The scalar calibration also provides information about the offsets. The measured offset temperature coefficients range from 0.03 nT/°C to 0.3 nT/°C. In most cases, they correspond well to values measured by an alternative method (*ie* measurement in a multi-layered magnetic shielding equipped with a thermostatic box).

Tab. 1. Summary of all measured parameters.

Parameter temp. dep.	Sensor 1	Sensor 2
$SENS_X$ (ppm/°C)	+41	+41
$SENS_Y$ (ppm/°C)	+33	+34
$SENS_Z$ (ppm/°C)	+36	+37
Orthog. – α (arcsec/°C)	+0.18	+0.17
Orthog. – β (arcsec/°C)	-0.25	-0.29
Orthog. – γ (arcsec/°C)	-0.38	-0.02

We expect that the matching between the alternative methods will be improved when the temperature of the sensor is better stabilized during scalar calibration. Currently, there was a difference in the sensor temperature ranging from 0.3 to 6.2°C between the beginning and the end of the 5-minute calibration period. An average value of the temperature was plotted into the graphs. The aim is to maintain the temperature within ±0.1°C in the sensor

area, and thus to eliminate the temperature gradient in the sensor body below ±1°C.

5 CONCLUSIONS

The results obtained with the use of the system described here correspond well to the expected theoretical values in the case of sensitivities. There is good agreement between alternative measurement methods in the case of offsets, and there is valuable new information concerning the temperature dependency of orthogonality. The average measured temperature sensitivity dependence value of 37 ppm/°C is unfortunately above the value that is required for high-precision instruments (~10 ppm/°C). A possible way to improve the values is by changing the main construction material for the sensor. The precision and accuracy achieved with the current system should be satisfactory for measurements made with the improved sensor.

The main way to improve the system now is by extending the operating temperature range. The upper value ~100°C is limited by the construction materials. The lower temperature limit could be extended simply by applying dry ice (solid carbon dioxide) to the thermostat. In this way, a measurement point at approximately -70 °C could be achieved.

Although quite complex and expensive equipment was used during the measurements, the setup can be greatly simplified. The positioning platform can be made "hand-driven", and the absence of the Overhauser scalar magnetometer will only slightly reduce the performance. The heating plates can be replaced by a non-magnetic heating wire wound around the sensor. Of course, the overall precision and comfort of operation will be reduced, but the results can still be well usable in practical applications.

REFERENCES

[1] MERAYO, J.M.G. — BRAUER, P. — PRIMDAHL, F. — PETERSEN, J.R. — NIELSEN, O. V.: Scalar Calibration of Vector Magnetometers; Measurement Science and Technology, 11 (2000), pp 120-132.

[2] PETRUCHA, V. — RIPKA, P. — KAŠPAR, P. — MERAYO, J. M. G.: Automated System for the Calibration of Magnetometers; Journal of Applied Physics, vol. 2009, no. 105, p. 07E704-1-07E704-3

[3] PETRUCHA, V. — KAŠPAR, P.: Compact Fluxgate Sensor with a Vector Compensation of a Measured Magnetic Field; IEEE Sensors 2010 - Proceedings: IEEE Sensors Council, 2010, p. 1795-1798.

Received 24 August 2012

Vojtěch Petrucha (Ing, PhD), born in Přerov, Czech Republic, in 1982. Graduated from the Faculty of Electrical Engineering, Czech Technical University in Prague, in 2007 in Measurements and Instrumentation, and was awarded his PhD degree in 2012 for his work on calibration of magnetometers at the same university. At present he works as a research assistant at the Department of Measurement, CTU in Prague. The main field of his research is the development and calibration of (magnetic) sensors.

Petr Kašpar (Doc, Ing, CSc), was born in Prague in 1955. He was awarded his Ing degree in electrical engineering in 1981 and his CSc degree in measurement technology from the Czech Technical University (CTU), Faculty of Electrical Engineering (FEE) in 1988. Since 1981 he has been working at FEE CTU, where he is presently an Associate Professor and the Executive Deputy Head of the Department of Measurements.
His teaching activities include lectures and laboratory exercises focused on magnetic measurements and magnetic elements. His research interests include electronic integration and systems for magnetic measurements.

7.3 Applications

7.3.1 refP 12

Kletetschka, G.; Vyhnánek, J.; Kawasumiova, D.; Nabelek, L.; Petrucha, V., "Localization of the Chelyabinsk Meteorite from Magnetic Field Survey and GPS Data," IEEE Sensors Journal. 2015, 2015(15), 4875-4881. ISSN 1530-437X

The Chelyabinsk meteorite event provided a unique opportunity to test our vectorially compensated, fluxgate magnetometer in underwater conditions while searching for the (presumably magnetic) meteorite body buried in the deep mud of the lake. This event also prompted the study of GNSS-referenced magnetic mapping, which is currently being used with our UAV fluxgate magnetometers. The author's contribution is 20%; he designed, constructed, tested and calibrated the underwater magnetometer and prepared the publication.

Localization of the Chelyabinsk Meteorite From Magnetic Field Survey and GPS Data

Gunther Kletetschka, Jan Vyhnanek, Darja Kawasumiova, Ladislav Nabelek, and Vojtech Petrucha

***Abstract*— The Chelyabinsk meteorite fragment that landed in the Chebarkul lake in Russia on February 15, 2013 weighed over half a ton. We provide magnetic field maps that were obtained during underwater measurements above the fragment. The data acquisition process was multiple global position system referenced magnetic surveys 0.5–1 m above the top of the lake sediment layer at 10 m water depth. Gradiometric configuration of the survey using two triaxial fluxgate magnetometers helped to suppress local geological anomalies. The location of the ice crater and the underwater magnetic anomaly provided final meteorite landing coordinates, which were made available during meteorite recovery.**

***Index Terms*— Gradient methods, fluxgate sensor, global positioning system, meteorite search.**

I. Introduction

CHELYABINSK bolide parameters indicated that the largest solid fragment surviving the decomposition by heat in the atmosphere landed in Lake Chebarkul, near the city of Chebarkul, on 15 February 2013. The Chelyabinsk meteorite is a rare end product of super bolide, whose initial mass started to defragment and evaporate over the Chelyabinsk region [1]. The initial body reduced down to the largest surviving fragment, with a mass of approximately 600 kg, which plunged through the 80 cm thick ice covering the water of Lake Cherbarkul. Its observed trajectory was 254 km long with an azimuth of 279.5°, and a slope of 16.5° to the horizontal. The speed was 4.3 km/s at the end of registration time at position of 54.922° N latitude, 60.606° E longitude, 14.94 km altitude [1], [2]. The largest fragment landed in Lake Chebarkul, where an 8 m diameter circular opening in ice was found shortly after this meteorite event. Fragments from the bolide event were collected soon after the fall and were of an ordinary chondrite composition [3] with iron/nickel component, providing a potential for magnetic detection [4]–[7]. On 5 March, our team arrived at the site and obtained Global Position System (GPS) coordinates of the crater (using a commercial Garmin 76 unit) whose boundary was outlined by wooden sticks inserted in the ice. A surface magnetic survey was done at this time using a single vector fluxgate magnetometer. An underwater magnetic survey of the impact site was performed on 19-22 June 2013 using a gradiometric configuration of two vector fluxgate magnetometers. Here we present a description of the hardware used for the survey, the results of the instrument calibration, the methodology of the magnetic and GPS data evaluation, and synchronization. Final survey results are confronted with simulations and information obtained during the meteorite recovery on October 2013.

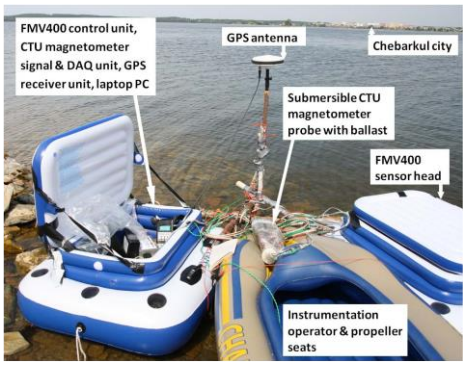

Fig. 1. Improvised non-magnetic vessel equipped with instrumentation for GPS referenced magnetic survey.

II. Instruments and Methods

In our magnetic survey and mapping we used a non-magnetic inflatable boat to cross the water surface in the area where the opening in the ice was created by meteorite impact in the winter. There were three substantial instruments: a geodetic-grade GPS system for precise positioning, one submersible fluxgate magnetometer (developed by CTU in Prague), and one on-board commercial fluxgate magnetometer (MEDA Inc.) that were used for magnetic measurements. There was also a laptop computer present in the boat, which served as a user display and logger for magnetic data (see Fig. 1). The GPS data were stored directly in the instrument and processed offline.

Manuscript received March 11, 2015; revised May 7, 2015; accepted May 10, 2015. Date of publication May 20, 2015; date of current version July 7, 2015. This work was supported in part by MEYS Grant LK21303, in part by Research Plans of the Institute of Geology AS CR RVO67985831, and in part by the Czech Science Foundation under Grant 13-39088P. The associate editor coordinating the review of this paper and approving it for publication was Prof. Kazuaki Sawada.

G. Kletetschka and L. Nabelek are with the Faculty of Science, Charles University in Prague, Prague 116 36, Czech Republic, and also with the Institute of Geology, Academy of Sciences of the Czech Republic, Prague 117 20, Czech Republic (e-mail: gunther.kletetschka@natur.cuni.cz; nabelekl@natur.cuni.cz).

J. Vyhnanek and V. Petrucha are with the Faculty of Electrical Engineering, Czech Technical University in Prague, Prague 166 36, Czech Republic (e-mail: jan.vyhnanek@fel.cvut.cz; vojtech.petrucha@fel.cvut.cz).

D. Kawasumiova is with CaJ Ltd., Prague 129 99, Czech Republic (e-mail: darjakawasumi@gmail.com).

Color versions of one or more of the figures in this paper are available online at http://ieeexplore.ieee.org.

Digital Object Identifier 10.1109/JSEN.2015.2435252

Meteorite localization by magnetic gradiometry was a very similar task to Unexploded Ordnance (UXO) detection, although the anomaly intensity is supposed to be significantly lower for the chondrite type meteorite. The authors deal with UXO detection in ground [8], [9] or underwater [10]–[13] conditions using various instruments and techniques. We considered the application of multi-sensor instruments measuring simple magnitude gradient or even full gradient tensor. The benefits of this multi-sensor approach include higher spatial resolution, wider coverage, and thus faster scanning. We finally decided to use the presented concept of two vector magnetometers because of a high potential risk of loss of the underwater probe (e.g. due to unknown underwater obstacles) and the limited carrying capacity of the expedition. Another suitable instrument developed at our laboratory was still in a test phase [14].

A. GPS for Accurate Positioning of Gradient Measurements

Ashtech's ProMark 2 GPS system was operated in differential mode utilizing a fixed base station and mobile rover receiver, thus reaching centimeter-level accuracy for relative positioning. The rover antenna was positioned above the submersible probe of the magnetometer to follow its position. The speed of the survey was 0.3 m/s at maximum and 0.1 m/s on average to avoid horizontal separation between the probe and antenna. With regards to relative positioning, simultaneous logs of the base and rover station included pseudo-range and carried-phase data, which enabled improved accuracy. Post-processing of the raw data in Ashtech Solutions software indicated the accuracy of each recorded point, which was 3 cm RMS in the worst case of all of the measurements.

The base station unit logged data in a static position. There were two substantial conditions to ensure the desired accuracy: an unobstructed sky view to receive the maximum number of satellites and a solid stand for the antenna. Most of the surrounding terrestrial area was covered with forest and the only suitable place was a sandy area near the anchorage. The antenna was placed on a 2 m tall wooden pole. Each day the base antenna was placed onto the pole, so the only additional error between measurements on different days was the antenna spatial shift after reassembling the base station. The wooden pole was kept on the site and no apparent shift of the pole was noticed between the days of the survey. The positioning error of the antenna attached to the pole was estimated to be 2 cm at maximum.

For absolute positioning in the world coordinate system, the absolute position of the base station was estimated. The most credible method was to place the rover unit on a known geodetic point, so the position of the base was estimated with the accuracy of the relative positioning. Unfortunately, there were no such points available in the survey area. We used data averaging of the long-lasting base station log. Apart from the simple averaging, we used an on-line service Precise Point Positioning (PPP) [15].

The PPP service applies corrected information of satellite orbits and atmosphere conditions for post-processed calculations. We used this to estimate the absolute position in Prague prior the actual survey. The base antenna was positioned in Prague at a point with known coordinates. The log took about 20 minutes in the area with restricted sky view due to buildings. The averaged point was 10.5 m away from the real coordinates. The PPP point showed a ten times lower error, about 1 meter, the indicated standard deviation was 3.3 m.

Three long-lasting base station logs were recorded at Chebarkul Lake: each lasted for about 4 hours. These were selected for averaging and PPP post-processing. Both averaging and PPP gave similar results for these 4-hour logs. We selected the PPP positions for the final coordinate calculation, given the Prague results. The PPP service indicates standard deviations of the estimated positions, which for our data were 1.7 m, 1.5 m, and 1.5 m (day 1, 2, 3, respectively). Assuming independent observations, the final base station coordinates are the result of averaging the three PPP points, each of which was obtained during one day of the magnetic survey. The final coordinates are in the WGS84 system: 54.95828749° N, 60.31818468° E with 0.9 m of combined standard uncertainty.

Synchronization of GPS with magnetometers and mapping positional accuracy needs to account for the fact that GPS and magnetometer data were logged separately and that for data synchronization we used timestamps from magnetometer logs. Time for both magnetometers was derived from the computer clock. The computer clock was manually synchronized each day at the beginning of the survey using a GPS receiver. The accuracy of the time synchronization t_{e_sync} was estimated to be ± 0.5 s. Position error s_{e_sync} in magnetic maps due to the limited synchronization accuracy can be obtained for each point according equation (1). The maximum velocity v during the survey (on 19.6. 2013) was 0.3 m/s, which is similar to other days. So the maximum positioning error is ± 0.15 m.

$$S_{e\_sync} = V \cdot t_{e\_sync} \tag{1}$$

B. Surface Fluxgate Vector Magnetometer (MEDA FVM400)

This compact commercially available tri-axial vector fluxgate magnetometer was used during the first visit to Chebarkul Lake on March 2013 for surface magnetic field mapping. It was used as a surface magnetometer to create a gradiometric configuration for magnetic field mapping during the final measurements on June 2013. The magnetometer has a digital data output (RS232 interface) with 1nT resolution and 1 Sa/s sample rate. The three vector components (X, Y and Z) provided the vector magnitude. The magnetometer offers National Institute of Standards and Technology traceable calibration, but a scalar calibration [16] has been performed to verify and improve its precision. We used a non-magnetic positioning device [17] to precisely collect 55 different vectors of the Earth's magnetic field. The calibration procedure was performed twice and the results are summarized in Table 1. The accuracy of the magnetic field vector magnitude measurement has been improved by a factor of 9 (reduction of magnitude peak-peak variation from 142 nT to 16 nT for differently oriented vectors). As indicated by the results, the sensitivities are well factory

TABLE I
MEDA FMV400 SCALAR CALIBRATION RESULTS

Axis	X	Y	Z
Sensitivity [-]	0.9997	0.9999	0.9997
Orthogonality [°]	0.0926	0.1024	0.0408
Offset [nT]	-3.6	-14.7	-8.9

TABLE II
CTU FLUXGATE MAGNETOMETER SCALAR CALIBRATION RESULTS

	X	Y	Z
Sensitivity [-]	1.0041	0.9904	1.0668
Orthogonality [°]	-0.3910	-0.0019	-0.0501
Offsets [nT]	9.73	-2.91	13.96

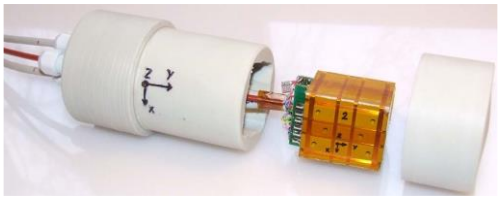

Fig. 2. Vector compensated tri-axial fluxgate sensor before embedding into a watertight package (sensor dimension 48 mm × 40 mm × 40 mm). The sensor was developed at CTU in Prague.

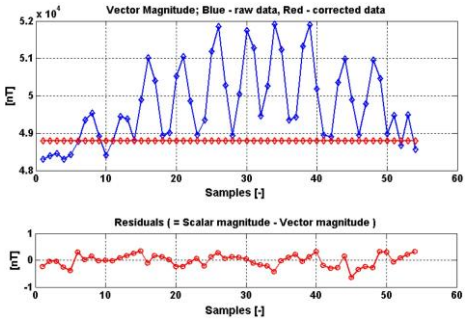

Fig. 3. Comparison of the calculated vector magnitude (vertical axis) before and after scalar calibration (top). Residuals are within 1 nT range (bottom). The calibration is essential for reaching good measurement results.

calibrated but the improvement comes from the calibration of the orthogonality angles.

Although the instrument noise was stable within units of nT during its testing, the recorded data showed up to 40 nT peaks, which were neither related to the real magnetic signal nor other electronic disturbance (verified). Given that these peaks are present only when the sensor is moving (e.g. waves on the lake), they suggest that an FMV400 is not suitable for dynamic measurements. Smoothing the raw waveform with a 20-second moving average resulted in acceptable data for further processing, although this allows only low-frequency homogeneous disturbances to be compensated in the differential data.

C. Submersible Vector Fluxgate Magnetometer

The magnetometer used for underwater survey (DIGMAG) was developed at the Department of Measurement of the Faculty of Electrical Engineering of the Czech Technical University in Prague. The research instrument is a vector compensated tri-axial vector fluxgate magnetometer [18], which has been modified for underwater operation. An improvised watertight plastic package filled with two-component silicone adhesive provided the desired water resistance (see Fig. 2). The sensor head was connected by an 11 m long cable to the signal conditioning and data acquisition electronics carried in the boat. The fluxgate magnetometer sensor head was based on three single-axis ring-core fluxgate sensors, which were embedded into a cuboidal compensation structure. The vector compensation improved the linearity of the sensor by virtually eliminating the cross-field errors and improved the overall stability of the sensor's calibration parameters. The magnetometer had a measurement range of ± 100 μT, the analog signal noise was below 20 pT/$\sqrt{\text{Hz}}$ at 1 Hz, the effective digital resolution was below 100 pT at sample rate of 10 measurements per second, and the offset temperature dependence was 0.1 - 0.5 nT/°C.

The magnetometer was calibrated before the actual survey to assure the best possible performance. The total vector magnitude was used for the gradient measurements to allow scalar calibration. Scalar calibration did not calibrate the sensor's sensitive axes orientation with respect to external reference frame because it is not needed when only the vector magnitude is calculated. The results of the scalar calibration (average of three calibrations) are presented in Table 2. The peak-peak value of magnitude variance was reduced from 3613 nT to 0.974 nT. The main effect came from the calibration of the sensitivities and orthogonality angles. Fig. 3 shows the difference between calibrated and non-calibrated magnitude for different (uniformly distributed) vectors. The regular pattern of the "raw magnitude" came from the positioning sequence. The ambient field was monitored by an Overhauser scalar magnetometer GEMSYS GSM-19 during the calibration (and was used in the data processing).

D. Magnetic Gradient Data

We obtained the magnetic field gradient by subtracting the calculated total field from the submersible and surface probes. Homogeneous fields affecting both probes were eliminated this way and the gradient anomalies were more pronounced. In this case, the improvement was limited to low frequencies. FMV400 logged with a 1-second interval but the data had to be smoothed with a 20-seconds moving average filter (see section B). The geomagnetic field was quiet during the measurement (see data from Novosibirsk Observatory - www.intermagnet.org, [19]) and relevant magnetic anomalies were apparent even without computing the gradient.

The submersible probe detected a low frequency (0.1 Hz) signal, mostly along the x axis (20 nT peak to peak), which

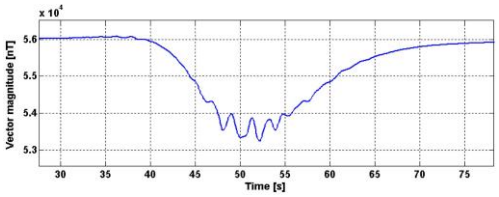

Fig. 4. Effect of waves on measured vector magnitude while crossing the magnetic anomaly area with high gradient.

was attributed to periodic rotation of the probe along the vertical axis. The submersible probe was equipped with ballast (five glass bottles filled with sand) but there was no fin to stabilize the sensor. This effect was probably due to a minor change in the calibration parameters that was induced by the internal pressure in the submersible magnetometer probe; otherwise this effect would not be visible in a gradient free area. The boat was too small (~3.5 m) to compensate the influence of water waves. Therefore, the rope with sensor was moving up and down in rhythm with the waves. When looking closely at the data, the magnetometer sensor in a gradient field showed a frequency signal that closely matched the frequency of the waves (see Fig. 4). These error sources were filtered out to reveal the actual anomalies, which have a lower time frequency because the scanning speed was slow (0.1-0.3 m/s).

III. Results

A. Magnetic Field Survey

The first measurement (March 5) with a single surface operated magnetometer showed a magnetic anomaly of about 80 m N-W of the ice crater. When we used two probes, the differential data indicate a geologic source (e.g. boundary of two geological units) because both magnetometers (i.e. the MEDA measuring on the surface and DIGMAG at 9.5 m depth) show comparable offsets.

Near the crater multiple scans revealed a major magnetic anomaly that was easily detectable by the submersible probe but not by the surface probe. The profiles over the anomaly were selected for the speed of the boat not exceeding 0.1 m/s and were used for further processing. The spatial shift of scans was caused both by the position shift of the GPS antenna and the submersible sensor on a 9.5 m long rope. Therefore, scans at a low speed with smooth narrow movement are preferred. Fig. 5 shows the result of the magnetic survey done during one day.

To align the scans, we developed the following rules. Minimum speed implies minimum spatial shift, and vice versa. Scans in opposite directions have opposite spatial shifts, the scans can be centered if the speed is similar. Once the scans are merged, a dipole-like map of the anomaly can be created. Three dimensional representation of the detected anomaly showed anomaly dominance against the geomagnetic field, which points to the remanent nature of the magnetic source. Fig. 6 presents the final magnetic gradient map that is composed of multiple surveys done during the three days of measurements at Chebarkul Lake. A significant magnetic

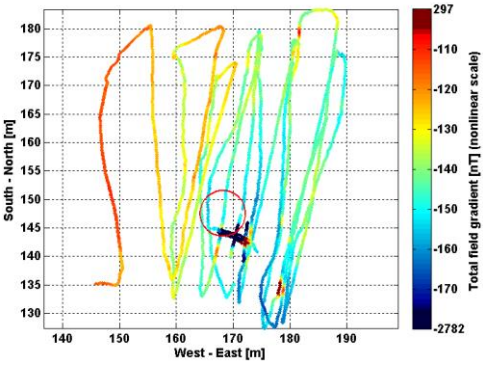

Fig. 5. Magnetic survey results (one day crossing), the red circle shows the probable ice crater position, coordinate axes indicate distances from the base station located at 54.95828749° N, 60.31818468° E.

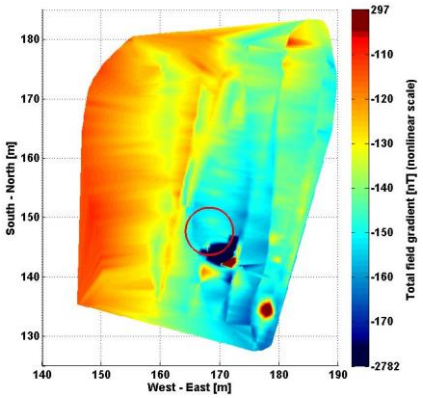

Fig. 6. Multiple survey data combined into one picture.

anomaly is visible at the S-E rim of the supposed ice crater position. The anomaly has a maximum amplitude of 3000 nT (peak - peak) at 9.5 m below water level. However, the 1/r^3 dipole field decay makes its surface detection difficult (i.e. there are few nT gradient levels). There is another anomaly with lower amplitude (450 nT) visible approximately 12 m in a S-E direction from the supposed crater rim, which may be a smaller fragment that has detached from the main meteorite body. The effect of the approaching bedrock is visible in the West side of the map.

Although the GPS antenna - sensor spatial shift error is systematic and is compensated by the corrections, the number of high quality scans is low and the spatial shift error cannot be perfectly eliminated. Considering the values of position corrections applied (e.g. for Y position: 0.6 m, 0.8 m, −0.8 m, 1 m, and 0 m), the error caused by the sensor spatial shift plus the error of estimating the anomaly center should be at maximum ±1 m. With this error estimation, we determined the resulting coordinates of the anomaly center (Fig. 7) as:

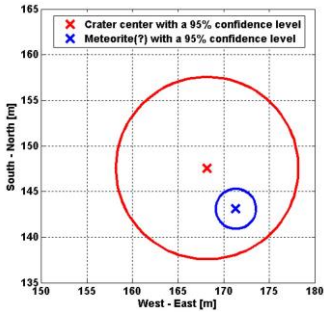

Fig. 7. This chart shows the uncertainty circles of position of both the meteorite impact location (ice crater) and predicted location of the largest meteorite fragment. The axes have their origin at base station coordinates at 54.958287° N, 60.318185° E.

54.959631° N 60.320772° E. For the absolute accuracy evaluation we combine position uncertainties of synchronization $u_{\mathbf{sync}}$, relative positioning $u_{\mathbf{rel}}$, and uncertainty of dipole position $u_{\mathbf{pole}}$, base $u_{\mathbf{base}}$, and rope lag $u_{\mathbf{rope\_lag}}$ (2). Coverage factor k=2 determines confidence interval of 95% to 2.2m.

B. Ice Crater and Meteorite Position

The horizontal shift of the ice crater and magnetic anomaly center is 5.5 m. The meteorite anomaly center was estimated with the absolute positioning accuracy of 2.2m, thus the confidence circle has a diameter of 4.4 m. The crater center was estimated with a Garmin GPS receiver using the internal averaging feature. Its operating manual states that it has an accuracy <10 m, 95%, and does not specify the accuracy of averaging. So the error of 10 m for the confidence level 95% is further considered. The confidence circle has a diameter of 20 m and, therefore, the confidence circles of both locations are overlapping (see Fig. 7)

$$
\begin{aligned}
&u_{total} \\
&= \sqrt{u_{sync}^2 + u_{rel}^2 + u_{pole}^2 + u_{base}^2 + u_{rope\_lag}^2} \\
&= \sqrt{\left(\frac{S_{sync}}{\sqrt{3}}\right)^2 + u_{rel}^2 + \left(\frac{S_{pole}}{\sqrt{3}}\right)^2 + u_{base}^2 + \left(\frac{S_{rope\_lag}}{\sqrt{3}}\right)^2} \\
&= \sqrt{\left(\frac{0.15}{\sqrt{3}}\right)^2 + 0.03^2 + \left(\frac{0.02}{\sqrt{3}}\right)^2 + 0.9^2 + \left(\frac{1}{\sqrt{3}}\right)^2} \\
&= 1.1m
\end{aligned}
\tag{2}
$$

IV. Simulations and Discussion

Simulations taking into account the published magnetic properties [20] suggest that the meteorite was sitting in the very upper layer of the sediment, approximately 10-12 m below the water surface (the sediment started in the depth of 9-11 m). We used several methods for the simulations (i.e. Finite Elements Methods simulations using ANSYS and Flux3D, experimental modeling - dike model and other), considering permanent magnetization as well as susceptibility effects. The simulations confirm the measurement if high values (60 Am^2) of magnetic moment are used in calculations. The meteorite fragment could have been magnetically influenced by the people who tried to pick up small meteorite fragments using strong permanent magnets shortly after the incident. This also brings the possibility that the anomaly was modified by permanent magnet(s) left at the site, which could create a magnetic footprint of similar amplitude.

The main fragment of the Chelyabinsk meteorite (mass of 540kg) was recovered from the bottom of Cherbarkul Lake on 16 October 2013 [21]. Unfortunately, there is no detailed information available concerning the recovery process (e.g. precise GPS coordinates and how deep was the meteorite initially buried in the lake sediments were not provided). The magnetic moment of the recovered main fragment is also unknown. Reference [21] mentions ultrasonic sonar was used to detect the meteorite, but also mentions that the search area was ~35 × 30 m and the divers used multiple pumps to remove large quantities of the sediment. Consequently, it is impossible to confirm our results or those of the other groups [22] who used different methods (GPR). The results of surface measurements of magnetic gradient at the crater location are presented in the supplementary information of [23]. The gradient map shows a magnetic anomaly located at a similar position with respect to the ice crater, but the presented GPS coordinates points to a location shifted by 28 m to the south.

V. Conclusion

Our GPS referenced magnetic survey attempted the absolute localization of both the impact in the ice crater and the final position of the major meteorite fragment from the Chelyabinsk event. Data analysis revealed that the impact location in the ice was centered at 54.95967° N and 60.32072° E, with a 95% confidence circle that has a diameter of 20 m. The magnetic anomaly indicates the possible location of the largest fragment of the meteorite that broke through the ice. This location was centered at 54.959631° N and 60.320772° E, with a 95% confidence circle that has a diameter of 2.2 m. Magnetic numerical and experimental modeling suggests that the source of this magnetic anomaly was shallow, probably not deeper than 1m in the sediment.

Acknowledgment

The authors would like to thank A. Orlov, V. Korolkov, S. Zacharov, and M. Klucar. Special thanks to P. Ripka for advice with the measurement procedure and securing the geodetic grade GPS receivers, B. Koska for help during the GPS system testing and data processing, V. Vigner for providing spare GPS time synchronization modules, and M. Janosek who helped with magnetometer calibration and magnetic data interpretation.

References

[1] J. Borovicka, P. Spurny, and L. Shrbeny, "Trajectory and orbit of the Chelyabinsk superbolide," Int. Astronomical Union, Cambridge, MA, USA, Electron. Telegram No. 3423, 2013.

[2] J. Borovička *et al.*, "The trajectory, structure and origin of the Chelyabinsk asteroidal impactor," *Nature*, vol. 503, pp. 235–237, Nov. 2013.
[3] E. M. Galimov *et al.*, "Analytical results for the material of the Chelyabinsk meteorite," *Geochem. Int.*, vol. 51, no. 7, pp. 522–539, 2013.
[4] N. S. Bezaeva, D. D. Badyukov, M. A. Nazarov, P. Rochette, and J. Feinberg, "Magnetic properties of the Chelyabinsk meteorite: Preliminary results," *Geochem. Int.*, vol. 51, no. 7, pp. 568–574, 2013.
[5] C. Cournède, J. Gattacceca, and P. Rochette, "Magnetic study of large apollo samples: Possible evidence for an ancient centered dipolar field on the moon," *Earth Planetary Sci. Lett.*, vols. 331–332, pp. 31–42, May 2012.
[6] J. Gattacceca *et al.*, "Can the lunar crust be magnetized by shock: Experimental groundtruth," *Earth Planetary Sci. Lett.*, vol. 299, nos. 1–2, pp. 42–53, 2010.
[7] L. Folco, P. Rochette, J. Gattacceca, and N. Perchiazzi, "In situ identification, pairing, and classification of meteorites from Antarctica through magnetic susceptibility measurements," *Meteoritics Planetary Sci.*, vol. 41, no. 3, pp. 343–353, 2006.
[8] G. Marin, S. Radu, G. Samoilescu, and O. Baltag, "The analysis of gradiometer signal in magnetic field measurement with fluxgate transducer," in *Proc. 10th Int. Conf. Commun. (COMM)*, May 2014, pp. 1–6.
[9] R. Wiegert, K. Lee, and J. Oeschger, "Improved magnetic STAR methods for real-time, point-by-point localization of unexploded ordnance and buried mines," in *Proc. OCEANS*, Sep. 2008, pp. 1–7.
[10] M. Tchernychev, J. Johnston, and R. Johnson, "Total magnetic field transverse gradiometer as UXO locating tool: Case study," in *Proc. EGM Int. Workshop*, Capri, Italy, 2010, pp. 1–3.
[11] Y. H. Pei and H. G. Yeo, "UXO survey using vector magnetic gradiometer on autonomous underwater vehicle," in *Proc. MTS/IEEE Biloxi-Marine Technol. Our Future, Global Local Challenges OCEANS*, Oct. 2009, pp. 1–8.
[12] E. Mersch, Y. Yvinec, Y. Dupont, X. Neyt, and P. Druyts, "Underwater magnetic target localization and characterization using a three-axis gradiometer," in *Proc. OCEANS-TAIPEI*, Apr. 2014, pp. 1–6.
[13] G. L. Allen, G. Sulzberger, J. T. Bono, J. S. Pray, and T. R. Clem, "Initial evaluation of the new real-time tracking gradiometer designed for small unmanned underwater vehicles," in *Proc. MTS/IEEE OCEANS*, 2005, vol. 3, pp. 1956–1962.
[14] M. Janosek, A. Platil, J. Vyhnanek, and J. Brinek, "Dual-core fluxgate gradiometer with gradient feedback," in *Proc. IEEE SENSORS*, Nov. 2013, pp. 1–3.
[15] Natural Resources Canada. *Precise Point Positioning*. [Online]. Available: http://webapp.geod.nrcan.gc.ca/geod/tools-outils/ppp.php?locale=en, accessed Jun. 12, 2013.
[16] J. M. G. Merayo, P. Brauer, F. Primdahl, J. R. Petersen, and O. V. Nielsen, "Scalar calibration of vector magnetometers," *Meas. Sci. Technol.*, vol. 11, no. 2, pp. 120–132, 2000.
[17] V. Petrucha, P. Ripka, P. Kaspar, and J. M. G. Merayo, "Automated system for the calibration of magnetometers," *J. Appl. Phys.*, vol. 105, no. 7, p. 07E704, 2009.
[18] V. Petrucha, M. Janosek, and M. A. Azpurua, "Vector feedback homogeneity and inner layout influence on fluxgate sensor parameters," *IEEE Trans. Instrum. Meas.*, vol. 64, no. 5, pp. 1293–1299, May 2014.
[19] D. Kerridge, "INTERMAGNET: Worldwide near-real-time geomagnetic observatory data," in *Proc. Workshop Space Weather*, 2001, pp. 1–4. [Online]. Available: http://www.intermagnet.org/publications/IM_ESTEC.pdf
[20] N. S. Bezaeva *et al.*, "Magnetic properties of the LL5 ordinary chondrite Chelyabinsk (fall of February 15, 2013)," *Meteoritics Planetary Sci.*, vol. 49, no. 6, pp. 958–977, 2014.
[21] A. V. Kocherov, A. V. Korochantsev, C. A. Lorenz, M. A. Ivanova, and V. I. Grokhovsky, "Recovery, laboratory preparation and current state of the main mass of the Chelyabinsk meteorite," in *Proc. 45th Lunar Planetary Sci. Conf.*, 2014, p. 2227.
[22] V. V. Kopeikin, V. D. Kuznetsov, P. A. Morozov, A. V. Popov, A. I. Berkut, and S. V. Merkulov, "GPR inspection of the Chelyabinsk meteorite impact site at the Chebarkul Lake bottom," in *Proc. 15th Int. Conf. Ground Penetrating Radar (GPR)*, Jun./Jul. 2014, pp. 1024–1027.
[23] O. P. Popova *et al.*, "Chelyabinsk airburst, damage assessment, meteorite recovery, and characterization," *Science*, vol. 342, no. 6162, pp. 1069–1073, Nov. 2013.

Gunther Kletetschka was born in Litomerice, Czech Republic, in 1964. He received the B.S. degree in physics/geophysics in 1989, the RNDr (Equivalent of M.S.) degree in physics/geophysics from the Charles University in Prague, Czech Republic, in 1989, and the M.S. and Ph.D. degrees in geology/geophysics from the University of Minnesota, Minneapolis, MN, USA, in 1994 and 1998, respectively.

He joined the Department of Geophysics and Meteorology, Faculty of Science, Charles University, in 1989, as a Teaching Assistant/Lecturer. Since 1991, he has been a member of the Department of Geology and Geophysics, University of Minnesota, where he was a Teaching Assistant/Lecturer. Since 1998, he has been with NASA GSFC, Greenbelt, MD, USA, first as a Post-Doctoral Researcher with the National Research Council and then as a Contractor via Research Professor at Howard University, Catholic University of America, Delaware University. In 2004, he joined the Institute of Geology, and Academy of Sciences of the Czech Republic as a Research Scientist. In 2011, he joined the Faculty of Science, Charles University in Prague, Czech Republic. Since 2010, he has been a Guest Researcher at NIST, Geithersburg, MD, USA, and the Lawrence Berkeley National Laboratory in Berkeley, CA, USA, since 2013.

His current research interests include planetary geophysics, magnetic mineralogy, climate change, and planetary instruments. He leads the group of extraterrestrial geology and geophysics and is serving on NASA panels for proposal reviews.

Jan Vyhnanek was born in Prague, Czech Republic, in 1987. He received the M.Sc. degree in measurements and instrumentation from the Faculty of Electrical Engineering, Czech Technical University in Prague, Prague, in 2011, where he is currently pursuing the Ph.D. degree at the Department of Measurement. He is mainly interested in magnetic sensors and their applications in object detection.

Darja Kawasumiova was born in Czech Republic in 1955. She received the bachelor's degree in liberal arts, intercultural/interhuman relationships from the International Christian University, Tokyo, in 1982.

She returned in 1992 from Japan back to Czech Republic and graduated from Charles University, Prague, Czech Republic, receiving Bachelor of Liberal Arts in 1994, Japanese Studies, and Mast of Liberal Arts in 1999. She then studied at the Wesley Theological Seminary, Washington DC, USA, and received the Master of Theology Studies in 2010. The art of hospitality as a tool to enhance understanding between nations, cultures, religions, religion, and science is her life academic theme. In her Master thesis, at Charles University, she searched for bonds between the Western Christian thought and the Eastern philosophy, as represented in the art of communication and hospitality, the core of the Japanese Tea Ceremony. In her Master thesis, at Wesley, she used the Tea Ceremony theme to support her theology, in which a great role is given to human hospitable creativity. She returned to Czech Republic in 2011, and searched for connections between science and art. She currently runs CaJ Ltd. (CaJ stands for Czech and Japan)

Ladislav Nabelek was born in Prague, Czech Republic, in 1991. He graduated with a Degree in electrical engineering from High School Technical F. Krizika, Prague, in 2011, and received the B.S. degree in geology from the Faculty of Science, Charles University in Prague, in 2014, where he is currently pursuing the Degree in applied geophysics.

He joined the Institute of Geology, Academy of Sciences of the Czech Republic, in 2011, as an Assistant and Laboratory Technician of Science and Research. In 2012, he joined the Extraterrestrial Geology and Geophysics Group, Faculty of Science, Charles University in Prague, Czech Republic. His current research interests include planetary geophysics, magnetic mineralogy, climate change, and planetary instruments.

Vojtech Petrucha was born in Prerov, Czech Republic, in 1982. He received the M.Sc. degree in measurement and instrumentation and the Ph.D. degree in measurement and instrumentation for work on the calibration of magnetometers from the Faculty of Electrical Engineering, Czech Technical University in Prague, Czech Republic, in 2007 and 2012, respectively.

He is currently a Research Assistant with the Department of Measurement, Faculty of Electrical Engineering, Czech Technical University in Prague. His research interests include the development, construction, and calibration of sensor systems, especially magnetic field sensors.

7.3.2 refP 13

Petrucha, V.; Ripka, P., "Rotational Speed Measurement and Angular Position Reference for a Cryogenic Propellant Electric Pump," Journal of Electrical Engineering. 2015, 66(7), 199-202. ISSN 1335-3632

This paper refers to the author's work done within the 7th Framework project - SPACE, where he participated on the project "In-Space-Propulsion-1". In this case, the sensor that was finally selected for the measurement of the magnetic field of the electric pump rotor was a Hall-effect sensor, mainly due to its small size and good cryogenic compatibility. The author's contribution was 50% and this three-year project provided great insight into space technologies testing and also to the peculiarities of cryogenic condition handling.

Journal of ELECTRICAL ENGINEERING, VOL 66. NO 7/s, 2015, 199-202

ROTATIONAL SPEED MEASUREMENT AND ANGULAR POSITION REFERENCE FOR A CRYOGENIC PROPELLANT ELECTRIC PUMP

Vojtěch Petrucha* — Pavel Ripka*

Hall sensors with an analog output were used as rotational speed sensors and provided an angular position reference for other diagnostics measurements during a cryogenic Propellant Electric Pump (PEP) test campaign. Frictionless foil bearing, which is a very important technology that needs to be well characterized during the tests, was tested in the PEP. Hall sensor outputs helped to process signals from eddy current radial and axial shaft displacement sensors and piezoelectric vibration sensors. The Hall sensor signal was also used as the main motor speed feedback signal for the test-bench control system.

Keywords: Hall sensor, electric motor, rotational speed measurement, angular reference

1 INTRODUCTION & MOTIVATION

Hall sensors with an analog output were used as rotational speed sensors and provided an angular position reference for other diagnostic measurements during a Propellant Electric Pump (PEP) test campaign. There is a strong scientific and commercial demand for a new generation of space propulsion systems. Several new technologies for re-ignitable medium thrust cryogenic in-space propulsion were evaluated and developed in a recent project [1]. The PEP designed for delivering liquid hydrogen or methane to the rocket motor was one of the core project topics [2]. The PEP development was led by Snecma (now Airbus Safran Launchers) together with Mikroma (who developed and delivered the electric motor). Czech Technical University in Prague provided a set of PEP sensors, signal conditioning, data acquisition and signal processing software. The measurement setup cooperated with a test-bench control system at the University of Liege, where the whole test campaign was conducted.

Frictionless foil bearing, which is a very important technology that needs to be well characterized during the tests, was tested in the PEP. There were multiple sensors on the PEP: three orthogonal shaft displacement sensors (based on eddy currents), temperature, pressure, vibration and shaft speed / angular position (SPD) sensors. Their layout is shown in Fig.1. Two linear output Hall sensors were used as the SPD sensors. The purpose of the SPD sensors was to provide reliable and redundant rotor speed information and improve the precision of shaft displacement measurement processing. This paper will present the effort to select an appropriate Hall sensor, its testing and qualifications for the application in the cryogenic conditions of the PEP, as well as the methodology for evaluating the rotor-permanent magnets' sensing and final measurement results.

Both digital and analog output Hall sensors are used for rotor position sensing while driving brushless DC electric motors. In conventional design, the position sensors are mounted at the end of the shaft outside the stator coils. In order to reduce the total rotor length and reduce the complexity of the mechanical design, we were forced to integrate the sensors between the stator coils so that they sensed the magnetic field of the rotor-permanent magnets. A similar approach was used in [3] for a compact pancake motor. An extensive effort was spent to prove that the Hall sensor will not be influenced by the motor currents; they will correctly sense the rotor-permanent magnets, and they will not pose any threat to other components or the whole system.

2 SENSOR SELECTION & TESTING

The space industry puts a lot of emphasis on using components that have already been successfully used in space projects and thus have the proper qualifications (Technology Readiness Level). If the component is new, it should be fully specified by its manufacturer for intended operating conditions, which usually increases the price and decreases the availability. In our case, the limiting parameters were the intended operating temperature range (-253–30°C; LH2 to ambient) and vibration resistance (20–2,000 Hz; 20 gr).

At first, we considered cryogenic Hall sensors supplied by Lakeshore or Arepoc, which fulfilled at least the operating temperature range. We ordered an HHP-NA from Arepoc and did preliminary testing in LN2. The sensor worked properly but we realized that its size (7 mm diameter, 8 mm length) and mechanical construction (not shock-vibration proof) was not optimal for our application. Additionally, there was a strong pressure to minimize the cost of the sensor since multiple pieces were needed (several prototypes of PEP motors built). The literature indicated that even a non-cryogenic Hall sensor can work in cryogenic conditions [4]. Finally, we ordered a CY-P3A sensor from Chenyang GmbH, which offered a very wide temperature range (−100°C to 180°C) and also

* Department of Measurement, Faculty of Electrical Engineering, Czech Technical University in Prague, Technická 2, Prague 6, 166 27; petruvoj@fel.cvut.cz

ISSN 1335-3632

a very acceptable price (<5 EUR/piece compared to 260 EUR for HHP-NA)—see Table 1 for the sensor's main parameters.

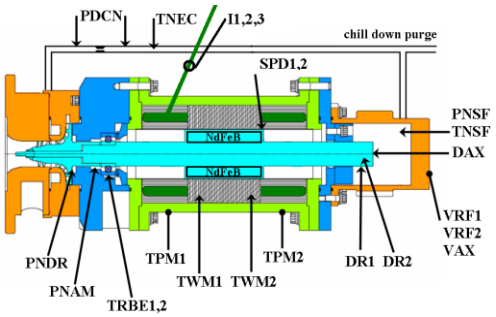

Fig. 1. Schematic model of the PEP, showing the location of various sensors: temperature (TRBE, TPM, TWM, TNSF, TNEC), pressure (PNDR, PNAM, PNSF, PDCN), shaft displacement (DR, DAX), vibrations (VR, VAX) and speed (SPD).

Table 1. CY-P3A Hall sensor main parameters

Sensitivity	380 V/A.T
Measurement range	0.1μT – 2 T
Input/output resistance	1.3 kΩ (typ.)
TempCo of Hall voltage	−0.08 %/°C
Linearity	1% (typ.)
Control current	1 mA (4.5 mA max.)
Package, Dimensions	SOT23, 3×2.5×1 mm

In order to qualify the sensor for our application, we successfully passed several tests: we tested sensitivity variation with respect to temperature (down to -196°C, using LN2), multiple ambient-cryogenic-ambient temperature cycling and vibration testing.

We used a permanent magnet placed outside of a little thermostatic chamber to provide a constant measured field and monitored the output of the probe with a DAQ card as well as the temperature using a PT100 sensor. The measurements were in line with the datasheet and no undesirable behavior was observed. The same applied for the temperature shock tests, however, the rate of change of the temperature was higher in this case (>100 °C/s). We looked for any discontinuity in the output signal during the procedure and cracks in the package after the test. Three randomly selected pieces of the CY-P3A sensors worked well. The vibration testing was done on a final assembly of the sensor; the SOT23 package was soldered directly to Vishay STC-32T-4, PTFE insulated, shielded cable and encapsulated with Stycast 2850FT epoxy (see Fig. 3). For testing, we used an improvised system consisting of a small vibration shaker, power amplifier, computer controlled arbitrary waveform generator, reference sensor with an amplifier and a DAQ system for monitoring the Hall sensor output. The sensor behaved correctly as we tried to copy the recommended Ariane 5 launcher vibration spectrum.

3 MEASUREMENT METHOD QUALIFICATION

As previously mentioned, it is essential in the space industry to prove that every component or system will work as expected and will not jeopardize any other system. The main concerns were related to the possibility of influencing the Hall sensor output signal with motor currents, which generate a magnetic field in the neighboring area. Another issue was connected to the proper installation of the sensor harness, as it could cause leakage problems if not treated properly.

The first prototype of the pump's electric motor, which was equipped with the Hall sensor, did not show acceptable results. It was proven by an X-ray inspection that the sensor was not installed correctly, its sensitivity axis was in the wrong direction and it was too far from its optimal position (see Fig. 2).

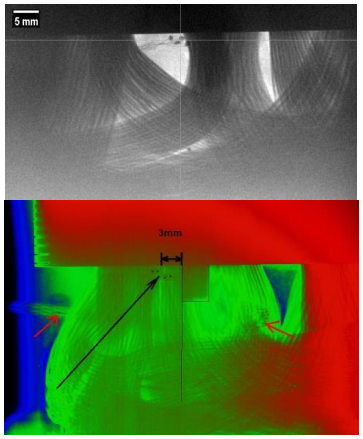

Fig. 2. X-ray inspection of the motor stator. The sensor position and orientation is visible thanks to a high-contrast Pb-Sn solder. Stator magnetic material sheets are on top and Cu winding is in the bottom part of the picture. The bottom picture shows the orientation with respect to a small permanent magnet placed to the nearest position in the rotor area.

This event triggered an even more detailed investigation of the sensor position's influence on the output signal. Additionally, we installed two Hall sensors into a prototype of the electric motor in such a way, that we could test the Hall sensor output signal with respect to its position to rotor-permanent magnets (see Fig. 4).

Fig. 3. Final construction: Hall sensor soldered to Vishay cable and protected by Stycast 2850FT epoxy

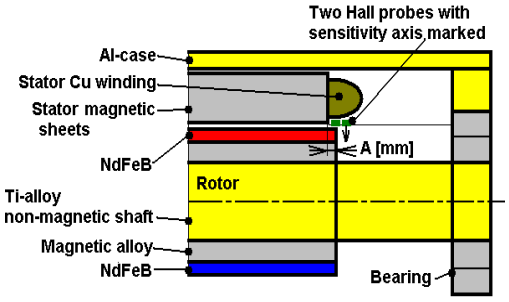

Fig. 4. Schematic drawing of the Hall sensor placement during its qualification tests. The "A" dimension is a distance between the end of the rotor permanent magnet section and the beginning of the stator magnetic sheets section. The Hall sensors were placed close to the stator sheets.

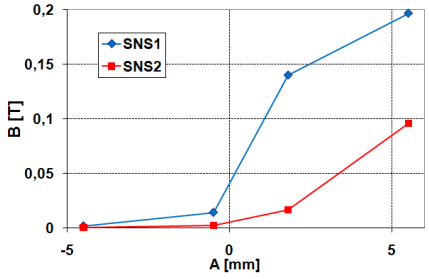

Fig. 5. Magnetic induction (max) measured by Hall probes with respect to "A" distance.

There were two rotors available, which differed very slightly in the linear position of the permanent magnet section. Because of these two rotors, and along with the fact that it was possible to mount the rotor "normally"—or, turned by 180 degrees to the stator - we were able to test four different distances, which are marked "A" in Fig. 4. Fig. 5 shows the maximal amplitude of a magnetic induction measured by the two Hall sensors. SNS1, which produced a higher amplitude, was always the one closer to the permanent magnet section. The expected normal operation position was at +2 mm, and the sensors were supposed to be mounted in SNS1 position, which gave a sufficient margin for reliable function. Finally, the Hall probes (shifted angularly by 90 degrees) were embedded into two stators, which differed slightly in nominal operation parameters (two Hall probes per each stator, see Fig. 6).

A specific setup of two mechanically coupled prototype motors was used to test the influence of the Hall sensor signal by stator winding currents. We monitored the Hall sensor output signal, which was placed in one of the motors (motor 1). At first, we used the other motor (motor 2) to spin motor 1. Therefore, there was no current in the stator windings of motor 1 (see Fig. 7: I = 0 A). Then, we connected motor 1 to the driver and used motor 2 as a brake (by connecting the load to its stator coils). In this way, we were able to see the influence of stator winding currents on the Hall sensor signal (see Fig. 7: I = 2.2 A and I = 5.3 A; nominal motor current). There is a visible influence; the shape of the signal is changed and there is a small increase in the amplitude of the signal. Finally, we concluded that the stator current's influence is acceptable and will not cause any trouble while processing the Hall sensor's signal for speed and raw angular position estimation (less than 10 degrees error thank to normalization of the signals prior to further processing).

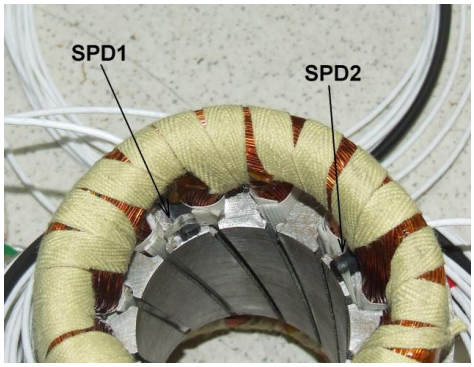

Fig. 6. Installation of the Hall sensors to the motor stator. Later, the assembly was placed into an aluminum alloy case and filled with epoxy.

4 TEST CAMPAIGN RESULTS

The SPD sensor proved to be reliable and useful during the PEP test campaign. Because of safety and cost issues, the PEP operated only with liquid nitrogen (LN2), although all components were tested and made as compatible to liquid methane and hydrogen as possible. The measured speed was in a range of 0-19000 rpm (LN2 operation), but the SPD sensors were tested to be usable up to 55000 rpm (LH2 operation, signal frequency of 917 Hz, two poles rotor). The measurement accuracy was excellent as the frequency measurements are usually very precise (< ±1 rpm, given by the measurement period). The Hall sensor signal was very useful during transient events; it clearly showed every irregularity in the pump function, which was caused, for example, by the tested foil bearing. The motor driver speed signal's bandwidth was too limited for this purpose. The angular position estimation precision was limited to approximately 10 degrees (due to the distortion of the signal and motor driver disturbances). Figure 8 shows a few of the start-up periods of the PEP rotation.

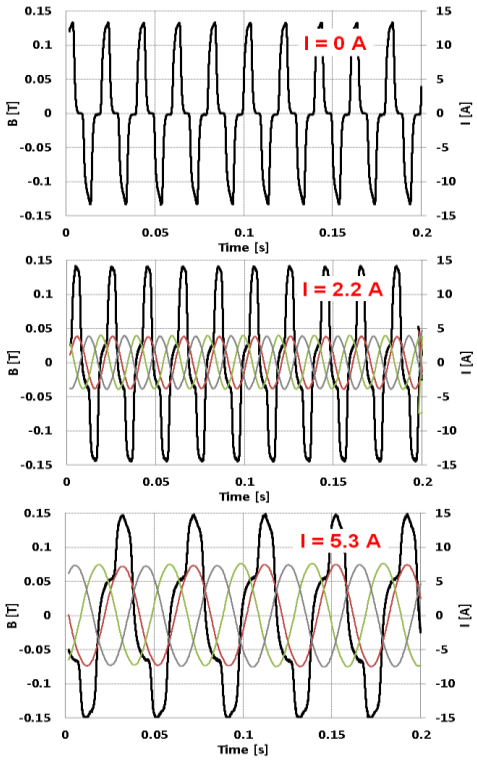

Fig. 7. Hall probe output waveforms for various motor currents (0 A, 2.2 A and 5.3 A)

.

5 CONCLUSION

The PEP operated well during all scheduled tests and the test campaign was prolonged to test several additional configurations of the foil bearing. Altogether, far more than 20 000 liters of LN2 were pumped. The SPD sensor proved to be very useful and reliable except in one issue, which it shared with the TWM sensors. The SPD and TWM sensors used a Vishay STC-32T-4, PTFE insulated cable. Together, four cables went from the motor body through one bushing. Despite the fact that the free volume of the stator was filled with Stycast 2850KT epoxy, and the PTFE outer cable insulation had an "activated" surface, there was a considerable leakage through the bushing after a certain time. It was a lesson in what thermal expansion can do and that even a small detail can cause serious troubles in some applications.

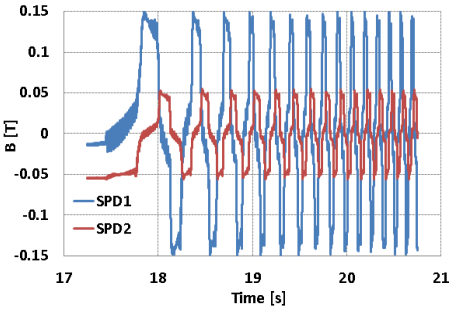

Fig.

Fig. 8. Hall sensors signal (non-filtered, with significant motor driver noise), recorded during the final test campaign. It shows the acceleration of the PEP from zero rpm. There is a ninety degree phase-shift clearly visible between the SPD1 and SPD2 sensors (given by their mechanical placement). The amplitude of SPD2 signal is lower, most probably because of a wrong gain setting in its signal conditioning circuit. It did not affect the results as both signals were normalized prior to further processing. The SPD signals were very useful during transient events; the motor driver speed signal bandwidth was too limited for this purpose.

Acknowledgement

The In Space Propulsion - 1 project was partly funded by the European Commission, grant No. 218849, under the 7-th Framework Program. The authors also thank all the partners who participated in the project.

REFERENCES

[1] MUSZYNSKI, M. – ALLIOT, P.: The In-Space Propulsion (ISP-1) Project. In Proceedings of the 61st International Astronautical Congress, ISBN: 978-1-61782-368-8, p. 4912, IAC-10-C4.3.10, Prague, Czech Republic, 2010 Available from: http://isp1-fp7.perso.sfr.fr/documents/iac_10_c4_3_10_isp1.pdf

[2] LEMAITRE, A. – MARCIQUET, C.: Propellant Electric Pump for low thrust cryogenic propulsive systems. 4th European Conference for Aerospace Sciences (EUCASS), Saint Petersburg, Russia, 2011 Available at: http://eucass2011.conferencecenter.ru/cs/upload/gF76bMq/papers/papers/978-1505-1-RV.pdf

[3] SIMPKINS, A. – TODOROV, E.: Position Estimation and Control of Compact BLDC Motors Based on Analog Linear Hall Effect Sensors. In Proceedings of the American Control Conference. New York: IEEE, 2010 ISBN: 978-1-4244-7427-1, Available from: https://homes.cs.washington.edu/~todorov/papers/SimpkinsACC10.pdf

[4] GONZALEZ-JORGE, H. – QUELLE, I. – CARBALLO, E. – DOMARCO G.: Working with non-cryogenic Hall sensors at 77 K. Cryogenics 46, 736–739, 2006.

Received 30 November 2015

7.3.3 refP 14

Fúra, V.; Petrucha, V.; Platil, A., "Construction of an AMR magnetometer for car detection experiments," In: Proceedings of 5th International Conference on Materials and Applications for Sensors and Transducers (IC-MAST2015). Bristol: IOP Institute of Physics, 2016. IOP Conference Series: Materials Science and Engineering. ISSN 1757-899X

This conference paper is related to **refP1**, in this case we were testing the concept and also available AMR magnetic sensors. A possible application was the mapping of various cars' magnetic signature and subsequently the detection of parking lot occupancy using a gradiometric sensor setup. One could expect that the manufacturing technology behind an AMR sensor is simple, but we proved that products manufactured by Memsic (AFF755) as a possible replacement of Honeywell's HMC1021 were suffering of anomalous offset jumps, most probably related to the bad quality of the Permalloy layer or the poor design choice of magnetizing flipping coils. The author's contribution was 34%, it includes the supervision of V. Fúra (a master's student of the author) and assistance with the magnetic measurements.

V Fúra et al 2016 IOP Conf. Ser.: Mater. Sci. Eng. 108 012028
DOI 10.1088/1757-899X/108/1/012028

Construction of an AMR magnetometer for car detection experiments

V Fúra, V Petrucha and A Platil[1]
Czech Technical University in Prague, Technicka 2, 166 27 Prague, Czech Republic

E-mail: platil@fel.cvut.cz

Abstract. A new construction of magnetometer with commercially available AMR (anisotropic magnetoresistive) sensors intended for vehicle detection experiments is presented. Initial experiments with simple AMR gradiometer indicated viability of the approach in a real-world setup. For further experiments and acquisition of representative data, a new design of precise multi-channel magnetometer was developed. The design supports two models of commercial AMR sensors: the proven and reliable, but obsolete Honeywell HMC1021-series sensors and newly available Sensitec AFF755B sensors. In the comparison the two types are similar in most achieved parameters, except offset stability in flipped operation regime. Unfortunately, the new AFF755B sensors seem to have perhaps inferior coupling of the flipping (set/reset) coil to the ferromagnetic core that causes insufficient saturation of the AMR material. The issue is being solved by Sensitec, current deliverables of the AFF755B have "product sample" status (September 2015).

1. Introduction

In the framework of an industrial cooperation project, we develop car detection system with AMR sensors as the preferred solution. Initial experiments with simple AMR gradiometer made of pair of Phillips KMZ51 (with fluxgate magnetometer Billingsley TFM100G2 as a reference) indicate viability of the scheme in accordance with literature [1, 2, 3]. The typical car signature is well in excess of 1 μT deviation from background in 4 m distance. In order to conduct further experiments and accumulate larger amount of representative real-world data in the field of car detection, a new construction of an AMR magnetometer is developed, offering flexible operating parameters (sample rate, flipping, feedback compensation).

Well established and proven AMR sensors (Honeywell HMC1001, HMC1021 and Phillips KMZ51) have unfortunately recently became obsolete and stock shortages are imminent. For modern constructions, new types of sensors with (at least nominally) comparable parameters are available, namely AFF755B from Sensitec. In order to compare the new sensors with their obsolete counterparts, we decided to make overall testing of their parameters when used in new AMR magnetometer. The design supports two possible types of 3-axis sensor probe construction, with slightly different magnetic field feedback compensation coils. Internal (on chip) compensation/test coils are not used

[1] To whom any correspondence should be addressed.

due to poor coil constant and thus high current needed. The flipping is frequently used in AMR sensors to periodically re-magnetize the ferromagnetic sensor core using another built-in (on chip) coil and short intense unipolar current pulses. It is also possible to alternate the core magnetization between two polarities (N-S or S-N) using positive and negative current pulses, effectively alternating the sensor response polarity which may help in suppressing offsets and/or hysteresis [4, 5, 6]. The flip current RMS value (i.e. thermal effects) must be carefully considered, which dictates short maximum pulse duration.

2. Experiment

The analog output signals from sensors are processed and sampled by a quad (or octal), max. 144 kSa/s, simultaneous sampling 24-bit delta sigma ADC (ADS1278 by Texas Instruments). In the basic configuration, three magnetic channels (x, y, z) and temperature is measured at 10.3 kSa/s rate. Lower than maximum sample rate is used in order to save power. Optionally, another 3-axis probe can be added, thus forming gradiometric configuration. Full scale range of the instrument is ±350 μT. The device is controlled by a 32-bit microcontroller Microchip PIC32MX795F512L (an FPGA is considered as an alternative solution), permitting change of many parameters on the fly.

In the current test implementation the feedback compensation of measured field is permanently active. The flipping pulses (set/reset in Honeywell parlance) can be optionally activated at 10 kHz (at the expense of theoretically limited signal bandwidth), deactivated, or single-fired at request. With flipping active, the signal is preprocessed with switching synchronous detector. The digital output rate can be configured in wide range (1 to 10 300 Sa/s) in order to suit target application. The output data are averages of raw inputs sampled at 10.3 kSa/s. Sleep mode with ADC and flipping deactivation is available. The block diagram of one channel is shown in figure 1. The data are transmitted via USB or RS232 interface to the host computer, processed and graphically displayed in custom application written in National Instruments LabView.

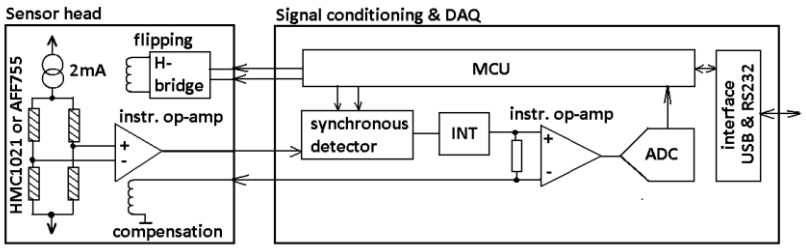

Figure 1. Block diagram of the magnetometer (one channel of analog signal is shown).

The magnetic calibration (determining offsets, scale factors and angular deviations from x-y-z orthogonality) was performed by scalar calibration method in homogenous field using nonmagnetic positioning device [7]. The noise data were acquired with sensors in a 6-layer permalloy tubular shield in lab environment. In all cases, the noise spectra are calculated from output digital data incoming at 206 Sa/s rate (each output value is an average of 50 raw ADC readings sampled at 10.3 kSa/s).

3. Results and discussion

The main focus of the current development was comparison of classical but obsolete sensors of Honeywell HMC1021-series with newly available Sensitec AFF755B-series. In most aspects, these

two models of sensors are quite comparable, e.g. open loop sensitivity is about 1 mV/V / 100uT in both models. However, we have observed strong differences in offset stability and noise behavior of these two sensors in flipped and non-flipped mode.

Firstly, the noise of electronics measured without the sensors connected was only some 46 pT/sqrtHz@1Hz, so it is safely below either sensor noise level. The output noise PSD (power spectral density) with HMC1021 sensors in operating mode *with* flipping (current pulse 454 mApk) is about 240 pT/sqrtHz@1Hz as shown in figure 2 (the best case was about 120 pT/sqrtHz@1Hz). Interestingly, *without* flipping the noise was somewhat worse, typically 800 pT/sqrtHz@1Hz.

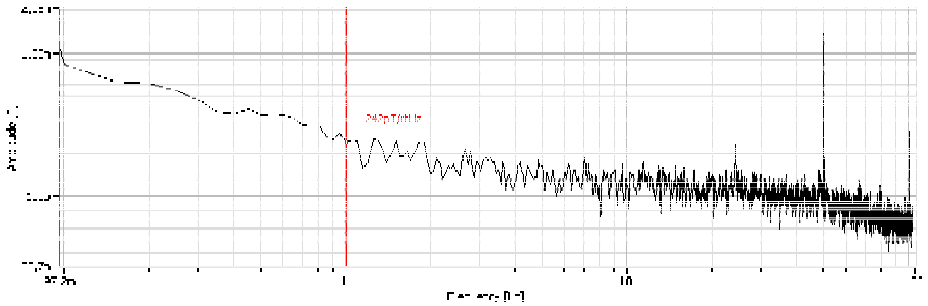

Figure 2. The noise PSD of the electronics with HMC1021 sensors, with flipping.

For the AFF755B sensors *without* flipping the PSD was similar (300 pT/sqrtHz@1Hz) to that of HMC1021 *with* flipping. However, *with* flipping, the AFF755B noise did not improve as expected, but was much worse: in the order of 10 nT/sqrtHz@1Hz - see figure 3.

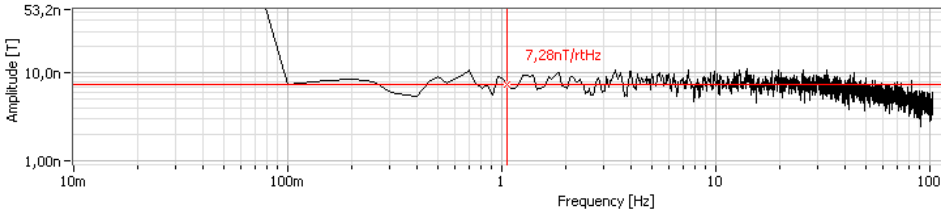

Figure 3. The noise PSD of the electronics with AFF755B sensors, with flipping.

Increasing the flipping current amplitude did not improve the noise either. The figure 4 (left) provides comparison of PSD measured values for various flipping currents. It was also observable that output offset in AFF755B is quite unstable with flipping - see figure 4 right.

4. Conclusions

We have constructed multiple-axis AMR magnetometer with feedback compensation and compared two types of commercially available AMR sensors. The only significant difference observed between the two models of AMR sensors was in flipped mode. The flipping (set/reset) in classical Honeywell HMC1021 works very well, suppressing offsets without compromising the noise quality. Also the current peaks needed for effective flipping is reasonably small: 450 mApk. In contrast, in Sensitec AFF755B sensors (sample deliverables), similar or even higher level of flipping current peaks perhaps

does not guarantee good saturation of the core and results in unacceptable offset instability after each flip pulse (the noise PSD is in the order of 10 nT/sqrtHz@1Hz, i.e. 50x worse than HMC1021).

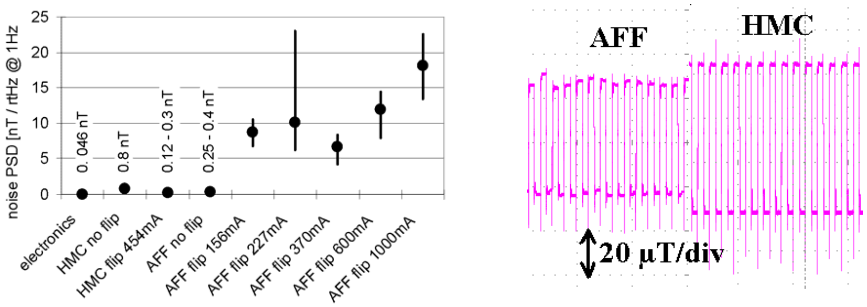

Figure 4. Left: noise PSD values for HMC and AFF sensors for various conditions and flipping current peak values. Right: oscilloscope screenshot of AFF and HMC sensors output signal (measured at the output of synchronous detector), offset instability caused by flipping is clearly visible for the AFF sensor.

Acknowledgments

The project TE02000202 is being realized with financial support of TACR, the Technology Agency of the Czech Republic.

References

[1] Kang M H, Choi B W, Koh K C, Lee J H and Park G T,, Experimental study of a vehicle detector with an AMR sensor, *Sensors and Actuators A* **118** (2005) 278–284

[2] Taghvaeeyan S and Rajamani R, The Development of Vehicle Position Estimation Algorithms Based on the Use of AMR Sensors, *IEEE Trans. Intel. Transportation Syst.*, Vol. **13**, No. 4, Dec 2012, 1845–1854

[3] Yang B, Lei Y, Vehicle Detection and Classification for Low-Speed Congested Traffic With Anisotropic Magnetoresistive Sensor, *IEEE Sensors Journal*, Vol. **15**, No. 2 (2015), 1132–1138

[4] Hauser H, Fulmek P L, Haumer P, Vopalensky M and Ripka P, Flipping field and stability in anisotropic magnetoresistive sensors, *Sensors and Actuators A: Physical* Volume **106**, Issues 1–3, 15 September 2003, 121–125

[5] Ripka P, Vopalensky M Platil A, Döscherd M, Lenssen K-M H, Hauser H, AMR magnetometer, *Journal of Magnetism and Magnetic Materials*, Volumes **254–255**, Jan. 2003, 639–641

[6] Vopalensky M, Ripka P, Platil A, Precise magnetic sensors, *Sensors and Actuators A: Physical*, Volume **106**, Issues 1–3, 15 September 2003, 38–42

[7] Petrucha V, Kaspar P, Calibration of a Triaxial Fluxgate Magnetometer and Accelerometer with an Automated Non-magnetic Calibration System, *IEEE SENSORS 2009 Conference*, 1510–1513, DOI: 10.1109/ICSENS.2009.5398466

7.3.4 refP 15

Ripka, P.; Grim, V.; Petrucha, V., "A Busbar Current Sensor With Frequency Compensation," IEEE Transactions on Magnetics. 2017, 53(4), 1-5. ISSN 0018-9464

This paper describes the application of an integrated fluxgate sensor made by Texas Instruments. The DRV425 is currently probably the only commercially available fluxgate sensor made on chip, **MAGLAB** was cooperating with Texas Instruments on the development and later also on the application of the sensor. The author's contribution is 30% and it includes the design and testing of the magnetic sensor kit and assistance during the measurements.

A Busbar Current Sensor With Frequency Compensation

Pavel Ripka, Václav Grim, and Vojtěch Petrucha

Faculty of Electrical Engineering, Czech Technical University in Prague, 166 27 Praha, Czech Republic

DC/AC yokeless galvanically insulated electric current sensors are required for applications, e.g., in automotive and aerospace engineering, where size, weight, and/or price are strictly limited. A busbar current sensor with differential fluxgate in the hole has 1000 A range and 10 mA resolution. Using an asymmetric shape, we achieved a frequency error below ±3% up to 1 kHz, while keeping high temperature stability and low sensitivity to mechanical misalignments. The 2.5 mA/°C maximum dc drift is four times better than when using an AMR sensor and 1000 times better than when using a Hall sensor. The sensor linearity error is below 0.1%.

Index Terms— **Current sensor, fluxgate, magnetic sensor.**

I. Introduction

COMPACT yokeless current sensors are small, lightweight, and cheap. They are used in mobile and embedded applications, and for measuring high dc/ac currents, for which a magnetic core would be too large [1]–[3].

A. Busbar Sensor With Magnetic Sensors on the Surface

Conventional busbar sensors use a pair of Hall sensors on the conductor surface [4], [5]. Differential configuration partly suppresses the external fields. A current range of 10 kA is easily achievable [6], but the sensor has high offset drift. A current sensor based on magnetostriction has a similar problem with stability [7]. The use of an integrated fluxgate allows us to increase the range of the sensor to 600 A with a similar offset stability and noise. A disadvantage of current sensors of this type is their high sensitivity to the distance between the sensor and the conductor surface, which changes due to temperature dilatation. Our experiments have shown that a 0.1 mm shift of the sensor causes a 2% change in sensitivity. Another disadvantage of this type of current sensor is its very high frequency dependence: for a magnetic sensor directly on the surface of the busbar, the sensitivity at 1 kHz drops to 12% of the dc sensitivity.

B. Busbar Sensor With Magnetic Sensors in the Hole

A dc/ac current sensor with a differential integrated fluxgate inside the busbar is described in [8]. An advantage of this solution is that the range can easily be adjusted by changing the distance of the sensor from the busbar center, where the sensitivity is zero.

A similar busbar sensor with a range of 300 A is described in [9]. It uses an AMR sensor bridge in a semi-cylindrical slot in the busbar. Unlike the sensor described in [9], we use a differential sensor, which suppresses the influence of external currents and magnetic fields much more effectively.

Manuscript received August 9, 2016; revised October 18, 2016; accepted October 20, 2016. Date of publication October 25, 2016; date of current version March 16, 2017. Corresponding author: P. Ripka (e-mail: ripka@fel.cvut.cz).

Color versions of one or more of the figures in this paper are available online at http://ieeexplore.ieee.org.

Digital Object Identifier 10.1109/TMAG.2016.2620959

The busbar sensor with a hole has the advantage over a sensor on the surface that the frequency dependence is lower. With a cylindrical hole, the frequency error is 14%, while for amphitheater geometry, the error was reduced to 9% [10]. Problems with amphitheater geometry were the large sensitivity to a geometrical mismatch, and increased manufacturing complexity.

This paper presents the new shape of the busbar and the optimization of the sensor position, which led to ±3% frequency error from dc to 1 kHz. Sensitivity to temperature dilatation and geometrical mismatch is also analyzed.

All electromagnetic field simulations were performed in Ansys Maxwell using a 3-D eddy current solver and adaptive meshing. The final solution uses approximately 600k tetrahedra. Effects of heating were examined by co-simulation between Maxwell 3-D (to calculate losses) and Ansys Mechanical (to get temperature distribution).

II. Sensor Design

A. Differential Fluxgate Sensor

For the current sensor, we use the integrated fluxgate DRV425, manufactured by Texas Instruments [11]. The main advantage of this sensor is its low offset drift with temperature 5 nT/°C compared with AMR (20 nT/°C) and the Hall sensor (5 μT/°C).

Two fluxgate sensors were connected in a differential mode. Each sensor is individually feedback compensated, and we process the difference between the compensation currents. All the necessary electronics is integrated inside the sensor chips. The only external components are the sensing resistors. The compensation current flowing through the microfabricated solenoid compensation coil is in the range of 10 mA for the measured current of 1000 A. This high ratio cannot be achieved by a fluxgate-based ac/dc current transformer, due to the high parasitic capacitance of the secondary winding [12].

The two fluxgate sensors are mounted on the opposite sides of the printed circuit board. The effective distance between the sensors was 2.7 mm.

B. Busbar Geometry

Fig. 1 shows the electric current distribution inside the 60 mm × 10 mm conductor and the magnetic field in the free air for a central cylindrical hole 19 mm in diameter. While

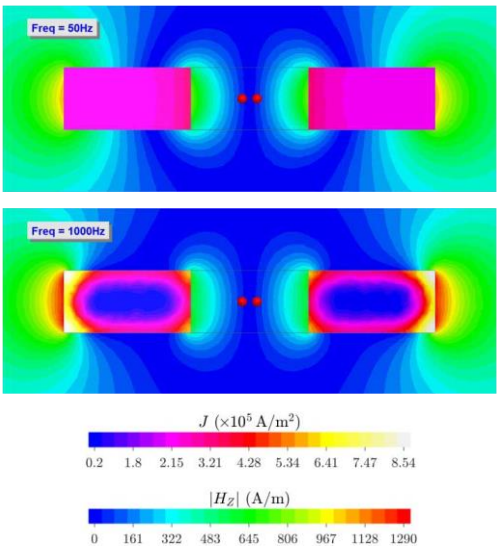

Fig. 1. Electric current distribution inside the 60 mm × 10 mm conductor and the magnetic field in the free air for a central cylindrical hole 19 mm in diameter. The FEM simulation was performed for $f = 50$ Hz and 1 kHz. Red dots: sensor positions.

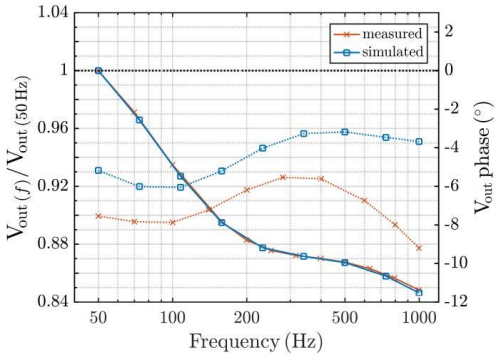

Fig. 2. Frequency dependence of the busbar current sensor with the traditional symmetrical design (measurement and 3-D simulation). Full line: amplitude characteristics. Dotted line: phase characteristics.

the current is very homogeneous for a frequency of 50 Hz, at 1 kHz, the effect of an eddy current increased the current density at the external corners by a factor of 1.5. As these regions are further away from the sensors, this results in a decreased sensitivity of the sensor.

The frequency dependence as a result of 3-D simulation and measurement is shown in Fig. 2 for a differential magnetic sensor having a gradiometric distance of 2.7 mm. The frequency error of 16% at 1 kHz should be compared with the 32% error of the transducer based on Hall sensors on the surface of the busbar [5]. The phase error at 1 kHz is 10°,

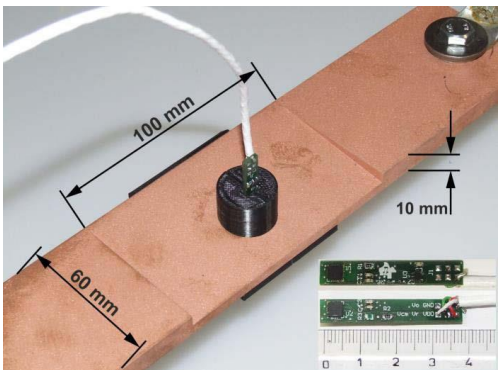

Fig. 3. New busbar sensor with a wedge-shaped profile. The circular hole is located asymmetrically and the position of the sensors in the hole is also asymmetrical.

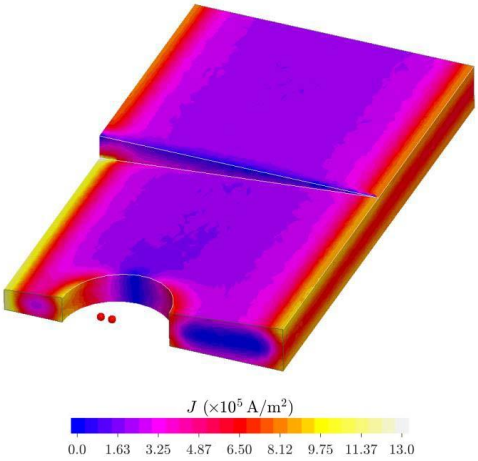

Fig. 4. Electric current distribution in the new busbar sensor at 1 kHz. Red dots: sensor positions.

which is too large for this sensor to be used for power and energy measurements. We attribute the difference between the simulated and measured phase characteristics to error in simulation, as we observed negligible phase error of the sensor itself at low frequencies.

In order to better compensate the frequency dependence, we analyzed a range of alternative geometries. Based on 3-D Finite-Element Modelling (FEM) simulations, we selected an asymmetric design with a wedge bar. The new sensor is shown in Fig. 3. The dimensions were selected, so that the sensitivity is approximately 1 mV/A. As the fluxgate sensitivity is 488 mV/mT (12.2 mA/mT with a 10 Ω sensing resistor and an instrumentation amplifier with gain of 4), the corresponding field factor is 500 A/mT.

Fig. 4 shows the 3-D FEM simulation of the current distribution of the new asymmetric design. Because of the

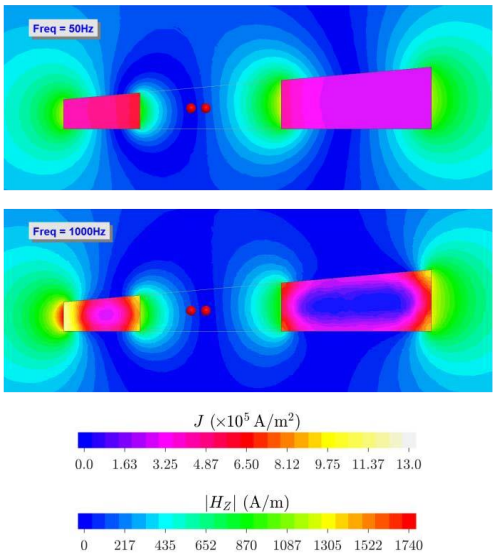

Fig. 5. Current and field distribution in the new busbar sensor with a wedge-shaped profile. 3-D FEM simulation at 50 Hz and 1 kHz. Red dots: sensor position.

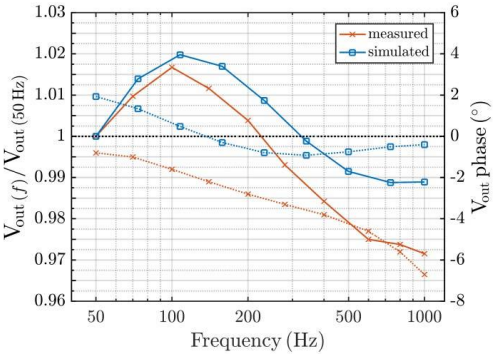

Fig. 6. Frequency dependence of the busbar current sensor with the new asymmetrical design (measurement and 3-D simulation). Full line: amplitude characteristics. Dotted line: phase characteristics.

modified shape, the current is even more redistributed due to the eddy currents. Fig. 5 shows the current and magnetic field distribution in the central plane, where both magnetic sensors are located. It is clear that the field gradient is more frequency dependent than the previous geometry. We solved the task of selecting the position of the differential sensor pair to minimize the frequency dependence while keeping a reasonable conversion factor and low sensitivity to misalignment. This optimization was made by parametric FEM simulation. The selected sensor locations are marked by red dots.

The measured frequency characteristics shown in Fig. 6 confirmed the expectations from the simulations. The measured

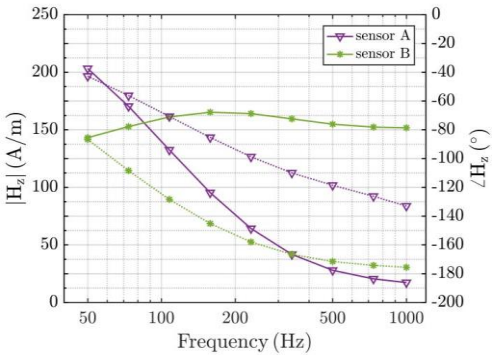

Fig. 7. Simulated frequency dependence of individual sensors.

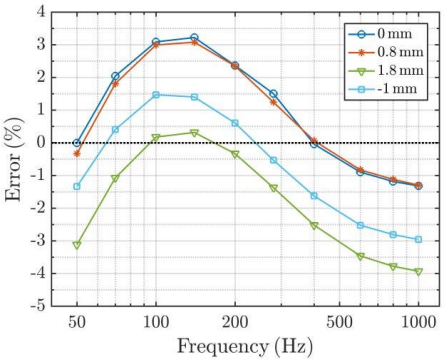

Fig. 8. Measured frequency characteristics for several values of the vertical position of the sensors in the hole. The graph shows deviation from sensitivity at 50 Hz.

frequency error up to 1 kHz is below 3%. The phase error was only slightly reduced to 8° at 1 kHz, but up to 600 Hz, the phase characteristics is linear.

Fig. 7 shows the principle of the compensation mechanism: the frequency dependence of the individual sensors is high. The differences are caused by different effect of eddy currents in each point. In this way, the frequency dependence of the differential signal is dramatically decreased. If we vectorially subtract voltages for A and B sensors, we obtain theoretical characteristics shown in Fig. 6.

The compensation technique based on the subtraction of two similar variables raises the question of the stability of this compensation in real conditions. We therefore studied the stability of the sensor with temperature and geometrical tolerances.

III. Sensor Stability and Resistance to External Currents

Fig. 8 shows how the frequency characteristics change with vertical sensor misalignment. It is clear that the changes in the shape of the frequency characteristics are negligible, but the

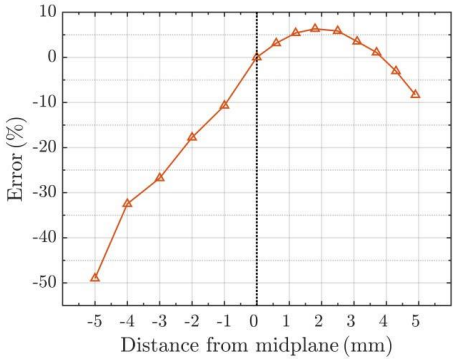

Fig. 9. Dependence of the sensitivity on the vertical position of the sensors in the hole. The graph shows deviation from sensitivity at the central point.

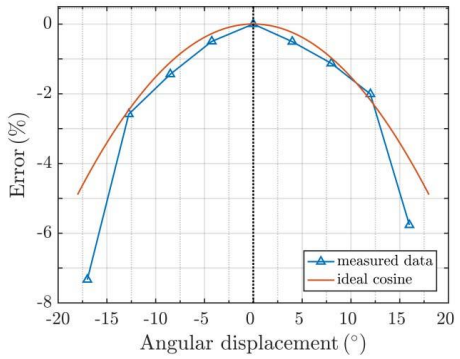

Fig. 10. Sensitivity error caused by rotational displacement of the sensor. The theoretical error caused by cosine dependence is shown for comparison.

sensitivity depends on the vertical position of the sensor, as shown in Fig. 9. The maximum sensitivity point is not in the central plane, as for a simple busbar sensor, but 2 mm above. In this optimum location, the sensitivity to position error is also minimized.

Fig. 10 shows the sensitivity to rotational displacement of the differential sensor. It is clear that the characteristics differ significantly from the cosine shape. By linear approximation, we may estimate that 0.2° angular displacement caused by temperature cycling would cause only 0.025% error, which is negligible in comparison with the 0.1% linearity error of the device.

We also examined the effect of self-heating by FEM simulations. At a maximum current of 1000 A, the temperature of the current bar is 50 °C. The sensitivity change caused by temperature effects is 1%. In comparison with this, the sensitivity change with the temperature of the fluxgate sensor itself is only 7 ppm/°C.

The dc offset stability depends mainly on the parameters of the fluxgate sensor. The specified maximum drift of 5 nT/°C would correspond to 2.5 mA/°C. The dc current resolution is limited to 10 mA, as the sensor noise power spectrum density is 2 mA/$\sqrt{\text{Hz}}$ at 1 Hz.

With a sensitivity of 500 A/mT, the calculated effect of an external 1000 A current at a distance of 15 cm is 3.4 μT, so the error is only 0.17%. We measured the influence of the external current in the real busbar and found a very similar error of 0.15%.

IV. Conclusion

The busbar fluxgate current sensor presented here has very small ferromagnetic cores inside the two integrated feedback-compensated fluxgate sensors. This keeps the power consumption of our device below 100 mW, even for the maximum measured current of 1000 A. This is much lower than the power consumption of around 15 W, even when using very efficient electronics, for another class of feedback-compensated fluxgate current sensors with large cores around the measured current conductor [13].

In addition to the advantages of the yokeless busbar current sensor, which are its small size, lightweight, and low power consumption, we also should mention its disadvantages. The sensor needs to be inserted into the measured circuit, which is not practical for ambulatory measurements. Compared with that, the yoke can be made openable as clamps. A yoke is also believed to better suppress the influence of external fields, but we have shown that the small distance of our differential sensor pair performs similarly, as the error for an external current at a distance of 15 cm is only 0.15%.

The new shape of the busbar sensor improved the frequency characteristics: the achieved error was ±3% in amplitude and 8° in phase at 1 kHz. The sensor linearity is 0.1%, in comparison with 1% in [9]. With 1000 A range, the sensor has 10 mA resolution and 2.5 mA/°C maximum dc drift. The temperature stability is, therefore, four times better than when using an AMR sensor and 1000 times better than when using Hall sensors. The external current in a 9 cm distant busbar is suppressed by a factor of 66.

Acknowledgment

The authors would like to thank A. Chirtsov, who performed some of the measurements. A. Chirtsov and V. Grim received student support from Texas Instruments, which also supplied the sensor boards.

References

[1] P. Ripka, "Electric current sensors: A review," *Meas. Sci. Technol.*, vol. 21, no. 11, pp. 1–23, Sep. 2010.
[2] G. Velasco-Quesada, M. Roman-Lumbreras, A. Conesa-Roca, and F. Jerez, "Design of a low-consumption fluxgate transducer for high-current measurement applications," *IEEE Sensors J.*, vol. 11, no. 2, pp. 280–287, Feb. 2011.
[3] X. Yang, Y. Li, W. Zheng, W. Guo, Y. Wang, and R. Yan, "Design and realization of a novel compact fluxgate current sensor," *IEEE Trans. Magn.*, vol. 51, no. 3, pp. 1–4, Mar. 2015.
[4] BBM. *Current Sensors Manufactured by Senis, Catalogue*, accessed Nov. 4, 2016. [Online]. Available: http://www.senis.ch/
[5] M. Blagojević, U. Jovanović, I. Jovanović, D. Mančić, and R. S. Popović, "Realization and optimization of bus bar current transducers based on Hall effect sensors," *Meas. Sci. Technol.*, vol. 27, no. 6, p. 065102, 2016.

[6] K.-L. Chen and N. Chen, "A new method for power current measurement using a coreless Hall effect current transformer," *IEEE Trans. Instrum. Meas.*, vol. 60, no. 1, pp. 158–169, Jan. 2011.

[7] F. Koga, T. Tadatsu, J. Inoue, and I. Sasada, "A new type of current sensor based on inverse magnetostriction for large current detection," *IEEE Trans. Magn.*, vol. 45, no. 10, pp. 4506–4509, Oct. 2009.

[8] M. F. Snoeij, V. Schaffer, S. Udayashankar, and M. V. Ivanov, "Integrated fluxgate magnetometer for use in isolated current sensing," *IEEE J. Solid-State Circuits*, vol. 51, no. 7, pp. 1684–1694, Jul. 2016.

[9] Z. Zhenhong, O. Syuji, A. Osamu, and K. Hideto, "Development of the highly precise magnetic current sensor module of +/−300 A utilizing AMR element with bias-magnet," *IEEE Trans. Magn.*, vol. 51, no. 1, pp. 1–5, Jan. 2015.

[10] P. Ripka, M. Přibil, V. Petrucha, V. Grim, and K. Draxler, "A Fluxgate Current Sensor With an Amphitheater Busbar," *IEEE Trans. Magn.*, vol. 52, no. 7, Jul. 2016, Art. no. 4002004.

[11] *DRV425 Fluxgate Magnetic-Field Sensor, Texas Instruments Datasheet*, accessed Nov. 4, 2016. [Online]. Available: http://www.ti.com/product/DRV425/datasheet

[12] P. Ripka, K. Draxler, and R. Styblikova, "AC/DC current transformer with single winding," *IEEE Trans. Magn.*, vol. 50, no. 4, Apr. 2014. Art. no. 8400504.

[13] G. Velasco-Quesada, M. Román-Lumbreras, R. Pérez-Delgado, and A. Conesa-Roca, "Class H power amplifier for power saving in fluxgate current transducers," *IEEE Sensors J.*, vol. 16, no. 8, pp. 2322–2330, Apr. 2016.

7.3.5 refP 16

Petrucha, V.; Novotný, D., "Testing and application of an integrated fluxgate sensor DRV425," Journal of Electrical Engineering. 2018, 2018(69), 418-421. ISSN 1335-3632

Another paper dealing with the integrated fluxgate sensor DRV425. In this case, we explored a strange behavior shared by several sensors we had in stock (increased low frequency noise) and presented an application of the DRV425 in a compact, USB-powered probe for magnetic field sensing. The author's contribution is 50%; it includes supervision by D. Novotný, hardware design, and assistance during the measurements.

DOI: https://doi.org/10.2478/jee-2018-0064
https://sciendo.com/article/10.2478/jee-2018-0064

Low-noise magnetic observatory variometer with race-track sensors

M Janošek[1], **V Petrucha**[1] **and M Vlk**[2]
[1]Czech Technical University in Prague, Technicka 2, 166 27 Prague, Czech Republic
[2]Institute of Geophysics, Bocni II/140, 141 31 Prague, Czech Republic

E-mail: janosem@fel.cvut.cz

Abstract. We present a low-noise, high-stability observatory magnetometer with race-track sensors, as developed by the Czech Technical University in Prague for National Observatory of Athens. As opposed to the standard instruments, we used our novel race-track fluxgate sensors with planar oval core which were cut by state-of-the art pico-second UV-laser. The noise performance of the complete electronics and sensor chain is below 6 pT/√Hz @ 1 Hz. The electronics uses 24-bit 200-Hz A/D converter with simultaneous sampling and all digital processing is done in FPGA. The variometer with the sensors mounted on a MACOR cube has been successfully calibrated by scalar method.

1. Introduction

The requirements on observatory variometers, as they are in service either officially in IAGA network, or for other purposes, are very demanding. It is necessary to achieve very high stability and low noise to record truly the diurnal Earth's field variations and possible magnetic storms (the IAGA dynamic range requirement is ± 3000 nT). Standard full-field magnetometers can be used for this purpose, if their limited dynamic range (about 130 dB for 24-bit converters) is not a problem. However, if there is a requirement of achieving very low noise, i.e. «20 pT/√Hz @ 1 Hz, compensation of the main Earth's field components (horizontal and vertical in the northern hemisphere) is inevitable [1]. Such low noise variometer, if having suitable bandwidth, can be used for advanced ionospheric or geomagnetic studies (i.e. observing Schumann resonances and other effects). We have implemented a low noise compensation of the main field components, which allowed us to use our low-noise race-track sensors (< 6 pT/√Hz) in the variometer.

2. Magnetometer construction

For the variometer, we used in-house race-track fluxgate sensors with laser-cut cores, slightly modified and downscaled of the heritage CTU sensor [2]. Two of the sensors (N-S and vertical) have an additional coil wound, which is used for main field component offset in the respective direction. For that purpose, we have implemented an ultra-low-noise (< 0.5 pT/√Hz) current source using LTC6655 reference, which feeds the additional coil wound directly on top of the feedback coil of the sensor. In that manner, the possible mutual angular imperfections and mainly their temperature instabilities are minimized. The sensor triplet (each sensor dimension are approx. 30x8x1mm^3) is mounted on a solid MACOR holder maintaining large thermal conductivity and geometric stability,

nevertheless, also the temperature of the holder is monitored – see Fig. 1. The sensor holder is attached to marble base plate, which is to be leveled. The "standard part" of the magnetometer electronics relies on a "standard low-noise magnetometer" manufactured by the CTU and CSRC (Czech Space Research Centre) company, it uses FPGA for signal clock generation and ADC driving and the power supply for the analog part is galvanically isolated. The electronics returns uncalibrated ADC data on RS232 for the three magnetometer axis and also the head temperature measurement. With the help of the low-noise current-source for the NS and vertical field offsets, the baseline noise due to electronics/ADC resolution is less than 1 pT/√Hz@ 1 Hz in the final variometer range of ±3750 nT.

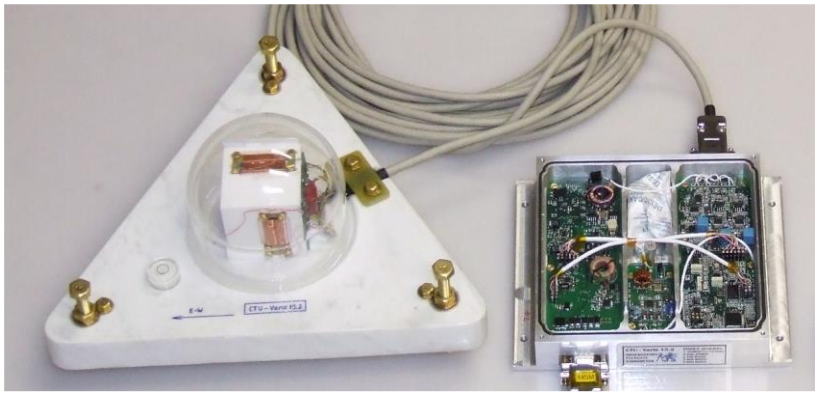

Figure 1. The presented variometer – left: the triaxial race-track fluxgate triplet mounted on MACOR holder on marble base plate, right: the electronics (cover removed).

3. Variometer calibration

A non-trivial task is variometer calibration. We used following approach using scalar calibration technique [3, 4]:

- First, the offset fields have been disabled and the magnetometer has been operated in ±75000 nT range, and a scalar calibration was done. The calibration RMS error was < 2nT.
- After the calibration, the sense resistor (the magnetometer is feedback operated) was measured .
- The resistor has been replaced with 20x larger value (again precisely measured after soldering), and the gain coefficients have been recalculated.
- In this manner, we can use the scalar calibration results, which are comparable or superior to standard techniques utilizing coils and flux density standards [5].

Valuable information has been obtained in trial tests of the magnetometer (before range expansion) during 1-month testing at the Budkov observatory (IAGA BDV). As seen from table 1, we could see ageing of the sense resistors (Vishay PLT thick film series) – the values changed by 250-300 ppm after one-month burn-in. T_c of the gain channels could be also computed: it was 8, 16 and 9 ppm/K, respectively which is a combination of thermal expansion of the compensating coil and sense resistors. From the table, it can be also seen that the mutual angular position was stable with temperature.

From the comparison of the total field computed from the variometer and values from standard instruments at the observatory, we can see that the gains have finally settled after 14 days (Figure 3).

Table 1 – The calibration results – after one month of running and with changed temperature.

Calibration date	temp [℃]	S1 [normalized]	S2 [normalized]	S3 [normalized]	O1 [nT]	O2 [nT]	O3 [nT]	Φ1 [°]	Φ2 [°]	Φ3 [°]
14.12.2014	12	1.2996	1.3068	1.2935	-18.77	-189.59	8.46	0.71	-0.09	0.11
23.1.2015	19	1.2991	1.3064	1.2933	-17.30	-190.25	7.95	0.72	-0.08	0.08
23.1.2015	6	1.2989	1.3062	1.2931	-18.22	-197.94	9.58	0.71	-0.09	0.08

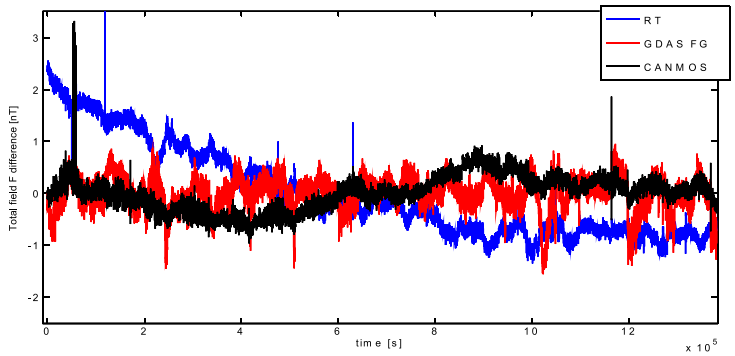

Fig. 3 – Instrument stability (before range expansion and with offsets off) – 14 days of total field (F) are displayed. Blue – CTU variometer, red and black – instruments of BDV observatory

4. Noise performance

Since the sensor head is too large to be tested in our in-house magnetic shield and also because of the need of creating a low-noise counter-acting magnetic field (simulating the NS and vertical Earth's field component), we have decided to do this test in the calm magnetic field at the BDV observatory. Typical record is depicted in the spectrogram on Figure 4: it can be seen that even at the quiet locality, man-made AC noise is present in the low-frequency spectra. AC traction noise at 16 2/3 Hz from Austria / Germany railways is also visible as burst. The source of the 3 Hz noise is still unknown.

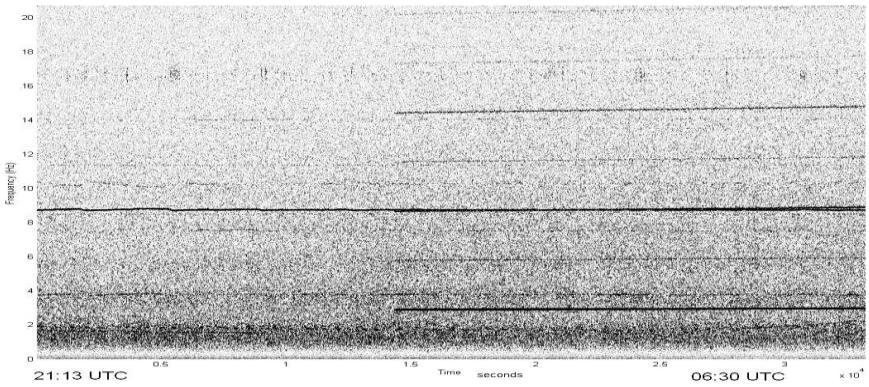

Fig. 4 – The 0.01-20 Hz spectrogram during 8-hours of logging (vertical axis)

If we have chosen a quiet part of the day, we were able to compute noise spectra as depicted in Fig.5: it can be seen, that in the vertical axis, the measured magnetic noise PSD was better than 6 pT/√Hz @ 1 Hz; however the EW and NS axes were noisier which is presumably by the magnetic field noise at the locality since the sensors in the triplet perform equally well.

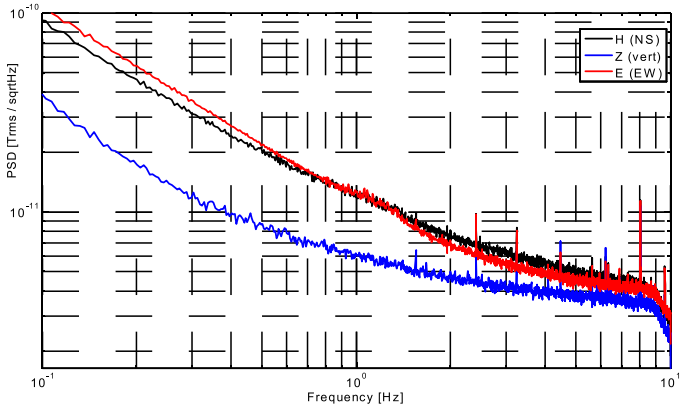

Fig. 5 – The magnetic field noise at the BDV observatory as logged with the variometer.

5. Conclusion

We have successfully built and calibrated a closed-loop operated, observatory variometer with race-track sensors. Its measured noise performance in real conditions of < 6 pT/√Hz @ 1 Hz is up to our knowledge on the state of the art in the field. We have used a simple yet effective calibrating method to obtain the instrument parameters. Further improvements are sought in terms of fluxgate sensors performance with a target of < 3 pT/√Hz. In this case however, from our experience, a large shielded room and low-noise artificial magnetic field generator would be necessary to confirm the instrument performance.

Acknowledgment
This research has been on-contract supported by the National Observatory of Athens. We would like to thank also to Dr. Tomas Bayer from the Budkov observatory for his help during calibrations at the Budkov observatory and Jan Vyhnanek of CTU for participating on the instrument development.

References

[1] Vlk M 2013, Modernisation of the Narod fluxgate electronics at Budkov Geomagnetic Observatory, *EGU General Assembly 2013, Vienna, Austria*, EGU2013-7721
[2] Ripka P 1993, Race-track fluxgate sensors, *Sensors and Actuators A: Physical*, **37** 417-421.
[3] Petrucha V et al 2009, Automated system for the calibration of magnetometers, *Journal of Applied Physics*, **105(7)** 07E704.
[4] Olsen N et al 2003, Calibration of the Ørsted vector magnetometer. *Earth, planets and space*, **55**(1) 11-18.
[4] Zikmund A and Janosek M 2014, Calibration procedure for triaxial magnetometers without a compensating system or moving parts, *IEE International Instrumentation and Measurement Technology Conference (I2MTC) Proceedings*, 473-476

7.3.6 refP 17

Petrucha, V.; Novotný, D.; Šobíšek, K., "Magnetometry package for LVICE2 mission - Triaxial fluxgate and AMR magnetometer for scientific data production near Moon," In: IEEE SENSORS 2023 CONFERENCE PROCEEDINGS. Piscataway, NJ: IEEE, 2023. ISBN 979-8-3503-0387-2

This article presents work on the LVICE2 (Lunar Vicinity Complex Environmental Explorer). The author was responsible for the development of the fluxgate magnetometer and integration with the AMR magnetometer to provide accurate measurements of the cis-lunar magnetic field for scientific purposes. The article presents two versions of the vector-compensated, triaxial fluxgate head along with the corresponding electronics and preliminary testing results. A new version of the AMR magnetometer is also introduced. The author's contribution was 60%.

Magnetometry package for LVICE2 mission

Triaxial fluxgate and AMR magnetometer for scientific data production near Moon

Vojtěch Petrucha, David Novotný, Kajetán Šobíšek

Department of Measurement, Faculty of Electrical Engineering, Czech Technical University in Prague, Czech Republic

petruvoj@fel.cvut.cz

***Abstract*—LVICE2 is a planned mission to the vicinity of the Moon. It is intended to measure dust particle concentrations in Kordylewski clouds, study turbulences in solar wind, and provide long-term monitoring. The probe will have three magnetometers. A fluxgate magnetometer with a unique inner structure placed on a 2-meter-long boom will provide the main scientific data, while a compact AMR magnetometer located at the edge of the boom will help minimize the residual magnetic signature of the probe itself. The development of both magnetometers is presented as well as the first testing results. The third (search-coil) magnetometer for measurement at higher frequencies is not covered here.**

Keywords—fluxgate; AMR; magnetometer

I. Introduction & Motivation

The Lunar VIcinity Complex Environmental Explorer—LVICE[2]—is a Czech Ambitious Mission project. It is currently finishing a one-year phase in its project development. During this period, a magnetometer package based on our previous experience and development was designed, manufactured using rapid prototyping methods, and partially tested. We used 3D printing to create a fluxgate sensor assembly in two versions. The first concentrated on small dimensions and weight. For the second, the focus was on better performance (lower noise) as a concept of the space probe developed from 16U CubeSat into the bigger microsat category allowing higher mass of the fluxgate sensor in order to serve as a counter-weight for a search-coil magnetometer located on the opposite side of the probe, on another boom (Fig. 1).

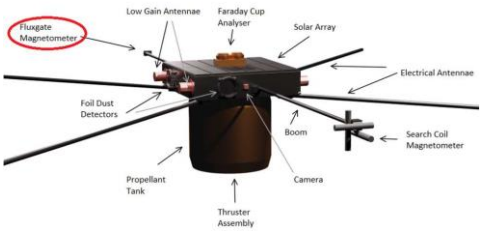

Fig. 1 Probe overall concept. Fluxgate and search-coil magnetometer sensor heads on opposite sides.

The magnetic field in the area of interest—cislunar space, far tail of the Earth's magnetosphere, lunar orbit, Lagrange points L4 and L5 of the Earth–Moon system—is relatively week (tens of nT max.) [1]. So, the offset time/temperature stability is a critical parameter, as a change in the temperature of the sensor of, for example, 20 K could lead to an offset change of 2 nT, which might be 50% of the measured field magnitude at some point. The magnetic cleanliness of the whole spacecraft will also be important [2]. A gradiometric configuration of a precise, low-noise fluxgate sensor and a noisier AMR magnetometer is proposed in order to suppress the perturbations caused by other probe components [3]; see Fig. 2.

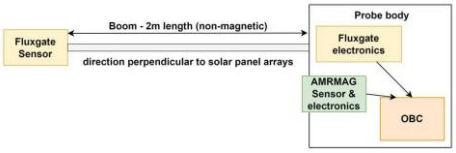

Fig. 2 Placement of fluxgate and AMR magnetometer to suppress the probe's magnetic disturbances (the algorithm will be run by on-board computer).

II. Fluxgate Magnetometer Design

A. Miniature fluxgate sensor head

The first fluxgate sensor design concentrated on mass and dimension minimization. As with other magnetometers designed for precise measurements in space [4]–[7], it uses vector compensation for the measured magnetic field. Separate compensation winding (modified 4-coil Merritt) is still needed, as the coil constant must be rather low—the measured field is small—while we want a coil with high sensitivity for signal pick-up. We wanted to keep the internal structure as symmetrical as possible, so six single-axis race-track sensors were used, two pieces per axis—a topology similar to that proposed in [8]; see Fig. 3. This sensor fits in a box with outer dimensions of $59 \times 39 \times 37$ mm^3 and provides 8 pT/√Hz at 1 Hz (for digital output at 250 Sa/s). The race-track sensor construction is described in [9].

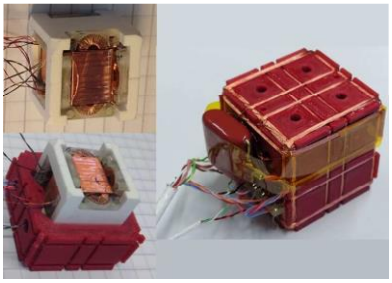

Fig. 3 Six 20 mm race-track sensors (17.4 mm magnetic core length) based on a triaxial fluxgate sensor with vector compensation (30 mm cube side).

2023 IEEE SENSORS | 979-8-3503-0387-2/23/$31.00 ©2023 IEEE | DOI: 10.1109/SENSORS56945.2023.10325159

B. *Low noise sensor head*

As mentioned, the magnetic field to be measured in the cislunar space can be just units of nanotesla, so there was a request to decrease the noise even further. A similar design was used incorporating only three race-track sensors (40 × 17 × 3 mm^3 dimensions) with a 30 mm amorphous magnetic core length. With only three sensors, the internal structure is much simpler, fixed together more reliably by screws rather than by gluing (as in the 30 mm cube), but not symmetrical. We plan to build another unit with a six-sensor symmetrical design for comparison. Fig. 4 illustrates the sensor production; the final outer protective box is not shown. As the probe as well as the sensor head will be almost continually exposed to sunlight, no heater is currently planned in the design.

Fig. 4 Three 40 mm race-track-sensor–based triaxial fluxgate sensor head with a vector compensation of measured field (50 mm cube side).

C. *Fluxgate sensor electronics*

The mission budget does not allow for full deployment of radiation-tolerant parts or ASICs designed specifically for fluxgate signal conditioning in the space environment. A traditional, single-range, analog signal–conditioning approach allowed us to reach a sufficient measurement resolution even with 16-bit ADC, as the full scale is limited to ±500 nT (while there are also 18- and 20-bit versions of the ADC). The whole unit is managed by an MSP430FR5969 16-bit low-power microcontroller, which has a direct replacement in the form of a radiation-hardened part (MSP430FR5969-SP). The MCU generates all necessary signals for fluxgate sensor excitation, synchronous demodulation, daisy-chained external ADC handling, housekeeping measurements (sensor and electronics temperature, power rail voltages using internal 12-bit ADC), step-down DCDC converter synchronization, and RS422 communication. See Fig. 5 for a block diagram of the concept. Active parts were selected based on our previous experience (^{60}Co radiation testing) or based on the availability of direct or similar radiation-tolerant replacements or published data [10]. The electronics were built on a four-layer PCB with PC104 format dimensions to be stackable in a cube-sat format (Fig. 6).

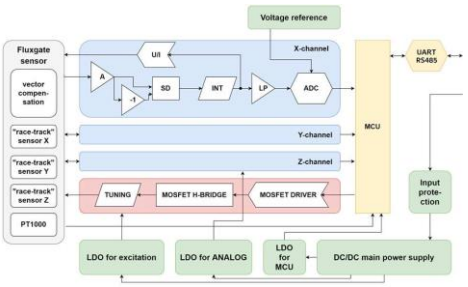

Fig. 5 Fluxgate magnetometer block diagram.

Fig. 6 Fluxgate magnetometer electronics prototype, PC104 format.

III. AMR Magnetometer Design

The anisotropic-magneto-resistance–based magnetometer is designed to sense perturbations coming from the probe itself (reaction-wheel operation, occasional switching of higher currents, etc.). It has a much higher full-scale range (currently ±100 μT), as it will be placed directly on the probe structure close to the boom release mechanism. The design is based on the construction described in [11]. HMC1021 sensors are used. We plan to test HMC1001, which has lower noise but also a compensation coil constant. That is problematic for Earth's like field full-scale range (compensation current 25 mA for 50 μT), but with a range limited, for example, to ±10 μT, it could provide significantly lower noise. The ratio between the fluxgate and AMR magnetometer noise defines the minimal length of the boom; the higher AMR sensor noise must be compensated by a $1/r^3$ field decay rate. Fig. 7 presents a simplified block diagram of the device. The main microcontroller is an STM32F334, which has proved to be well resistant to radiation when tested for TID by ^{60}Co gamma source [11].

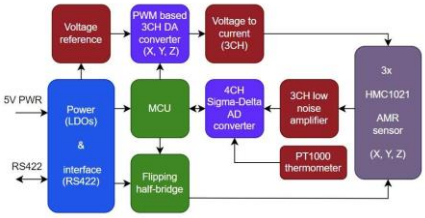

Fig. 7 Simplified block diagram of the AMR magnetometer.

Fig. 8 Triaxial AMR magnetometer prototype.

Recently, we also gathered some data from He nuclei irradiation of the whole magnetometer. The unit had to be restarted due to multiple SEL events, but as the power supply was cycled, there was no permanent damage. The magnetometer prototype is shown in Fig. 8. Components (only commercial off-the-shelf) are populated on both sides of the four-layer PCB.

IV. Results

A test campaign is in progress. Noise, linearity, and temperature dependencies were measured for the fluxgate magnetometer. Magnetic noise was measured in a six-layered MuMETAL magnetic shield; the results are shown in Fig. 9. The value of 5 $pT_{RMS}/\sqrt{Hz}$ at 1 Hz for the larger sensor is comparable to the best instruments used in space missions. It would be possible to go down to 2.3 $pT_{RMS}/\sqrt{Hz}$ at 1 Hz as indicated in the figure, but the power consumption and dimensions would be higher, which is not acceptable for the LVICE2 mission (mainly the increased power).

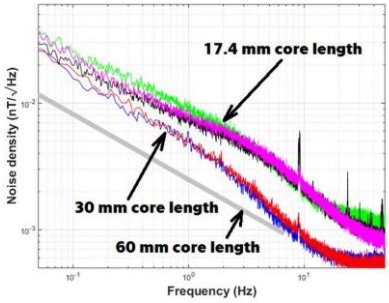

Fig. 9 Fluxgate sensor noise for digital output data, for two sensor heads of different sensor size—magnetic core length. The noise is 5 and 8 pT/√Hz at 1 Hz for 30 and 17.4 mm race-track cores, respectively. For comparison only, noise for a 60 mm long magnetic core is also drawn.

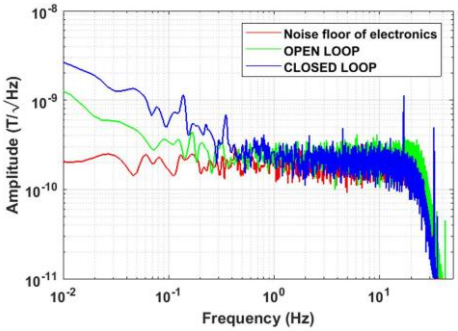

Fig. 10 AMR sensor noise (approx. 250 $pT_{RMS}/\sqrt{Hz}$ at 1 Hz for standard closed loop operation).

Fig. 10 presents the noise of the AMR magnetometer in open and closed loop modes, the second being the default. All other available parameters are summarized in Table 1.

TABLE I. AMR & FMAG Parameter Summary

Parameter	*AMR*	*Fluxgate*
Range	±100 µT	±500 nT
Noise	250 pT/√Hz at 1Hz	5 / 8* pT/√Hz at 1Hz
Linearity	±0.01% of full scale	±0.1% of full scale
Sampling	up to 3906 Sa/s	up to 250 Sa/s
Temp. coef.	<2 nT/K offset, <20 ppm/K sensitivity	<50 pT/K offset (sensor)
Orthogonality	<0.1°	<0.1° (after calibration)
Power	~0.6 W	~2 W
Dimensions	107 × 57 × 15 mm^3	electronics PC104 format, sensor (see text)
Mass	120 g with case (20 g bare PCB)	190/360* g sensor in box inc. cable, 350 g electronics in box

*see text; 30 mm or 50 mm cube side dimension sensor

In continuing work, we will concentrate on offset temperature stability improvement of the fluxgate sensor, as this will be critical for reliable magnetic field measurements, radiation testing of the fluxgate magnetometer prototype, and further testing of the AMR magnetometer (e.g., heavy ion irradiation, HMC1001 sensor application). Most important is the development and testing of the magnetic disturbance correction algorithms, as discussed e.g. in [5], including the algorithms for in-space calibration of mutual alignment of the AMR and fluxgate sensor and development of in-flight calibration algorithms [12, 13], as the possibility to calibrate the sensor offsets by motorized rotation of the whole spacecraft is not very feasible (potential navigation/motor firing risks and loss of fuel). The mission will also suffer from limited bandwidth for scientific data download, and we expect to explore ways to minimize the required bandwidth [14].

Acknowledgments

The presented work was funded through an ESA Contract in the Czech Third-Party Framework Project and by a grant (SGS22/170/OHK3/3T/13) by Czech Technical University in Prague.

REFERENCES

[1] J. H. Piddington, "The cis-lunar magnetic field," *Planet. Space Sci.*, vol. 9, no. 6, pp. 305–18, 1962. doi:10.1016/0032-0633(62)90021-1

[2] M. de Soria-Santacruz et al., "An approach to magnetic cleanliness for the Psyche Mission," *2020 IEEE Aerosp. Conf., Big Sky, MT, USA, 2020*, pp. 1–15. doi:10.1109/AERO47225.2020.9172801

[3] O. D. Constantinescu, H. U. Auster, M. Delva, O. Hillenmaier, W. Magnes, and F. Plaschke, "Maximum-variance gradiometer technique for removal of spacecraft-generated disturbances from magnetic field data," *Geosci. Instrum.* vol. 9, pp. 451–69, 2020. doi:10.5194/gi-9-451-2020

[4] C. T. Russell et al., "The magnetospheric multiscale magnetometers," *Space Sci. Rev.*, vol. 199, pp. 189–256, 2016. doi:10.1007/s11214-014-0057-3

[5] W. Magnes et al., "Space weather magnetometer aboard GEO-KOMPSAT-2A", *Space Sci. Rev.*, vol. 216, Art. num. 119, 2020. doi:10.1007/s11214-020-00742-2

[6] H. U. Auster et al., "The THEMIS fluxgate magnetometer," *Space Sci. Rev.*, vol. 141, pp. 235–64, 2008. doi:10.1007/s11214-008-9365-9

[7] B. P. Weiss, "The Psyche magnetometry investigation," *Space Sci. Rev.*, vol. 219, p. 22, 2023. doi:10.1007/s11214-023-00965-z

[8] K. Greene, C. Hansen, B. B. Narod, R. Dvorsky, and D. M. Miles, "Tesseract – a high-stability, low-noise fluxgate sensor designed for constellation applications," *Geosci. Instrum. Method. Data Syst.*, vol. 11, pp. 307–21, 2022. doi:10.5194/gi-11-307-2022

[9] V. Petrucha and M. Butta, "Race-track fluxgate sensor scaling versus noise," *2021 IEEE Sensors, Sydney, Australia, 2021*, pp. 1–4. doi:10.1109/SENSORS47087.2021.9639560

[10] S. M. Guertin, M. Amrbar and S. Vartanian, "Radiation test results for common cubesat microcontrollers and microprocessors," *2015 IEEE Radiation Effects Data Workshop (REDW), Boston, MA, USA, 2015*, pp. 1–9. doi:10.1109/REDW.2015.7336730

[11] D. Novotny, V. Petrucha, M. Dressler and A. Platil, "Characterization of a digital AMR magnetometer for space applications," in *IEEE Trans. Instrum. Meas.*, vol. 70, pp. 1–9, 2021, Art no. 9504309, doi:10.1109/TIM.2020.3043867

[12] H. K. Leinweber, C. T. Russell, K. Torkar, T. L. Zhang and V. Angelopoulos, "An advanced approach to finding magnetometer zero levels in the interplanetary magnetic field," *Meas. Sci. Technol.*, vol. 19, p. 055104 (15 pp.), 2008. doi:10.1088/0957-0233/19/5/055104

[13] F. Plaschke, "How many solar wind data are sufficient for accurate fluxgate magnetometer offset determinations?" *Geosci. Instrum. Method. Data Syst.*, vol. 8, pp. 285–291, 2019 doi:10.5194/gi-8-285-2019

[14] D. Fischer, G. Berghofer, W. Magnes and T. L. Zhang, "A lossless compression method for data from a spaceborne magnetometer," *2008 6th Int. Symp. Comm. Syst., Networks Digital Signal Process., Graz, Austria, 2008*, pp. 326–30, doi:10.1109/CSNDSP.2008.4610829